Catalytic behaviour of nickel-based catalysts operating on simulated biogas: optimisation through oxygen addition, temperature variation and catalyst modification

David J. Nixon

Doctor of Philosophy

June 2013

Keele University

Abstract

The use of catalytic systems operating on waste products such as biogas offers a potentially attractive alternative for renewable and sustainable energy generation. To investigate the potential viability of such catalytic systems for operation on biogas, a detailed study of nickel-based catalysts for the reforming of simulated biogas (methane:carbon dioxide = 2) to synthesis gas has been undertaken. The influence of oxygen addition in varied concentrations to the simulated biogas mixture has been investigated with regards to catalyst activity, selectivity and stability. This influence has been studied over an extended temperature range from room temperature to 1000 °C.

Additionally, the effect of H_2S within the simulated biogas mixture on the catalyst activity, selectivity and stability has been studied. Also, the influence of ceria-doping of the nickel catalyst on catalytic behaviour has been investigated.

Temperature programmed and conventional catalytic reaction measurements have been used to analyse the catalytic behaviour and long term stability of the catalyst system over a full range of reaction temperatures. Carbon deposits from the simulated biogas reforming were analysed using post-reaction temperature programmed oxidation to assess the extent and nature of carbon deposition.

The addition of oxygen significantly increases catalyst activity and shows a variation in product selectivity with temperature. Increased catalyst stability through reduced carbon deposition and increased sulfur tolerance is also observed with oxygen addition. Doping of the nickel catalyst with ceria enhances the influence of oxygen, apart from at high oxygen levels where total oxidation of methane is prevalent. Catalyst regeneration from sulfur poisoning has also been shown through oxygen addition to the simulated biogas mixture and ceria-doping of the nickel catalyst.

Fuel cell studies have shown the successful operation of solid oxide fuel cells on simulated biogas and the substantial improvements in electrical performance through addition of oxygen and increased temperature.

‘Continuous effort - not strength or intelligence - is the key to unlocking our potential’

Sir Winston Churchill

Acknowledgements

I would like to thank all of the friends and colleagues at Keele University who have provided the inspiration, camaraderie and support that has proved vital to the production of this study.

In particular, I must convey my special thanks and appreciation to Prof R. Mark Ormerod for granting such a once in a lifetime opportunity, for his wealth of knowledge and for the support and guidance that has been a constant for the duration of the study. I would also like to thank Dr. John Staniforth, as without your daily assistance, guidance and positivity, this study would not have been made possible.

Past and present colleagues from the University and specifically the research group including Dr. Richard Darton, Dr. Christian Laycock, Dr. Lina Meghani, Matthew French, Samuel Evans and Oliver Good must receive acknowledgement for their friendship and advice, and for providing welcome company during visits to the KPA bar.

I would also like to thank David Evans for providing the technical and manual expertise and assistance to keep the study on track and on time.

Thanks must go to Elizabeth Norris, with whom I have shared this journey, and who has ensured that I have made it this far despite times of great difficulty and stress, and that I can look back and view this experience as being one of enormous enjoyment and fulfilment.

Finally, I would like to convey my appreciation and thanks to my family for their unconditional support and unfaltering belief over the previous years. I hope I have made you proud.

Table of contents

List of Figures

List of Abbreviations

AFC	-	*Alkaline Fuel Cell*
BET	-	*Brunauer Emmett Teller Theory*
CHP	-	*Combined Heat and Power*
DMFC	-	*Direct Methanol Fuel Cell*
ISO	-	*Isothermal reaction*
LSM	-	*Lanthanum Strontium Manganate*
MCFC	-	*Molten Carbonate Fuel Cell*
MSW	-	*Municipal Solid Waste*
PAFC	-	*Phosphoric Acid Fuel Cell*
PEMFC	-	*Proton Exchange Membrane Fuel Cell*
QMS	-	*Quadrupolar Mass Spectrometry*
RDS	-	*Rate Determining Step*
RGA	-	*Residual Gas Analyser*
SOFC	-	*Solid Oxide Fuel Cell*
SPARG	-	*Sulfur Passivated Reforming*
TPB	-	*Three Phase Boundary*
TPO	-	*Temperature Programmed Oxidation*
TPR	-	*Temperature Programmed Reduction*
TPX	-	*Temperature Programmed Reaction*
TWC	-	*Three-Way Catalyst*
XRD	-	*X-Ray Diffraction*
YSZ	-	*Yttria Stabilised Zirconia*

1 Introduction

1.1 The energy situation

One of the primary challenges to current society is the issue of energy supply and climate change [1, 2]. This issue has become increasingly apparent and time-sensitive over the previous twenty years due to increasing world population, increased affluence and also diminishing fossil fuel reserves [2, 3].

The human population has increased substantially to over 6 billion over the last 50 years, as shown in Figure 1.1 below. This increasing population, when coupled with the increasing proportion of society considered affluent and also increased energy use, has resulted in worldwide energy consumption increasing at a rate that is unsustainable with current energy production methods (+8.7 % from 1990 to 2008) [4].

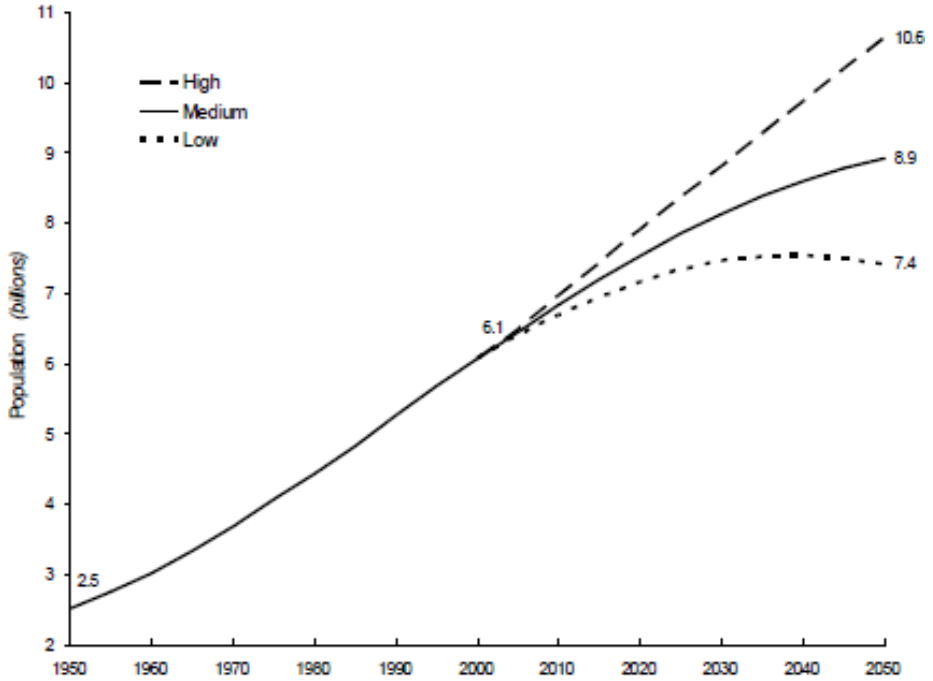

Figure 1.1: World population trends and forecast (Taken from page 5 of reference [5]).

The increasing energy consumption, fuelled primarily by fossil fuels (approximately 80 %) [2], has resulted in increased greenhouse gas emissions and subsequent climate change. The relationship

between increasing global temperature and increasing greenhouse gas emissions since 1880 is shown in Figure 1.2 [1, 2].

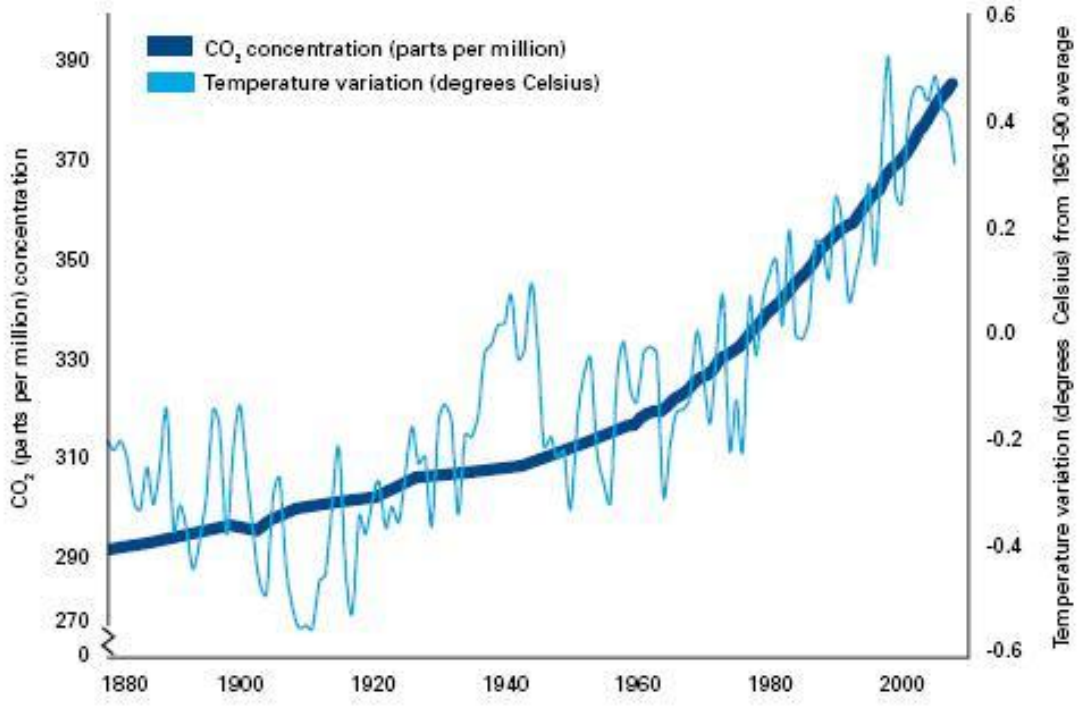

Figure 1.2: Variation in global mean temperature and greenhouse gas emission from 1880 to 2010 (Taken from page 24 of reference [1]).

There is a financial incentive for nations to actively reduce their greenhouse gas emissions due to the targets that have been agreed by the United Nations Framework Convention on Climate Change (UNFCCC) [6]. Failure to meet such targets can result in substantial fines and stricter targets moving forward. The UK has set its own emissions targets to reduce greenhouse gas emissions by 18 % of 2008 emissions by 2020 [1] in addition to those set by the UNFCCC. One of the primary measures to achieve this target is to increase electricity production from renewable sources to approximately 30 % by 2020 [1]. Significant advances are required in the next decade to reach this target, with current production of electricity from renewable sources at 9.4 % [7].

A potentially more urgent and time-sensitive issue to society, particularly to the UK, is the secure supply of energy for the future. With decreasing fossil fuel reserves, and also the instability of

many of the fossil fuel-rich nations, there is a strong drive towards the utilisation of renewable energy sources and increasing the efficiency and performance of current sources. The strong dependence of the UK on importing energy is illustrated in that UK energy production has reduced by 13.2 % in 2011 compared to 2010, and the dependency on energy imports has increased by 36 % from 2010 to 2011 [7], which is also shown in Figure 1.3 below. Despite the fact that power generation through renewable resources in the UK is increasing (6.8 % of total electricity generation in 2010 to 9.4 % in 2011 [7]), the figures regarding the decreased electricity generation in the UK and increased dependence on other nations for energy shows that significantly greater developments are necessary to enable the UK to secure a future energy supply.

Figure 1.3. United Kingdom import dependency from 1970 -2011 (Adapted from [3])

One particular source of renewable energy that is significantly underdeveloped is that of bioenergy. Bioenergy contributed 4.2 % of the total energy supplied from renewable sources worldwide in 2010 [2]. This area is evidently one that has potential to accommodate significant expansion and potentially offer a substantially greater supply of renewable energy. The economic and environmentally positive potential of bioenergy and particularly waste to energy is apparent when the emissions released from biological waste are considered. This provides the prospect of not only producing energy in a clean and sustainable manner using waste, but also to reduce emissions of greenhouse gases by utilising a material that would otherwise emit significant quantities of such gases. Atmospheric methane emissions are particularly environmentally harmful as the global

warming potential is 23 times greater than that of carbon dioxide. Bioenergy and energy from waste, and the emissions associated are discussed in detail in Section 2.1.

Although the utilisation of bioenergy and energy from waste is increasing, the current techniques for energy generation are inefficient and dated [2]. For bioenergy and energy from waste to become a stable, primary energy source, more advanced and efficient techniques such as catalysis and fuel cells are required. To allow such techniques to become economically viable and therefore widely available, substantial research and investment is needed to improve efficiency and performance.

1.2 Foundations for research

The approach to using catalysis and fuel cells as a technique to generate energy from waste offers a clean and efficient alternative to current energy generation techniques and also for synthesis gas production as a chemical commodity. This technique has been researched extensively by many groups worldwide, including over the previous 15 years by the Clean Energy and Technology Group at Keele University led by Professor R. Mark Ormerod, and is discussed in detail throughout Section 3.

During this period, research has been focused towards several different aspects of catalysis and methane reforming. This includes the different individual methane reforming approaches (steam reforming, partial oxidation and dry reforming) and optimisation of these approaches through variations in operating conditions, catalyst composition and method of catalyst manufacture. A large feature of the research conducted by the Clean Energy and Technology Group is in the use of waste biogas as a methane source, and also the operation and optimisation of fuel cells powered on biogas and natural gas [8-12]. Researchers at Keele University were one of the first to illustrate the potential for fuel cells to be powered by biogas in 1998 [13], where a solid oxide fuel cell was powered successfully and the power output compared between different landfill gas samples and pure hydrogen gas.

This original publication has led to substantial advances in the field, particularly exhibited in the recent publication by C Laycock *et al.* [14] in which the performance of catalytic techniques and fuel cells powered by biogas were optimised through variation in temperature, addition of H_2S and also variation in the catalyst material.

Through assessment of previous research, from both inside and outside of the research group, it is apparent that certain issues are still restricting the development of catalysis and fuel cell technology. These are discussed in more detail in Section 3. Through this research project, the controlled addition of oxygen as a co-oxidant is used to try and reduce the extent of these issues and increase the performance, and therefore viability of these techniques.

Research aim: *To assess the potential of using waste biogas for synthesis gas production or energy generation using catalysis through simulating biogas composition over nickel based catalysts and optimising the active catalyst material and operating conditions*

The specific objectives set throughout this project to progress towards the research aim are:

- To assess the influence of oxygen addition on the activity and selectivity of Ni/YSZ for the catalytic reforming of simulated biogas.

- To assess the influence of oxygen concentration on the activity and selectivity of Ni/YSZ for the catalytic reforming of simulated biogas.

- To assess the influence of oxygen addition and concentration on the tolerance of Ni/YSZ towards deactivation via carbon deposition during the reforming of simulated biogas.

- To assess the influence of 5 mol% CeO_2 addition to Ni/YSZ on catalytic behaviour during simulated biogas reforming and variation of operating conditions, including oxygen addition and temperature dependence.

- To assess the influence of oxygen addition and concentration on the tolerance of both Ni/YSZ and 5 mol% CeO_2-Ni/YSZ towards deactivation via sulfur poisoning during the reforming of simulated biogas and also the influence of oxygen on recovery from sulfur deactivation.
- To assess the influence of oxygen addition and concentration on the performance of a solid oxide fuel cell with a Ni/YSZ anode material operating on simulated biogas.

- To assess the influence of oxygen addition and concentration on the performance of solid oxide fuel cell with a 5 mol% CeO_2-Ni/YSZ anode material operating on simulated biogas.

It is hoped that from the research conducted throughout this study, and the subsequent findings, the potential for viable use of catalysis and fuel cells as a primary energy technology and method of synthesis gas production as a chemical feedstock from waste biogas will be further demonstrated.

1.3 References

1. *HM Government, The UK Low Carbon Transition Plan; National strategy for climate and energy*. 2009. p. 4-24.
2. *Renewables Energy Network for the 21st Century, Global Status Report*. 2012. p. 21-29.
3. *Department of Energy and Climate Change, UK Energy in Brief*. 2012. p. 8-20.
4. *International Energy Association, Key World Energy Statistics*. 2010. p. 28-29.
5. *United Nations Department for Economic and Social Affairs, World Population to 2300*. 2004: New York. p. 5.
6. UNFCC, *Kyoto Procol reference manual on accounting of emissions and assigned amount*. 2008. p. 40-45, 77-90.
7. *Department of Energy and Climate Change, Digest of United Kingdom Energy Statistics*. 2012. p. 121.
8. R.M. Ormerod, *Solid oxide fuel cells.* Chemical Society Reviews, 2003. **32**(1): p. 17-28.
9. C.M. Finnerty and R.M. Ormerod, *Internal reforming over nickel/zirconia anodes in SOFC operating on methane: influence of anode formulation, pre-treatment and operating conditions.* Journal of Power Sources, 2000. **86**: p. 390-394.
10. C.M. Finnerty, R.H. Cunningham, and R.M. Ormerod, *In situ catalytic and electrocatalytic studies of internal reforming in solid oxide fuel cells running on natural gas.* Studies in Surface Science and Catalysis, 2000. **130**: p. 425-430.
11. J. Staniforth, *The use of biogas to power a small tubular solid oxide fuel cell, PhD Thesis*. 2000, Keele University.
12. J. Staniforth and K. Kendall, *Cannock landfill gas powering a small tubular solid oxide fuel cell - a case study.* J. Power Sources, 2000. **86**: p. 401-403.
13. J. Staniforth and K. Kendall, *Biogas powering a small tubular solid oxide fuel cell.* J. Power Sources, 1998. **71**: p. 275-277.
14. C.J. Laycock, J.Z. Staniforth, and R.M. Ormerod, *Biogas as a fuel for solid oxide fuel cells and synthesis gas production: effects of ceria-doping and hydrogen sulfide on the*

performance of nickel-based anode materials. Dalton Transactions, 2011. **40**(20): p. 5494-5504.

2 Literature study

To fully understand the nature and potential of biogas reforming through use of nickel based catalysts, an extensive study of the appropriate literature was performed.

2.1 Biofuels including biogas

Biofuels are one source of renewable energy that is substantially under-utilised. Biofuel can be distinguished into two main categories; high value biofuel and biofuel from waste. High value biofuel consists of any biomass that is purposely grown for use as a fuel. This can include plants such as rapeseed, soybean, palm, and sunflower for the production of biodiesel. High value biofuels can also include high yield crops (energy crops) such as poplar [1], willow [2], and miscanthus [3]. Whilst such high value biofuel crops may provide some capacity for a reduction in the use of non-renewable energy, they also require large land areas, significant investment and long term commitments to be economically viable.

However, with biofuels obtained from waste, the main input is the technology required to harness their potential. Biofuels from waste can be utilised in a variety of different methods. The primary method for the utilisation of solid biomass is through combustion [4]. This method is inefficient (approximately 30 % [5]) due to heat loss and produces a significant quantity of carbon dioxide. Also, the solid matter (ash) remaining post-combustion has little value or use as it contains easily soluble salts, heavy metals and dioxins which are detrimental to the environment [6]. Consequently, it is usually disposed of by adding to construction materials such as concrete or by placing in landfill [6-8].

Certain biofuels from waste can also be utilised to produce liquid biodiesel through transesterification [9]. This approach has a limited capacity as the waste must not contain oils from animal or food waste. Biodiesel production from waste is often supplemented using high value oil crops due to this limited capacity. This supplementation results in biodiesel having a greater cost than petroleum based diesel, therefore making it economically unfavourable. There is also

significant concern that the requirement for crops to produce biodiesel will compete with the requirement for food production [10].

The second most popular method of utilizing energy from waste is through gasification to produce biogas. Biogas is a methane-rich gas produced from organic waste and has been used as an energy source for over 100 years [11]. Biogas can be generated by two distinct methods. One method is to use a fast, high temperature process known as pyrolysis to convert biomass to biogas. The temperature used determines the phase of the product whether it be solid charcoal, liquid bio-oil or biogas [5, 9]. This method requires a significant energy input and also produces ash as a waste product. Alternatively, biogas can be produced from the digestion of the organic matter in the absence of oxygen. The low temperatures required for anaerobic digestion and the production of a high value digestate that can be used as a fertiliser [12-14] makes the production of biogas through anaerobic methods significantly more attractive than through pyrolysis.

2.1.1 Anaerobic digestion

Anaerobic digestion is a naturally occurring process and occurs to produce biogas in various sources such as municipal solid waste and landfill, agricultural waste, animal manure and wastewater. The natural prevalence and availability makes biogas a potentially viable major source of renewable energy. It is estimated that over 100 million tonnes of organic material that could be used to produce biogas are generated in the UK each year. The UK Government suggest that this biogas could contribute 10-20 TWh of energy by 2020, providing approximately 3.8-7.5 % of the legal requirement that 15 % of UK energy is derived from renewable sources by 2020 [12, 15].

The typical composition of biogas is 48-65 % methane, 36-41 % carbon dioxide, <1-17 % nitrogen, <1 % oxygen, hydrogen sulfide concentrations ranging from >0.1 – 427 ppm and a number of trace compounds can also be present [16]. The composition can vary significantly depending on type of organic material, location and age of source. Factors such as temperature and humidity have a significant influence on the gas composition [17-19]. Bogner and Spokes [18] suggest that the

water content of the biogas source is the most influential factor determining biogas production and composition.

Temperature influences the biogas composition and rate of production through determining the bacteria cultures present. Anaerobic digestion is often classified by which temperature range it operates most efficiently at [9]:

- Psychrophilic (Optimum temperature range: 12-16 °C)

  Occurs naturally and is prevalent in biomass sources such as landfill and wastewater.
- Mesophilic (Optimum temperature range: 35-37 °C)

  Can occur naturally providing climate is appropriate. This is the dominant temperature range used within man-made anaerobic digesters,
- Thermophilic (Optimum temperature range: 55-60 °C)

  Only occurs within man-made digesters or geothermally heated systems.

Temperature increases within each range can increase the biogas production rate due to an increased metabolic rate of the bacteria. This increases to an optimum temperature, above which the particular bacteria cannot survive and biogas production ceases.

Higher temperature ranges have shown increased rates of biogas production due to the higher metabolic rate of the particular bacteria. Zupancic and Ros [20] showed that thermophiles have a significantly greater metabolic rate than mesophiles digesting similar organic matter. Despite this improved rate of biogas production, the energy input required to operate digestion at thermophilic temperatures has inhibited its use.

The process of anaerobic digestion occurs in four stages as shown in Figure 2.1.

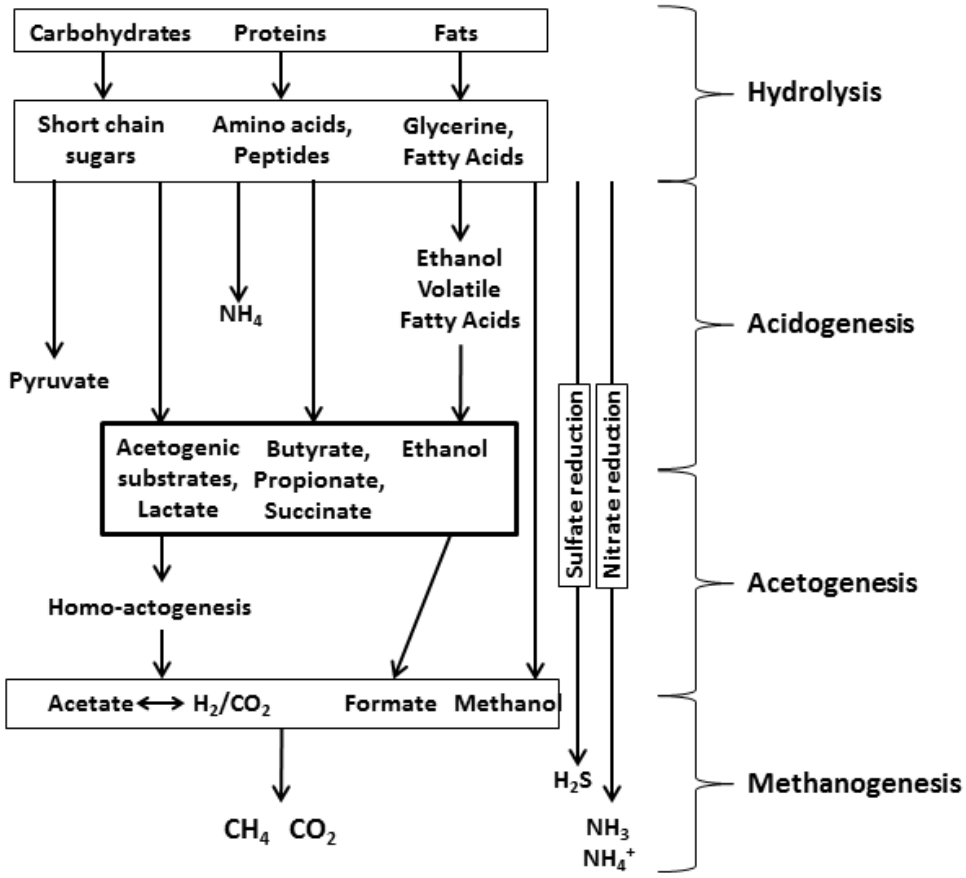

Figure 2.1: Anaerobic digestion pathway. Adapted from Deublien [11]

During the hydrolysis stage of anaerobic digestion, organic, water soluble polymeric units are broken down into smaller monomeric or dimeric units. Hydrolases break down carbohydrates to produce short chain sugars, proteases break down proteins to amino acids and peptides and lipases break down fats to produce glycerine and fatty acids. Borja *et al* [21] suggest that the hydrolysis stage is the rate limiting step of anaerobic digestion.

In the acidogenesis (fermentation) stage, the products from hydrolysis are further decomposed to give a range of molecules including hydrogen, carbon dioxide, hydrogen sulfide, alcohols, acids and small chain (C_1-C_5) molecules. In particular, short chain sugars are degraded to pyruvate, which can then be further degraded through the methymalonyl, acetyl, or butyric pathway to produce a number of different compounds. Amino acids are degraded by *Clostridium botulium* to produce ammonia, acetate and carbon dioxide [11]. Fatty acids are degraded by a range of bacterium, producing alcohols and acetate.

The acetogenic stage of anaerobic digestion is the primary hydrogen production stage in which the products from acidogenesis are further degraded. The main products of this stage are hydrogen, carbon dioxide, acetate and various acids. Gerardi [22] suggests that the acetogenic stage acts as the rate determining step within the digestion of complex organic molecules whereas for poorly biodegradable compounds, hydrolysis is more likely to be the rate determining step, supporting the suggestion by Borja *et al.* [21].

The methanogenic stage occurs simultaneously with the acetogenic stage as the methanogenic bacteria require high hydrogen partial pressures and a strict anaerobic environment. During this stage, the products of acetogenesis hydrolyse, reduce or decompose to produce primarily methane and carbon dioxide. A summary of the reactions occurring during the methanogenic stage is shown in Table 2.1

Table 2.1: Summary of reactions occurring during the methanogenic stage in anaerobic digestion [11]

Chemical reaction	$\Delta G`_f$ (kJ mol^{-1})
$4H_2 + HCO^-_3 + H^+ \rightarrow CH_4 + 3H_2O$	-135.4
$CO_2 + 4H_2 \rightarrow CH_4 + 2H_2O$	-131.0
$4HCOO^- + H_2O + H^+ \rightarrow 3HCO^-_3$	-130.4
$CH_3COO^- + H_2O \rightarrow CH_4 + HCO^-_3$	-30.9
$4CH_3OH \rightarrow 3CH_4 + HCO^-_3 + H^+ + H_2O$	-314.3
$CH_3OH + H_2 \rightarrow CH_4 + H_2O$	-113.0
$2CH_3CH_2OH + CO_2 \rightarrow CH_4 + 2CH_3COOH$	-116.3

2.1.2 Sources of biogas

Municipal Solid Waste (MSW) is by far the largest contributor of biogas worldwide due to the quantity of biomass associated with it. In the UK alone, 26.5 million tonnes of MSW were generated in 2009, of which 47 % was disposed of in landfill [23] whilst Themelis and Ulloa [24]

estimate that globally, 1.5 billion tonnes of MSW is placed in landfill per year. MSW that is not disposed of in landfill sites is either recycled or combusted to produce energy as discussed in Section 2.1. Landfill sites are sealed vessels in which the MSW is left to decompose naturally. As the organic material decomposes, biogas is produced which is either dissipated into the atmosphere or flared [25]. Flaring concerns the controlled combustion of biogas and takes place to reduce the methane concentration surrounding the landfill site to reduce the risk of explosion that can occur with high methane concentrations [25]. Both of these approaches waste a potential energy source whilst also releasing environmentally harmful methane and carbon dioxide into the atmosphere. In 2006, approximately 23 % of the methane produced in the US was from landfill emissions, equivalent to an estimated 30 million metric tonnes of carbon equivalent [26]. Projected increases of methane emissions from landfill sites [27, 28] makes this an issue requiring attention. Despite the lower quantity of methane emitted than carbon dioxide, the greater potency of methane as a greenhouse gas due to its greater ability to form radicals and decompose ozone makes the control and reduction of methane emissions highly desirable.

Generally, biogas is constantly extracted from landfill sites through a network of vertical pipes throughout the site which are used to direct the gas as required [29]. The utilization of landfill gas through catalytic reforming [30-36] has been extensively studied including early work by this research group [37-39]; however the major issues with catalytic reforming discussed in Section 2.6 have restricted its use.

A clean and efficient method in which biogas is produced is through an anaerobic digester. This is very similar to a landfill site in principle, as municipal solid waste is anaerobically decomposed within a sealed tank to produce biogas. The advantages with this approach are that the optimum conditions for anaerobic digestion can be employed to maximise biogas production and the issues with leaching and gas pressure are not present. Due to the lack of environmental issues and the relative small sizes available for anaerobic digesters, they have become a popular method of waste utilization and energy generation for isolated or small communities or farms, especially in developing countries [40].

Biogas can also be produced from wastewater and sewage, industrial waste and manure or agricultural waste. Due to the prevalence of landfill, this will be the primary focus to which this research will be aimed. Also, prior work by this research group has been focused towards the utilization of landfill gas through catalytic reforming [37-39].

2.1.3 Methods of biogas utilization

Biogas can be utilized in a number of ways with varying levels of efficiency and current use. The primary method of biogas utilization is through combustion to produce heat. Despite the greater applicability of this approach, the high levels of CO_2 produced are undesirable from an environmental viewpoint. This method is used extensively worldwide, particularly in developing countries where biogas is used as a replacement for natural gas and is extensively used for cooking and heating.

Biogas can also be used through combustion to produce electricity and heat in a combined heat and power (CHP) plant. This is achieved through the production of steam which is then used with devices such as steam turbines, steam piston engines, organic Rankine cycle systems and Cheng power systems [11, 41]. The carbon dioxide emissions from this approach make it environmentally unfriendly. Alternatively, combined heat and power can be generated through combustion in an internal combustion engine or gas turbine [41]. This is an established method of natural gas utilization and is therefore highly applicable for use with biogas. The main problem with using biogas within combustion engines is the lower methane content compared to natural gas and the variability in the composition of biogas. Increased concentrations of CO_2 within biogas significantly decrease the engine efficiency and can result in ignition problems at low methane levels [42]. Contaminants within the biogas can also result in corrosion of the system causing further decreases in efficiency [43].

One method of biogas utilization is through upgrading to be fed into the natural gas network. This method is desirable due to the current extensive, widespread use of natural gas. The main issue

with biogas is the strict specifications required in order to feed into the natural gas network, which are shown below in Table 2.2.

Table 2.2: UK requirements for feeding to natural gas network [44].

Content	**Requirement**
H_2S	≤ 5 mg/ m^3
Total Sulfur (including H_2S)	≤ 50 mg/ m^3
H_2	≤ 0.1 % (molar)
O_2	≤ 0.2 % (molar)
Impurities	Gas shall contain no solids or liquids.
Odour	Stenching agent to be added to any gas below 7 bar.
Wobbe Number (Calorific value/ density)	47.20 – 51.41 MJ/ m^3

The cost associated with biogas upgrading can be substantial, with a CH_4 content of >96 % [11] required before in-feeding, and the quantity of CO_2 that must consequently be removed. The CO_2 can be removed using various methods such as pressure swing adsorption, water absorption, carbon molecular sieves, membrane separation and polyethylene glycol absorption, all of which have significant costs associated with them [11, 45, 46].

Another issue with the upgrading of biogas is the estimated £10 bn cost associated with the alterations required in infrastructure to accommodate widespread biogas in-feeding [47]. Despite this, the probability for biogas in-feeding to the UK natural gas network is high, with significant financial incentives available through the UK government.

Another method of biogas utilisation without combustion is through catalysis. This process involves the reforming of the major components within biogas, CH_4 and CO_2, to produce H_2 and CO (synthesis gas). The details of methane reforming are discussed in Section 2.3 with specific reference to CO_2 reforming of methane in Section 2.3.3. The catalytic approach to biogas utilization is environmentally friendly as all undesirable products (H_2O and CO_2) can be recycled within the catalyst system and the synthesis gas produced has a number of different applications such as an energy source or as a chemical feedstock for other chemical processes. The uses of

synthesis gas as a chemical feedstock and energy source are discussed in Sections 2.4 and 2.5 respectively.

In comparison to the other methods of biogas utilization, catalytic reforming is the least established and widespread. The environmentally friendly nature and under-development of this approach provides significant incentive for further research and development.

2.2 Catalysis

The process of catalysis is and has been key in the discipline of chemistry. The definition of a catalyst described by Friedrich Ostwald states: "a catalyst accelerates a chemical reaction without affecting the position of equilibrium". A catalyst is used to lower the activation energy required for the rate determining step of a reaction and can be used to influence the activity and/or selectivity of a reaction. It is known that the properties of a catalyst can alter during reaction processes but do so in a cyclic fashion that allow for their continuous involvement with the reaction. Catalysis can either occur homogenously (same phase) or heterogeneously (different phase). With respect to the use of gaseous reagents, heterogeneous catalysis is usually operated with the catalyst present in solid form. Catalysts in heterogeneous reactions are used to adsorb reagents which interact with other reagents within the gas phase through surface-gas interactions, or adsorbed on the catalyst surface through surface-surface interactions, and influence reaction characteristics through increasing the concentration of absorbents at a particular site.

2.2.1 Physisorption and chemisorption

The process of adsorption can occur either through physisorption or chemisorption. Physisorption consists of adsorption through weak van der Waal's interactions between the catalyst and adsorbate. Due to the nature of the interaction, the adsorbate does not undergo any dissociation and therefore can only bind associatively to the catalyst. The occurrence of substantial physisorption within a catalytic reaction such as methane reforming discussed in Section 2.3 is highly unlikely

due to the necessity for methane to dissociate to be able to reform and the high temperatures used mean that any physisorbed species would be lost almost instantaneously.

Chemisorption consists of adsorption through a chemical bond. In chemisorption, adsorbates can undergo dissociation to allow the reagent to chemically bond to the catalyst. This dissociation or fragmentation of adsorbates is often the primary operation in catalysts and the driving force for the reaction to occur. Adsorbates can also bind associatively if there is a site for bonding available without dissociation and reagents are stable, such as aromatic hydrocarbon structures.

2.2.2 Eley-Rideal and Langmuir-Hinshelwood mechanisms

Heterogeneous catalysis is described to occur by one of two standard mechanisms, the Eley-Rideal mechanism (Figure 2.2) or the Langmuir-Hinshelwood mechanism (Figure 2.3). The Eley-Rideal mechanism dictates that the reaction occurs between a gas phase molecule and a molecule adsorbed on the catalyst surface.

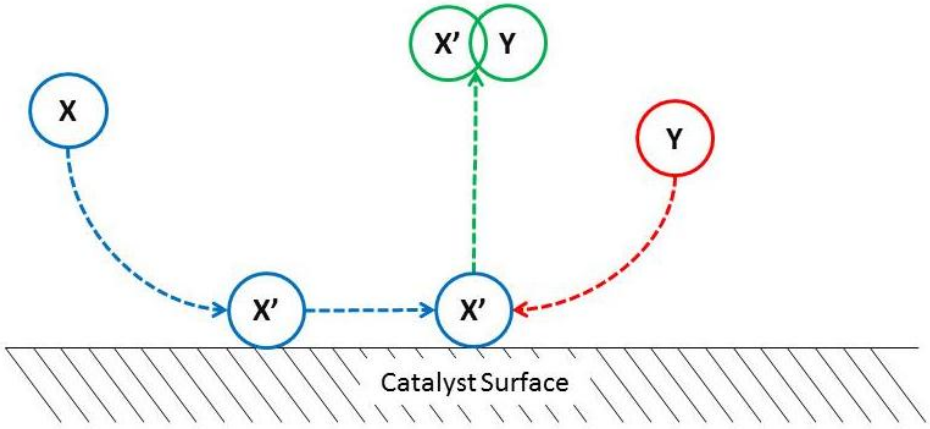

Figure 2.2: Simple representation of the Eley-Rideal mechanism on a catalyst surface.

Examples of industrial scale catalytic reactions proposed to occur via Eley-Rideal mechanisms are shown in Equations 2.1 – 2.3 [48].

$$CO_2 + H_{2(ads)} \rightarrow H_2O + CO \qquad (2.1)$$

$$2NH_3 + 3/2\ O_{2(ads)} \rightarrow N_2 + 3H_2O \quad (\text{Pt catalyst}) \qquad (2.2)$$

$$HC \equiv CH + H_{2(ads)} \rightarrow H_2C = CH_2 \quad \text{(Ni or Fe catalyst)} \qquad (2.3)$$

The Langmuir-Hinshelwood mechanism assumes that for the reaction to occur, all involved species must adsorb onto the catalyst surface on which they can react.

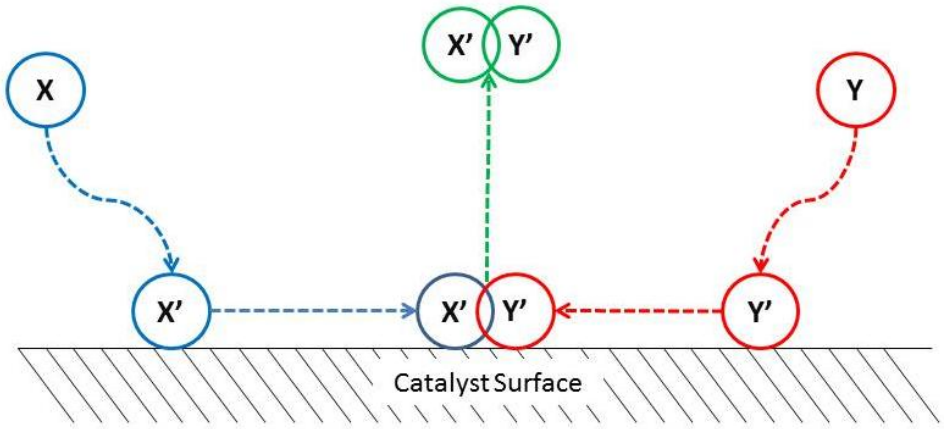

Figure 2.3: Simple representation of the Langmuir-Hinshelwood mechanism on a catalyst surface.

Examples of industrial scale catalytic reactions proposed to occur via Langmuir-Hinshelwood mechanisms are shown in Equations 2.4 – 2.8 [48].

$$2CO + O_2 \rightarrow 2CO_2 \quad \text{(Pt catalyst)} \qquad (2.4)$$

$$CO + 2H_2 \rightarrow CH_3OH \quad \text{(ZnO catalyst)} \qquad (2.5)$$

$$C_2H_4 + H_2 \rightarrow C_2H_6 \quad \text{(Cu catalyst)} \qquad (2.6)$$

$$N_2O + H_2 \rightarrow N_2 + H_2O \quad \text{(Pt or Au catalyst)} \qquad (2.7)$$

$$CH_2 = CH_2 + O_2 \rightarrow CH_3CHO \quad \text{(Pd catalyst)} \qquad (2.8)$$

Both mechanisms have been suggested for catalytic reforming processes, however the support for Langmuir-Hinshelwood type mechanisms seems to be greater [49]. It is feasible that neither one of the two mechanisms completely dominate a reaction and that a combination of the two processes

occurs. Examples of both types of mechanisms with particular reference to methane reforming are discussed in Section 2.3.

2.3 Methane reforming

The reforming of methane is an established chemical process with a huge number of applications worldwide. Methane reforming is classified by the nature, or lack of reformant used to convert the methane into hydrogen and carbon monoxide (synthesis gas). The production of hydrogen is the primary required product from the majority of methane reforming processes due to the high hydrogen requirements of the chemical industry and also the increased requirement of hydrogen for energy generation.

The reforming can occur without a reformant, where temperature alone is used to decompose the methane, whilst steam, carbon dioxide and oxygen are all possible reformants, each with particular advantages and disadvantages that are discussed within this chapter. Reforming in the absence of a reformant is known as autothermal reforming and consists of methane decomposition to produce hydrogen and significant quantities of solid carbon (Equation 2.9) [50].

The reforming of methane within a heterogeneous catalyst system is highly complex with interactions between gas-solid, bulk-surface, surface-surface, gas-gas as well as diffusion and transfer effects of which a number of these reactions can occur simultaneously.

2.3.1 Elementary reactions

There are numerous reactions that occur within all methods of methane reforming. Each of these reactions can have a significant influence on the characteristics of the overall reforming reactions. The Ellingham diagram showing the influence of temperature on the thermodynamic potential of these elementary reactions is shown in Figure 2.4.

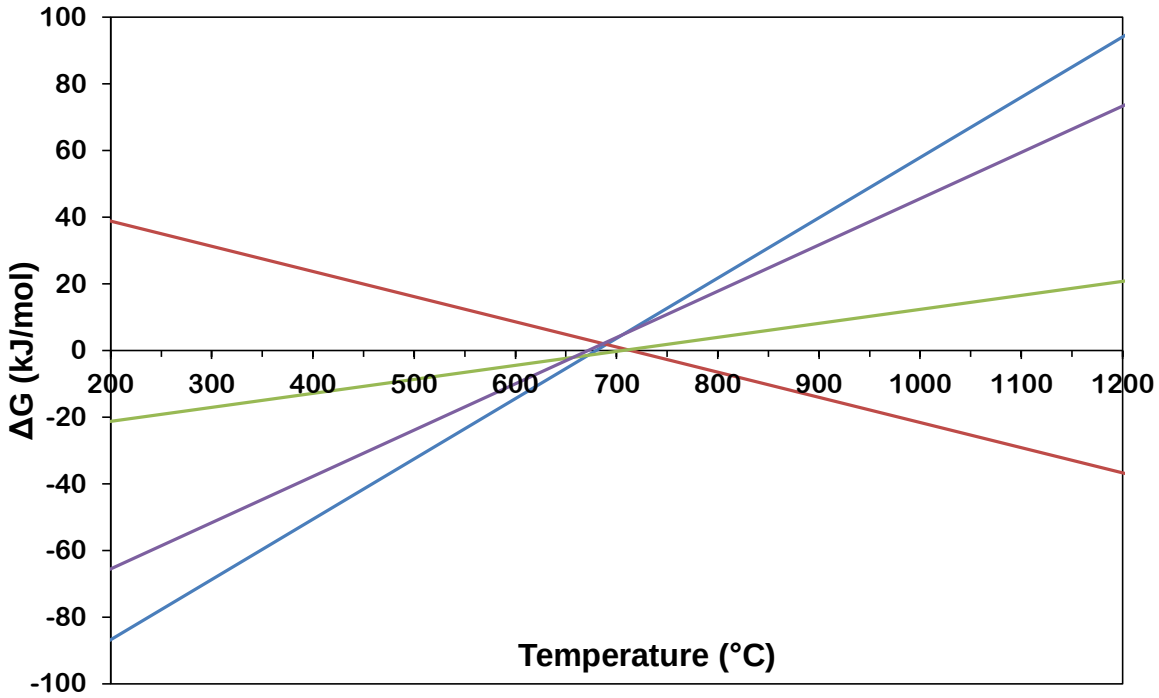

Figure 2.4: Ellingham diagram for elementary gas phase reactions that occur within methane reforming (Red = Equation 2.9, Blue = Equation 2.11, Green = Equation 2.10, Purple = Equation 2.12). Produced using data from Lide [51].

2.3.1.1 Methane decomposition

Methane decomposition (Equation 2.9) occurs when there is not sufficient reformant available or at very high temperatures (>700 °C). Despite being advantageous in terms of hydrogen production, the solid carbon deposited can cause significant deactivation as discussed in Section 2.6.2.

$$CH_4 \rightarrow 2H_2 + C_{(s)} \qquad (2.9)$$

Solymosi *et al.* [52] and Erdohelyi *et al.* [53] showed that the decomposition of methane over a palladium and rhodium catalyst respectively can occur at temperatures as low at 200 °C.

2.3.1.2 Water gas shift and reverse water gas shift reactions

$$CO + H_2O \rightleftharpoons H_2 + CO_2 \qquad (2.10)$$

The water gas shift and reverse water gas shift reactions occur to a significant extent in all reforming reactions due to the presence of the species involved. Vermeiren *et al.* [54] show that increased temperatures favour the reverse water gas shift reaction as ΔG_r^{θ} increases with temperature towards 0 kJ mol^{-1} at *ca.* 750 °C for the forward reaction. This observation is supported by free energy calculations which are shown in Figure 2.4.

2.3.1.3 Boudouard Reaction

$$2CO \rightleftharpoons CO_2 + C_{(s)} \tag{2.11}$$

The Boudouard reaction and its reverse reaction can contribute significantly to the reaction activity and selectivity through the substantial influence of deposited carbon. The forward reaction occurs at lower temperatures due to its exothermicity as shown in Figure 2.4 and results in unfavourable carbon deposition and an increase in the H_2:CO ratio, whilst the reverse reaction can act to clean the catalyst surface of deposited carbon and decrease the H_2:CO ratio. A number of studies [55, 56] incorporating the use of isotopes within CO_2 reforming of CH_4 have suggested that for rhodium in particular, the Boudouard reaction is the primary source of carbon deposition whereas for nickel, the Boudouard reaction is not believed to contribute significantly to carbon deposition. The extent to which these reactions occur can vary substantially with reaction conditions such as temperature, oxidant and carbon/oxidant ratio. The Boudouard and reverse Boudouard reaction are discussed in more detail in Section 2.7.1.

2.3.1.4 CO reduction

$$CO + H_2 \rightarrow H_2O + C_{(s)} \tag{2.12}$$

CO reduction to produce water and solid carbon is undesirable as it increases carbon deposition, whilst also reducing H_2 and CO product yields. As can be seen from Figure 2.4 the hydrogenation of CO is thermodynamically favourable below 670 °C. Above this temperature, the reverse reaction

becomes thermodynamically favourable and is desirable due to its potential to remove solid carbon from the catalyst surface.

2.3.1.5 Total oxidation

$$CH_4 + 2O_2 \rightleftharpoons CO_2 + 2H_2O \quad (2.13)$$

The occurrence of total oxidation is largely undesirable due to the product composition and energy release incorporated with such a highly exothermic reaction that can produce hotspots, which are discussed in more detail in Section 2.3.4. The presence of NiO is proposed to favour total oxidation due to the increased oxidation potential [57, 58], whilst lower temperature and increased O_2 concentration also favour total oxidation. Total oxidation is proposed to have a significant influence on partial oxidation, as discussed in Section 2.3.4.

2.3.1.6 Methane Coupling

$$2CH_4 + 1/2O_2 \rightleftharpoons C_2H_6 + H_2O \quad (2.14)$$

$$CH_4 + Z \rightleftharpoons ZCH_3 + H \qquad 2ZCH_3 \rightleftharpoons C_2H_6 \quad (2.15)$$

(where *Z* denotes an adsorption site)

The specific coupling of methane to produce ethane, ethene and ethyne (acetylene) has been researched since the 1980's with Keller and Bhasin [59] reporting a range of active catalysts for the proposed reaction. Keller and Bhasin proposed that the most active catalysts for C_2 formation were the oxides of tin, lead, antimony, bismuth, titanium, cadmium and manganese and that the activity of nickel towards oxidative methane coupling was minimal (1 % yield). More recently, Dooley and co-worker [60-62] have shown that through the addition of potassium and calcium, the activity of nickel for oxidative methane coupling is increased. It is suggested that the redox ability of the catalyst and presence of available oxygen significantly influences its ability to couple methane as oxygen assists in the formation of methyl radicals [59, 63]. Certain research has shown

that doping with alkaline earth or rare earth oxides improves the catalyst activity towards oxidative methane coupling through the presence of basic sites at which CH_4 dehydrogenation and C_2 formation can occur [60, 63].

Erdöhelyi *et al.* [53, 64] have shown that ethane can be produced from methane decomposition on rhodium and palladium. They suggest this occurs through the dimerization of CH_3 species, as shown in Equation 2.15, although no CH_3 species were isolated and analysed and as such, propose that CH_x species have a very short lifetime. Verykios [55] also found that no CH_x species could be isolated and analysed through infra-red spectroscopy, however isotope studies conducted support the presence of CH_x species.

The major drawback of methane coupling is the low yield (maximum 20 %) due to the high reactivity of higher hydrocarbons making them difficult to isolate [65, 66].

2.3.2 Steam reforming

$$CH_4 + H_2O \rightarrow 3H_2 + CO \quad \Delta H^{\theta}_{298} = +206 \text{kJ mol}^{-1} \qquad (2.16)$$

The primary method of methane reforming used throughout the world is steam reforming (Equation 2.16). This is especially evident in the USA, where 95 % of all hydrogen production (9 million tonnes/year) is via steam reforming of methane [67]. Steam reforming of methane was first published in 1924 by Neumann and Jacob, and the first commercial steam reformer was commissioned in 1936 in Baton Rouge, USA by Standard Oil [68 and references therein]. Due to the maturity and prevalence of steam reforming, the knowledge of the process in terms of kinetics and mechanisms is far more advanced than for the other methods of reforming. Steam reforming is an endothermic reaction that is generally perceived to proceed first order with respect to methane [69]. Due to the excess quantity of steam present within the system required to inhibit carbon deposition, the water gas shift reaction (Equation 2.10) will occur simultaneously [69] at appropriate temperatures.

The nature of the steam reforming reaction and the combination with the water gas shift reaction results in a hydrogen:carbon monoxide ratio of between 3 and 4 [70]. This is the highest ratio that can be obtained through methane reforming excluding methane decomposition and is one of the primary reasons behind its widespread use. The cost involved with producing and using large quantities of steam has led to an increased effort to improve the efficiency and viability of the other methane reforming approaches [71]. The coupling of the methane steam reforming reaction and the water gas shift reaction gives the overall reaction shown in Equation 2.17.

$$CH_4 + 2H_2O \rightarrow CO_2 + 4H_2 \quad \Delta H^{\theta}_{298} = +165\text{kJ mol}^{-1} \qquad (2.17)$$

The mechanism of steam reforming has been extensively studied and a number of mechanisms have been proposed [72-74]. However, there is still no universally agreed mechanism. This is due to the range in catalyst material, method of manufacture and different temperatures and pressures in which the steam reforming has been studied [75, 76]. One of the earliest and most popular mechanisms was proposed by Temkin in 1989 [77] as shown in Table 2.3.

Table 2.3: Early mechanism of steam reforming proposed by Temkin [77] including elementary steps and the extent to which each elementary step occurred within the steam reforming reaction (2.16) and water gas shift reaction (2.10).

		No. of elementary steps within reaction	
	Elementary step	**Equation 2.16**	**Equation 2.10**
1.	$CH_4 + Z \rightleftharpoons ZCH_2 + H_2$	1	0
2.	$ZCH_2 + H_2O \rightleftharpoons ZCHOH + H_2$	1	0
3.	$ZCHOH \rightleftharpoons ZCO + H_2$	1	0
4.	$ZCO \rightleftharpoons Z + CO$	1	0
5.	$Z + H_2O \rightleftharpoons ZO + H_2$	0	1
6.	$ZO + CO \rightleftharpoons Z + CO_2$	0	1

In the mechanism above, *Z* represents a free adsorption site on the nickel catalyst surface and if Z precedes a chemical species, this implies that the species is chemisorbed to the adsorption site.

Steps 1-4 are associated with the methane steam reforming reaction (Equation 2.16) and Steps 5-6 are associated with the water gas shift reaction (Equation 2.10). with the stoichiometric quantities for each step shown for each reaction equation.

A more recent expansion of this mechanism has been performed by Xu and Froment [73] which took into account the possibility of adsorbed species reacting with each other through surface species migration. This mechanism identifies the sequential dissociation of methane that occurs during the reforming reaction.

Avetisov *et al.* [74] have proposed variations of the Temkin and Xu/Froment mechanisms by carrying out methane steam reforming with variations in temperature, steam partial pressure, overall pressure and isotope substitution. From this study, they propose the mechanism shown in Table 2.4.

Table 2.4: Early mechanism of steam reforming proposed by Avetisov *et al.* [74] including elementary steps and the extent to which each elementary step occurred within the steam reforming reaction (2.16) and water gas shift reaction (2.10).

		No. of elementary steps with reaction	
Order	**Elementary step**	**Equation 2.16**	**Equation 2.10**
1.	$CH_4 + 2Z \rightleftharpoons ZCH_3 + ZH$	1	1
2.	$ZCH_3 + Z \rightleftharpoons ZCH_2 + ZH$	1	1
3.	$ZCH_2 + Z \rightleftharpoons ZCH + ZH$	1	1
4.	$ZCH + Z \rightleftharpoons ZC + ZH$	1	1
5.	$ZC + ZOH \rightleftharpoons ZCOH + Z$	1	1
6.	$ZCOH + Z \rightleftharpoons ZCO + ZH$	1	1
7.	$ZCO \equiv Z + CO$	1	0
8.	$ZCO + ZO \rightleftharpoons 2Z + CO_2$	0	1
9.	$H_2O + 2Z \equiv ZOH + ZH$	1	2
10.	$ZOH + Z \equiv ZO + ZH$	0	1
11.	$2ZH \equiv 2Z + H_2$	3	4

In the above mechanism, *Z* represents an adsorption site as with the mechanism shown in Table 2.3 whilst the ≡ symbol is used to illustrate a quasi-equilibrium step. The numbers to the right of the mechanism show the stoichiometric number associated with the relevant reaction. This mechanism identifies the occurrence of the steam reforming reaction (Equation 2.16) and also the coupling of steam reforming with the water gas shift reaction (Equation 2.10). The difference from the Xu/Froment mechanism is minimal, but focuses on the improbability of methane binding to the catalyst surface without dissociation.

Jones *et al.* [78] studied steam reforming over a range of catalyst materials including group VIII and noble metals. From this study, they proposed that the Rate Determining Step (RDS) for steam reforming changes with temperature and catalyst activity, in that at lower temperatures and with less active catalysts, CO formation is the RDS whereas at higher temperature and more active catalysts, CH_4 dissociation becomes the RDS. They suggest that the change in RDS is a primary reason for the inconsistency present with steam reforming studies and different mechanisms proposed. This is also suggested by Bodrov *et al.* [69] and Temkin *et al.* [77]. Hou and Hughes support the proposal that CO formation is the RDS, whilst also suggesting that the other reactions between species absorbed on the catalyst surface, such as step 6 in the mechanism shown in Table 2.4, are also rate determining steps [75].

2.3.3 CO_2 (Dry) reforming

$$CH_4 + CO_2 \rightarrow 2H_2 + 2CO \quad \Delta H_{298}^{\theta} = +247 \text{kJ mol}^{-1} \qquad (2.18)$$

Dry reforming was first published by Franz Fischer and Harold Tropsch in 1928 but has not become as common as steam reforming due to its highly endothermic nature and high capacity for carbon deposition. Despite the issue concerning carbon deposition, this approach is attractive due to the low H_2:CO ratio which is desirable for the production of oxygenated chemicals [79] and is environmentally favourable due to the utilization of two greenhouse gases in CH_4 and CO_2. The process of carbon deposition and methods of inhibition are discussed in Section 2.6.2.

For studies involving the reforming of biogas, the dry reforming reaction is fundamental due to the high levels of CO_2 in biogas. The reforming of biogas without CO_2 removal is highly desirable due to the added cost associated with such CO_2 removal, as discussed in Section 2.1.3.

The dry reforming reaction is widely used within the CALCOR process developed by Caloric GmbH to produce high purity CO as a feedstock for the production of organic acids, polycarbonates and phosgene. The CALCOR process involves the reforming of methane with excess CO_2 using low pressure and high temperatures to produce a syngas with a H_2:CO ratio of 0.42:1. The exit gases undergo CO_2 removal and possible H_2 removal depending on the purity of the CO required [80].

Another industrial process that successfully operates dry reforming is the SPARG (Sulfur Passivated Reforming) process in which sulfur is used to reduce the system activity to an extent where carbon deposition is reduced. This process was studied by Rostrup-Nielsen [81] amongst others using steam reforming of methane, but has also been shown to reduce carbon deposition with dry reforming [82]. The SPARG process and influence of sulfur on methane reforming and catalyst activity is discussed in greater detail in Section 2.6.1.

Dry reforming of methane has been studied extensively over a wide range of catalyst materials and conditions, with the primary focus towards the reduction of carbon deposition on the active catalyst material. As with steam reforming, there is no universally agreed mechanism for dry reforming, in part due to the range of conditions in which the dry reforming reaction has been studied. It is generally agreed however, that the reaction proceeds with first order kinetics with respect to CO_2 and CH_4 [76, 83]. It has been shown by various studies that the choice of catalyst material can have a very significant influence on catalytic activity, which can influence the mechanism [76]. Several studies [84, 85] have shown that the catalyst support can also influence the mechanism due to the preferential reactivity of the support. The occurrence of carbon deposition and ability to favour certain reactions such as the reverse Boudouard reaction can increase the difficulty in determination of reaction mechanisms through distorting product yields and ratios.

There are two main mechanisms suggested for dry reforming of methane which differ in the extent to which surface-surface interactions occur. The Eley-Rideal type mechanism (Section 2.2.2) has been suggested, as shown by Equation 2.19 and 2.20 [53, 64, 83, 86, 87]. This mechanism is concerned primarily with the decomposition of methane, followed by the reverse Boudouard reaction. The water gas shift reaction and process of steam reforming are suggested to accompany the mechanism. The decomposition of methane is proposed as the RDS.

$$\mathrm{CH_4} + Z \rightleftharpoons Z\mathrm{C} + 2\mathrm{H_2} \quad (2.19)$$

$$Z\mathrm{C} + \mathrm{CO_2} \rightleftharpoons 2\mathrm{CO} + Z \quad (2.20)$$

Alternatively, a Langmuir-Hinshelwood type mechanism (See Section 2.2.2) has been suggested as shown in Equation 2.21 – 2.33 [76, 88-90].

$$\mathrm{CH_4} + 2Z \rightleftharpoons Z\mathrm{CH_3} + Z\mathrm{H} \quad (2.21)$$

$$Z\mathrm{CH_3} + Z \rightleftharpoons Z\mathrm{CH_2} + Z\mathrm{H} \quad (2.22)$$

$$Z\mathrm{CH_2} + Z \rightleftharpoons Z\mathrm{CH} + Z\mathrm{H} \quad (2.23)$$

$$Z\mathrm{CH} + Z \rightleftharpoons Z\mathrm{C} + Z\mathrm{H} \quad (2.24)$$

$$\mathrm{H_20} + Z \rightleftharpoons Z\mathrm{H_2O} \quad (2.25)$$

$$Z\mathrm{H_2O} + Z \rightleftharpoons Z\mathrm{OH} + Z\mathrm{H} \quad (2.26)$$

$$Z\mathrm{C} + Z\mathrm{OH} \rightleftharpoons ZZ\mathrm{CHO} \quad (2.27)$$

$$\mathrm{CO_2} + 2Z \rightleftharpoons ZZ\mathrm{CO_2} \quad (2.28)$$

$$ZZ\mathrm{CO_2} + Z\mathrm{H} \rightleftharpoons ZZ\mathrm{COOH} + Z \quad (2.29)$$

$$ZZ\mathrm{COOH} + Z\mathrm{H} + 2Z \rightleftharpoons ZZ\mathrm{CHO} + Z\mathrm{OH} + 2Z \quad (2.30)$$

$$ZZ\mathrm{CHO} + 3Z \rightleftharpoons ZZ\mathrm{CO} + Z\mathrm{H} + 2Z \quad (2.31)$$

$$ZZ\mathrm{CO} \rightleftharpoons \mathrm{CO} + 2Z \quad (2.32)$$

$$2Z\mathrm{H} \rightleftharpoons \mathrm{H_2} + 2Z \quad (2.33)$$

As with prior mechanisms, *Z* represents an adsorption site.

This Langmuir-Hinshelwood type mechanism places significant emphasis towards the interactions between chemisorbed species and is very similar to that suggested for steam reforming of methane (Table 2.4). Rostrup-Nielsen and Hansen [76] amongst others [68 and references therein, 91] suggest that the primary function of CO_2 within dry reforming is to produce H_2O through the RWGS reaction, which then reforms the methane through the mechanism shown in Table 2.4. The main discrepancy within the mechanism shown in Equations 2.21 – 2.33 is the manner in which CO_2 adsorbs and also the rate determining step. CO_2 adsorption has been suggested to occur non-dissociatively as shown in Equation 2-28, dissociatively [55, 92-94] as shown in Equation 2.34, and also through reacting with hydrogen as shown in Equation 2.35 [53, 55].

$$CO_2 + 2Z \rightleftharpoons ZCO + ZO \tag{2.34}$$

$$ZCO_2 + ZH \rightleftharpoons ZCO + ZOH \tag{2.35}$$

Due to the range of catalysts and support materials which have been used to study dry reforming of methane, a number of rate determining steps have been proposed including methane dissociation [95], CH_xO decomposition [95], CHO formation [90], CO_2 adsorption [94] and the surface reaction between adsorbed CH_x and O [96].

2.3.4 Partial oxidation

$$CH_4 + 1/2\,O_2 \rightarrow 2H_2 + CO \qquad \Delta H^{\theta}_{298} = -38\text{kJ mol}^{-1} \tag{2.36}$$

Partial oxidation of methane is an established technology and has been used industrially with and without the use of a catalyst. Non-catalytic partial oxidation however, requires high pressure and temperatures above 1200 °C, whereas catalytic partial oxidation does not require pressure and can be achieved at temperatures below 1000 °C [97]. The H_2:CO ratio produced through partial oxidation is suitable for Fischer-Tropsch synthesis and the exothermicity of the reaction makes it a highly desirable process. However, this exothermicity is also problematic. Highly exothermic total oxidation can often occur when methane and oxygen are initially mixed under temperature. This

results in a significant temperature increase which can cause catalyst or equipment damage, and explosions can also occur in severe cases [98]. Industrial scale partial oxidation reforming plants require a pre-mixing facility to ensure the methane and oxygen are mixed thoroughly before heat is applied.

The occurrence of temperature increases at the inlet of the catalyst bed, known as hotspots, have resulted in differences in kinetic and mechanistic studies. Two main mechanisms are proposed for the partial oxidation of methane; Direct Partial Oxidation (Equations 2.37 – 2.45) [71, 99-102] and Indirect Partial Oxidation (Equations 2.46 – 2.54) [103-108]. The mechanisms could also be thought of as Eley-Rideal type (Direct) and Langmuir-Hinshelwood type (Indirect). Both mechanisms will undergo the elementary reactions described in Section 2.3.1 to a certain extent. It is suggested that the primary factor in determining whether direct or indirect partial oxidation occurs is the oxidation state of the metal catalyst or the presence of oxygen species on the catalyst surface, such as lattice oxygen. The increased oxidative ability will shift the reaction towards the indirect route [57, 101, 109]. Therefore, the catalyst and support materials used have a significant influence on the mechanism of partial oxidation that occurs. Rhodium and platinum have been suggested to catalyse the direct mechanism [110], whereas iron and nickel catalyse the indirect mechanism [108, 111].

Direct partial oxidation is concerned primarily with the dissociation of methane and oxygen and the interaction between the dissociation products, or between the dissociated methane and gas-phase oxygen and is illustrated in Equations 2.37 – 2.45. Where more than one species on the left of the equilibrium is adsorbed to the surface, this illustrates a Langmuir-Hinshelwood type mechanism.

$$\mathrm{CH_4} + 2Z \rightleftharpoons Z\mathrm{CH_3} + Z\mathrm{H} \tag{2.37}$$

$$Z\mathrm{CH_3} + Z \rightleftharpoons Z\mathrm{CH_2} + Z\mathrm{H} \tag{2.38}$$

$$Z\mathrm{CH_2} + Z \rightleftharpoons Z\mathrm{CH} + Z\mathrm{H} \tag{2.39}$$

$$Z\mathrm{CH} + Z \rightleftharpoons Z\mathrm{C} + Z\mathrm{H} \tag{2.40}$$

$$\mathrm{O_2} + 2Z \rightleftharpoons 2Z\mathrm{O} \tag{2.41}$$

$$ZC + ZO \rightleftharpoons ZCO \quad (2.42)$$

$$ZCO \rightleftharpoons CO \quad (2.43)$$

$$ZH + ZH \rightleftharpoons ZH_2 + Z \quad (2.44)$$

$$ZH_2 \rightleftharpoons H_2 + Z \quad (2.45)$$

Indirect partial oxidation takes into account the occurrence of total oxidation at the inlet of the catalyst to produce H_2O and CO_2 which then act as the main reforming agent and is illustrated in Equation 2.46 – 2.54.

$$CH_4 + 2Z \rightleftharpoons ZCH_3 + ZH \quad (2.46/2.37)$$

$$ZCH_3 + Z \rightleftharpoons ZCH_2 + ZH \quad (2.47/2.38)$$

$$ZCH_2 + Z \rightleftharpoons ZCH + ZH \quad (2.48/2.39)$$

$$ZCH + Z \rightleftharpoons ZC + ZH \quad (2.49/2.40)$$

$$ZC + O_2 \rightleftharpoons CO_2 + Z \quad (2.50/2.44)$$

$$ZH + ZH \rightleftharpoons ZH_2 + Z \quad (2.51)$$

$$2ZH_2 + O_2 \rightleftharpoons 2H_2O + 2Z \quad (2.52)$$

Dry Reforming: $CH_4 + CO_2 \rightleftharpoons 2H_2 + 2CO$ (2.53)

Steam Reforming: $CH_4 + H_2O \rightleftharpoons 3H_2 + CO$ (2.54)

Prettre *et al.* [112] were one of the first to suggest the indirect method as they saw a varied temperature profile which exhibited a temperature rise at the inlet, which was attributed to exothermic total oxidation, and a temperature decrease at the outlet, which was attributed to the endothermic steam and dry reforming reactions. The significant quantities of CO_2 and H_2O produced also support the proposal of the indirect mechanism. Heitnes *et al.* [107] saw similar temperature profiles to that shown by Prettre *et al.* [112]. Product compositions within these studies have also suggested the occurrence of total oxidation as significant quantities of CO_2 and H_2O are formed which are unlikely to be attributed to the water gas shift or Boudouard reactions, due to the

lack of sufficient carbon deposition [57]. This does not suggest however, that carbon deposition does not occur during partial oxidation of methane as Tsipouriari *et al.* [108] demonstrated. The likelihood of carbon deposition for this reforming method is significantly less than for the dry reforming reaction. Carbon deposition occurs due to a lack of oxygen present. One issue with partial oxidation is the requirement for a limited oxygen content to reduce the extent to which total oxidation can occur. The range in which partial oxidation can occur without carbon deposition and minimal total oxidation is very small. Therefore, the development of a catalyst that neither encourages total oxidation or carbon deposition is highly sought after.

It has been suggested by Fleys *et al.* [106] that direct partial oxidation occurs at lower temperatures and contact times, whereas at high temperatures and contact times both direct and indirect partial oxidation occur simultaneously.

Due to the similarity between the partial oxidation and the steam reforming and dry reforming reactions, it is plausible to assume that the rate determining step for partial oxidation is the same as for dry reforming and steam reforming, with Hu and Ruckenstein [101] stating that the surface reaction between adsorbed carbon and oxygen was the RDS.

A substantial review on the mechanisms of partial oxidation of methane over various transition metals, including nickel, has been published by Enger *et al.* [98].

2.3.5 Oxidative steam reforming

$$CH_4 + H_2O + xO_2 \rightarrow yH_2 + zCO \qquad (2.55)$$

The combination of steam reforming and partial oxidation of methane is a widely used approach and is often known as autothermal reforming. This is however, a completely different process from the autothermal reforming described in Section 2.3. The oxidative steam reforming of methane was first used in the 1950's by Societe Belge de l'Azote and Haldor Topsoe where a nickel based

catalyst was used to produce syngas for use in methanol and ammonia synthesis [113]. This method of reforming is advantageous in that oxygen is not as expensive as steam and that the coupling of the endothermic steam reforming reaction with the exothermic partial oxidation reaction lowers the system energy requirements. Another advantage of the combined oxidative steam reforming is the ability to control the H_2:CO product ratios through variation in reactant gas composition [114, 115].

2.3.6 Combined steam and dry reforming

$$CH_4 + H_2O + CO_2 \rightarrow yH_2 + zCO \quad (2.56)$$

As with oxidative steam reforming, the combination of steam and dry reforming of methane is often known as autothermal reforming. This method of reforming is rarely used due to the energy requirements of both processes. Steam has been used in addition with reforming of CH_4/CO_2 containing mixtures as a method of reducing carbon deposition and also to improve reforming in CH_4 rich gas mixtures, such as biogas where extra reformant is required. One advantage, as with oxidative steam reforming, is the ability to control the H_2:CO product ratio [116-120].

2.3.7 Oxidative CO_2 reforming

$$2CH_4 + CO_2 + xO_2 \rightarrow yH_2 + zCO \quad (2.57)$$

Oxidative CO_2 reforming consists of a combination of dry reforming and partial oxidation. As with the other combined approaches, it is often known as autothermal reforming. Oxidative CO_2 reforming was first reported by Vernon and co-workers [121, 122] in the early 1990's. This approach is relatively undeveloped in comparison to the other reforming methods. The reasons for this are not obvious, other than that the use of steam has dominated the reforming industry and that when combinations of reformants are used, the reaction system becomes more complex. Despite

the under-development of this approach, the combination of the endothermic dry reforming reaction with the exothermic partial oxidation offers numerous advantages:

- The combination of an endothermic reaction with an exothermic reaction results in a lower energy requirement than if the dry reforming reaction occurs individually.
- The hot-spot issue discussed in 2.3.4 is reduced as the heat is utilised though the dry reforming reaction [123, 124], whilst also improving reforming activity at lower reaction temperatures [125].
- The composition of biogas discussed in Section 2.1 and its high carbon nature means that reforming of pure biogas will inevitably result in significant carbon deposition. The addition of oxygen can reduce the extent to which carbon deposition occurs through reducing the amount of unreformed methane, whilst also acting to oxidize surface carbon that may be deposited [123].
- Through variation in reactant gas compositions, the H_2:CO product ratio can be tailored to a particular requirement [121-123, 125-127].

The main disadvantages of the oxidative CO_2 reforming approach is that oxygen can oxidize the catalyst if excess oxygen is present [128], oxygen addition can result in increased total oxidation and therefore loss of CO yield, and that the addition of pure oxygen to the system increases the cost.

Oxidative CO_2 reforming has been selected for this research due to the relative under-development of the approach, its applicability to biogas as a methane source and its potentially greater economic viability compared to steam-based approaches.

2.4 Uses of synthesis gas

Synthesis gas and its uses have been mentioned previously within Section 2.3, with respect to particular reforming processes. This section describes the uses of synthesis gas in more detail. The

extensive use of synthesis gas as a feedstock for a wide range of different chemical processes and applications has been reviewed in detail by Wender [79].

The main processes in which synthesis gas is used are methanol synthesis, Fischer-Tropsch synthesis, hydroformylation of olefins, ammonia synthesis and as a fuel within a number of different devices for electricity generation. The primary use of synthesis gas is the utilisation of the hydrogen content within the Haber process for ammonia synthesis (Equation 2.58). The Haber process was first demonstrated in 1913 and was the first industrial scale chemical process to use high pressure [48, 129]. In 2002, ammonia production reached approximately 108 million tonnes [129] and this figure has continued to increase to-date. Steam reforming is the primary method to produce synthesis gas for use in ammonia synthesis due to its high H_2:CO ratio.

$$N_2 + 3H_2 \rightarrow 2NH_3 \qquad \Delta H_{298}^{\theta} = -92.22\text{kJ mol}^{-1} \tag{2.58}$$

Methanol synthesis and Fischer-Tropsch synthesis are the two largest consumers of synthesis gas that also utilise its CO content. Methanol synthesis (Equation 2.59) was first performed industrially in 1923 by BASF [48, 79].

$$CO + 2H_2 \rightleftharpoons CH_3OH \qquad \Delta H_{298}^{\theta} = -92\text{kJ mol}^{-1} \tag{2.59}$$

Methanol production reached approximately 42 million tonnes in 2009, of which approximately 30 % was used for formaldehyde synthesis [130].

Fischer-Tropsch synthesis involves the synthesis of higher hydrocarbons from synthesis gas through the hydrogenation of CO. The first industrial scale Fischer-Tropsch plant was built in 1935 by BASF [79]. This process is used to produce alkanes (Equation 2.60), alkenes (Equation 2.61) and alcohols (Equation 2.62) which can be used to produce synthetic fuels [79]. Elementary reactions (Water Gas Shift, Boudouard, CO hydrogenation) discussed in Section 2.3.1 also occur within the Fischer-Tropsch process.

$$(2n+1)H_2 + nCO \rightarrow C_nH_{2n+2} + nH_2O \quad (2.60)$$

$$2nH_2 + nCO \rightarrow C_nH_{2n} + nH_2O \quad (2.61)$$

$$2nH_2 + nCO \rightarrow C_nH_{2n+1}OH + (n-1)H_2O \quad (2.62)$$

Both methanol and Fischer-Tropsch synthesis require a H_2:CO ratio of 2, which can be achieved through the partial oxidation of methane.

The use of synthesis gas through oxo-synthesis involves using syngas with olefins to produce aldehydes and alcohols with a chain length one unit greater than the olefin chain length (Equation 2.63) [79].

$$H_2C = CH_2 + CO + H_2 \rightarrow CH_3CH_2CHO \quad (2.63)$$

Oxo-synthesis was first performed by Roelen in 1938 and the production rate of hydroformylated products in 1998 was 9.3 million tonnes [48, 131]. The dry reforming process is most applicable for the production of synthesis gas with a H_2:CO ratio of 1 required for oxo-synthesis.

Electrochemical devices such as fuel cells offer significant potential for syngas utilization and energy production. The low emissions and range of fuel sources possible for fuel cells, including renewable sources such as biogas, makes their development and operation highly desirable. There are various types of fuel cells that are classified by the nature of the electrolyte material used. These are discussed in detail (Section 2.5), with a particular emphasis on Solid Oxide Fuel Cells.

2.5 Fuel cells

The concept of using hydrogen as a fuel to produce electricity using electrochemical devices was first demonstrated by Christian Schönbein in 1839 and Sir William Grove in 1842 [132]. However,

significant advances in fuel cells were not made until the mid-1900's despite numerous suggestions that hydrogen could become one of the main fuel sources in the 20th century. The first practical fuel cell was produced in 1933 by Thomas Bacon, yet despite this development, the potential of fuel cells has still not been achieved, with fuel cells only being operated in small scale units or still being in the research and development stage. Possible reasons for this lack of development were the apparent abundance of fossil fuels and the lack of knowledge towards their limits, lack of knowledge towards the importance of greenhouse gas emissions and climate change during the late 20th and early 21st centuries, and also the associated cost required for fuel cells to become primary energy generation devices. There is presently a significant move towards the use and discovery of renewable fuels, and significant reductions in greenhouse gas emissions, which have made the widespread commercial deployment of fuel cells highly desirable.

A fuel cell is a device that produces direct current from the electrochemical oxidation of the fuel. The primary fuel for fuel cells is generally hydrogen, which is electrochemically oxidised to produce water as the only direct product (Equation 2.65). The two electrochemical half equations that contribute to the overall reaction within a Solid Oxide Fuel Cell fuelled with hydrogen are shown in Equation 2.65 and 2.66. All fuel cells consist of three main components; anode, electrolyte and cathode. The nomenclature of fuel cell types are derived from the type of electrolyte. A schematic of a solid oxide fuel cell fuelled with hydrogen is shown in Figure 2.5. The different types of fuel cells and some of their characteristics are shown in Table 2.5.

$$\text{Overall: } H_2 + \tfrac{1}{2}O_2 \rightarrow H_2O \tag{2.64}$$

$$\text{Anode: } H_2 + O^{2-} \rightarrow H_2O + 2e^- \tag{2.65}$$

$$\text{Cathode: } \tfrac{1}{2}O_2 + 2e^- \rightarrow O^{2-} \tag{2.66}$$

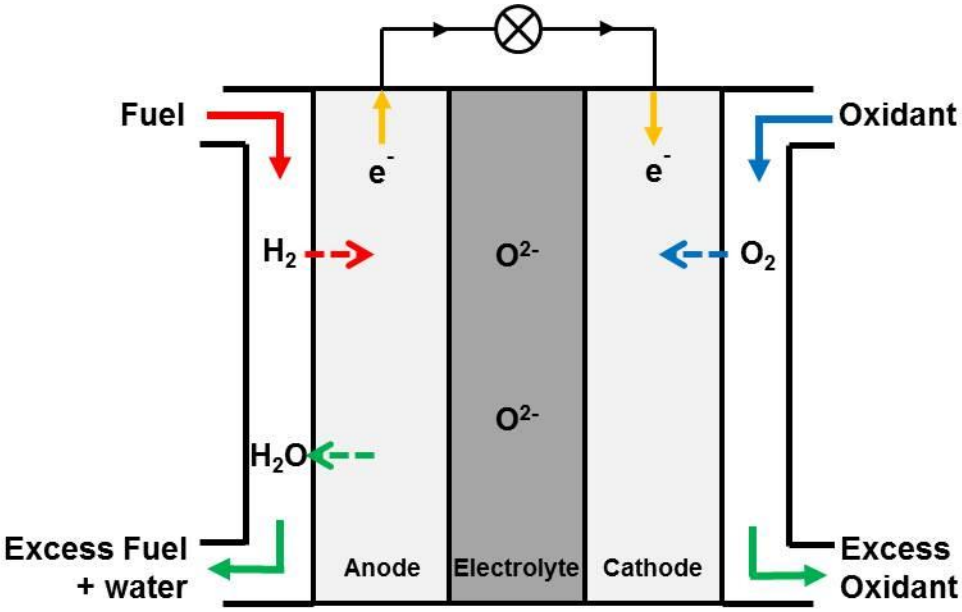

Figure 2.5 Simple representation of a solid oxide fuel cell.

Table 2.5: Table showing types of fuel cells and their characteristics [11, 48, 133, 134]

	Electrolyte	Power Range	Operating Temperature (°C)	Development Status	Applications	Fuel
Alkaline Fuel Cells (AFC)	Liquid alkaline (KOH)	>100 kW	90-100	Mature Expensive, used in few niche applications.	Used in space systems. Transport demonstration.	H_2
Phosphoric Acid Fuel Cells (PAFC)	Phosphoric Acid (H_3PO_3)	200 kW-11 MW	175-200	Mature, 200kW systems available.	Tested with biogas (separate reformer), CHP, stationary power.	H_2, reformed methane
Proton exchange membrane fuel cells (PEMFC)	Solid Polymer	>00's kW	60-120	Marketable in niche applications. 1-2kW commercial products available.	Stationary power, CHP, Transport demonstration.	H_2, reformed Methanol and methane
Direct Methanol Fuel Cells (DMFC)	Solid Polymer	50-150 W	60-120	Advanced product trials, commercialisation imminent.	Portable equipment, transport possible.	Methanol
Molten Carbonate Fuel Cell (MCFC)	Molten carbonate (Li_2CO_3-K_2CO_3)	25 kW-2 MW	600-800	Further R & D required, 5-20 kW prototype units, 1-2 MW plants demonstrated.	CHP, stationary power generation, transport demonstration.	Methane, H_2, CO
Solid Oxide Fuel Cells (SOFC)	Solid oxide (Yttria-doped ZrO_2)	100 W- 10 MW	600-1000	Marketable, significant costs apply, long lifetimes exhibited.	250kW demonstrations, CHP, stationary power, transport.	Methane, H_2, CO

Utilisation of renewable energy, in particular biogas, is key to the direction of this study due to issues with emissions reductions and reducing fossil fuel dependence. Therefore, only the fuel cells with high operating temperatures that provide the direct capacity to use methane (MCFC and SOFC) will be discussed in detail.

2.5.1 Molten Carbonate Fuel Cells (MCFC)

Molten carbonates were first examined as electrolyte materials in 1960 by Broers and Ketelaar [132]. As the name suggests, the electrolyte material in a Molten Carbonate fuel cell is a molten mixture of carbonates (Li_2CO_3 and K_2CO_3). The CO_3^{2-} ion within this mixture acts as the charge carrier for the fuel cell, resulting in the half reactions shown in Equation 2.67 and Equation 2.68.

$$\text{Anode: } H_2 + CO_3^{2-} \rightarrow CO_2 + H_2O + 2e^- \quad (2.67)$$

$$\text{Cathode: } \tfrac{1}{2}O_2 + CO_2 + 2e^- \rightarrow CO_3^{2-} \quad (2.68)$$

The high operating temperature and use of CO_2 within MCFCs makes them highly applicable for use with biogas and CH_4/CO_2 gas mixtures. As MCFCs are not poisoned by carbon oxide species, CO can also be used as a fuel in a similar fashion to H_2 with the CO being oxidised to produce CO_2 (Equation 2.69) on the anode.

$$\text{Anode: } CO + CO_3^{2-} \rightarrow 2CO_2 + 2e^- \quad (2.69)$$

The high operating temperatures associated with MCFCs enables non-precious metals to be used as catalysts, which significantly reduces costs. Common materials used within MCFCs are nickel/chromium (anode) and lithiated nickel oxide (cathode) [48, 135-137].

The primary disadvantages of MCFCs are [11, 132, 134, 135, 138]:

- Corrosive nature of the electrolyte material results in deterioration of the fuel cell, resulting in short lifetime.
- Costs associated with high temperature operation.
- Deterioration of electrolyte on cooling during shutdown or start-up makes discontinuous power generation unviable, therefore reducing the range of applications.
- High intolerance to sulfur (<1.5 ppm) causes deterioration of anode.
- Liquid electrolyte poses issues with handling.
- Nickel oxide anode can incorporate into electrolyte, decreasing efficiency.

2.5.2 Solid Oxide Fuel Cells (SOFC)

In solid oxide fuel cells, (see Figure 2.5) a ceramic material is used as the electrolyte and oxygen vacancies within the material act as the oxide (charge) carrier. The oxygen vacancies result in the half reactions shown in Equations 2.70 and 2.71.

$$\text{Anode: } H_2 + O^{2-} \rightarrow H_2O + 2e^- \quad (2.70)$$

$$\text{Cathode: } \tfrac{1}{2}O_2 + 2e^- \rightarrow O^{2-} \quad (2.71)$$

As with MCFCs, SOFCs are not poisoned by carbon oxides but use CO as a fuel similar to H_2, to produce CO_2 at the anode (Equation 2.72). The use of oxide ions as charge carriers allow for any combustible gas to be used as a fuel source.

$$\text{Anode: } CO + O^{2-} \rightarrow CO_2 + 2e^- \quad (2.72)$$

Common materials used within SOFCs are Yttria-Stabilised-Zirconia (electrolyte), Ni/Yttria-Zirconia (anode) and calcium or strontium doped $LaMnO_3$ (cathode) [132, 135, 139-142]. The high temperature allow for non-precious metals to be used. SOFCs are combined to improve performance through an interconnect material that is resistant to high temperatures and both

reducing and oxidising environments. The combination of SOFCs is called a stack and can be of tubular, planar or monolithic design, which differ in the orientation that the cells are stacked [143].

The primary disadvantages of SOFCs are [132, 139]:

- High operating temperatures can cause significant deterioration of cells with time through agglomeration (sintering) of catalyst particles. This is discussed in detail in Section 2.6.3.
- High operating temperatures necessitate that the fuel cell components must have similar thermal expansion coefficients to ensure the cell is not damaged on heating and cooling.
- Moderate intolerance to sulfur, particularly at the anode (Section 2.6.1).
- Carbon deposition can occur due to the presence of carbon containing fuel sources. This is discussed in detail in Section 2.6.2.
- Cost associated with high temperature operation

SOFCs are deemed superior to MCFCs in the following aspects:

- A higher power density can be achieved through an SOFC than a MCFC [132].
- There are no issues with electrolyte handling are associated with an SOFC as the electrolyte is solid.
- SOFCs have a significantly greater tolerance to sulfur (<50 ppm).
- Electrolyte deterioration is significantly lower for SOFCs than for MCFCs on start-up and shutdown, making SOFCs applicable for use with transport as well as stationary power. High temperature operation does present certain issues with transport applications however.
- The use of oxide ions as charge carriers allow for a wider range of fuels to be used within SOFCs. This is desirable due to the presence of higher hydrocarbons with biogas.

The catalyst material used as a basis for this research project is chosen to represent a possible anode material within a SOFC. This stems from prior research conducted within this research

group led by Professor R. Mark Ormerod into the utilisation of biogas over such catalyst materials [37-39], and also the greater potential of SOFCs as an economically viable technology for the production of energy and commodity chemicals from renewable sources such as biogas.

2.6 Catalyst deactivation

Catalyst deactivation is one of the main limitations with methane reforming and the use of fuel cells. The loss in activity and therefore limited lifetime of catalysts used for methane reforming is caused by three primary processes; poisoning of the active site, blocking of the active site and reduction in active surface area due to thermal degradation. Each of these processes can induce deactivation in various ways and are often highly complex processes influenced significantly by numerous variables, particularly temperature, as will be discussed in the following subsections.

2.6.1 Sulfur poisoning

One of the primary issues associated with operating nickel based catalysts is their propensity for deactivation through poisoning. Numerous electronegative species such as phosphorous arsenic, antimony, oxygen, sulfur, selenium and tellurium are known to deactivate Group 8 metals due to their strong interaction with the partially filled d-orbital of the metal [144].

Sulfur is a poison of particular interest due to its presence within methane containing sources. Hydrogen sulfide is produced naturally within biogas through the degradation of proteins to produce sulphates, which are then reduced to H_2S [145]. Although other sulfur-containing species are also present within biogas, they will be converted to H_2S in a high temperature reforming environment [146, 147]. Natural gas contains a small quantity of sulfur containing compounds which are added in ppm concentrations to act as an odorant and are a legal requirement for any natural gas used within the national grid, as mentioned in Table 2.2.

2.6.1.1 Method of poisoning

Deactivation through sulfur poisoning can occur though different mechanisms, which poison to different extents and are influenced by various factors. The primary mechanism of sulfur deactivation is through the reversible chemisorption of sulfur on the catalyst metal surface (Equation 2.73) [148-152].

$$H_2S_{(g)} + Ni_{(s)} \rightleftharpoons NiS_{(ads)} + H_{2(g)} \quad (2.73)$$

The adsorption of sulfur onto metal sites actively blocks the metal active site for methane reforming and therefore reduces activity. Due to the high electronegativity of the sulfur atom and the partially unfilled d-orbital of nickel, sulfur desorption is unlikely apart from at high temperatures (>800 °C) [153, 154].

Temperature has been shown to have an influence on the manner in which H_2S can bind to nickel. At lower temperatures it has been suggested that the H_2S binds dissociatively [150, 155, 156] using either 3 or 4 metal sites, as can be seen in Equation 2.74 and Equation 2.75 respectively. At higher temperatures, the hydrogen will desorb and it has been proposed that S binds to a single metal site as shown in Equation 2.73 [151, 155]. Rostrup-Nielsen and Pedersen [157] also suggest that the presence of a chemisorbed sulfur atom on nickel can partially deactivate adjacent nickel atoms in a close packed structure through electronic interactions.

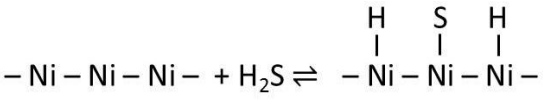

(2.74)

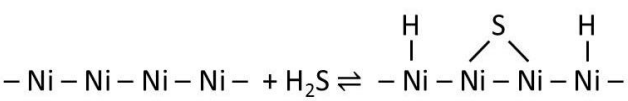

(2.75)

Deactivation through sulfur poisoning has also been suggested to occur through the formation of bulk nickel sulfides (Ni_3S_2, Ni_3S_4). Numerous studies have reported the presence of bulk nickel sulfides, particularly through the use of Raman spectroscopy [158, 159]. However, this has been rejected by Cheng and Liu [160] who performed *in situ* and *ex situ* Raman spectroscopy and discovered that the bulk nickel sulfides were seen in *ex situ* studies, in agreement with other findings [159], but were not present at high temperature *in situ* studies. This was attributed to the formation of bulk nickel sulfides on cooling prior to *ex situ* studies. Zaza *et al.* [161] and Lohsoontorn *et al.* [162] predicted that bulk nickel sulfides are not possible at low H_2S concentrations below 100 ppm and temperatures above 400 °C.

It has also been proposed that sulfur can induce a change in the structure and morphology of the catalyst to cause deactivation. This is primarily attributed to the formation of bulk sulfides which have a significantly greater volume than nickel, therefore causing structural change [160]. However, as the formation of bulk sulfides is uncertain, this mode of deactivation should be viewed with caution. Such structural changes are likely to result in irreversible damage which may explain an inability to recover complete activity upon sulfur removal, as discussed in Section 2.6.1.2 [163]. Surface reconstruction due to sulfur binding to nickel has also been suggested in which a change in the distribution of more active sites, such as edges and steps changes, resulting in a less active surface [155].

Numerous studies have shown that sulfur deactivation with time occurs through different phases due to different mechanisms of deactivation [160, 164]. The first phase of deactivation is rapid and is caused by the initial chemisorption of sulfur on the catalyst surface, preventing the reforming reaction [160]. As this phase of deactivation ends and the activity becomes more stable, this shows the catalyst surface has become saturated with sulfur or that the equilibrium between chemisorption and desorption is being approached. The position at which this point is achieved is highly influenced by sulfur concentration and temperature. As sulfur concentration increases, the rate at which surface saturation is achieved will increase as will the coverage at which the reaction

approaches equilibrium. The influence of temperature is complex as the chemisorption of sulfur on nickel is an exothermic process and the desorption process is endothermic.

The second stage of deactivation is comparatively very slow and considered as more irreversible. Possible causes for this stage are the chemisorption of sulfur on less accessible nickel such as in pores, formation of bulk sulfides or changes to surface or bulk structure [160].

2.6.1.2 Regeneration from poisoning

One approach to improving activity and increasing lifetime of catalysts that have undergone deactivation through sulfur poisoning is through post-reaction recovery. The largely reversible nature of sulfur chemisorption means that the majority of activity can often be recovered by desorption of the sulfur from the nickel, which can be achieved using various methods.

One method of recovering catalyst activity is through carrying out the reaction with H_2S-free fuel gas at high temperatures [146, 165-168]. The high temperature is used to facilitate the endothermic desorption of sulfur (S_2) from nickel. The hydrogen-rich atmosphere present during methane reforming also enhances the desorption of sulfur through the formation of H_2S. Regeneration can also be achieved using high temperatures and inert gas. However, this is a very slow process and requires very high temperatures to form S_2. The influence of temperature on sulfur desorption is shown by Marecot *et al.* [169] who propose the presence of three sulfur species (surface metal sulfides, polysulfides and bulk sulfides), which each desorb at different temperatures.

Another method is through using hydrogen, steam or oxygen. Hydrogen is used extensively to assist in the desorption of sulfur from nickel due to the formation of H_2S [146, 148, 152, 155, 169, 170]. Hydrogen is often favoured over steam and oxygen for recovery as it does not result in the oxidation of the nickel that can occur when using steam or oxygen. Despite the potential for nickel oxidation when steam or oxygen are used to encourage sulfur desorption, their use has been shown in numerous studies to exhibit a greater capacity to induce S desorption through the formation of

SO_2 [163, 171-174]. As SO_2 is more stable than H_2S, the possibility for its decomposition and further poisoning is significantly less [175].

An alternative method of surface regeneration when poisoning is occurring within a fuel cell system is through increasing the current to electrochemically oxidize sulfur to SO_2 (Equation 2.76 and 2.77). However, this method has significant issues regarding oxidation of nickel [175].

$$H_2S + 3O^{2-} \rightleftharpoons H_2O + SO_2 + 6e^- \quad (2.76)$$

$$S + 2O^{2-} \rightleftharpoons SO_2 + 4e^- \quad (2.77)$$

Regeneration of nickel catalysts deactivated by sulfur poisoning has been shown to varied extents. Numerous studies have shown that complete regeneration can be achieved [176, 177], whereas other studies have shown that only partial regeneration is achievable, even over significant timescales [148, 152, 163]. The extent of recovery is influenced significantly by temperature and gas atmosphere. Lack of complete recovery is primarily attributed to formation of bulk nickel sulfides, inaccessible nickel-sulfides and changes to the catalyst structure [161, 178].

2.6.1.3 Influence of sulfur chemisorption on nickel with regards to carbon deposition

Despite the significant detrimental effect that sulfur poisoning can have on reforming activity, the presence of sulfur has also been shown to have a positive effect regarding the partial inhibition of carbon deposition. This competitive process has been optimised using a small level of deactivation from sulfur poisoning to inhibit the greater deactivation that would be caused by carbon deposition, to give an improved long-term stability. The improvements available through this approach are significant and have been introduced into industrial scale reforming through what is known as the SPARG (Sulfur Passivated Reforming) process [179].

Three primary explanations are used to explain how sulfur chemisorption can cause a significantly greater loss in the carbon depositing reactions than the methane reforming reactions.

One explanation is the inhibition of carbon dissolution through the nickel particle due to the presence of sulfur preventing any carbon-containing species adsorbing to the nickel [153, 157]. This lack of dissolution will prevent the formation of any filamentous carbon species, discussed in Section 2.6.2.1. This was reported by Rostrup-Nielsen [81], who observed filamentous carbon for the steam reforming of methane reaction in the absence of H_2S, whereas only amorphous carbon is observed when H_2S is present.

Another explanation proposed is the effect of ensemble size. This has been proposed primarily by Rostrup-Nielsen and co-workers [81, 153, 157] and suggests that a nickel ensemble of 3-4 particles is required for methane reforming (H_xC-H bond cleavage), whereas an ensemble size of 6 or greater is required for carbon formation reactions (CO dissociation/ Boudouard, C-H bond cleavage). It is also suggested that an ensemble greater than 4 is required for sulfur adsorption, therefore competing with the carbon formation reactions to a greater extent than the reforming reactions.

The third explanation relates to the activity of sites with different coordination numbers. It is well established that step and edge sites are highly reactive and are favoured by sulfur and also carbon forming reactions (CO dissociation/ Boudouard, C-H bond cleavage) [154, 180, 181]. The methane reforming reactions have a lower energy requirement than the carbon formation reactions and can occur on a range of other sites. The competitive adsorption between sulfur and carbon on step sites has been extensively reported [81, 159, 167, 174, 180-182]. Bengaard *et al.* [183] have shown that atomic carbon is more stable on step sites than on terraces on a Ni(211) crystal structure. They also showed that the energy barrier for sulfur adsorption on nickel is significantly less for step sites rather than terraces. Step sites have been proposed as the primary sites for nucleation of carbon by numerous researchers [159, 167, 180, 184]. This provides a possible explanation as to why Rostrup-Nielsen [81] saw a change in carbon morphology from filamentous to amorphous on the introduction of H_2S to the reactant gas feed. As a result of the lack of step sites available for carbon in the presence of sulfur, carbon will migrate to less active surfaces. The lower stability of

the carbon on these surfaces means there is greater potential for carbon gasification, which results in a lower overall carbon deposition [81, 159].

2.6.1.4 Approaches for increasing the sulfur tolerance of catalysts

The deactivating nature of sulfur-containing compounds within methane sources such as biogas and landfill gas, mean it is often common practice to implement sulfur removal techniques on the feed gas prior to reforming. However, the high cost of using pre-reforming sulfur removal methods makes the development of sulfur tolerant catalyst materials and operating conditions highly desirable. As discussed in Section 2.6.1.2, one method of improving sulfur tolerance is through the use of very high temperatures to achieve optimum sulfur desorption. However, this method has issues in relation to increased sintering and methane decomposition. Another method to increase sulfur tolerance is by adding a reductant or oxidant to the gas feed to such an extent to encourage production of H_2S or SO_2. The issue with this method as noted previously, is the tendency for catalyst oxidation when using an oxidant, as well as the additional cost associated.

A common method of increasing sulfur tolerance is through catalyst modification and doping the catalyst with oxide materials such as ceria (CeO_2) [164, 170, 177, 185-188]. The high redox capacity of these materials increases the potential for sulfur oxidation to SO_2 or reduction to H_2S, shown through Equations 2.78 – 2.81.

$$CeO_2 + (2 - n)H_2 \rightleftharpoons CeO + (2 - n)H_2O \quad (2.78)$$

$$2CeO_2 + H_2S + (2n - 3)H_2 \rightleftharpoons Ce_2O_2S + 2(n - 1)H_2O \quad (2.79)$$

$$Ce_2O_2S + H_2 \rightleftharpoons 2CeO + H_2S \quad (2.80)$$

$$Ce_2O_2S + O_2 \rightleftharpoons 2CeO + SO_2 \quad (2.81)$$

2.6.2 Carbon deposition

Carbon deposition is of particular importance for biogas reforming due to the high carbon content within the feed gas and therefore, the increased potential for carbon deposition. Carbon deposition is often considered as the primary source of deactivation for nickel based catalysts. This is due to the greater solubility of carbon within nickel than other catalyst materials [76]. Rostrup-Nielsen *et al.* [76] showed that the order of carbon formation over a range of catalyst materials at 500 °C was Ni > Rh > Ir > Ru > Pt > Pd. It is well supported that non-noble metal catalysts are significantly more susceptible to carbon deposition than noble metal catalysts [76, 122, 189-193].

As discussed previously in Section 2.3.1, carbon deposition occurs via three processes in methane reforming; CH_4 decomposition ($CH_4 \rightleftharpoons 2H_2 + C$), Boudouard reaction ($2CO \rightleftharpoons CO_2 + C$) and CO reduction ($CO + H_2 \rightleftharpoons H_2O + C$). The extent of each of these processes is influenced significantly by temperature (see Figure 2.4) and the catalyst material as shown by Au *et al*. [194] for methane decomposition. Goula *et al*. [56] and Osaki and Mori [195] have suggested through isotopic studies that the primary mechanism of carbon deposition over nickel catalysts is via methane decomposition, whilst Verykios [55] used isotopic studies to suggest that carbon deposition over rhodium is primarily caused by the Boudouard reaction.

Carbon deposition can cause a reduction or complete loss in catalyst activity through reducing the availability of active sites for methane reforming or through mechanical failure, often resulting in severe damage to the system. The availability of active sites is reduced through either the competitive chemisorption of carbon onto the active site or through the blocking of pores within the catalyst material, reducing the flow of fuel. Mechanical failure is caused by the formation of large carbon structures which exert physical pressure on the reaction system or through the physical blocking of the reaction system, inhibiting the flow of fuel to the catalyst and causing back pressure in the system.

The manner in which carbon deposition causes catalyst deactivation is determined by the morphology of the carbon that is formed. There is a lack of universally agreed nomenclature for the

various types of carbon, possibly due to the extent to which the types can vary and the range of variables that influence their formation. For the purpose of this study, the types of carbon that will be discussed are encapsulating, filament and pyrolytic carbon. The types chosen are those primarily discussed in relation to methane reforming and can be used to encompass variations of each type as is discussed below [144].

2.6.2.1 Carbon morphologies

Encapsulating carbon is the primary carbon morphology associated with reducing the active surface area available for methane reforming, through chemisorption of carbon onto the metal to an extent to which the nickel particle is completely enveloped in a thin layer of carbon (See Figure 2.6) [196]. Encapsulating carbon is often described as atomic, which concerns a layer of individual carbon atoms that are highly reactive to gasification. Alternatively, encapsulating carbon can also be described as a type of pyrolytic or graphitic carbon in which the polymeric structures can form on the metal particles. Pyrolytic or graphitic carbon however, is not limited to encapsulation as is discussed later in this section. Encapsulation of nickel particles can extend up to 30-40 layers of carbon, forming a significant barrier to methane chemisorption on the metal [197] and can also detach the metal particle from the support, reducing stability [198].

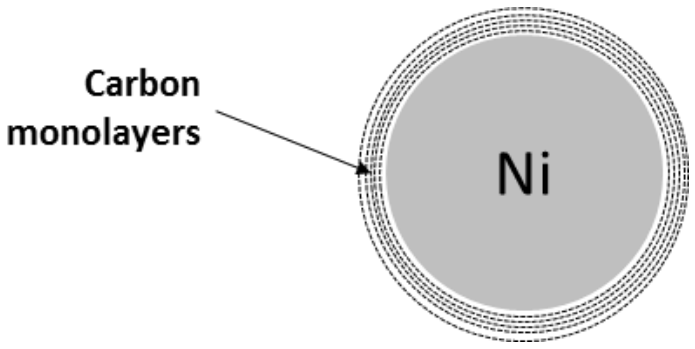

Figure 2.6: Graphical representation of nickel encapsulation with carbon (not to scale)

Carbon filaments are ordered structures that can raise the metal particles from the catalyst bed but cause minimal loss in activity due to only a very small reduction, if any, in the available surface area of the active metal [192, 199-201]. This can be seen in Figure 2.7, where the carbon binds to the surface of the nickel and diffuses through the metal to the support. The lower solubility of noble metals compared to non-noble metals means filament formation is not as prevalent with noble metals. The carbon forms layered graphite sheets producing filamentous structures. The driving force behind the diffusion of carbon to the support side of the metal is the concentration gradient caused by the high concentration of carbon that is adsorbed on the top of the nickel particle [202, 203]. Therefore, carbon filament formation is significantly influenced by the C/O and C/H ratios within the gas [204]. Filaments can also grow through nucleation if the temperature and carbon concentration are sufficient [205].

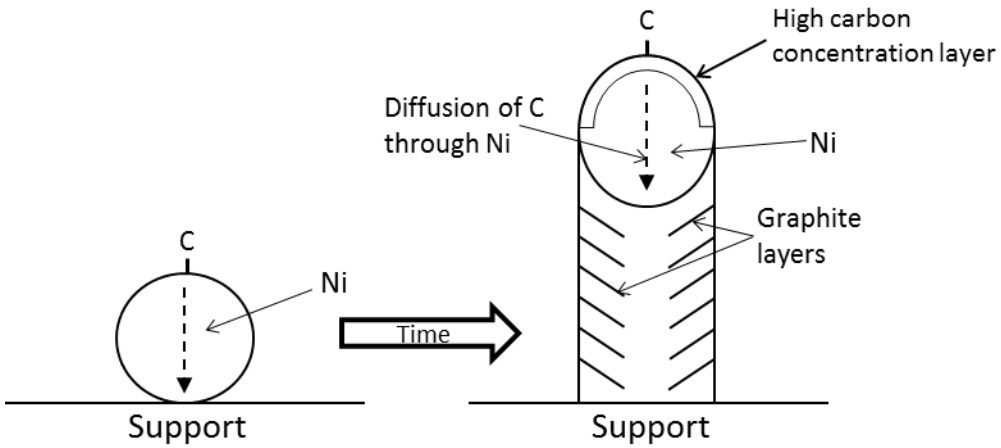

Figure 2.7: Graphical representation of carbon filament formation. Adapted from [197, 202, 205].

Temperature has a significant influence on the morphology of the filament and also the extent to which the nickel particle is deformed. At lower temperatures, carbon diffusion through the metal particle is slow, resulting in a highly ordered filament which reduces the interaction between the metal and the support. At higher temperatures, the diffusion is faster resulting in less order and increasing the metal-support interaction. This can cause the metal particle to deform into a 'pear' shape as shown in Figure 2.8. High metal distortion can be caused from the formation of hollow

filaments (Figure 2.8), which occur at high temperatures when the rate of nucleation is greater than the rate of diffusion, causing filaments to only grow at the three phase boundary [205]. The lack of carbon between the metal and the support means that the metal-support interaction is very strong, resulting in the distortion shown in Figure 2.8.

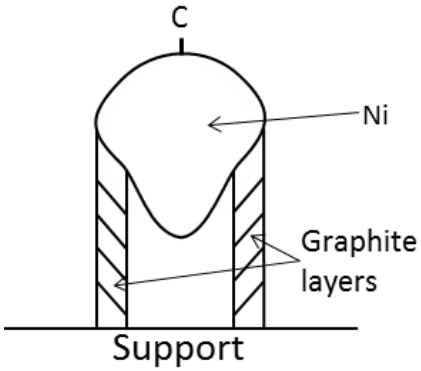

Figure 2.8: Graphical representation of a hollow carbon filament and metal deformation. Adapted from [205].

Filamentous carbon is used as a general term used to incorporate other carbon structures, such as carbon nanotubes. Carbon nanotubes differ from standard filaments in the orientation of the graphite layers towards the tube axis. Carbon filaments contain layers that are not parallel to the tube axis and can be perpendicular, whereas nanotubes contain parallel layers as shown in Figure 2.9 [197, 206]. Despite the minimal decrease in activity caused by carbon filaments through reduction in surface area, filamentous structures can be highly damaging to reactor systems as they can result in mechanical failure from plugging or shattering of the catalyst and operating system [207].

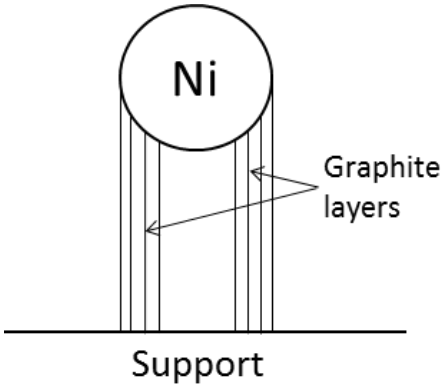

Figure 2.9: Graphical representation of multiwalled carbon nanotube on Ni. Adapted from [197].

Pyrolytic carbon consists of graphite crystallites that, unlike with graphitic structures, contain a level of disorder in the form of lattice defects and imperfections [208]. The disorder within pyrolytic carbon allows for numerous different structures to form including columnar (which can lead to filament formation), laminar (which can lead to encapsulation) and isotropic (small grains of carbon). Isotropic carbon is the primary form of pyrolytic carbon considered within this research.

2.6.2.2 Factors influencing carbon deposition

The morphology and extent of carbon deposited is determined by a number of different variables; temperature, particle size, relative gas ratios, catalyst material and duration of processes. The influence of temperature on carbon deposition has been discussed in Section 2.3.1, with regard to the extent to which the carbon formation reactions (Boudouard, methane decomposition and CO reduction) occur as a function of temperature.

The relationship between carbon morphology and temperature is complex and is affected by other variables, such as gas ratio and catalyst material. High temperatures favour the deposition of carbon but also the decomposition or gasification of carbon deposits. At lower temperatures, more reactive and less structured types of carbon such as amorphous and atomic carbon are formed. As

temperature increases, the capacity to form less reactive and more structured carbon morphologies such as filaments, graphite sheets and pyrolytic increases [50, 144]. These less reactive carbon morphologies can be produced directly or indirectly through the polymerisation and conversion of more reactive species [144]. The indirect conversion is favoured at high temperatures and duration [55]. The complex interaction between carbon deposition and temperature is amplified by the different stabilities of different morphologies. Increased temperatures required to produce more structured morphologies are also required for the oxidation or hydrogenation in high O/C or H/C conditions, illustrating the influence of gas ratio on carbon deposition. That hydrogen is required for filament formation and not nanotube formation also demonstrates the influence of gas ratio on carbon morphology [197, 208].

The influence of catalyst particle and ensemble size on carbon deposition has been discussed significantly within the literature [93, 206, 209-214]. It is well supported that increased metal particle size results in an increase in the overall level of carbon deposition. Catalyst particle size also has a significant influence on carbon morphology, especially regarding the formation of filamentous structures. Numerous studies [93, 153, 206] suggest that the diameter of the filament is proportional to the size of the particle to which it is bound. Tang *et al.* [207] and Kock *et al.* [215] both suggest that the minimum nickel particle size that carbon filaments can form upon is 10 nm, whereas Martinez *et al.* [211] suggest a minimum size of 9 nm. Italiano *et al.* [204] suggest that filaments will only form on nickel particles that have a diameter between 20-100 nm, as below 20 nm the interaction between metal and support is large enough to inhibit carbon deposition between the metal and the support, and above 100 nm, the diffusion of carbon through the particle becomes unfavourable. Sinnott *et al.* [216] suggest that filament formation is unfavourable at low metal particle size as a result of the stress placed on the graphite planes within the filament due to their close proximity, and that nanotubes will be favoured at lower particle sizes.

Ensemble size has been suggested to influence the extent of carbon deposition, Chen *et al.* [217] have suggested that an ensemble of 6 nickel atoms is required for encapsulating carbon to form, compared to 3 for the methane reforming reaction. Ensemble size can significantly influence the

extent of deactivation via sulfur poisoning as discussed in Section 2.6.1. Thermal agglomeration or sintering can occur during reforming reactions and is a primary cause of increased particle size, and is discussed in detail in Section 2.6.3.

The nature of the catalyst material and support has been shown to have a significant influence on the extent of carbon deposition and morphology. As discussed previously, nickel catalysts are significantly more susceptible to carbon deposition than noble metal catalysts, due to the greater solubility of carbon within nickel. The activity of the catalyst material towards methane reforming also determines the quantity of metal, or loading, required for sufficient performance. This significantly influences the catalyst particle size, as increased loading increases the potential for particle agglomeration [93, 218] which as discussed previously, can lead to increased carbon deposition [219].

Catalyst support basicity has also been suggested to have a significant influence on the extent of carbon deposition during methane reforming reactions. With increased basicity, the availability to accept an electron from C-H bond cleavage decreases. This therefore reduces the potential for methane decomposition and subsequent carbon deposition [209, 211, 220]. Increased basicity also increases the potential for donation of electrons into the vacant antibonding orbital of CO_2, resulting in its decomposition. CO_2 decomposition favours the reverse Boudouard reaction (Equation 2-11) and acts to reduce the level of carbon deposited [220, 221]. Lercher *et al.* [93] have shown that carbon deposition is favoured on the metal-support-gas boundary, often known as the Three Phase Boundary (TPB).

The catalyst material can also be doped with a small quantity of material to influence the activity and selectivity of the reforming reaction, and also the susceptibility to carbon deposition. Dopant materials can be used to increase the availability of oxygen within the catalyst material. One example of this is doping with rare earth oxides, such as ceria (CeO_2). The high redox/oxygen storage capacity of these dopants increases the presence of surface oxygen and therefore the potential for the oxidation of any carbon deposits [222-225]. Doping can also act as a barrier

between active metal particles, therefore reducing the potential for sintering and increased particle size [211, 225] which, as discussed previously, can influence carbon deposition.

The presence of sulfur within the gas feed can have a significant influence on the extent to which carbon deposition occurs. The adsorption of sulfur on the metal particles competes with the adsorption of methane and carbon monoxide on the metal particles and the subsequent carbon deposition that can occur. The competitive binding of sulfur to metal particles is discussed in detail in Section 2.6.1.

2.6.2.3 Non-deactivating carbon

As discussed previously, certain carbon morphologies have a limited or negligible effect on catalyst activity and are often discussed as spectator species [55]. However, these species will inevitably influence activity through the sheer quantity of carbon present. Carbon deposition has been shown to be a partially reversible process through the use of dopant materials with high oxygen storage capacity such as ceria [225], and also when placed under electrical load within a fuel cell, which can remove surface carbon through electrochemical oxidation [142].

Deposited carbon is also suggested to be a favourable process within some catalytic materials. Otsuka *et al.* [226] have shown the successful use of methane reforming over nickel supported on carbon fibres, whilst Naito [66] reported the significant activity of surface carbides for methane reforming reactions.

2.6.3 Thermal degradation

Thermal degradation or sintering involves the increase in metal particle size at high temperature. This process plays a significant role in catalyst deactivation due to the influence of particle size on both sulfur poisoning and carbon deposition, as discussed in Sections 2.6.1 and 2.6.2 respectively. An increase in metal particle size also results in a decreased active surface area, therefore

decreasing the reforming activity of the catalyst. A number of studies have shown the substantial particle size growth when nickel is subjected to temperatures in excess of 700 °C [207, 227] , with Zhang *et al.* [228] suggesting that nickel can undergo coalescence at temperatures as low at 470 °C (Hüttig Temperature). Three mechanisms have been proposed for thermal degradation; particle migration, vapour transport and Ostwald ripening [144].

Particle migration concerns the movement of complete metal particles across the support and the subsequent coalescence of particles when they come into contact. Vapour transport concerns the movement of metal particles through the gas phase. This process will only occur at very high temperatures due to the energy required to break the metal-support interaction. Ostwald ripening, or atom migration as it is also known, concerns the movement of metal atoms from one metal particle across the support to a different larger metal particle which receives the atom and subsequently increases in size. The high surface energy and high solubility of smaller particles is the driving force for atom migration [229-233]. Sehested [147] and Rostrup-Nielsen *et al.* [234] have suggested that particle migration is the dominant mechanism at lower temperatures (<600 °C) and that at higher temperatures, Ostwald ripening dominates. In contrast, Rasmussen *et al.* [232] suggest, using particle size distributions, that atom migration does not contribute to sintering until approximately 800 °C. A significant disparity appears to be present regarding the use of particle size distributions to assess mechanisms of sintering, and the influence of parameters such as atmosphere and catalyst character makes assigning an accurate temperature at which one mechanism dominates very problematic [229, 232]. Particle and atom migration are shown in Figure 2.10 and Figure 2.11 respectively.

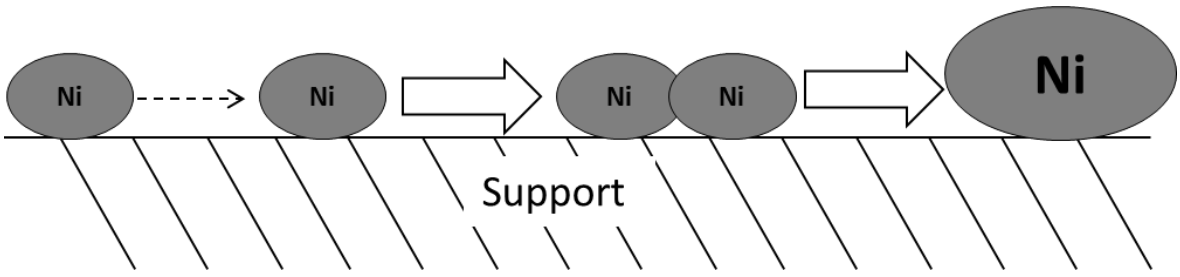

Figure 2.10: Schematic diagram of crystallite growth via particle migration.

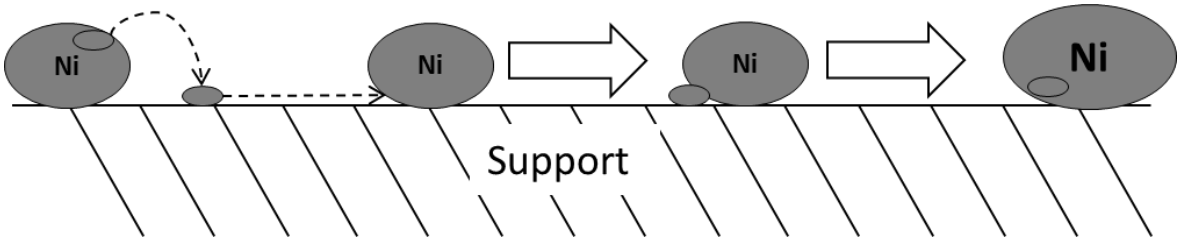

Figure 2.11: Schematic diagram of crystallite growth via atom migration (Ostwald ripening).

Unlike with sulfur poisoning and carbon deactivation, degradation through thermal methods is largely irreversible. A small number of studies have shown a recovery from thermal degradation by redispersion of catalysts particles using highly specific conditions. Bartholomew [144] discusses this recovery as a process of crystallite decomposition and subsequent redispersion of catalysts particles. This process is favoured under O_2 or Cl_2 rich atmospheres due to the formation of volatile oxides and chlorides which easily decompose. This recovery from thermal degradation has also been seen by Hashemnejad and Parvari [146] using CO_2 as a partial oxidative atmosphere. The main factors that influence the type and rate of thermal degradation are temperature, atmosphere, nature of the metal, metal dispersion and loading, and nature of the support.

Temperature is understandably seen as the primary factor in influencing the rate of thermal degradation and has been shown to have a strong relationship with sintering rate [144, 232, 235]. The influence that the atmospheric composition has on the rate of thermal degradation has been discussed widely and is viewed as one of the most influential factors [144, 147, 233, 236, 237]. The presence of steam in particular has been shown to significantly enhance the sintering rate due to the formation of hydroxyl species, such as Ni_2OH [147, 236]. These species have a lower activation energy and higher diffusivity than metal adatoms, therefore increasing their mobility and potential for agglomeration. The ability of species adsorbing on the metal to enhance the rate of sintering has sometimes been attributed to an interaction known as the skyhook effect [147, 238]. This effect concerns the adsorbent on the metal reducing the electron density localized on the face of the metal interacting with the support. This therefore reduces the bond strength and increases bond length between the metal and support, increasing the mobility of the metal from the support [238]. The

ability of hydrogen to reduce sintering and oxygen to facilitate sintering has been discussed by Bartholomew [144], whilst the effect of CO_2 has been discussed previously.

The nature of the catalyst material significantly affects the susceptibility to sintering due to the particle size, bond strength to the support and also the activity towards reforming, as this will control the loading. Low metal loading and small particle size favour high dispersion. High dispersion is favourable for increased activity and surface area but is also prone to sintering due to the minimal distance between metal atoms and associated high probability for collisions and coalescence. Bond strength between metal and support can vary significantly with metal and support [239, 240]. Numerous studies have been conducted illustrating the influence on sintering rate through the addition of a dopant to the catalyst. Pompeo *et al.* [225] and Liu *et al.* [218] have both shown a reduction in sintering rate through the doping with mixed metal oxides. These dopants can reduce sintering by reducing the metal mobility through acting as spacers to prevent coalescence of particles and also through acting as trapping agents which produce strong interactions with the metal atoms [144, 230, 233, 235]. In contrast, Rasmussen *et al.* [232] and Sehested *et al.* [233] have shown that doping of nickel catalysts with alkali metals can enhance sintering rate.

2.7 References

1. N.D. Mortimer, A.K.F. Evans, O. Mwabonje, and C.L. Whitttaker, *Analysis of the Greenhouse Gas Emissions for Thermochemical BioSNG Production and Use in the United Kingdom*. 2010, NNFCC & North Energy.
2. NNFCC, *Short Rotation Coppice Willow (SRC) Crop Fact Sheet*. November 2010.
3. NNFCC, *Miscanthus Crop Fact Sheet*. November 2010.
4. *Proceedings*. in *IPCC Scoping Meeting On Renewable Energy Sources*. 2008. Germany: International Panel On Climate Change.
5. *IEA Energy Technology Essentials: Biomass for Power Generation and CHP*. 2007, International Energy Association.
6. T. Astrup, *Management of APC residues from W-t-E Plants*. 2008, IWSA.
7. M. Izquierdo, E. Vazquez, X. Querol, M. Barra, A. Lopez, and F. Plana, *Use of bottom ash from municipal sold waste incineration as a road material*, in *International Ash Utilization Symposium*. 2001: USA. p. Paper #37.
8. J.M. Chimenos, M. Segarra, M.A. Fernández, and F. Espiell, *Characterization of the bottom ash in municipal solid waste incinerator.* Journal of Hazardous Materials, 1999. **64**(3): p. 211-222.
9. M. Fatih Demirbas, M. Balat, and H. Balat, *Biowastes-to-biofuels.* Energy Conversion and Management, 2011. **52**(4): p. 1815-1828.
10. A.A. Refaat, *Correlation between the chemical structure of biodiesel and its physical properties.* International Journal of Environmetal Science and Technology, 2009. **6**(4): p. 677-694.
11. D. Deublein and A. Steinhauser, *Biogas from Waste and Renewable Resources - An Introduction*. 2011, Viley-VCH Verlag GmbH & Co. p. 31-34, 101-108.
12. DEFRA, *Anaerobic Digestion - Shared Goals*. 2009.
13. DEFRA, *Accelerating the Uptake of Anaerobic Digestion in England: an Implementation Plan*. 2010.

14. *Environment Agency, Waste Protocols Project: Anaerobic digestate*. 2008.

15. *Department of Energy and Climate Change, The UK Renewable Energy Strategy*. 2009.

16. S. Rasi, A. Veijanen, and J. Rintala, *Trace compounds of biogas from different biogas production plants.* Energy, 2007. **32**(8): p. 1375-1380.

17. A. Demirbas, *Biofuels sources, biofuel policy, biofuel economy and global biofuel projections.* Energy Conversion and Management, 2008. **49**(8): p. 2106-2116.

18. J. Bogner and K. Spokas, *Landfill CH_4 : Rates, fates, and role in global carbon cycle.* Chemosphere, 1991. **26**: p. 369-386.

19. A.S. Sambo, B. Garba, and B.G. Danshehu, *Effect of some operating parameters on biogas production rate.* Renewable Energy, 1995. **6**(3): p. 343-344.

20. G.D. Zupancic and M. Ros, *Heat and energy requirements in thermophilic anaerobic sludge digestion.* Renewable Energy, 2003. **28**(14): p. 2255-2267.

21. R. Borja, C.J. Banks, A. Martín, and B. Khalfaoui, *Anaerobic digestion of palm oil mill effluent and condensation water waste: an overall kinetic model for methane production and substrate utilization.* Bioprocess and Biosystems Engineering, 1995. **13**(2): p. 87-95.

22. M.F. Gerardi, *The Microbiology of Anaerobic Digesters*. 2003, Wiley VCH. p. 17-20.

23. DEFRA, *Municipal Waste Management Statistics For England 2009/10*. 2010.

24. N.J. Themelis and P.A. Ulloa, *Methane generation in landfills.* Renewable Energy, 2007. **32**(7): p. 1243-1257.

25. M. Caine, *Biogas Flares: State of the Art and Market Review*. 2000, International-Energy-Association.

26. *US Environmental Protection Agency, Clean Energy Strategies for Local Governments*. 2008.

27. IPCC, *Ch 10.3 Emission Trends*, in *IPCC Fourth Assessment Report: Climate Change*. 2007.

28. S. Monni, R. Pipatti, A. Lehtila, I. Savolainen, and S. Syri, *Global climate change mitigation scenarios for solid waste management*. 2006, VTT Report.

29. H.C. Willumsen. *Energy recovery fron Landfill Gas in Denmark and Worldwide*. in *International Workshop for Utilization of Landfill Gas for Energy Production*. 2001. Kaunas, Lithuania.

30. H. Shiga, K. Shinda, K. Hagiwara, A. Tsutsumi, M. Sakurai, K. Yoshida, and E. Bilgen, *Large-scale hydrogen production from biogas.* International Journal of Hydrogen Energy, 1998. **23**(8): p. 631-640.

31. F.P. Nagel, T.J. Schildhauer, and S.M.A. Biollaz, *Biomass-integrated gasification fuel cell systems - Part 1: Definition of systems and technical analysis.* International Journal of Hydrogen Energy, 2009. **34**(16): p. 6809-6825.

32. C. Xu, J.W. Zondlo, M. Gong, F. Elizalde-Blancas, X. Liu, and I.B. Celik, *Tolerance tests of H_2S-laden biogas fuel on solid oxide fuel cells.* Journal of Power Sources, 2010. **195**(15): p. 4583-4592.

33. J. Van herle, Y. Membrez, and O. Bucheli, *Biogas as a fuel source for SOFC co-generators.* J. Power Sources, 2004. **127**: p. 300-312.

34. J. Van herle, F. Maréchal, S. Leuenberger, Y. Membrez, O. Bucheli, and D. Favrat, *Process flow model of solid oxide fuel cell system supplied with sewage biogas.* Journal of Power Sources, 2004. **131**(1-2): p. 127-141.

35. P. Piroonlerkgul, W. Wiyaratn, A. Soottitantawat, W. Kiatkittipong, A. Arpornwichanop, N. Laosiripojana, and S. Assabumrungrat, *Operation viability and performance of solid oxide fuel cell fuelled by different feeds.* Chemical Engineering Journal, 2009. **155**(1-2): p. 411-418.

36. P. Piroonlerkgul, S. Assabumrungrat, N. Laosiripojana, and A.A. Adesina, *Selection of appropriate fuel processor for biogas-fuelled SOFC system.* Chem. Eng. J., 2008. **140**: p. 341-351.

37. J. Staniforth and K. Kendall, *Cannock landfill gas powering a small tubular solid oxide fuel cell - a case study.* J. Power Sources, 2000. **86**: p. 401-403.

38. J. Staniforth and K. Kendall, *Biogas powering a small tubular solid oxide fuel cell.* J. Power Sources, 1998. **71**: p. 275-277.

39. J. Staniforth, *The use of biogas to power a small tubular solid oxide fuel cell, PhD Thesis*. 2000, Keele University.

40. C. Muller, *Anaerobic Digestion of Biodegradable Solid Waste in Low- and Middle-Income Countries*. 2007, Eawag.

41. R. Bove and P. Lunghi, *Electric power generation from landfill gas using traditional and innovative technologies.* Energy Conversion and Management, 2006. **47**(11-12): p. 1391-1401.

42. J. Huang and R.J. Crookes, *Assessment of simulated biogas as a fuel for the spark ignition engine.* Fuel, 1998. **77**(15): p. 1793-1801.

43. S.O. Bade Shrestha and G. Narayanan, *Landfill gas with hydrogen addition - A fuel for SI engines.* Fuel, 2008. **87**(17-18): p. 3616-3626.

44. *Department of Energy and Climate Change, Biomethane into the Gas Network: A Guide for Producers*. 2009.

45. P. Wheeler, *Biogas upgrading and utilisation*, in *Task 24: Energy from biological conversion of organic waste*. 2000, International-Energy-Association.

46. A. Petersson and A. Wellinger, *Biogas upgrading technologies - developments and innovations*, in *Task 37 - Energy from biogas and landfill gas*. 2009, International-Energy-Association.

47. National-Grid, *The potential for Renwable Gas in the UK*. 2009.

48. J. Hagen, *Industrial Catalysis: A Practical Approach*. 2006, Wiley VCH p. 109-111.

49. G. Rothenberg, *Catalysis: Concepts and Green Applications*. 2008, Wiley VCH. p. 129-132.

50. R.T. Baker and I.S. Metcalfe, *Study of the Activity and deactivation of Ni-YSZ cermet in dry CH_4 using temperature programmed techniques.* Ind. Eng. Chem. Res., 1995. **34**: p. 1558-1565.

51. D.R. Lide, ed. *CRC Handbook of Chemistry and Physics*. 76th ed. 1995: Chapter 5.

52. F. Solymosi, A. Erdohelyi, J. Cserenyi, and A. Felvegi, *Decomposition of CH_4 over Supported Pd Catalysts.* Journal of Catalysis, 1994. **147**(1): p. 272-278.

53. A. Erdohelyi, J. Cserenyi, and F. Solymosi, *Activation of CH_4 and its Reaction with CO_2 over Supported Rh Catalysts.* Journal of Catalysis, 1993. **141**(1): p. 287-299.

54. W.J.M. Vermeiren, E. Blomsma, and P.A. Jacobs, *Catalytic and thermodynamic approach of the oxyreforming reaction of methane.* Catalysis Today, 1992. **13**(2-3): p. 427-436.

55. X.E. Verykios, *Mechanistic aspects of the reaction of CO_2 reforming of methane over Rh/Al_2O_3 catalyst.* Applied Catalysis A: General, 2003. **255**(1): p. 101-111.

56. M.A. Goula, A.A. Lemonidou, and A.M. Efstathiou, *Characterization of Carbonaceous Species Formed during Reforming of CH_4 with CO_2 over Ni/CaO-Al_2O_3 Catalysts Studied by Various Transient Techniques.* Journal of Catalysis, 1996. **161**(2): p. 626-640.

57. Q.G. Yan, W.Z. Weng, H.L. Wan, H. Toghiani, R.K. Toghiani, and C.U. Pittman, *Activation of methane to syngas over a Ni/TiO_2 catalyst.* Applied Catalysis A: General, 2003. **239**(1-2): p. 43-58.

58. N.C. Triantafyllopoulos and S.G. Neophytides, *Dissociative adsorption of CH_4 on NiAu/YSZ: The nature of adsorbed carbonaceous species and the inhibition of graphitic C formation.* Journal of Catalysis, 2006. **239**(1): p. 187-199.

59. G.E. Keller and M.M. Bhasin, *Synthesis of ethylene via oxidative coupling of methane : I. Determination of active catalysts.* Journal of Catalysis, 1982. **73**(1): p. 9-19.

60. A. Toebes, K.M. Dooley, and J.R.H. Ross, *Oxidative coupling of methane over K/Ni/Ca oxide and K/Ni/Mg oxide catalysts.* Catalysis Today, 1994. **21**(2-3): p. 401-408.

61. K.M. Dooley and J.R.H. Ross, *Potassium/calcium/nickel oxide catalysts for oxidative coupling of methane.* Applied Catalysis A: General, 1992. **90**(2): p. 159-174.

62. K.M. Dooley, S.Y. Chen, and J.R.H. Ross, *Stable Nickel-Containing Catalysts for the Oxidative Coupling of Methane.* Journal of Catalysis, 1994. **145**(2): p. 402-408.

63. A.M. Maitra, I. Campbell, and R.J. Tyler, *Influence of basicity on the catalytic activity for oxidative coupling of methane.* Applied Catalysis A: General, 1992. **85**(1): p. 27-46.

64. A. Erdöhelyi, J. Cserényi, E. Papp, and F. Solymosi, *Catalytic reaction of methane with carbon dioxide over supported palladium.* Applied Catalysis A: General, 1994. **108**(2): p. 205-219.

65. J.R.H. Ross, A.N.J. van Keulen, M.E.S. Hegarty, and K. Seshan, *The catalytic conversion of natural gas to useful products.* Catalysis Today, 1996. **30**(1-3): p. 193-199.

66. S. Naito, *Methane conversion by various metal, metal oxide and metal carbide catalysts.* Catalysis Surveys from Japan, 2000. **4**(1): p. 3-15.

67. *Department of Energy, National Hydrogen Energy Roadmap*. 2002, United-States-Department-of-Energy.

68. A.P.E. York, T.C. Xiao, M.L.H. Green, and J.B. Claridge, *Methane oxyforming for synthesis gas production.* Catalysis Reviews-Science and Engineering, 2007. **49**(4): p. 511-560.

69. I.M. Bodrov and L.O. Apel'baum, *Kinetics for the reaction of methane with steam on the surface of nickel at 400 - 600C.* Kinetics and Catalysis, 1968. **9**: p. 877-881.

70. H.H. Gunardson and J.M. Abrardo, *Produce CO-rich synthesis gas.* Hydrocarbon Processing (International Edition), 1999. **78**(4): p. 87.

71. S.S. Bharadwaj and L.D. Schmidt, *Catalytic partial oxidation of natural gas to syngas.* Fuel Processing Technology, 1995. **42**(2-3): p. 109-127.

72. M.I. Temkin, *The Kinetics of Some Industrial Heterogeneous Catalytic Reactions*, in *Advances in Catalysis*, H.P. D.D. Eley and B.W. Paul, Editors. 1979, Academic Press. p. 173-291.

73. J.G. Xu and G.F. Froment, *Methane steam reforming, methanation and water-gas shift. 1. Intrinsic kinetics.* Aiche Journal, 1989. **35**(1): p. 88-96.

74. A.K. Avetisov, J.R. Rostrup-Nielsen, V.L. Kuchaev, J.H. Bak Hansen, A.G. Zyskin, and E.N. Shapatina, *Steady-state kinetics and mechanism of methane reforming with steam and carbon dioxide over Ni catalyst.* Journal of Molecular Catalysis A: Chemical, 2010. **315**(2): p. 155-162.

75. K. Hou and R. Hughes, *The kinetics of methane steam reforming over a Ni/[alpha]-Al_2O catalyst.* Chemical Engineering Journal, 2001. **82**(1-3): p. 311-328.

76. J.R. Rostrup-Nielsen and J.H.B. Hansen, *CO_2-Reforming of Methane over Transition Metals.* Journal of Catalysis, 1993. **144**(1): p. 38-49.

77. M. Temkin, *The Kinetics of Some Industrial Heterogeneous Catalytic Reactions.* Advances in Catalysis, 1989. **28**: p. 173.

78. G. Jones, J.G. Jakobsen, S.S. Shim, J. Kleis, M.P. Andersson, J. Rossmeisl, F. Abild-Pedersen, T. Bligaard, S. Helveg, B. Hinnemann, J.R. Rostrup-Nielsen, I. Chorkendorff, J. Sehested, and J.K. Nørskov, *First principles calculations and experimental insight into methane steam reforming over transition metal catalysts.* Journal of Catalysis, 2008. **259**(1): p. 147-160.

79. I. Wender, *Reactions of synthesis gas.* Fuel Processing Technology, 1996. **48**(3): p. 189-297.

80. S.C. Teuner, P. Neumann, and F. Von Linde, *CO through CO_2 Reforming; The Calcor Standard and Calcor Economy Processes*, in *OIL GAS*. 2001. p. 44-46.

81. J.R. Rostrup-Nielsen, *Sulfur-passivated nickel catalysts for carbon-free steam reforming of methane.* Journal of Catalysis, 1984. **85**(1): p. 31-43.

82. A. Erdohelyi, K. Fodor, and T. Szailer, *Effect of H_2S on the reaction of methane with carbon dioxide over supported Rh catalysts.* Applied Catalysis B: Environmental, 2004. **53**(3): p. 153-160.

83. M.F. Mark and W.F. Maier, *Active Surface Carbon - A Reactive Intermediate in the Production of Synthesis Gas from Methane and Carbon Dioxide.* Agnew. Chem. Int. Ed. Engl., 1994. **33**: p. 1657-1660.

84. A.M. O'Connor, Y. Schuurman, J. Ross, and C. Mirodatos, *Transient studies of carbon dioxide reforming of methane over Pt/ZrO_2 and Pt/Al_2O_3.* Catal. Today, 2006. **115**: p. 191-198.

85. J.H. Bitter, K. Seshan, and J.A. Lercher, *Deactivation and Coke Accumulation during CO_2/CH_4 Reforming over Pt Catalysts.* Journal of Catalysis, 1999. **183**(2): p. 336-343.

86. M.F. Mark and W.F. Maier, *CO_2-Reforming of Methane on Supported Rh and Ir Catalysts.* Journal of Catalysis, 1996. **164**(1): p. 122-130.

87. A. Erdöhelyi and F. Solymosi, *Effects of the support on the adsorption and dissociation of CO and on the reactivity of surface carbon on Rh catalysts.* Journal of Catalysis, 1983. **84**(2): p. 446-460.

88. C.E. Quincoces and M.G. Gonzalez, *Kinetic Study on CO_2 Reforming of Methane.* Chinese Journal of Chemical Engineering, 1991. **9**: p. 190-195.

89. U. Olsbye, T. Wurzel, and L. Mleczko, *Kinetics and reaction engineering studies of dry reforming of methane over a Ni/La/Al_2O_3 catalyst.* Industrial & Engineering Chemistry Research, 1997. **36**(12): p. 5180-5188.

90. L.M. Aparicio, *Transient Isotopic Studies and Microkinetic Modeling of Methane Reforming over Nickel Catalysts.* Journal of Catalysis, 1997. **165**(2): p. 262-274.

91. I.M. Bodrov and L.O. Apelbaum, *Kinetics of the reaction of methane with CO_2 over nickel.* Journal of Catalysis, 1968. **10**(1): p. 99-99.

92. G.F. Froment, *Production of synthesis gas by steam- and CO_2-reforming of natural gas.* Journal of Molecular Catalysis A: Chemical, 2000. **163**(1-2): p. 147-156.

93. J.A. Lercher, J.H. Bitter, W. Hally, W. Niessen, K. Seshan, J.W. Hightower., W.N.D.E. Iglesia., and A.T. Bell, *Design of stable catalysts for methane-carbon dioxide reforming*, in *Studies in Surface Science and Catalysis*. 1996, Elsevier. p. 463-472.

94. S.M. Stagg-Williams, F.B. Noronha, G. Fendley, and D.E. Resasco, *CO_2 Reforming of CH_4 over Pt/ZrO_2 Catalysts Promoted with La and Ce Oxides.* Journal of Catalysis, 2000. **194**(2): p. 240-249.

95. M.C.J. Bradford and M.A. Vannice, *Catalytic reforming of methane with carbon dioxide over nickel catalysts II. Reaction kinetics.* Applied Catalysis A: General, 1996. **142**(1): p. 97-122.

96. T. Osaki, T. Horiuchi, K. Suzuki, and T. Mori, *Catalyst performance of MoS_2 and WS_2 for the CO_2-reforming of CH_4 :Suppression of carbon deposition.* Applied Catalysis A: General, 1997. **155**(2): p. 229-238.

97. N. Padban and V. Becher, *Literature and State-of-the-Art review (Re: Methane Steam Reforming)*, in *Clean Hydrogen-rich Synthesis Gas*. 2005, CHRISGAS.

98. B. Christian Enger, R. Lødeng, and A. Holmen, *A review of catalytic partial oxidation of methane to synthesis gas with emphasis on reaction mechanisms over transition metal catalysts.* Applied Catalysis A: General, 2008. **346**(1-2): p. 1-27.

99. V.R. Choudhary, A.S. Mammam, and S.D. Sansare, *Selective oxidation of methane to CO and H_2 over Ni/MgO at low temperatures.* Agnew. Chem. Int. Ed. Engl., 1992. **31**: p. 1189-1190.

100. V.R. Choudhary, A.M. Rajput, B. Prabhakar, and A.S. Mamman, *Partial oxidation of methane to CO and H_2 over nickel and/or cobalt containing ZrO_2, ThO_2, UO_2, TiO_2 and SiO_2 catalysts.* Fuel, 1998. **77**(15): p. 1803-1807.

101. Y.H. Hu and E. Ruckenstein, *Transient kinetic studies of partial oxidation of CH_4.* Journal of Catalysis, 1996. **158**(1): p. 260-266.

102. D.A. Hickman and L.D. Schmidt, *Synthesis Gas-Formation by Direct Oxidation of Methane over Monoliths.* Acs Symposium Series, 1993. **523**: p. 416-426.

103. W.S. Dong, K.W. Jun, H.S. Roh, Z.W. Liu, and S.E. Park, *Comparative study on partial oxidation of methane over Ni/ZrO_2, Ni/CeO_2 and Ni/Ce-ZrO_2 catalysts.* Catalysis Letters, 2002. **78**(1-4): p. 215-222.

104. S. Eriksson, S. Rojas, M. Boutonnet, and J.L.G. Fierro, *Effect of Ce-doping on Rh/ZrO_2 catalysts for partial oxidation of methane.* Applied Catalysis A: General, 2007. **326**(1): p. 8-16.

105. S. Liu, W. Li, Y. Wang, and H. Xu, *Catalytic partial oxidation of methane to syngas in a fixed bed reactor with an O_2 distributor: The axial temperature profile and species profile study.* Fuel Process. Technol., 2008. **89**: p. 1345-1350.

106. M. Fleys, Y. Simon, D. Swierczynski, A. Kiennemann, and P.-M. Marquaire, *Investigation of the Reaction of Partial Oxidation of Methane over Ni/La_2O_3 Catalyst.* Energy & Fuels, 2006. **20**(6): p. 2321-2329.

107. K. Heitnes, S. Lindberg, O.A. Rokstad, and A. Holmen, *Catalytic partial oxidation of methane to synthesis gas.* Catalysis Today, 1995. **24**(3): p. 211-216.

108. V.A. Tsipouriari, Z. Zhang, and X.E. Verykios, *Catalytic Partial Oxidation of Methane to Synthesis Gas over Ni-Based Catalysts: I. Catalyst Performance Characteristics.* Journal of Catalysis, 1998. **179**(1): p. 283-291.

109. A.M. Diskin, R.H. Cunningham, and R.M. Ormerod, *The oxidative chemistry of methane over supported nickel catalysts.* Catalysis Today, 1998. **46**(2-3): p. 147-154.

110. D.A. Hickman and L.D. Schmidt, *Synthesis gas formation by direct oxidation of methane over Pt monoliths.* Journal of Catalysis, 1992. **138**(1): p. 267-282.

111. A. Slagtern, H.M. Swaan, U. Olsbye, I.M. Dahl, and C. Mirodatos, *Catalytic partial oxidation of methane over Ni-, Co- and Fe-based catalysts.* Catalysis Today, 1998. **46**(2-3): p. 107-115.

112. M. Prettre, C. Eichner, and M. Perrin, *The catalytic oxidation of methane to carbon monoxide and hydrogen.* Transactions of the Faraday Society, 1946. **42**: p. 335b-339.

113. A. Chauvel and G. Lefebvre, *Petrochemical Processes 1: Synthesis-Gas Derivatives and Major Hydrocarbons*. 1989, Editions Technip, France. p. 89.

114. H.S. Roh, K.W. Jun, W.S. Dong, S.E. Park, and Y.S. Baek, *Highly stable Ni catalyst supported on Ce-ZrO_2 for oxy-steam reforming of methane.* Catalysis Letters, 2001. **74**(1-2): p. 31-36.

115. D.C.R.M. Santos, L. Madeira, and F.B. Passos, *The effect of the addition of Y_2O_3 to Ni/[alpha]-Al_2O_3 catalysts on the autothermal reforming of methane.* Catalysis Today, 2008. **149**(3-4): p. 401-406.

116. H.S. Roh, K.Y. Koo, J.H. Jeong, Y.T. Seo, D.J. Seo, Y.S. Seo, W.L. Yoon, and S. Bin Park, *Combined reforming of methane over supported Ni catalysts.* Catalysis Letters, 2007. **117**(1-2): p. 85-90.

117. H.S. Roh, K.Y. Koo, U.D. Joshi, and W.L. Yoon, *Combined H_2O and CO_2 reforming of methane over Ni-Ce-ZrO_2 catalysts for gas to liquids (GTL).* Catalysis Letters, 2008. **125**(3-4): p. 283-288.

118. K.Y. Koo, H.S. Roh, U.H. Jung, and W.L. Yoon, *CeO_2 Promoted Ni/Al_2O_3 Catalyst in Combined Steam and Carbon Dioxide Reforming of Methane for Gas to Liquid (GTL) Process.* Catalysis Letters, 2009. **130**(1-2): p. 217-221.

119. D.V. Demidov, I.V. Mishin, and M.N. Mikhailov, *Gibbs free energy minimization as a way to optimize the combined steam and carbon dioxide reforming of methane.* International Journal of Hydrogen Energy, 2011. **36**(10): p. 5941-5950.

120. S. Özkara-AydInoglu, *Thermodynamic equilibrium analysis of combined carbon dioxide reforming with steam reforming of methane to synthesis gas.* International Journal of Hydrogen Energy, 2010. **35**(23): p. 12821-12828.

121. P.D.F. Vernon, M.L.H. Green, A.K. Cheetham, and A.T. Ashcroft, *Partial oxidation of methane to synthesis gas, and carbon dioxide as an oxidising agent for methane conversion.* Catalysis Today, 1992. **13**(2-3): p. 417-426.

122. A.T. Ashcroft, A.K. Cheetham, M.L.H. Green, and P.D.F. Vernon, *Partial oxidation of methane to synthesis gas using carbon dioxide.* Nature, 1991. **352**: p. 225-226.

123. A.M. O'Connor and J.R.H. Ross, *The effect of O_2 addition on the carbon dioxide reforming of methane over Pt/ZrO_2 catalysts.* Catalysis Today, 1998. **46**(2-3): p. 203-210.

124. E. Ruckenstein and Y.H. Hu, *Combination of CO_2 reforming and partial oxidation of methane over NiO/MgO solid solution catalysts.* Industrial & Engineering Chemistry Research, 1998. **37**(5): p. 1744-1747.

125. C.S. Lau, A. Tsolakis, and M.L. Wyszynski, *Biogas upgrade to syn-gas (H_2-CO) via dry and oxidative reforming.* International Journal of Hydrogen Energy, 2011. **36**(1): p. 397-404.

126. V.R. Choudhary, K.C. Mondal, and T.V. Choudhary, *Oxy-CO_2 reforming of methane to syngas over $CoO_x/MgO/SA$-5205 catalyst.* Fuel, 2006. **85**: p. 2484-2488.

127. J. Gao, J. Guo, D. Liang, Z. Hou, J. Fei, and X. Zheng, *Production of syngas via authothermal reforming of methane in a fluidized-bed reactor over a combined CeO_2-ZrO_2/SiO_2 supported Ni catalysts.* Int. J. Hydrogen Energy, 2008. **33**: p. 5493-5500.

128. Z. Hou, J. Gao, J. Guo, D. Liang, H. Lou, and X. Zheng, *Deactivation of Ni catalysts during methane autothermal reforming with CO_2 and O_2 in a fluidized-bed reactor.* Journal of Catalysis, 2007. **250**(2): p. 331-341.

129. D.A. Kramer, *Mineral Commodity Profiles: Nitrogen*, United-States-Geological-Survey, Editor. 2004.

130. SRI-Consulting, *World Petrochemical Report: Methanol*. 2011.

131. K. Weissermel and H.-J. Arpe, *Industrial Organic Chemistry*. 2003. p. 127.

132. J.M. Andújar and F. Segura, *Fuel cells: History and updating. A walk along two centuries.* Renewable and Sustainable Energy Reviews, 2009. **13**(9): p. 2309-2322.

133. *Department of Trade and Industry, UK Fuel Cell Development and Deployment Roadmap*. 2005.

134. *United States Department of Energy, Fuel Cell Technologies Program: Comparison of Fuel Cell Technologies*. 2011.

135. R. O'Hayre, S.-W. Cha, W. Colella, and F.B. Prinz, *Fuel Cell Fundamentals*. 2006, Wiley VCH. p. 303.

136. Y. Hishinuma and M. Kunikata, *Molten carbonate fuel cell power generation systems.* Energy Conversion and Management, 1997. **38**(10-13): p. 1237-1247.

137. A.L. Dicks, *Molten carbonate fuel cells.* Current Opinion in Solid State and Materials Science, 2004. **8**(5): p. 379-383.

138. G. Crawley, *Technology Article: Molten Carbonate Fuel Cells (MCFC)*. 2007, Fuel Cell Today.

139. S.P.S. Badwal, *Stability of solid oxide fuel cell components.* Solid State Ionics, 2001. **143**(1): p. 39-46.

140. N.Q. Minh, *Solid oxide fuel cell technology--features and applications.* Solid State Ionics, 2004. **174**(1-4): p. 271-277.

141. C. Sun and U. Stimming, *Recent anode advances in solid oxide fuel cells.* Journal of Power Sources, 2007. **171**(2): p. 247-260.

142. J.-H. Koh, Y.-S. Yoo, J.-W. Park, and H.C. Lim, *Carbon deposition and cell performance of Ni-YSZ anode support SOFC with methane fuel.* Solid State Ionics, 2002. **149**(3-4): p. 157-166.

143. G.J.K. Acres, *Recent advances in fuel cell technology and its applications.* Journal of Power Sources, 2001. **100**(1-2): p. 60-66.

144. C.H. Bartholomew, *Mechanisms of catalyst deactivation.* Applied Catalysis A: General, 2001. **212**(1-2): p. 17-60.

145. R. Ciccoli, V. Cigolotti, R. Lo Presti, E. Massi, S.J. McPhail, G. Monteleone, A. Moreno, V. Naticchioni, C. Paoletti, E. Simonetti, and F. Zaza, *Molten carbonate fuel cells fed with biogas: Combating H_2S.* Waste Management, 2010. **30**(6): p. 1018-1024.

146. S.M. Hashemnejad and M. Parvari, *Deactivation and Regeneration of Nickel-Based Catalysts for Steam-Methane Reforming.* Chinese Journal of Catalysis, 2011. **32**(1): p. 273-279.

147. J. Sehested, *Four challenges for nickel steam-reforming catalysts.* Catalysis Today, 2006. **111**(1-2): p. 103-110.

148. T.R. Smith, A. Wood, and V.I. Birss, *Effect of hydrogen sulfide on the direct internal reforming of methane in solid oxide fuel cells.* Applied Catalysis A: General, 2009. **354**(1-2): p. 1-7.

149. L. Li, C. Howard, D.L. King, M. Gerber, R. Dagle, and D. Stevens, *Regeneration of Sulfur Deactivated Ni-Based Biomass Syngas Cleaning Catalysts.* Industrial & Engineering Chemistry Research, 2010. **49**(20): p. 10144-10148.

150. J.R. Rostrup-Nielsen, *Chemisorption of hydrogen sulfide on a supported nickel catalyst.* Journal of Catalysis, 1968. **11**(3): p. 220-227.

151. C.H. Bartholomew and R.B. Pannell, *Sulfur poisoning of hydrogen and carbon monoxide adsorption on supported nickel.* Applied Catalysis, 1982. **2**(1-2): p. 39-49.

152. R.B. Pannell, K.S. Chung, and C.H. Bartholomew, *The stoichiometry and poisoning by sulfur of hydrogen, oxygen and carbon monoxide chemisorption on unsupported nickel.* Journal of Catalysis, 1977. **46**(3): p. 340-347.

153. J.R. Rostrup-Nielsen, *Promotion by Poisoning*, in *Studies in Surface Science and Catalysis*, C.H. Bartholomew and J.B. Butt, Editors. 1991, Elsevier. p. 85-101.

154. F. Abild-Pedersen, O. Lytken, J. Engbæk, G. Nielsen, I. Chorkendorff, and J.K. Nørskov, *Methane activation on Ni(1 1 1): Effects of poisons and step defects.* Surface Science, 2005. **590**(2-3): p. 127-137.

155. J.L. Oliphant, R.W. Fowler, R.B. Pannell, and C.H. Bartholomew, *Chemisorption of hydrogen sulfide on nickel and ruthenium catalysts : I. Desorption isotherms.* Journal of Catalysis, 1978. **51**(2): p. 229-242.

156. I.E. Den Besten and P.W. Selwood, *The chemisorption of hydrogen sulfide, methyl sulfide, and cyclohexene on supported nickel catalysts.* Journal of Catalysis, 1962. **1**(2): p. 93-102.

157. J.R. Rostrup-Nielsen and K. Pedersen, *Sulfur poisoning of Boudouard and methanation reactions on nickel catalysts.* Journal of Catalysis, 1979. **59**(3): p. 395-404.

158. J. Dong, Z. Cheng, S. Zha, and M. Liu, *Identification of nickel sulfides on Ni-YSZ cermet exposed to H_2 fuel containing H_2S using Raman spectroscopy.* Journal of Power Sources, 2006. **156**(2): p. 461-465.

159. J.N. Kuhn, N. Lakshminarayanan, and U.S. Ozkan, *Effect of hydrogen sulfide on the catalytic activity of Ni-YSZ cermets.* Journal of Molecular Catalysis A: Chemical, 2008. **282**(1-2): p. 9-21.

160. Z. Cheng and M. Liu, *Characterization of sulfur poisoning of Ni-YSZ anodes for solid oxide fuel cells using in situ Raman microspectroscopy.* Solid State Ionics, 2007. **178**(13-14): p. 925-935.

161. F. Zaza, C. Paoletti, R. LoPresti, E. Simonetti, and M. Pasquali, *Studies on sulfur poisoning and development of advanced anodic materials for waste-to-energy fuel cells applications.* Journal of Power Sources, 2010. **195**(13): p. 4043-4050.

162. P. Lohsoontorn, D.J.L. Brett, and N.P. Brandon, *Thermodynamic predictions of the impact of fuel composition on the propensity of sulphur to interact with Ni and ceria-based anodes for solid oxide fuel cells.* Journal of Power Sources, 2008. **175**(1): p. 60-67.

163. C.H. Bartholomew, G.D. Weatherbee, and G.A. Jarvi, *Sulfur poisoning of nickel methanation catalysts : I. in situ deactivation by H_2S of nickel and nickel bimetallics.* Journal of Catalysis, 1979. **60**(2): p. 257-269.

164. P. Lohsoontorn, D.J.L. Brett, and N.P. Brandon, *The effect of fuel composition and temperature on the interaction of H_2S with nickel-ceria anodes for Solid Oxide Fuel Cells.* Journal of Power Sources, 2008. **183**(1): p. 232-239.

165. Y. Matsuzaki and I. Yasuda, *The poisoning effect of sulfur-containing impurity gas on a SOFC anode: Part I. Dependence on temperature, time, and impurity concentration.* Solid State Ionics, 2000. **132**(3-4): p. 261-269.

166. M. Ashrafi, C. Pfeifer, T. ProÌˆll, and H. Hofbauer, *Experimental Study of Model Biogas Catalytic Steam Reforming: 2. Impact of Sulfur on the Deactivation and Regeneration of Ni-Based Catalysts.* Energy & Fuels, 2008. **22**(6): p. 4190-4195.

167. N. Lakshminarayanan and U.S. Ozkan, *Effect of H_2O on sulfur poisoning and catalytic activity of Ni-YSZ catalysts.* Applied Catalysis A: General, 2011. **393**(1-2): p. 138-145.

168. J.P. Trembly, A.I. Marquez, T.R. Ohrn, and D.J. Bayless, *Effects of coal syngas and H_2S on the performance of solid oxide fuel cells: Single-cell tests.* Journal of Power Sources, 2006. **158**(1): p. 263-273.

169. P. Mare´cot, E. Paraiso, J.M. Dumas, and J. Barbier, *Deactivation of nickel catalysts by sulphur compounds: II. Chemisorption of hydrogen sulphide.* Applied Catalysis A: General, 1992. **80**(1): p. 89-97.

170. J.W. Yun, S.P. Yoon, S. Park, H.S. Kim, and S.W. Nam, *Analysis of the regenerative H_2S poisoning mechanism in $Ce_{0.8}Sm_{0.2}O2$-coated Ni/YSZ anodes for intermediate temperature solid oxide fuel cells.* International Journal of Hydrogen Energy, 2011. **36**(1): p. 787-796.

171. J. Hepola and P. Simell, *Sulphur poisoning of nickel-based hot gas cleaning catalysts in synthetic gasification gas: II. Chemisorption of hydrogen sulphide.* Applied Catalysis B: Environmental, 1997. **14**(3-4): p. 305-321.

172. J.-H. Wang and M. Liu, *Surface regeneration of sulfur-poisoned Ni surfaces under SOFC operation conditions predicted by first-principles-based thermodynamic calculations.* Journal of Power Sources, 2008. **176**(1): p. 23-30.

173. J.R. Rostrup-Nielsen, *Some principles relating to the regeneration of sulfur-poisoned nickel catalysts.* Journal of Catalysis, 1971. **21**(2): p. 171-178.

174. J.F.B. Rasmussen and A. Hagen, *The effect of H_2S on the performance of Ni-YSZ anodes in solid oxide fuel cells.* J. Power Sources, 2009. **191**: p. 534-541.

175. M. Gong, X. Liu, J. Trembly, and C. Johnson, *Sulfur-tolerant anode materials for solid oxide fuel cell application.* Journal of Power Sources, 2007. **168**(2): p. 289-298.

176. C. Lombard, S. Le Doze, E. Marencak, P.-M. Marquaire, D. Le Noc, G. Bertrand, and F. Lapicque, *In situ regeneration of the Ni-based catalytic reformer of a 5 kW PEMFC system.* International Journal of Hydrogen Energy, 2006. **31**(3): p. 437-440.

177. V.R. Choudhary, K.C. Mondal, and T.V. Choudhary, *Oxy-methane reforming over high temperature stable $NiCoMgCeO_x$ and $NiCoMgO_x$ supported on zirconia-hafnia catalysts: Accelerated sulfur deactivation and regeneration.* Catal. Commun., 2007. **8**: p. 561-564.

178. J.-H. Wang and M. Liu, *Computational study of sulfur-nickel interactions: A new S-Ni phase diagram.* Electrochemistry Communications, 2007. **9**(9): p. 2212-2217.

179. H.C. Dibbern, P. Olesen, J.R. Rostrupnielsen, P.B. Tottrup, and N.R. Udengaard, *Make low H_2/CO syngas using sulfur passivated reforming.* Hydrocarbon Processing, 1986. **65**(1): p. 71-74.

180. J. Rostrup-Nielsen and J.K. Norskov, *Step sites in syngas catalysis.* Topics in Catalysis, 2006. **40**(1-4): p. 45-48.

181. M.P. Andersson, E. Abild-Pedersen, I.N. Remediakis, T. Bligaard, G. Jones, J. Engbwk, O. Lytken, S. Horch, J.H. Nielsen, J. Sehested, J.R. Rostrup-Nielsen, J.K. Norskov, and I. Chorkendorff, *Structure sensitivity of the methanation reaction: H_2-induced CO dissociation on nickel surfaces.* Journal of Catalysis, 2008. **255**(1): p. 6-19.

182. M.M. Yung, W.S. Jablonski, and K.A. Magrini-Bair, *Review of Catalytic Conditioning of Biomass-Derived Syngas.* Energy & Fuels, 2009. **23**(4): p. 1874-1887.

183. H.S. Bengaard, J.K. Nørskov, J. Sehested, B.S. Clausen, L.P. Nielsen, A.M. Molenbroek, and J.R. Rostrup-Nielsen, *Steam Reforming and Graphite Formation on Ni Catalysts.* Journal of Catalysis, 2002. **209**(2): p. 365-384.

184. W. Vielstich, H. Yokokawa, and H.A. Gasteiger, *Handbook of Fuel cells - Fundamentals, Technology and Applications*. 2009, John Wiley & Sons, Ltd. p. 159-171.

185. C.J. Laycock, J.Z. Staniforth, and R.M. Ormerod, *Biogas as a fuel for solid oxide fuel cells and synthesis gas production: effects of ceria-doping and hydrogen sulfide on the performance of nickel-based anode materials.* Dalton Transactions, 2011. **40**(20): p. 5494-5504.

186. H.P. He, A. Wood, D. Steedman, and M. Tilleman, *Sulphur tolerant shift reaction catalysts for nickel-based SOFC anode.* Solid State Ionics, 2008. **179**(27-32): p. 1478-1482.

187. Y. Zeng, S. Kaytakoglu, and D.P. Harrison, *Reduced cerium oxide as an efficient and durable high temperature desulfurization sorbent.* Chemical Engineering Science, 2000. **55**(21): p. 4893-4900.

188. H. Kim, J.M. Vohs, and R.J. Gorte, *Direct oxidation of sulfur-containing fuels in a solid oxide fuel cell.* Chemical Communications, 2001(22): p. 2334-2335.

189. M.C.J. Bradford and M.A. Vannice, *CO_2 Reforming of CH_4 over Supported Ru Catalysts.* Journal of Catalysis, 1999. **183**(1): p. 69-75.

190. K. Nagaoka, K. Seshan, K.-i. Aika, and J.A. Lercher, *Carbon Deposition during Carbon Dioxide Reforming of Methane--Comparison between Pt/Al2O3 and Pt/ZrO2.* Journal of Catalysis, 2001. **197**(1): p. 34-42.

191. S. Wang, G.Q. Lu, and G.J. Millar, *Carbon Dioxide Reforming of Methane To Produce Synthesis Gas over Metal-Supported Catalysts: State of the Art.* Energy & Fuels, 1996. **10**(4): p. 896-904.

192. F. Pompeo, N.N. Nichio, M.M.V.M. Souza, D.V. Cesar, O.A. Ferretti, and M. Schmal, *Study of Ni and Pt catalysts supported on [alpha]-Al_2O_3 and ZrO_2 applied in methane reforming with CO_2.* Applied Catalysis A: General, 2007. **316**(2): p. 175-183.

193. M.E.S. Hegarty, A.M. O'Connor, and J.R.H. Ross, *Syngas production from natural gas using ZrO_2-supported metals.* Catalysis Today, 1998. **42**(3): p. 225-232.

194. C.T. Au, C.F. Ng, and M.S. Liao, *Methane dissociation and syngas formation on Ru, Os, Rh, Ir, Pd, Pt, Cu, Ag, and Au: A theoretical study.* Journal of Catalysis, 1999. **185**(1): p. 12-22.

195. T. Osaki and T. Mori, *Kinetics of the reverse-Boudouard reaction over supported nickel catalysts.* Reaction Kinetics and Catalysis Letters, 2006. **89**: p. 333-339.

196. T. Wurzel, S. Malcus, and L. Mleczko, *Reaction engineering investigations of CO_2 reforming in a fluidized-bed reactor.* Chemical Engineering Science, 2000. **55**(18): p. 3955-3966.

197. P.E. Nolan, D.C. Lynch, and A.H. Cutler, *Carbon deposition and hydrocarbon formation on group VIII metal catalysts (vol 102B, pg 4165, 1998).* Journal of Physical Chemistry B, 1998. **102**(36): p. 7073-7073.

198. T. Chen, W.G. Wang, H. Miao, T. Li, and C. Xu, *Evaluation of carbon deposition behavior on the nickel/yttrium-stabilized zirconia anode-supported fuel cell fueled with simulated syngas.* Journal of Power Sources, 2011. **196**(5): p. 2461-2468.

199. O.S. Joo and K.D. Jung, *CH_4 dry reforming on alumina-supported nickel catalyst.* Bulletin of the Korean Chemical Society, 2002. **23**(8): p. 1149-1153.

200. S. Xu, R. Zhao, and X. Wang, *Highly coking resistant and stable Ni/Al_2O_3 catalysts prepared by W/O microemulsion for partial oxidation of methane.* Fuel Processing Technology, 2004. **86**(2): p. 123-133.

201. J. Juan-Juan, M.C. Román-Martínez, and M.J. Illán-Gómez, *Nickel catalyst activation in the carbon dioxide reforming of methane: Effect of pretreatments.* Applied Catalysis A: General, 2009. **355**(1-2): p. 27-32.

202. M. Audier and M. Coulon, *Kinetic and microscopic aspects of catalytic carbon growth.* Carbon, 1985. **23**(3): p. 317-323.

203. J.W. Snoeck, G.F. Froment, and M. Fowles, *Kinetic Study of the Carbon Filament Formation by Methane Cracking on a Nickel Catalyst.* Journal of Catalysis, 1997. **169**(1): p. 250-262.

204. G. Italiano, C. Espro, F. Arena, F. Frusteri, and A. Parmaliana, *Catalytic decomposition of natural gas for CO_x-free hydrogen production in a structured multilayer reactor.* Applied Catalysis A: General, 2009. **357**(1): p. 58-65.

205. J.W. Snoeck, G.F. Froment, and M. Fowles, *Filamentous Carbon Formation and Gasification: Thermodynamics, Driving Force, Nucleation, and Steady-State Growth.* Journal of Catalysis, 1997. **169**(1): p. 240-249.

206. Y.H. Hu and E. Ruckenstein, *High-resolution transmission electron microscopy study of carbon deposited on the NiO MgO solid solution catalysts.* Journal of Catalysis, 1999. **184**(1): p. 298-302.

207. S. Tang, L. Ji, J. Lin, H.C. Zeng, K.L. Tan, and K. Li, *CO_2 Reforming of Methane to Synthesis Gas over Sol-Gel-made Ni/[gamma]-Al_2O_3 Catalysts from Organometallic Precursors.* Journal of Catalysis, 2000. **194**(2): p. 424-430.

208. H.O. Pierson, *Handbook of carbon, graphite, diamond and fullerenes: properties, processing and applications*. 1993, Noyes Publications. p. 2.

209. S. Corthals, J. Van Nederkassel, J. Geboers, H. De Winne, J. Van Noyen, B. Moens, B. Sels, and P. Jacobs, *Influence of composition of $MgAl_2O_4$ supported $NiCeO_2ZrO_2$ catalysts on coke formation and catalyst stability for dry reforming of methane.* Catalysis Today, 2008. **138**(1-2): p. 28-32.

210. Y.-Q. Song, D.-H. He, and B.-Q. Xu, *Effects of preparation methods of ZrO_2 support on catalytic performances of Ni/ZrO_2 catalysts in methane partial oxidation to syngas.* Applied Catalysis A: General, 2008. **337**(1): p. 19-28.

211. R. Martínez, E. Romero, C. Guimon, and R. Bilbao, *CO_2 reforming of methane over coprecipitated Ni-Al catalysts modified with lanthanum.* Applied Catalysis A: General, 2004. **274**(1-2): p. 139-149.

212. J.M. Wei, B.-Q. Xu, J.L. Li, Z.X. Cheng, and Q.M. Zhu, *Highly active and stable Ni/ZrO_2 catalyst for syngas production by CO_2 reforming of methane.* Appl. Catal. A, 2000. **196**: p. L167-L172.

213. J. Wei and E. Iglesia, *Isotopic and kinetic assessment of the mechanism of reactions of CH_4 with CO_2 or H_2O to form synthesis gas and carbon on nickel catalysts.* Journal of Catalysis, 2004. **224**(2): p. 370-383.

214. K.O. Christensen, D. Chen, R. Lødeng, and A. Holmen, *Effect of supports and Ni crystal size on carbon formation and sintering during steam methane reforming.* Applied Catalysis A: General, 2006. **314**(1): p. 9-22.

215. A.J.H.M. Kock, P.K. de Bokx, E. Boellaard, W. Klop, and J.W. Geus, *The formation of filamentous carbon on iron and nickel catalysts : II. Mechanism.* Journal of Catalysis, 1985. **96**(2): p. 468-480.

216. S.B. Sinnott, R. Andrews, D. Qian, A.M. Rao, Z. Mao, E.C. Dickey, and F. Derbyshire, *Model of carbon nanotube growth through chemical vapor deposition.* Chemical Physics Letters, 1999. **315**(1-2): p. 25-30.

217. D. Chen, R. Lødeng, A. Anundskås, O. Olsvik, and A. Holmen, *Deactivation during carbon dioxide reforming of methane over Ni catalyst: microkinetic analysis.* Chemical Engineering Science, 2001. **56**(4): p. 1371-1379.

218. S. Liu, L. Guan, J. Li, N. Zhao, W. Wei, and Y. Sun, *CO_2 reforming of CH_4 over stabilized mesoporous Ni-CaO-ZrO_2 composites.* Fuel, 2008. **87**: p. 2477-2481.

219. S. Therdthianwong, C. Siangchin, and A. Therdthianwong, *Improvement of coke resistance of Ni/Al_2O_3 catalyst in CH_4/CO_2 reforming by ZrO_2 addition.* Fuel Process. Technol., 2008. **89**: p. 160-168.

220. L. Xiancai, W. Min, L. Zhihua, and H. Fei, *Studies on nickel-based catalysts for carbon dioxide reforming of methane.* Applied Catalysis A: General, 2005. **290**(1-2): p. 81-86.

221. J.Z. Luo, Z.L. Yu, C.F. Ng, and C.T. Au, *CO_2/CH_4 Reforming over Ni-La_2O_3/5A: An Investigation on Carbon Deposition and Reaction Steps.* Journal of Catalysis, 2000. **194**(2): p. 198-210.

222. H.S. Roh, K.W. Jun, S.C. Baek, and S.E. Park, *A highly active and stable catalyst for carbon dioxide reforming of methane: Ni/Ce-ZrO_2/theta-Al_2O_3.* Catalysis Letters, 2002. **81**(3-4): p. 147-151.

223. C. Li, K. Domen, K. Maruya, and T. Onishi, *Dioxygen adsorption on well-outgassed and partially reduced cerium oxide studied by FT-IR.* Journal of the American Chemical Society, 1989. **111**(20): p. 7683-7687.

224. S.H. Kim, J.H. Chung, Y.T. Kim, J. Han, S.P. Yoon, S.W. Nam, T.-H. Lim, and H.-I. Lee, *SiO_2/Ni and CeO_2/Ni catalysts for single-stage water gas shift reaction.* International Journal of Hydrogen Energy, 2010. **35**(7): p. 3136-3140.

225. F. Pompeo, D. Gazzoli, and N.N. Nichio, *Stability improvements of Ni/[alpha]-Al_2O_3 catalysts to obtain hydrogen from methane reforming.* International Journal of Hydrogen Energy, 2009. **34**(5): p. 2260-2268.

226. K. Otsuka, H. Ogihara, and S. Takenaka, *Decomposition of methane over Ni catalysts supported on carbon fibers formed from different hydrocarbons.* Carbon, 2003. **41**(2): p. 223-233.

227. M. Rezaei, S.M. Alavi, S. Sahebdelfar, and Z.-F. Yan, *A highly stable catalyst in methane reforming with carbon dioxide.* Scripta Materialia, 2009. **61**(2): p. 173-176.

228. J. Zhang, H. Wang, and A.K. Dalai, *Development of stable bimetallic catalysts for carbon dioxide reforming of methane.* Journal of Catalysis, 2007. **249**(2): p. 300-310.

229. A.K. Datye, Q. Xu, K.C. Kharas, and J.M. McCarty, *Particle size distributions in heterogeneous catalysts: What do they tell us about the sintering mechanism?* Catalysis Today, 2006. **111**(1-2): p. 59-67.

230. A.C.S.C. Teixeira and R. Giudici, *A Monte Carlo model for the sintering of Ni/Al_2O_3 catalysts.* Chemical Engineering Science, 2001. **56**(3): p. 789-798.

231. R. Finsy, *On the Critical Radius in Ostwald Ripening.* Langmuir, 2004. **20**(7): p. 2975-2976.

232. F.B. Rasmussen, J. Sehested, H.T. Teunissen, A.M. Molenbroek, and B.S. Clausen, *Sintering of Ni/Al_2O_3 catalysts studied by anomalous small angle X-ray scattering.* Applied Catalysis A: General, 2004. **267**(1-2): p. 165-173.

233. J. Sehested, J.A.P. Gelten, and S. Helveg, *Sintering of nickel catalysts: Effects of time, atmosphere, temperature, nickel-carrier interactions, and dopants.* Applied Catalysis A: General, 2006. **309**(2): p. 237-246.

234. J.R. Rostrup-Nielsen, K. Pedersen, and J. Sehested, *High temperature methanation: Sintering and structure sensitivity.* Applied Catalysis A: General, 2007. **330**: p. 134-138.

235. A.C.S.C. Teixeira and R. Giudici, *Deactivation of steam reforming catalysts by sintering: experiments and simulation.* Chemical Engineering Science, 1999. **54**(15-16): p. 3609-3618.

236. J. Sehested, J.A.P. Gelten, I.N. Remediakis, H. Bengaard, and J.K. Nørskov, *Sintering of nickel steam-reforming catalysts: effects of temperature and steam and hydrogen pressures.* Journal of Catalysis, 2004. **223**(2): p. 432-443.

237. M. Pihlatie, A. Kaiser, and M. Mogensen, *Redox stability of SOFC: Thermal analysis of Ni-YSZ composites.* Solid State Ionics, 2009. **180**(17-19): p. 1100-1112.

238. P.J. Feibelman and G.L. Kellogg, *Surfactant-Modified Diffusion on Transition-Metal Surfaces*. 1999, Sandia National Laboratories - On behalf of the United States Department of Energy.

239. P. Ferreira-Aparicio, A. Guerrero-Ruiz, and I. Rodríguez-Ramos, *Comparative study at low and medium reaction temperatures of syngas production by methane reforming with carbon dioxide over silica and alumina supported catalysts.* Applied Catalysis A: General, 1998. **170**(1): p. 177-187.

240. S. Wang and G.Q. Lu, *Catalytic Activities and Coking Characteristics of Oxides-Supported Ni Catalysts for CH_4 Reforming with Carbon Dioxide.* Energy & Fuels, 1998. **12**(2): p. 248-256.

3 Experimental

3.1 Catalyst formulation

3.1.1 90% Nickel supported on 10% Yttria Stabilized Zirconia (Ni/YSZ)

A 90 wt% Ni supported on 10 wt% YSZ catalyst was produced using the standard physical mixing procedure, using the reagents and quantities displayed in Table 3.1.

Table 3.1: Reagents and quantities used for the formulation of Ni/YSZ catalyst

Reagent	Supplier	Purity	Accurate Mass/ g
11 mol% Y_2O_3 Supported on ZrO_2 (YSZ)	Unitec Ceramics	99.9+ %	1.8030
NiO	Alfa Aeser	99 %	19.0529
1, 1, 1, Trichloroethene	BDH Chemicals Ltd.	99 %	5.8000
MeOH	Sigma-Aldrich	Analytical grade	4.4200
Glyceroltrioleate	BDH Chemical Ltd.	≥ 99 %	0.3990

ZrO_2 (Supported on 11 mol% Y_2O_3) was calcined prior to its use as a reagent to increase crystallinity and reduce the range in particle size. This is shown in the XRD pattern of both calcined and uncalcined samples shown in Figure 3.1. The calcination temperature program used was from room temperature to 1200 °C with increments of 10 °C/minute and held at 1200 °C for 2 hours. The calcined YSZ was then sieved using a sieve with 150 μm apertures.

The resulting slurries from mixing of the reagents shown in Table 3.1 were milled within polyethylene containers containing 5 Zirconia beads for 3 hours. Zirconia beads were used to enhance the mixing of the reagents. Once milled, a spatula tip of polyvinyl butyral was added to act as a binding agent and the container milled for a further 5 minutes. The slurry was then poured into 88 x 15 x 11 mm high refractory material combustion boats purchased from Fisher Scientific Ltd and calcined using a temperature program consisting of an incline from room temperature of 1 °C/minute to 500 °C followed by an incline of 5 °C/minute from 500 °C to a maximum of 1200 °C. The temperature was then held for 60 minutes followed by a decline of 10 °C/minute from 1200 °C

to room temperature. The temperature program described is shown in a visual manner in Figure 3.2.

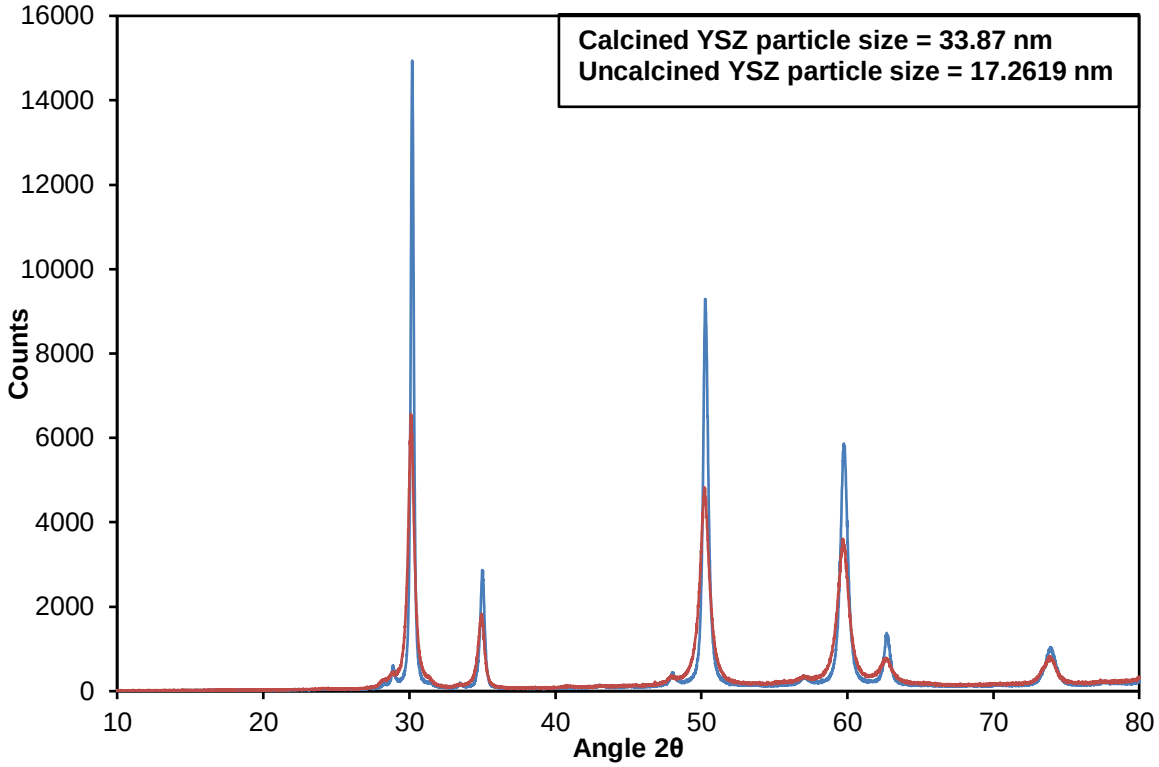

Figure 3.1: XRD pattern for uncalcined (red) and calcined (blue) samples of 11 mol% Yttria on ZrO_2. Particle sizes measured using Scherrer equation (Equation 3.15)

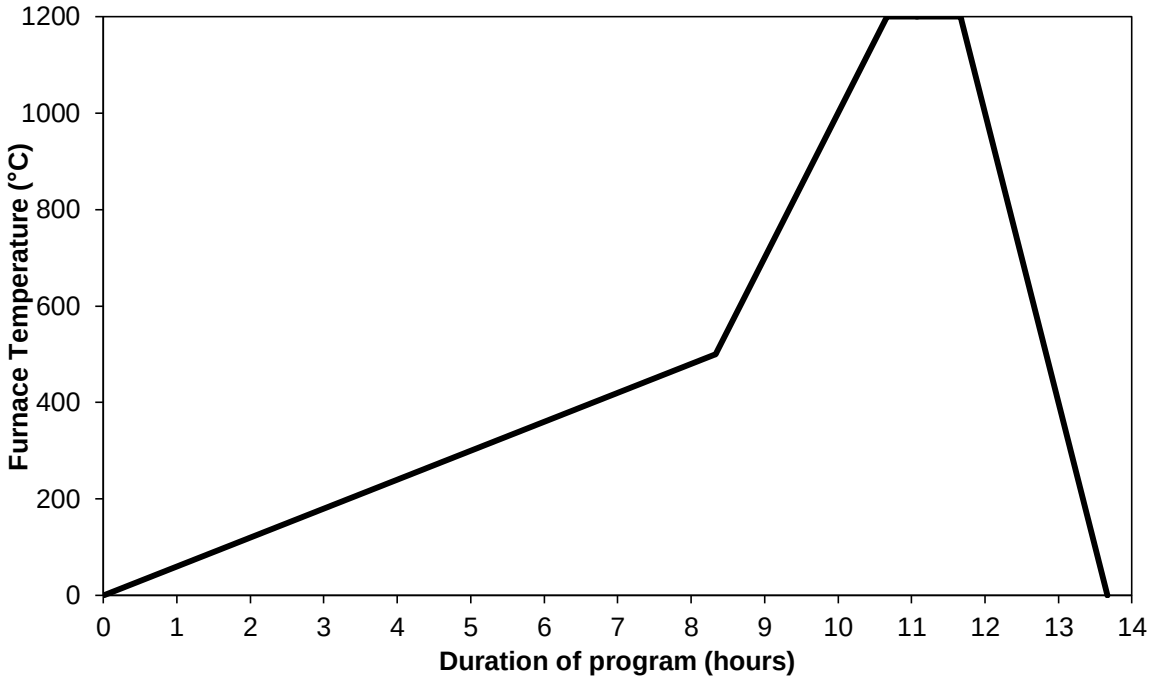

Figure 3.2: Visual representation of furnace temperature program used for catalyst calcination

After calcination, the resulting product was present as a brittle solid that was bright green in colour. This product was ground using a ceramic pestle and mortar, then sieved using a stainless steel sieve with 150 µm size apertures to restrict the range of particle size and therefore the influence it may have on catalyst performance.

3.1.2 90% Nickel supported on 10% Yttria Stabilised Zirconia with the addition of 5 mol% Ceria (5 mol% CeO_2-Ni/YSZ)

This catalyst was also produced through the standard physical mixing procedure using the reagents shown in Table 3.2.

Table 3.2: Reagents and quantities used for the formulation of 5 mol% CeO_2-Ni/YSZ

Reagent	Supplier	Purity	Accurate Mass/ g
11 mol % Y_2O_3 supported on ZrO_2 (YSZ)	Unitec Ceramics	99.9+ %	1.8020
NiO	Alfa Aeser	99 %	19.0182
1, 1, 1, Trichloroethene	BDH Chemicals Ltd.	99 %	5.8024
MeOH	Sigma Aldrich	Analytical grade	4.4079
Glyceroltrioleate	BDH Chemicals Ltd.	≥ 99 %	0.4486
CeO_2	Aldrich	99.9% trace metals basis	2.1938

The mass of CeO_2 used produces a catalyst with a CeO_2 content of 5 mol% with respect to the number of moles of Ni. The mass of CeO_2 required was derived using the equations below.

$$M_r\ NiO = 58.69 + 15.9994 = 74.6894 \quad \textbf{(3.1)}$$

$$\frac{Ni}{NiO} = \frac{58.69}{74.6894} = 0.7858 = 78.58\% \quad \textbf{(3.2)}$$

$$19.0182\text{g NiO} \times 78.58\% = 14.9445\text{g Ni} \quad \textbf{(3.3)}$$

$$\text{Mol} = \frac{\text{Mass}}{\text{M}_\text{r}} = \frac{14.9445}{58.69} = 0.2546\text{mol} \quad \textbf{(3.4)}$$

$$0.2546\text{mol} \times 5\% = 0.0127\text{mol} \quad \textbf{(3.5)}$$

$$\text{M}_\text{r}\ \text{CeO}_2 = (15.9994 \times 2) + 140.12 = 172.1188 \quad \textbf{(3.6)}$$

$$\text{Mass} = \text{Mol} \times \text{M}_\text{r} = 0.0127 \times 172.1188 = 2.1859\text{g}\ \text{CeO}_2 \quad \textbf{(3.7)}$$

The milling, calcination and sieving were all conducted in an identical fashion to what was used for the undoped Ni/YSZ catalyst discussed in Section 3.1.1.

After calcination, the 5 mol% CeO_2-Ni/YSZ catalyst was a brittle solid as with the undoped Ni/YSZ catalyst, however the 5 mol% CeO_2-Ni/YSZ catalyst was of a lighter green colour than the undoped catalyst.

All catalyst calcination took place in a 3 L capacity RHF 1600 chamber furnace supplied by Carbolite Ltd.

3.2 Experimental setup

A custom designed system was used to conduct all reactions, both temperature-programmed and conventional catalytic measurements. This custom design is shown schematically in Figure 3.3.

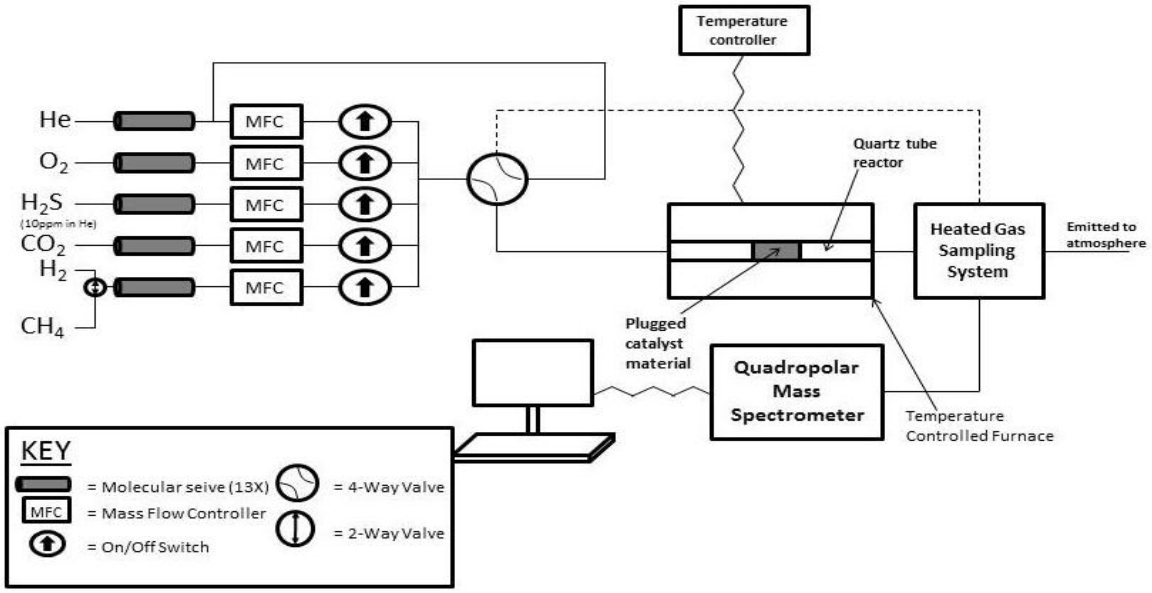

Figure 3.3: Schematic representation of experimental setup used to perform all catalyst performance testing

All tubing used from gas cylinder to heated gas sampling system was 1/8 inch diameter stainless steel seamless tubing purchased through Swagelok Ltd. The solid line from the heated gas sampling system in Figure 3.5 represents a metre long capillary tube used to deliver product gases to a Quadrupolar Mass Spectrometer (QMS). This length of capillary was enclosed within a heated sheath to ensure no phase changes post reaction. Connections and switches were all high quality vacuum products purchased through Swagelok Ltd. All gas cylinders were purchased from BOC Chemicals Ltd and were of a high purity (>99 %). These gases are passed through individual 13X molecular sieves consisting of 10 Å zeolites housed within a stainless steel tube (internal diameter = 5 mm) to absorb any water or impurities present. The molecular sieves were prepared through drying in the catalyst furnace at 145 °C with a flow of helium to purge any water present.

Each gas was controlled individually using a Mass Flow Controller (See Table 3.3) with the exception of a helium line that was used as a bypass gas to ensure the continuous flow of gas through the QMS during setup of reactant gas composition. This line was controlled using a Swagelok needle valve. All lines apart from bypass Helium then converge into a single line, which

proceeds to a four-way valve, which determines whether the bypass Helium or the controlled gases pass through to the furnace. The convergence of all lines was carried out in a way to ensure that the pressure of combined gases cannot inhibit any individual gas flow. Helium was used within the system as a diluent and ensured an overall flow rate of 20 ml min^{-1} (± 0.5 ml min^{-1}) for each test. This ensures a steady gas flow through the quadrupolar mass spectrometer and a standard contact time on the catalyst.

Table 3.3: Details of mass flow controllers associated with individual gas flows

Gas	**Mass Flow Controller Manufacturer**	**Model**	**Calibrated for:**	**Maximum flow (ml/min^{-1})**
Helium	Manger & Wittman	D-5111	Helium	50
Hydrogen/Methane	Manger & Wittman	D-5111	Methane	20
Carbon Dioxide	Manger & Wittman	D-5111	Oxygen	20
Oxygen	Manger & Wittman	D-5111	Oxygen	20
Hydrogen Sulphide (10 ppm in Helium)	Manger & Wittman	D-5111	Hydrogen	20

The furnace consisted of two partially hollowed furnace bricks with the dimensions 210 X 210 X 110 mm. Each furnace brick contained 900 mm of temperature-annealed Ni/Cr wire with a resistance of 2 MΩ/ m purchased from Advent Research Materials Ltd. This length of wire was wound around six alumina tubes (60 mm in length) and connected to a temperature controller. The temperature controller used was an 818 type Eurotherm with a K type thermocouple positioned within the furnace to measure the temperature. The temperature controller allows for temperatures between room temperature and 1000 °C to be used and also the use of temperature programs including multiple ramps and dwell periods.

A quartz tube (240 mm in length) with an inner diameter of 5 mm and thickness of 1 mm passed through the centre of the furnace. This quartz tube was used to house the catalyst, which was held in position by plugging with filtration grade quartz wool purchased through Fischer Scientific. Cajon Ultra-Torr reducing unit fittings with Fluorocarbon FKM O-rings purchased through Swagelok were used to connect the quartz tube to the gas flow system.

All gas flow rates were accurately measured using a standard bubble flow meter. The individual reactant gases could be directed through the bypass line to the heated gas sampling system, where it could then be directed direct into the bubble flow meter. The bypass system allowed for all reactant gas flow rates to be measured without coming into close proximity with the furnace and also means that helium can be passed through the furnace and on to the quadrupolar mass spectrometer whilst the reactant gas flows are measured.

A bubble flow meter was favoured over the QMS and RGA program display to measure the reactant gas quantities as due to the nature of a QMS, certain gases are ionised to varied extents and therefore cannot give an accurate account of the reactant quantity unlike the bubble flow meter, with which the only error involved is human.

The heated gas sampling system consisted of a four-way valve located within a heated steel vessel. The vessel was heated using a small brick furnace similar in design to those used to heat the catalyst material and quartz tube. This system was used to ensure that no phase changes occurred and particular that there is no accumulation of carbon or water at the four way valve. The temperature of the heated gas sampling system was controlled separately from the main furnace using a variable transformer.

The quadrupolar mass spectrometer used was a Leda Mass Spectra Satellite Model. The system was placed under vacuum using an Edwards and a Pfeiffer Rotary pump in conjunction with a Varian V70 LP MacroTorr Turbo pump operating at 70 kRPM. The ionisation source used was a Thoria coated Iridium filament purchased through MKS Instruments Inc.

RGA (Residual Gas Analyser) for Windows was used as the software to control the analyser and display a real-time analysis of chosen masses. All data was stored using the RGA for Windows

program onto the interfaced computer in a text format. Microsoft Excel was then used to format the data into Excel format and this was the standard program used to manipulate and display the data.

3.3 Catalyst pre-treatment – Temperature Programmed Reduction (TPR)

The prefix of TPR is used to identify any pre-treatment undertaken on the catalysts samples. Prior to all catalytic activity tests, each catalyst sample was subject to a standard pre-treatment method. The standard method consists of a flow of 10 % H_2 in He passing over the catalyst, whilst being heated to 900 °C using increments of 10 °C min^{-1}. This action was taken to ensure that the Ni present within the catalyst was fully reduced to metallic Ni and not NiO. To ensure complete reducibility of reducible species within the different catalysts, the reduction proceeded to 900 °C and was then held at this temperature until the H_2 quantity had stabilised and H_2O was no longer produced. The first measurement of bulk NiO reduction was reported by Benton and Emmett in 1924 [1], whilst Taylor and Starkweather [2] were one of the first to study the rate of reduction in metal oxides through monitoring hydrogen consumption.

As can be seen from the example TPR shown in Figure 3.4, H_2 is consumed and H_2O produced from the NiO reduction, as displayed in Equation 3.8. The CeO_2 present within the 5 mol% CeO_2-Ni/YSZ can also be reduced during the temperature-programmed reduction as displayed in Equation 3.9, often producing a slightly different pattern of H_2 consumption and H_2O production. Any variation between the TPR graphs are identified and discussed in Section 4.3.

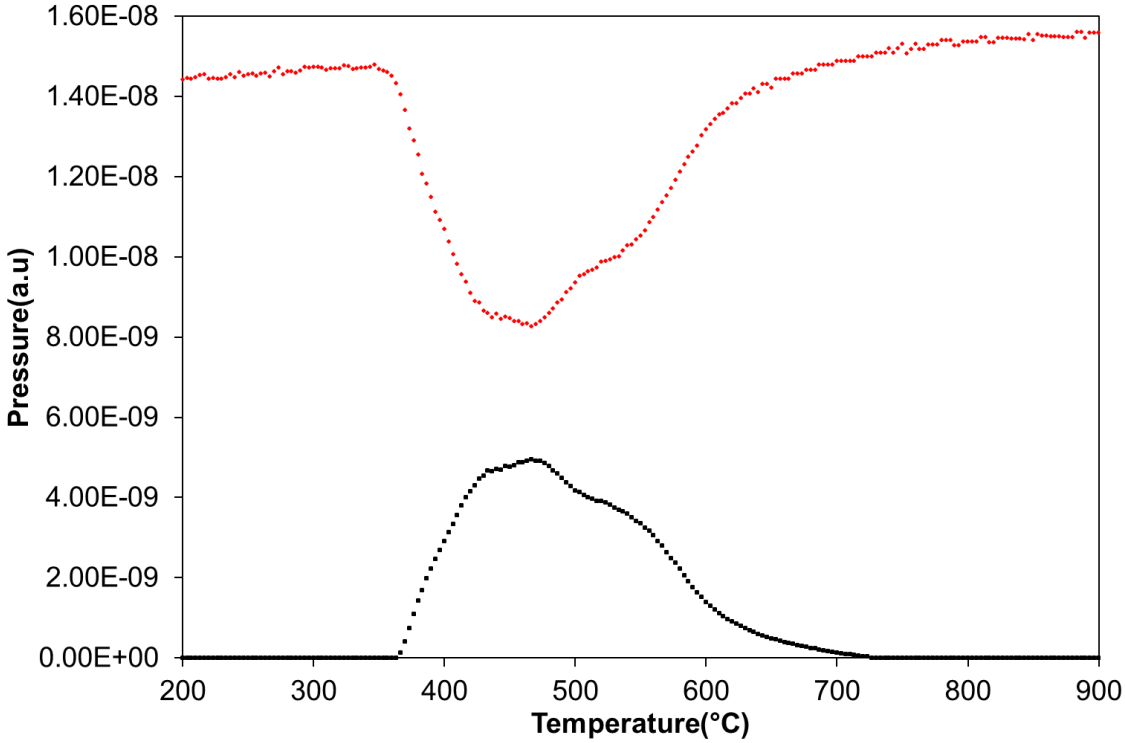

Figure 3.4: H_2 consumption and H_2O evolution from the reduction of Ni/YSZ (45.1 mg) across a temperature profile.

$$NiO + H_2 \rightarrow Ni + H_2O \quad \textbf{(3.8)}$$

$$CeO_2 + nH_2 \rightarrow CeO_{2-n} + nH_2O \quad \textbf{(3.9)}$$

3.4 Temperature Programmed Reactions (TPX)

The prefix of TPX is used to identify any catalytic activity data that has been produced using a temperature program. Two different temperature programs were used within this research; these are a forward temperature program and a reverse temperature program. With the forward temperature program, the measured reactant gas mixture was passed over the catalyst material at room temperature. At this point, the gases were monitored using the QMS and RGA program at this temperature to give a measure of the gas quantities to allow for calculations to be made once the reaction had been completed. All of the calculations are shown in Section 3.9. The furnace temperature was then raised to 1000 °C using 5 °C min^{-1} increments. Once the furnace temperature reached 1000 °C, the reactant gas flows were directed through the bypass and measured. The gases

were measured to ensure that no change in the reactant gas quantities had occurred during the course of the reaction. In the reverse temperature program, the measured reactant gases were passed through the bypass system and monitored using the QMS and RGA program, whilst the furnace temperature was raised to 1000 °C. When the furnace was at 1000 °C, the reactant gases were passed over the catalysts material and the furnace temperature was reduced to room temperature at increments of 5 °C min^{-1}. Once the reaction has reached room temperature, the gases were measured to ensure no change in gas quantities had occurred during the course of the reaction.

3.5 Isothermal (conventional) reactions (ISO)

The prefix ISO is used to identify any catalytic activity data that has been produced using an isothermal (conventional) reaction. All isothermal reactions were conducted at a constant temperature for a period of 20 hours. The measured reactant gas mixture was passed through the bypass system and monitored using the QMS and RGA program, whilst the furnace was heated to the required temperature. Once the furnace was at the required temperature, the reactant gas mixture was directed over the catalyst material for the 20 hour period. At the end of this period, the reactant gas mixture was passed through the bypass and measured whilst the furnace cooled. The following isothermal temperatures have been used during this research; 600 °C, 700 °C, 800 °C, 900 °C and 1000 °C. These temperatures were chosen as they cover the operating temperatures of SOFC's and the majority of temperatures at which nickel can catalyse methane reforming for synthesis gas production.

3.6 Catalyst post-treatment – Temperature programmed oxidation (TPO)

The prefix TPO is used to identify any data concerned with the treatment of the catalyst material following a catalyst activity reaction. Following a catalyst activity reaction, the catalyst material underwent a standard post-treatment method [3-5]. This standard method consists of a flow of 12.5 % O_2 in He passing over the catalyst, whilst being heated to 900 °C with increments of 10 °C min^{-1}. This post-treatment was undertaken to oxidize any carbon that may have been deposited on the

catalyst surface and surroundings during the catalyst activity test. The oxidized carbon was detected using the QMS as either CO (Mass 28) or CO_2 (Mass 44). This post-treatment allows for the level of carbon produced during the catalyst activity test to be quantified using a calibration graph. This calibration is discussed in further detail in Section 3.7.2. During the TPO, the Ni metal present within the catalyst was also reoxidized to NiO. An example of a TPO is shown in Figure 3.5.

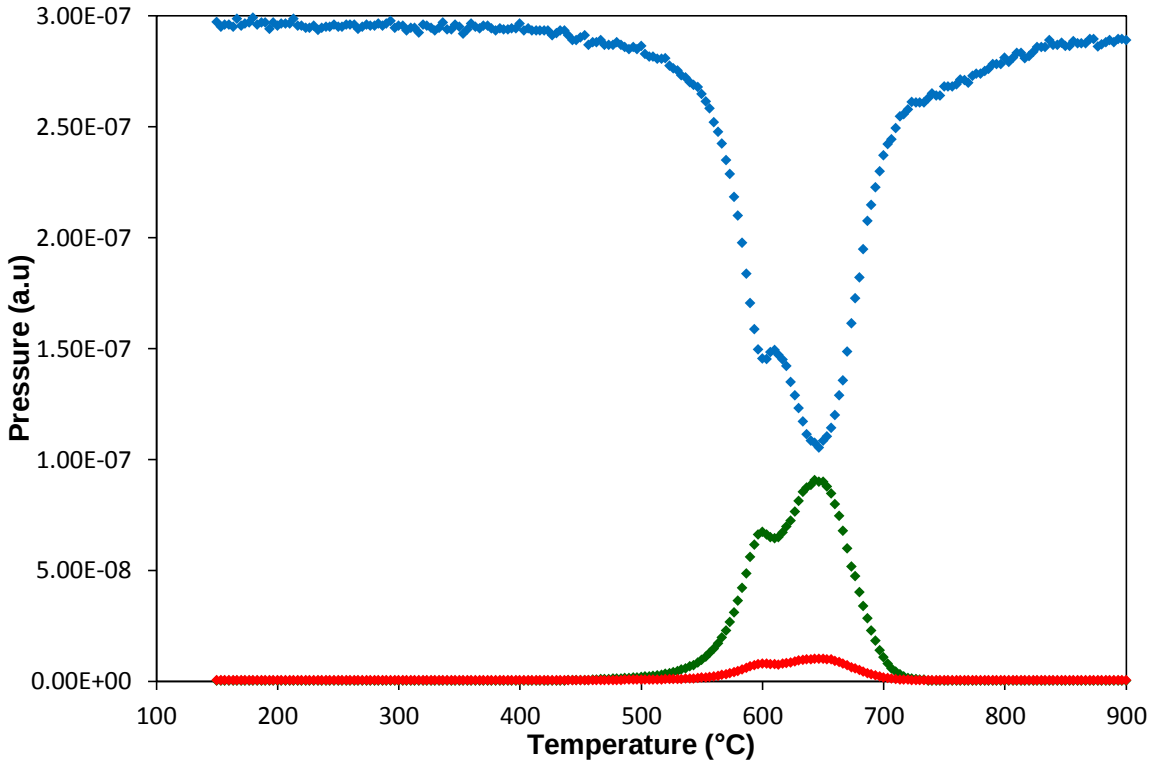

Figure 3.5: CO_2 and CO production and O_2 consumption from the oxidation of 5 mol% CeO_2-Ni/YSZ (45.3 mg) following a CH_4+½CO_2+¼O_2 reaction at 700 °C for 20 hours (Blue = O_2, Dark Green = CO_2, Red = CO)

3.7 Quadrupolar Mass Spectrometry (QMS)

3.7.1 Theory of QMS

Quadrupolar Mass Spectrometry is a branch of mass spectrometry which was developed in the 1950's and was first reported by Wolfgang Paul in 1953 [6]. A quadrupolar mass spectrometer operates in a similar manner to all other mass spectrometers in that the sample atoms are ionised

and the separated by their m/z ratios (m = mass, z = charge). In this research, a Yttria coated Thoria filament is used as the ion source. The quadrupole aspect of the mass spectrometer consists of four metal poles positioned parallel to each other, along which a fixed DC current and a variable radiofrequency are applied. The voltage applied to these poles causes the ions to oscillate as they pass through the quadrupole and control their trajectory. The voltage applied controls which specific m/z will have a stable trajectory through the quadrupole. All other m/z will have unstable trajectories and will collide with the poles. Only the ion with the stable trajectory will pass through to the detector. Therefore, through a variation in the radiofrequency, ions of specific m/z can be selected and quantified. This allows for a range of particular masses to be chosen to produce a mass spectrum by continuously varying the radiofrequency [7]. The masses which are focused on in this research are shown in Table 3.4.

The quadrupolar mass spectrometer provides the user with an on-line spectrum of masses to allow the user to determine what is passing through the system at any one time. Therefore, the reaction products can be seen at any particular time or temperature and can produce product composition profiles along temperature programs or time periods.

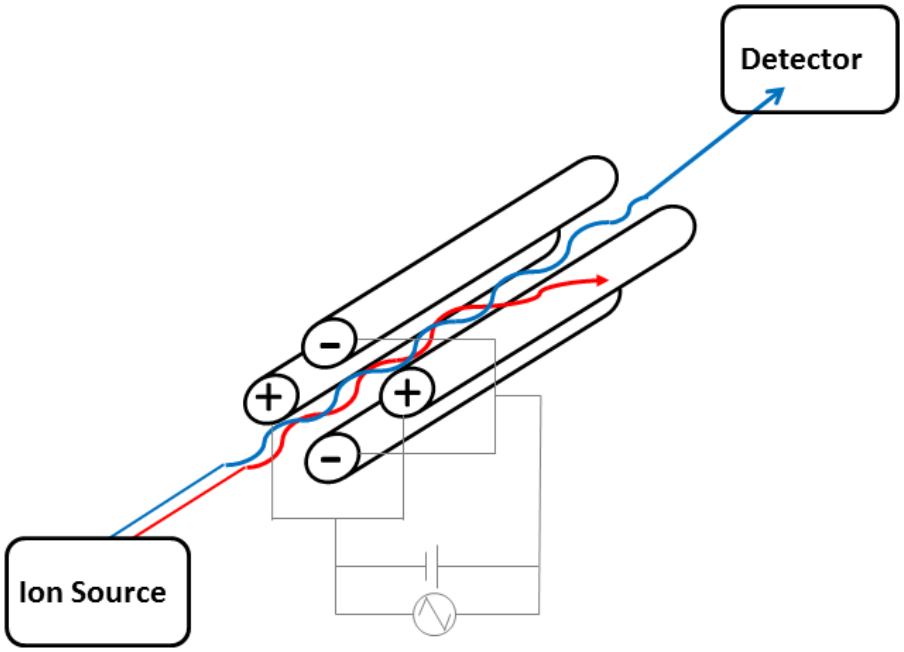

Figure 3.6: Illustration of the main aspects of a QMS. Red line illustrates non-resonant ion, blue line illustrates stable resonant ion

3.7.2 Calibration of QMS

Due to the manner in which a QMS operates, different gases are ionized to different extents. This means that for certain masses, there is a greater possibility of fragmentation. Therefore, the quantity of each gas that is analysed by the QMS analyser will be slightly distorted. Due to this, it is necessary to perform a calibration in order to be able to quantify the data accurately.

The masses shown in Table 3.4 are monitored in detail and therefore require correction.

Table 3.4: Masses and appropriate compounds selected for detection on QMS

Mass	Appropriate compound
2	Hydrogen
4	Helium
15	Methane fragment
16	Methane
18	Water
26	Possibly ethene
27	Possibly ethene
28	Carbon monoxide
29	Possibly ethane
30	Possibly ethane
32	Oxygen
44	Carbon dioxide

Each mass is corrected relative to one particular mass. The mass used is 2 due to its lack of fragmentation within the QMS.

3.7.2.1 Room temperature calibration procedure

For each reactant gas, the following procedure was used to assess its relative response compared to mass 2 (Hydrogen):

- A series of flow values were chosen for each respective gas. These were chosen to relate closely to a series of values chosen for the standard gas, which in this case is hydrogen. In the case of methane (mass 15), the flow values of 1.0, 1.5, 2.0 and 2.5 ml min^{-1} were chosen alongside the same values for hydrogen flow. Each of the methane flows were directed into the QMS at the same time as the corresponding or the next greatest flow of hydrogen. Therefore, a methane flow of 1.0 was seen together with either 1.0 or 1.5 ml min^{-1} of hydrogen.
- Helium was added to each gas combination appropriately to ensure that an overall flow rate of 20 ml min^{-1} was passing to the QMS.
- At each different combination of flow rates, the pressure of the appropriate gases shown by the QMS was recorded.

- For each combination, Equation 3.10 was used to produce a figure that is indicative of the variation between the quantity of the gases measured using a bubble flow meter and measured using the QMS.

$$\frac{\text{Hydrogen flow rate}}{\text{Methane flow rate}} \times \frac{\text{Methane pressure}}{\text{Hydrogen pressure}} \quad \textbf{(3.10)}$$

- A value was produced for each combination using this equation. Using these values, an average was calculated to give the sensitivity value for the particular gas, in this case, methane.
- This value was then used in conjunction with those produced during the temperature programmed calibration procedure to give a final average.

3.7.2.2 Temperature programmed calibration procedure

To ensure a greater accuracy in the sensitivity value produced and to obtain a sensitivity value for H_2O (Mass 18), it was necessary to perform a number of simple experiments under a temperature program. These simple experiments are shown in Equations 3.11 and 3.12 below:

$$\text{Water reaction: } H_2 + 0.5\ O_2 \rightarrow H_2O \quad \textbf{(3.11)}$$

$$\text{Synthesis Gas experiment: } H_2 + CO + O_2 \rightarrow H_2O + CO_2 \quad \textbf{(3.12)}$$

In each of these experiments, the following reaction was conducted using a standard temperature program of 10 °C min^{-1} and 45 mg (±0.2) of Ni/YSZ catalyst. For each experiment, the quantity of each gas consumed or produced was calculated and then divided by the quantity of hydrogen consumed.

The gases were passed through to the QMS at a ratio of 2:1 for H_2:O_2 with the appropriate quantity of Helium. At lower temperatures, the reaction does not occur and the QMS records the pressures

of each gas. As the temperature increases, H_2 and O_2 were consumed and H_2O produced. At 900 °C, the reaction equilibrium has fully shifted to the right and all of the H_2 is consumed. The amount of H_2 and O_2 consumed and H_2O produced can then be calculated from the difference in pressure for each gas between room temperature and 900 °C. Equation 3.13 shows how the relative sensitivity for H_2O is calculated:

$$\mathrm{H_2O\ relative\ sensitivity} = \frac{\mathrm{H_2O\ produced}}{\mathrm{H_2 consumed}} \tag{3.13}$$

3.7.2.3 Incorporation of relative sensitivity value into experimental data

To ensure that all data is relative and comparable, the data obtained using the QMS during any TPR, TPO, TPX or ISO reactions was corrected using the relative sensitivity values calculated. This accommodates for any change in diluent level that may have occurred during the course of the reaction. The correction is shown in Equation 3.14 and 3.15.

$$\frac{\text{Gas pressure at particular time or temperature}}{\text{corresponding relative sensitivity value}} \times \text{Helium correction value} \tag{3.14}$$

$$\text{Helium correction value} = \frac{\text{He pressure at particular time or temperature}}{\text{Original He pressure at r.t or 0:00}} \tag{3.15}$$

3.7.2.4 Calibration of carbon monoxide and carbon dioxide production from known quantities of carbon for use with TPO

As previously mentioned in Section 3.6, a calibration graph was required for use with all TPO data to allow for any carbon deposited during the catalytic activity reactions to be quantified.

The calibration graph was produced by weighing a certain mass of carbon into the quartz tube and passing 12.5 % O_2 in He over it, whilst under a temperature program and holding at 900 °C until CO or CO_2 production ceases. The quantity of CO and CO_2 was monitored using the QMS and then summed to give the quantity of CO and CO_2 produced from a known mass of carbon. This was repeated with different quantities of carbon to produce a calibration graph such as Figure 3.7. This was then used to estimate the quantity of carbon produced during a reaction by summing the amount of CO and CO_2 produced during the TPO.

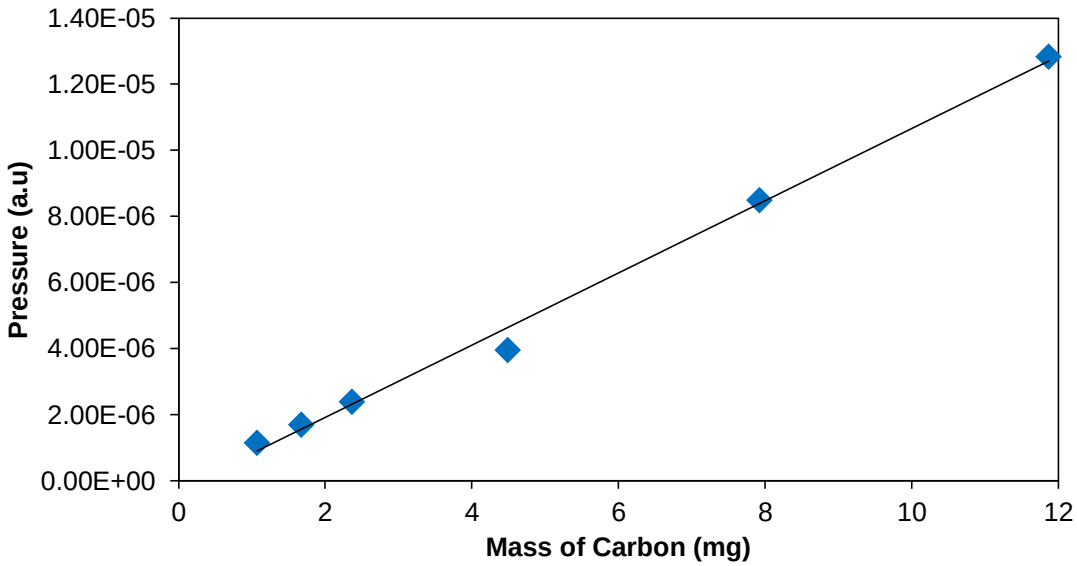

Figure 3.7 Carbon calibration graph demonstrating the quantity of CO + CO_2 produced from the oxidation from known amounts of carbon (produced April 2010.)

One difficulty with the TPO procedure was that due to the limited nature of the oxidant, in this case 12.5% in Helium (2.5 ml min^{-1} O_2 in 17.5 ml min^{-1} He), it means that if an excessively large quantity of carbon is deposited during the reaction (approx. >30 mg) then incomplete combustion occurs. This means that the regime to which the oxygen was used to produce carbon monoxide and carbon dioxide changes to one where the oxygen was used to produce only carbon monoxide due to the limited oxygen. This change in regime means that for any TPO's that exhibit incomplete combustion, the carbon deposition cannot be accurately quantified using the carbon calibration graph as shown above. An example of a TPO that has bottomed out is shown in Figure 3.8.

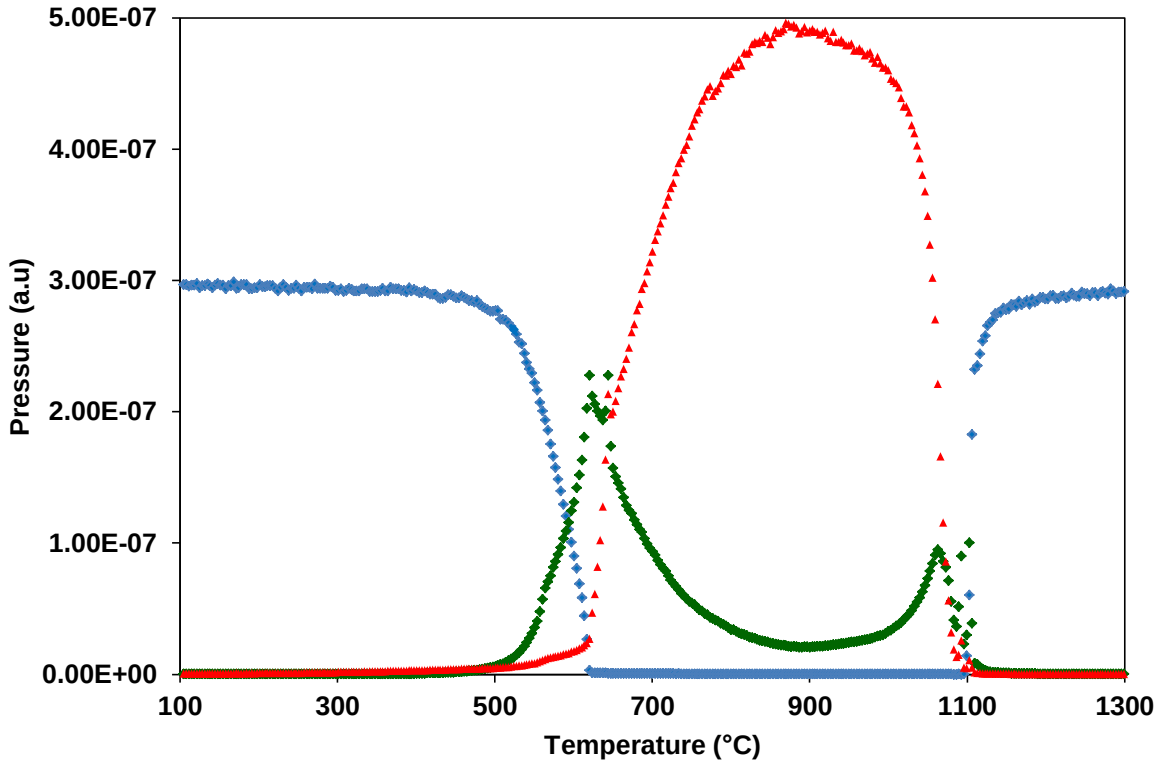

Figure 3.8: CO_2 and CO production and O_2 consumption of a TPO following the CH_4 + 0.5 CO_2 + 0.17O_2 reaction over 5 mol% CeO_2 -Ni/YSZ at 1000 °C for 20 hours. Bottoming out occurs from 500-1100 °C. Data shown above 900 °C is where the reaction temperature is held at 900 °C (Blue=O_2, Green=CO_2, Red=CO)

3.8 Data analysis calculations

To effectively compare the quantity of data that is produced from these experiments, it is necessary to perform a number of different calculations on the corrected data so that the key reaction characteristics can be identified. These key characteristics are methane conversion (%), hydrogen yield (%), carbon monoxide yield (%), hydrogen:carbon monoxide ratio, water production (%), carbon dioxide consumption (%). The equations used to calculate these characteristics are shown from Equations 3.16 – 3.21.

$$\mathrm{CH_4\ Conversion\ (\%)} = \frac{\mathrm{CH_4\ Original} - \mathrm{CH_4\ Current}}{\mathrm{CH_4\ Original}} \times 100$$

(3.16)

$$\mathrm{H_2\ Yield\ (\%)} = \frac{\mathrm{H_2\ Current}}{2 \times\ \mathrm{CH_4\ Original}} \times 100$$

(3.17)

$$\mathrm{CO\ Yield\ (\%)} = \left(\frac{\mathrm{CO\ Current} - \left(\mathrm{CO_2\ Original}\ \times \left(\frac{\mathrm{CO\ Original}}{\mathrm{CO_2\ Original}} \right) \right)}{(\mathrm{CO_2\ Original} +\ \mathrm{CH_4\ Original})} \right) \times 100$$

(3.18)

$$\mathrm{H_2{:}\,CO\ Ratio} = \frac{\mathrm{H_2\ Current}}{\mathrm{CO\ Current}}$$

(3.19)

$$\mathrm{H_2O\ Production\ (\%)} = \frac{\mathrm{H_2O\ Current} -\ \mathrm{H_2O\ Original}}{(2 \times \mathrm{CH_4\ Original}) + \mathrm{O_2 Original}} \times 100$$

(3.20)

$$\mathrm{CO_2\ Conversion\ (\%)} = \frac{\mathrm{CO_2\ Original} -\ \mathrm{CO_2\ Current}}{\mathrm{CO_2\ Original}} \times 100$$

(3.21)

All values noted as 'Current' or 'Original' are obtained from the QMS and RGA program. 'Original' values correspond to those measured whilst the gas in question is passing through the bypass system. 'Current' values correspond to the QMS/RGA display at a particular time or temperature in question.

Equation 3.18 was used to calculate CO yield and takes into account the fragmentation of CO_2 to CO within the QMS. The proportion of CO present due to this fragmentation is therefore calculated

and subtracted to give a more accurate value of the original CO quantity in the reactant gas mixture.

It should be noted, that in addition to the normalisation and calculations conducted on the data, repeat experiments were carried out and have shown a maximum variation of 6.5 % for the calculated values, such as CH_4 conversion and H_2 yield. This valuee should be considered when analysing the data shown in Sections 5-8.

3.9 Catalyst characterisation techniques

To provide a more detailed assessment of the catalyst properties and structure, specific characterisation tests were conducted on the catalysts and the raw materials. The findings of these characterisation tests are discussed in Section 4. BET adsorption analysis was conducted to assess the surface area of the materials and XRD analysis was conducted to provide an indication of catalyst composition and purity.

3.9.1 BET apparatus

All BET adsorption analysis was conducted using a Quantochrome Autosorb-1 Surface Area and Pore Size analyser. Approximately 1 g of catalyst was used per sample from which analysis was gained towards the surface area per gram. Prior to each measurement, the sample was degassed at 200 °C for 12 hours to remove surface contaminants such as oil and water from the sample material. Following the degassing, the sample was brought to a constant temperature of 77 K through immersing the sample holder in liquid nitrogen. BOC scientific high purity (>99.9995%) nitrogen gas was used as the adsorbate for the adsorption measurements.

3.9.2 BET theory

BET theory for the analysis of surface area and pore distribution was originally proposed by Brunauer, Emmett and Teller in 1938 [8]. At equilibrium, a surface will adsorb a certain quantity of gas at a certain temperature and pressure. Through variation of the pressure, an adsorption isotherm can be produced. The adsorption isotherm and BET equation (Equation 3.22) can then be used to calculate the surface area of the material [9].

$$\frac{1}{W\left(\left(\frac{P_0}{P}\right)-1\right)} = \frac{1}{W_m C} + \frac{C-1}{W_m C}\left(\frac{P}{P_0}\right) \quad \textbf{(3.22)}$$

W_m = volume of adsorbate gas constituting a monolayer

W = volume of gas adsorbed

P = equilibrium pressure at temperature of adsorption

P_0 = saturation pressure at temperature of adsorption

C = BET constant (relative to energy of adsorption of first monolayer)

From the adsorption isotherm, a linear plot of $1/(W(P_0/P)-1)$ against P/P_0 is produced. From the slope and intercept of the linear plot, W_m can be deduced (Equation 3.23 and 3.24):

$$s = \frac{C-1}{W_m C} \quad \textbf{(3.23)}$$

$$i = \frac{1}{W_m C} \quad \textbf{(3.24)}$$

Using W_m, the total surface area can be calculated using Equation 3.25:

$$S_t = \frac{W_m . N . A_{cs}}{M} \quad \textbf{(3.25)}$$

N = Avagadro's constant

A_{cs} = Cross sectional area of adsorbate molecule (N_2=16.2 $Å^2$)

The surface area per gram can then be calculated simply by dividing the total surface area by the mass of sample analysed. The analytical technique used in this study automatically calculates the BET surface area per gram from the adsorption isotherm generated.

3.9.3 XRD apparatus

All X-Ray diffraction data was obtained using a Bruker D8 Advance. Diffraction patterns were measured using a step size of 0.2° and a time per step of 5 seconds across the range of 5-80°. Each sample was loaded onto a PMMA specimen holder with a 25 mm diameter and 1 mm depth which was then mounted onto an automated sample changing unit.

All X-Ray diffraction data was evaluated within the DIFFRAC^{plus} EVA program. K_2 stripping was performed on the patterns to remove any contribution from $K\alpha_2$ radiation. The XRD patterns were compared using the DIFFRAC^{plus} SEARCH and ICDD-PDF-2 powder diffraction databases to assess the nature of the peaks and reference all diffraction patterns. All XRD patterns were then transferred into Microsoft Excel to allow for manipulation/annotation and display purposes.

3.9.4 XRD theory

X-ray diffraction was suggested in 1923 by a German physicist named Max von Laue [10] and was developed by William and Lawrence Bragg [11], with the first atomic structure determined using x-ray scattering in 1914.

X-ray diffraction operates through directing x-rays into a crystalline material and measuring the interference from objects (atoms) in its path. The x-rays are produced through bombarding a metal with high-energy electrons. These electrons cause an electron within the metal to be expelled, leaving a vacancy. A higher energy electron then moves into this lower energy vacancy, emitting the excess energy as it does so. This excess energy is in the form of an x-ray photon. The x-ray's produced using the instrument described in 5.9.3 are produced using a Copper metal which expels

x-rays with a wavelength of 154 pm due to the expulsion of an electron from the K shell and the movement of an electron from an outer electron into the vacancy.

Crystalline materials are highly ordered and consist of unit cells which can be categorised depending on their symmetry. The ordering of the crystal structure means that planes of symmetry through atoms are present and the distance between these planes is known as the d-spacing. This is calculated using the Bragg law (Equation 3.14). Bragg's law states that the angle in which the x-rays are reflected is proportional to the d-spacing, therefore through varying the incidence angle of the x-rays using a monochromator and monitoring any reflection that may occur, the d-spacing value can be obtained.

$$\boldsymbol{\lambda = 2d \sin \theta} \qquad \textbf{(3.1)}$$

In Equation 3.1, λ is the wavelength, d is the d-spacing value and θ the reflection angle.

Through x-ray diffraction, it is possible to calculate the particle size for each element. This is achieved using the Scherrer equation (Equation 3.15).

$$\textbf{Particle size} = \frac{\mathbf{k\lambda}}{\left(\frac{\pi}{180}\right)(B^2 - b^2)^{\frac{1}{2}} \cos\theta} \qquad \textbf{(3.2)}$$

In Equation 3.15, k = particle shape factor (0.89), B^2 = peak width at half maximum, b^2 = instrumental line broadening, θ = diffraction angle. All particle size values are shown in radians. The particle factor value shown above is for spherical particles. The instrumental line broadening value was specific to this apparatus and calculated using a material of known particle size. All particle size values are shown in Section 4.2.

3.10 Solid oxide fuel cell operation

All fuel cells were manufactured by John Staniforth using the procedure described in the PhD thesis by John Staniforth in 2000 and are illustrated schematically in Figure 3.9 below [12].

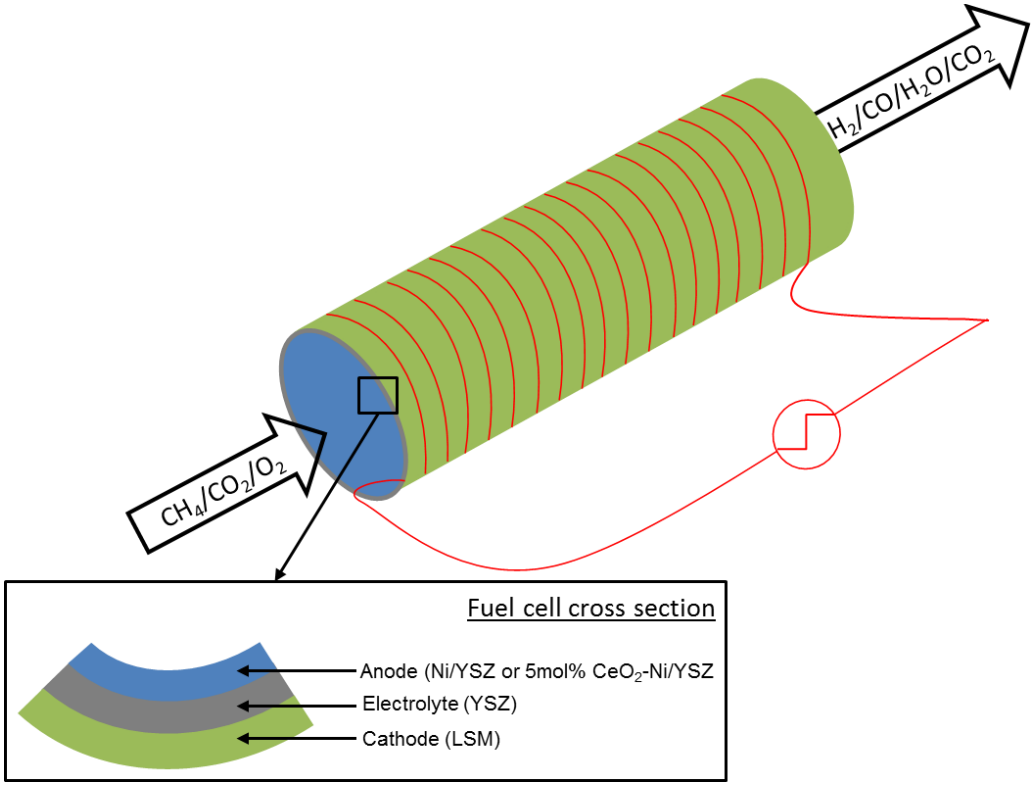

Figure 3.9. Schematic illustration of Solid Oxide Fuel Cell used to test anode materials and operating conditions (not to scale).

To accommodate for the fuel cell tests, the experimental setup was altered in that a tubular fuel cell illustrated above (Figure 3.9) replaced the quartz tube within the furnace to ensure that the reactive gases flowed through the inside of the tubular fuel cell and across the anode material. The cathode material was open to the furnace environment to allow for oxide ions to be generated. To assess the electrical performance of the cells, standard *i-V* curves (discussed in more detail in Section 9.1) were conducted with a voltage range of 0.1-1V and the current generated was measured using a Sycopel Scientific Ltd, Analytical Electrochemical Workstation AEW2-1000mA potentiostat that was attached to both the cathode and anode of the cell using silver wire. Data was recorded using the ProcessEye program provided with the potentiostat whilst Microsoft Excel was used to manipulate and display the data.

A significant issue associated with operation of the fuel cell above 900 °C was that thermal failure and degradation occurred within the cell attributed to the melting of the silver wire to break the electrical circuit. Therefore, temperatures above 900 °C were not researched in this study and further research is required to enable operation of these cells at such temperatures.

3.11 References

1. A.F. Benton and P.H. Emmett, *The reduction of nickelous and ferric oxides by hydrogen.* Journal of the American Chemical Society, 1924. **46**(12): p. 2728-2737.
2. G.B. Taylor and H.W. Starkweather, *Reduction of metal oxides by hydrogen.* Journal of the American Chemical Society, 1930. **52**: p. 2314-2325.
3. C.M. Finnerty and R.M. Ormerod, *Internal reforming over nickel/zirconia anodes in SOFC operating on methane: influence of anode formulation, pre-treatment and operating conditions.* Journal of Power Sources, 2000. **86**: p. 390-394.
4. C.M. Finnerty, N.J. Coe, R.H. Cunningham, and R.M. Ormerod, *Carbon formation on and deactivation of nickel-based/zirconia anodes in solid oxide fuel cells running on methane.* Catalysis Today, 1998. **46**(2-3): p. 137-145.
5. H. He and J.M. Hill, *Carbon deposition on Ni/YSZ composites exposed to humidified methane.* Applied Catalysis A: General, 2007. **317**(2): p. 284-292.
6. S.T. Borman, H. Russell, and G. Siuzdak, *A Mass Spec Timeline.* Today's Chemist At Work, 2003. **September**: p. 47-49.
7. I.V. Chernushevich, A.V. Loboda, and B.A. Thomson, *An introduction to quadrupole-time-of-flight mass spectrometry.* Journal of Mass Spectrometry, 2001. **36**(8): p. 849-865.
8. S. Brunauer, P.H. Emmett, and E. Teller, *Adsorption of Gases in Multimolecular Layers.* Journal of the American Chemical Society, 1938. **60**(2): p. 309-319.
9. G. Fagerlund, *Determination of specific surface by the BET method.* Materials and Structures, 1973. **6**: p. 239-245.
10. M.v. Laue, *Concerning the detection of X-ray interferences.* Nobel Lecture, 1915.
11. W.H. Bragg and W.L. Bragg, *"for their services in the analysis of crystal structure by means of X-rays".* Nobel Prize in Physics, 1915.
12. J. Staniforth, *The use of biogas to power a small tubular solid oxide fuel cell, PhD Thesis*. 2000, Keele University.

4 Catalyst Characterisation

To provide a further insight into the nature of the catalyst materials used within this study, several analytical characterisation techniques have been used including temperature programmed reduction (4.3), powder X-ray diffraction (4.4) and BET surface area analysis (4.5).

4.1 Nickel as an active catalyst material for methane reforming

The discovery of nickel was made in 1751 by Alex Cronstedt. Since then it has become one of the most widely used metals in current society. Nickel is found in numerous ores/minerals such as pentlandite, garnierite and limonite and although abundance is low in the Earth's crust, it is proposed that nickel is highly abundant below the Earth's Crust and that the primary metal within the Earth's core is nickel. Uses of nickel are wide-ranging with primary uses including within coins, rechargeable batteries and steel alloys. The use of nickel within currency is evident particularly within the USA currency denomination of a nickel ($0.05) which is composed of 25 % nickel. The role of nickel within rechargeable batteries is through operation of Nickel (III) Oxide as the cathode material. The largest use of nickel is within steel alloys such as stainless steel to increase steel strength and resistance to corrosion. It is reported that over 70 % of nickel consumption in the USA is in the production of steel alloys [1].

Nickel is a transition metal with an electronic configuration of [Ar] $4s^2$ $3d^8$ or [Ar] $4s^1$ $3d^9$ with oxidation states of 0, +1, +2, +3 and +4, with +2 the most common state.

The majority of Group VIII elements have been shown to be active for methane reforming by many researchers. An extensive review of the literature reporting the use of Group VIII elements for methane reforming has been published by Enger *et al.* [2]. Noble metals such as platinum and palladium are used substantially in methane reforming as they show very high activity and resistance towards carbon deposition [3]. However, the substantial costs associated with the noble

metals make the formulation and use of non-noble metal catalysts highly desirable. Nickel has been shown to have comparable activity to noble metals at higher temperatures [4, 5], while its widespread availability and relatively low cost compared to precious metal based catalyst materials makes nickel a preferred metal for use as a solid oxide fuel cell anode material or as a stand-alone methane reforming catalyst. The major limitations of use of nickel compared to other catalyst materials is the significantly greater susceptibility towards carbon deposition [4, 6-8] and deactivation by poisons such as sulfur [6, 9-12], which is discussed in Sections 2.6.1 and 2.6.2.

4.2 Yttria-Stabilised Zirconia (YSZ) as a support material

Yttria-Stabilised Zirconia is a ceramic oxide material used as an electrolyte material in high temperature solid oxide fuel cells. The mixing of Yttria (Y_2O_3) in zirconia (ZrO_2) introduces oxygen vacancies within the structure as Zr^{4+} cations are partially replaced by Y^{3+} cations within the ZrO_2 lattice [13-15]. These oxygen vacancies and also the high thermal stability of yttria-stabilised zirconia (YSZ) provides the capacity for its use as an electrolyte material. In this study, YSZ is used as a support material to increase the dispersion, surface area and thermal stability of the nickel metal.

4.3 Temperature-Programmed Reduction (TPR)

Prior to all catalytic measurements, a temperature-programmed reduction (TPR) measurement was performed on all catalyst samples. Details on how the TPR study was carried out are provided in Section 3.3. Temperature programmed reduction as a characteristic technique was first reported by Benton and Emmett in 1924 [16]. It is performed to reduce the nickel from a +2 or +3 oxidation state (nickel oxide) present in the catalyst material to nickel metal with an oxidation state of 0, as this is an active nickel state for methane reforming.

Variations in reduction temperature can be caused by the nature of the oxide material, for example whether the oxide is present as a bulk or surface species, the extent of the interaction between the

oxide species and other species within the catalyst such as the support material, the oxidation state of the metal, particle size and dispersion and the nature of the reducing atmosphere.

From the TPR profile of NiO/YSZ shown in Figure 4.1, it is apparent that reduction occurs over the temperature range 310-800 °C and that two peaks may be present, suggesting the presence of two different forms of reducible species. The reduction temperature of these peaks is characteristic of the reduction of nickel oxide [17]. It is difficult to draw definitive conclusions from the TPR profile as the possible second peak is only present as a shoulder of the overall peak. However, this behaviour is observed for all TPR profiles performed with this NiO/YSZ material.

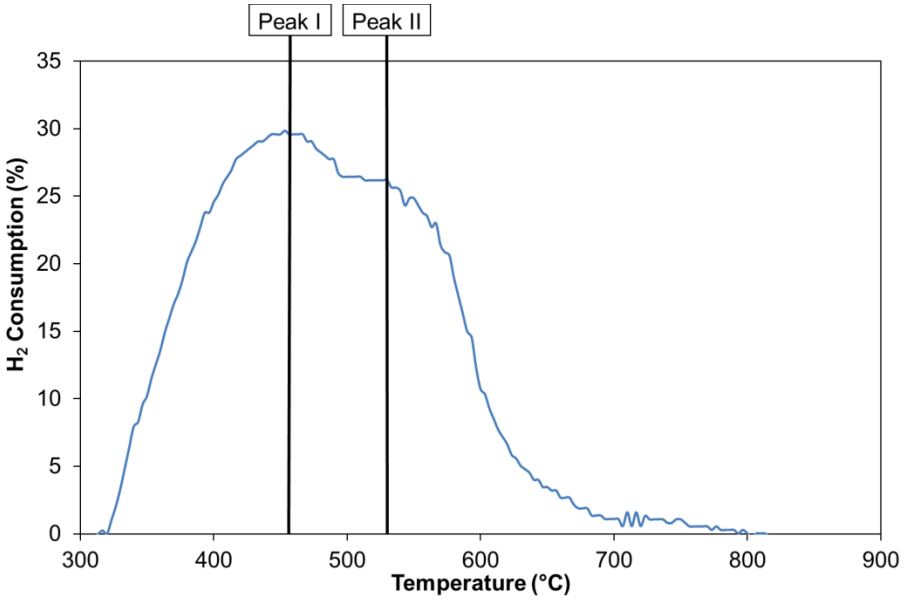

Figure 4.1: Hydrogen consumption during temperature-programmed reduction of NiO/YSZ with 10% H_2 in helium

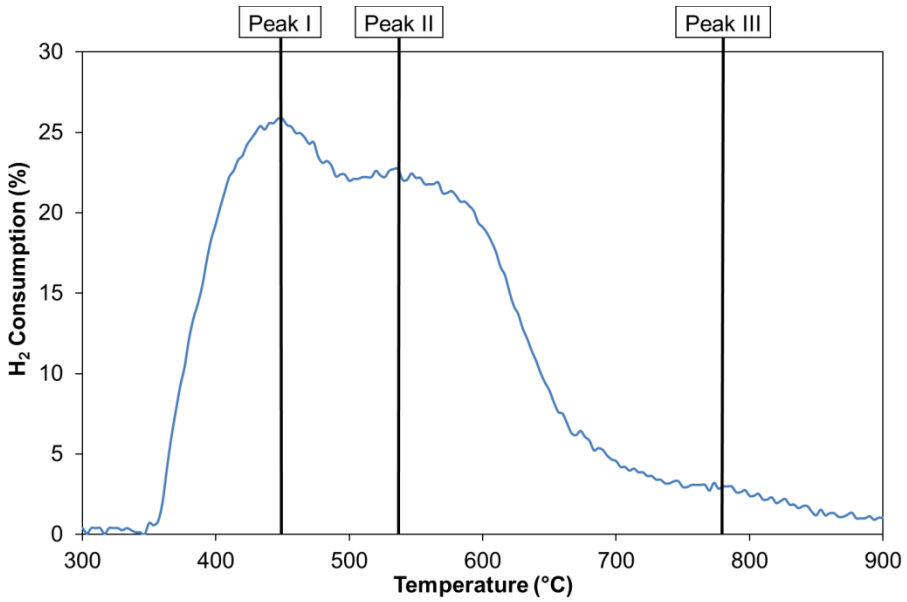

Figure 4.2: Hydrogen consumption during temperature-programmed reduction of 5 mol% CeO_2-NiO/YSZ with 10% H_2 in helium

Comparison of the TPR profiles for NiO/YSZ (Figure 4.1) and 5 mol% CeO_2-NiO/YSZ (Figure 4.2) show that the onset reduction temperature for 5 mol% CeO_2-NiO/YSZ is *ca.* 50 °C greater than that for NiO/YSZ and that the reduction process continues to a greater maximum temperature. Peaks I and II are more discernible in the profile for 5 mol% CeO_2-Ni/YSZ than for Ni/YSZ as Peak II occurs at a slightly higher temperature. In addition, a third peak is also evident for 5 mol% CeO_2-NiO/YSZ at *ca.* 770 °C, which may be due to the reduction of the CeO_2 species present within the sample, which has been reported to reduce in the temperature range 750-850 °C [17-19].

Temperature programmed reduction suggests that different forms of nickel oxide may be present within the NiO/YSZ sample and that similar forms are seen for the 5 mol% CeO_2-NiO/YSZ, with the additional presence of a third peak that may be due to the reduction of the CeO_2.

4.4 Powder X-Ray Diffraction

X-ray diffraction analysis was performed on all reagents used (NiO, YSZ, CeO_2) and catalysts samples prior to any pre-treatment to act as a method of quality control to establish sample purity

and chemical composition. The nature of XRD as a technique is discussed in detail in Section 3.9, as is the Scherrer equation which is used to calculate crystallite size.

The XRD patterns for all samples are shown in Figure 4.3. From this figure, it can be seen that each catalyst sample contains the desired components and that no impurities or undesired phases can be identified.

The average NiO crystallite sizes have been calculated using the Scherrer equation (Equation 3.15) to give some insight into any influence that CeO_2 addition can have on particle size. The majority of the published literature suggests that doping of nickel with CeO_2 acts to reduce the nickel crystallite size through acting as a barrier for nickel crystallite agglomeration. Table 4.1 suggests the addition of CeO_2 has resulted in a larger nickel crystallite size.

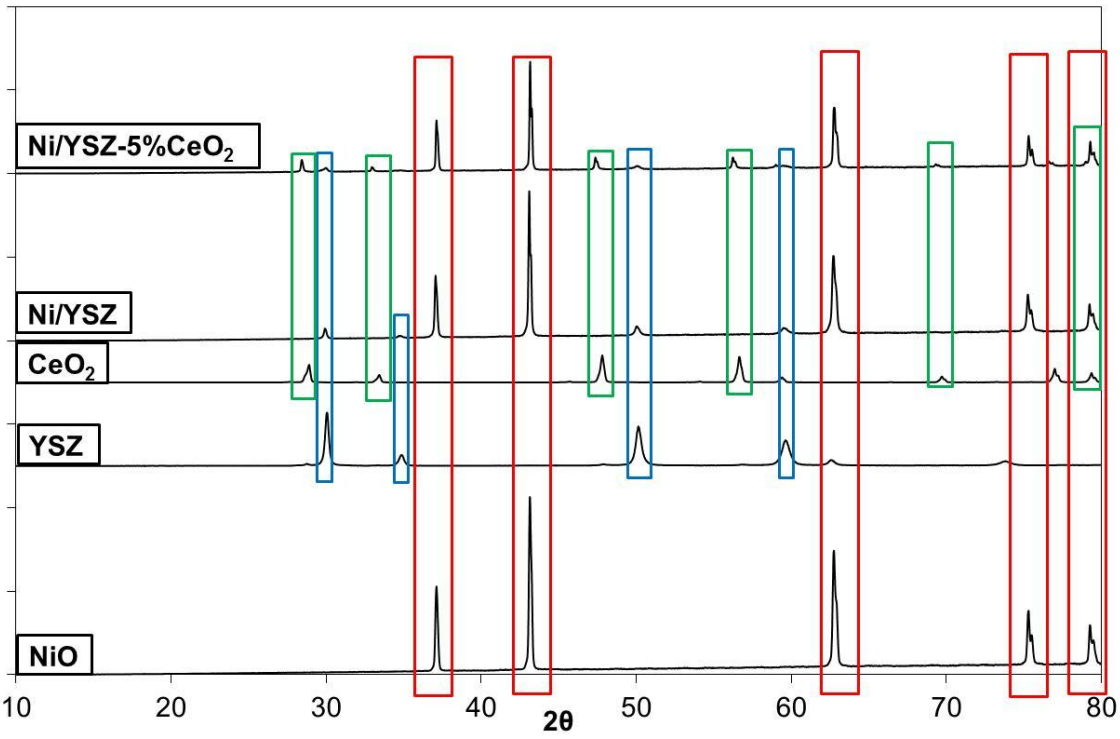

Figure 4.3: Powder X-Ray diffraction pattern for reagents (NiO, YSZ, CeO_2) and catalyst materials (NiO/YSZ, 5 mol% CeO_2-NiO/YSZ). Red = NiO, Blue = YSZ, Green = CeO_2

Table 4.1: Approximate nickel crystallite size determined using the Scherrer Equation for NiO, Ni/YSZ and 5 mol% CeO_2-Ni/YSZ.

	NiO raw material		**Ni/YSZ**		**5 mol% CeO_2-Ni/YSZ**	
Peak position (2θ/°)	37.10	43.13	37.06	43.039	37.12	43.15
Crystallite size (nm)	69	82	86	127	119	178
Average nickel crystallite size (nm)	76		107		148	

4.5 BET surface area analysis

BET surface area analysis was performed on both catalyst samples to determine their comparative total surface area. More detail regarding the nature of BET and apparatus used is discussed in Section 3.9. It is apparent from Table 4.2 that the addition of 5 mol% to Ni/YSZ induces a substantial increase in the total surface area.

Table 4.2: NiO/YSZ and 5 mol% CeO_2-NiO/YSZ surface area analysed using BET

Catalyst	**Surface area (m^2/g)**
NiO/YSZ	1.00
5 mol% CeO_2-NiO/YSZ	1.40

4.6 Summary

Sample characterisation has only been used within this research as a relatively simple qualitative approach to providing a greater insight into the nature of the catalyst samples due to the small quantity of different catalysts used and also the extensive prior use of catalysts prepared by the same method within the research group [20, 21]. Temperature programmed reduction of the different catalyst materials has shown the presence of multiple forms of reducible species in that two peaks are seen for Ni/YSZ and three peaks seen for 5 mol% CeO_2-Ni/YSZ. The additional

peak for 5 mol% CeO_2-Ni/YSZ may be due to the reduction of CeO_2. X-ray diffraction studies have shown that the required composition for both catalyst materials has been achieved with no undesired impurities or phase changes. X-ray diffraction has also been used to show that catalyst preparation method results in a greater nickel crystallite size compared to pure nickel oxide and ceria doping results in a greater nickel crystallite size compared to the undoped catalyst. BET surface area analysis has illustrated a significant increase in the total surface area of the catalyst material with ceria doping.

More detailed characterisation work could be focused towards the influence that the pre-reaction temperature programmed reduction procedure can have on the catalyst nature and how this is affected when CeO_2 is present within the catalyst, including at different concentrations of ceria doping. Post-reaction analysis would also provide more insight into the extent of sintering of nickel oxide in the catalyst samples and whether variations in reaction atmosphere can influence this.

4.7 References

1. D.J. Hanson, *Nickel.* Chemical & Engineering News, 2003. **81**(36): p. 82.
2. B. Christian Enger, R. Lødeng, and A. Holmen, *A review of catalytic partial oxidation of methane to synthesis gas with emphasis on reaction mechanisms over transition metal catalysts.* Applied Catalysis A: General, 2008. **346**(1-2): p. 1-27.
3. J.A. Lercher, J.H. Bitter, W. Hally, W. Niessen, K. Seshan, J.W. Hightower., W.N.D.E. Iglesia., and A.T. Bell, *Design of stable catalysts for methane-carbon dioxide reforming*, in *Studies in Surface Science and Catalysis*. 1996, Elsevier. p. 463-472.
4. J.R. Rostrup-Nielsen and J.H.B. Hansen, *CO_2-Reforming of Methane over Transition Metals.* Journal of Catalysis, 1993. **144**(1): p. 38-49.
5. F. Pompeo, N.N. Nichio, M.M.V.M. Souza, D.V. Cesar, O.A. Ferretti, and M. Schmal, *Study of Ni and Pt catalysts supported on [alpha]-Al_2O_3 and ZrO_2 applied in methane reforming with CO_2.* Applied Catalysis A: General, 2007. **316**(2): p. 175-183.
6. J. Sehested, *Four challenges for nickel steam-reforming catalysts.* Catalysis Today, 2006. **111**(1-2): p. 103-110.
7. A.T. Ashcroft, A.K. Cheetham, M.L.H. Green, and P.D.F. Vernon, *Partial oxidation of methane to synthesis gas using carbon dioxide.* Nature, 1991. **352**: p. 225-226.
8. C.M. Finnerty, N.J. Coe, R.H. Cunningham, and R.M. Ormerod, *Carbon formation on and deactivation of nickel-based/zirconia anodes in solid oxide fuel cells running on methane.* Catalysis Today, 1998. **46**(2-3): p. 137-145.
9. V. Karakoussis, N.P. Brandon, M. Leach, and R. van der Vorst, *The environmental impact of manufacturing planar and tubular solid oxide fuel cells.* Journal of Power Sources, 2001. **101**(1): p. 10-26.
10. J.N. Kuhn, N. Lakshminarayanan, and U.S. Ozkan, *Effect of hydrogen sulfide on the catalytic activity of Ni-YSZ cermets.* Journal of Molecular Catalysis A: Chemical, 2008. **282**(1-2): p. 9-21.

11. P. Mare´cot, E. Paraiso, J.M. Dumas, and J. Barbier, *Deactivation of nickel catalysts by sulphur compounds: II. Chemisorption of hydrogen sulphide.* Applied Catalysis A: General, 1992. **80**(1): p. 89-97.

12. C.H. Bartholomew, P.K. Agrawal, and J.R. Katzer, *Sulfur Poisoning of Metals*, in *Advances in Catalysis*. 1982, Academic Press. p. 135-242.

13. R. Devanathan, W.J. Weber, S.C. Singhal, and J.D. Gale, *Computer simulation of defects and oxygen transport in yttria-stabilized zirconia.* Solid State Ionics, 2006. **177**(15-16): p. 1251-1258.

14. R.F. Martins, M.C. Brant, R.Z. Domingues, R.M. Paniago, K. Sapag, and T. Matencio, *Synthesis and characterization of NiO-YSZ for SOFCs.* Mater. Res. Bull., 2009. **44**: p. 451-456.

15. R. O'Hayre, S.-W. Cha, W. Colella, and F.B. Prinz, *Fuel Cell Fundamentals*. 2006, Wiley VCH. p. 303.

16. A.F. Benton and P.H. Emmett, *The reduction of nickelous and ferric oxides by hydrogen.* Journal of the American Chemical Society, 1924. **46**(12): p. 2728-2737.

17. S. Xu, X. Yan, and X. Wang, *Catalytic performances of NiO-CeO_2 for the reforming of methane with CO_2 and O_2.* Fuel, 2006. **85**(14-15): p. 2243-2247.

18. H.S. Roh, K.W. Jun, W.S. Dong, S.E. Park, and Y.S. Baek, *Highly stable Ni catalyst supported on Ce-ZrO_2 for oxy-steam reforming of methane.* Catalysis Letters, 2001. **74**(1-2): p. 31-36.

19. S. Xu and X. Wang, *Highly active and coking resistant Ni/CeO_2-ZrO_2 catalyst for partial oxidation of methane.* Fuel, 2005. **84**(5): p. 563-567.

20. J. Staniforth, *The use of biogas to power a small tubular solid oxide fuel cell, PhD Thesis*. 2000, Keele University.

21. C.J. Laycock, J.Z. Staniforth, and R.M. Ormerod, *Biogas as a fuel for solid oxide fuel cells and synthesis gas production: effects of ceria-doping and hydrogen sulfide on the performance of nickel-based anode materials.* Dalton Transactions, 2011. **40**(20): p. 5494-5504.

5 Influence of O_2 addition in varied concentrations on the CO_2 reforming of CH_4 over Ni/YSZ catalyst

5.1 Biogas reforming and potential for improvement through O_2 addition

The catalytic reforming of biogas is highly inefficient due to its methane-rich nature and susceptibility towards carbon deposition. One approach towards improving the efficiency of biogas reforming and reducing the propensity towards carbon deposition is through the addition of a reformant to the reaction gas mixture. In this study, oxygen has been chosen as the additional reformant. To study the influence of O_2 on the activity of the reforming reaction, various different oxygen concentrations have been used. A study has been undertaken in the absence of additional O_2 to provide an understanding into the nature of biogas reforming. Subsequently, a detailed study has been undertaken with O_2:CH_4 ratios of 0.17, 0.25 and 0.33 which represent oxygen deficient, sufficient oxygen and excess oxygen respectively, assuming an ideal situation in which only the dry reforming reaction and partial oxidation reactions occur without side reactions.

The addition of oxygen to the CH_4:CO_2 biogas simulating mixture has been proposed to substantially improve activity and reduce carbon deposition [1], whilst also providing the ability for a degree of control regarding the H_2:CO product ratio [2-4]. In this research, both temperature programmed and isothermal studies have been conducted to assess how the addition of oxygen to the CH_4:CO_2 mixture, and the subsequent influence on reforming varies with temperature and time. Temperature programmed studies, whilst useful, should be viewed with caution as surpassed temperatures can substantially distort the reforming characteristics at certain temperatures through features such as ‘light-offs’ and carbon deposition.

5.2 Temperature programmed CO_2 reforming over Ni/YSZ with addition of O_2 in different quantities

Initial temperature programmed reactions were performed with reaction mixtures of $CH_4 + 0.5CO_2 + xO_2$ where x=0.00, 0.17, 0.25 and 0.33. Temperature programmes were conducted from room temperature to 1000 °C at a rate of 5 °C min^{-1}. Figures 5.1 – 5.5 show the influence of O_2 addition to the biogas simulated mixture on reaction characteristics.

From the temperature programmed studies, it is clearly apparent that the addition of O_2 to the CH_4:CO_2 mixture results in a significant change in the reaction characteristics. For the reaction in the absence of O_2, the activity increases steadily above approximately 510 °C. It can also be seen that the methane conversion is low (50-60 %), even at the highest temperature. This is not surprising, due to the 1:1 stoichiometry of the dry reforming reaction coupled with the 2:1 CH_4:CO_2 ratio used. As the methane conversion exceeds 50 % above 900 °C, this indicates the occurrence of methane decomposition. Methane decomposition is thermodynamically favourable above 700 °C as illustrated by the Ellingham diagram shown in Figure 2.4. The reaction in the absence of oxygen also shows a significant difference from those in the presence of O_2 in that there is essentially no 'light off' feature present.

Addition of O_2 to the CH_4:CO_2 mixture results in a substantial increase in overall activity across the complete temperature range. At lower reaction temperatures (400-600 °C), the addition of O_2 increases the methane conversion without increasing the H_2 or CO yield. This can be attributed to an increase in the extent of the total oxidation of methane reaction (Equation 5.1), where the reaction in the presence of O_2 results in significant production of CO_2 and H_2O, as can be seen in Figure 5.4 and Figure 5.5 respectively. The greater exothermic nature of the total oxidation of methane reaction favours the selectivity of total oxidation over partial oxidation (Equation 5.2) at lower reaction temperatures. As may be expected, the extent of total oxidation increases with O_2 concentration.

$$CH_4 + 2O_2 \rightleftharpoons CO_2 + 2H_2O \qquad \Delta H^o_{298K} = -890 \text{kJ mol}^{-1} \qquad \textbf{(5.1)}$$

$$CH_4 + \frac{1}{2}O_2 \rightleftharpoons 2H_2 + CO \qquad \Delta H^o_{298K} = -36 \text{kJ mol}^{-1} \qquad \textbf{(5.2)}$$

At approximately 650 °C, a 'light off' feature is observed when O_2 is present in the reaction mixture. This 'light off' feature results from a high concentration of oxidant in the atmosphere surrounding the catalyst at lower temperatures, resulting in a sudden saturation of the catalyst with oxidant when a temperature is reached at which partial oxidation becomes spontaneous. This results in a sudden increase in the conversion of CH_4 and production of H_2 and CO. Immediately following the 'light off' feature, a substantial drop in catalyst activity is visible. This is due to a sudden lack of available active surface due to the prior saturation of the catalyst. The activity then steadily increases with temperature as the catalyst surface becomes more available and the reforming reactions increase in rate. It can be seen that the O_2 concentration influences the temperature at which the light off occurs. As O_2 concentration increases, the light off temperature increases slightly. This is due to the increased capacity for total oxidation with increased O_2 concentration, which delays the shift to partial oxidation, as shown in Figure 5.6. This behaviour was also published by Eriksson *et al.* [5] regarding partial oxidation of methane with different CH_4:O_2 ratios.

At higher reaction temperatures (800-1000 °C), the influence of temperature on catalyst activity decreases as the reaction becomes reactant limited. At these higher temperatures, the addition of oxygen results in an increase in reforming activity due to increased reactant availability. This is seen to a lesser extent with the methane conversion at high reaction temperatures due to increased capacity for methane decomposition, and the reaction becoming methane limited. Figure 5.1 shows that the methane conversion increases with increasing O_2 concentration. However, from Figure 5.2 and Figure 5.3 it can be seen that increasing the O_2 concentration actually decreases the H_2 and CO yields. This can explained by increased total oxidation, and subsequent production of CO_2 and H_2O occurring at these temperatures, which can be seen in Figure 5.4 and Figure 5.5 respectively.

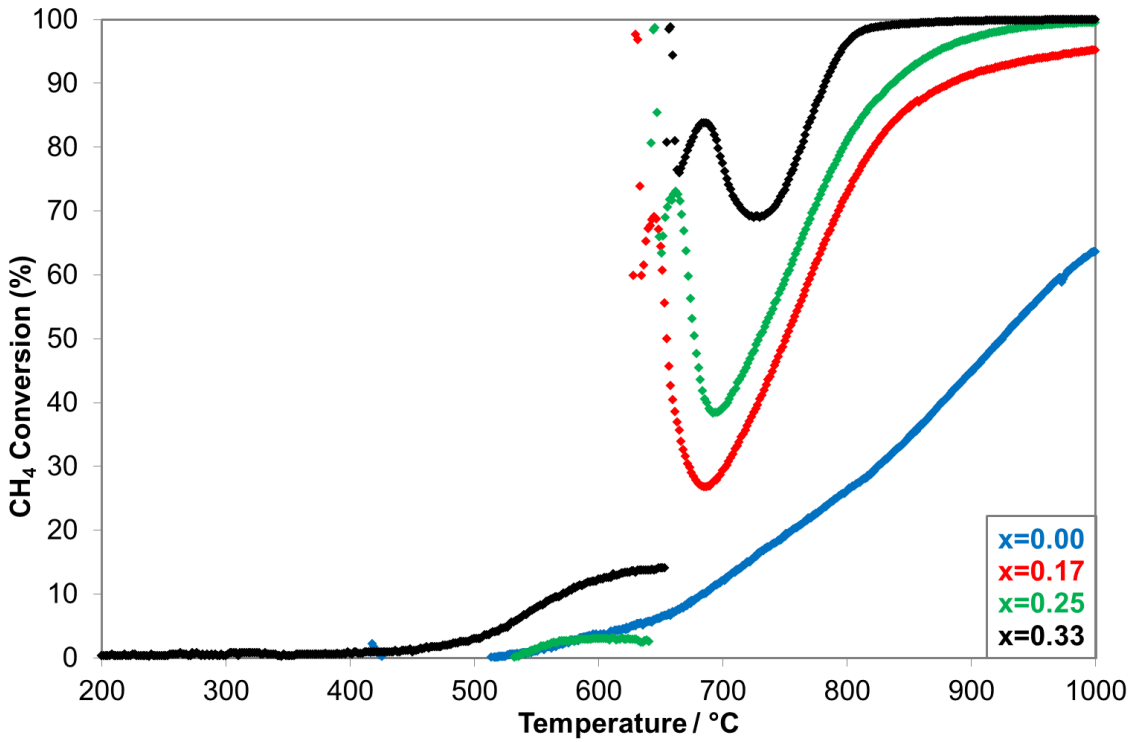

Figure 5.1: CH_4 conversion for reaction of $CH_4 + 0.5CO_2 + xO_2$ over Ni/YSZ during a temperature programme

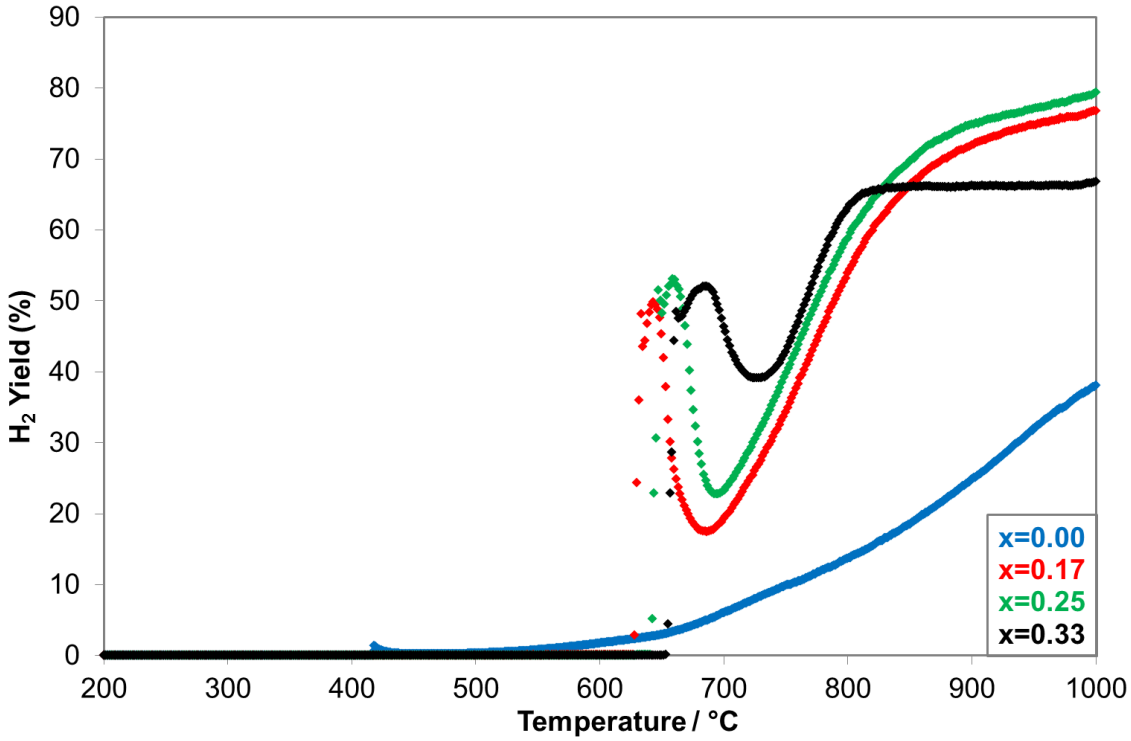

Figure 5.2: H_2 yield for reaction of $CH_4 + 0.5CO_2 + xO_2$ over Ni/YSZ during a temperature programme

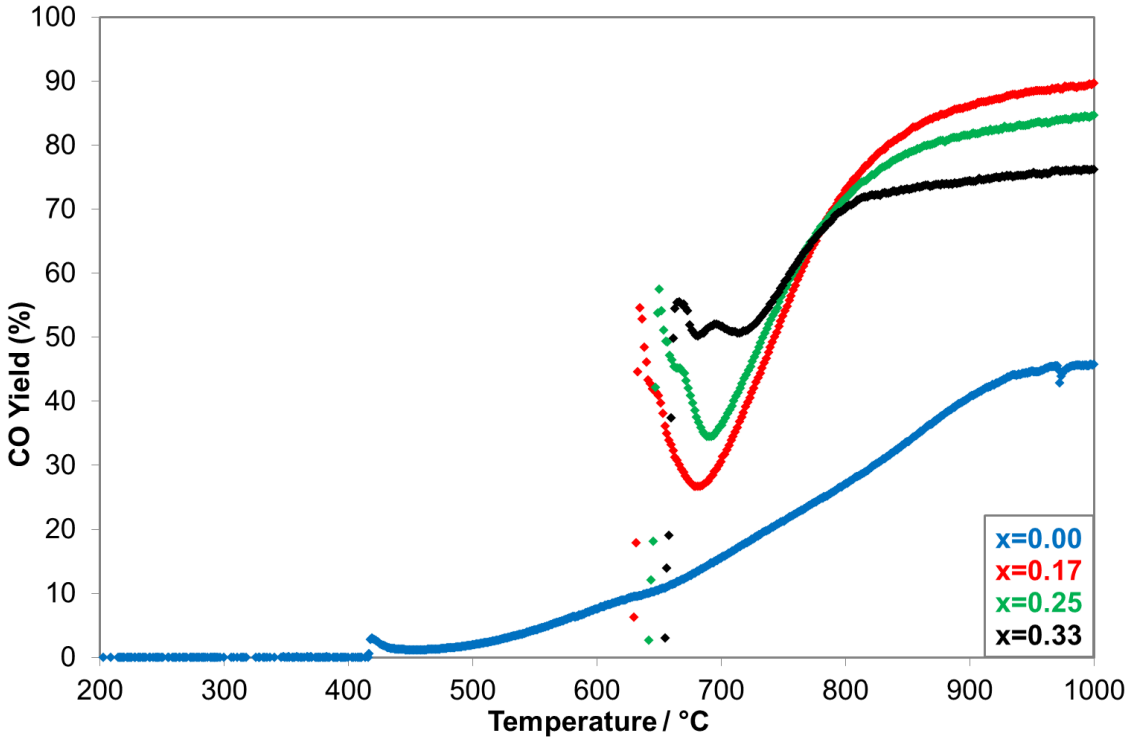

Figure 5.3: CO yield for reaction of CH_4 + 0.5CO_2 + xO_2 over Ni/YSZ during a temperature programme

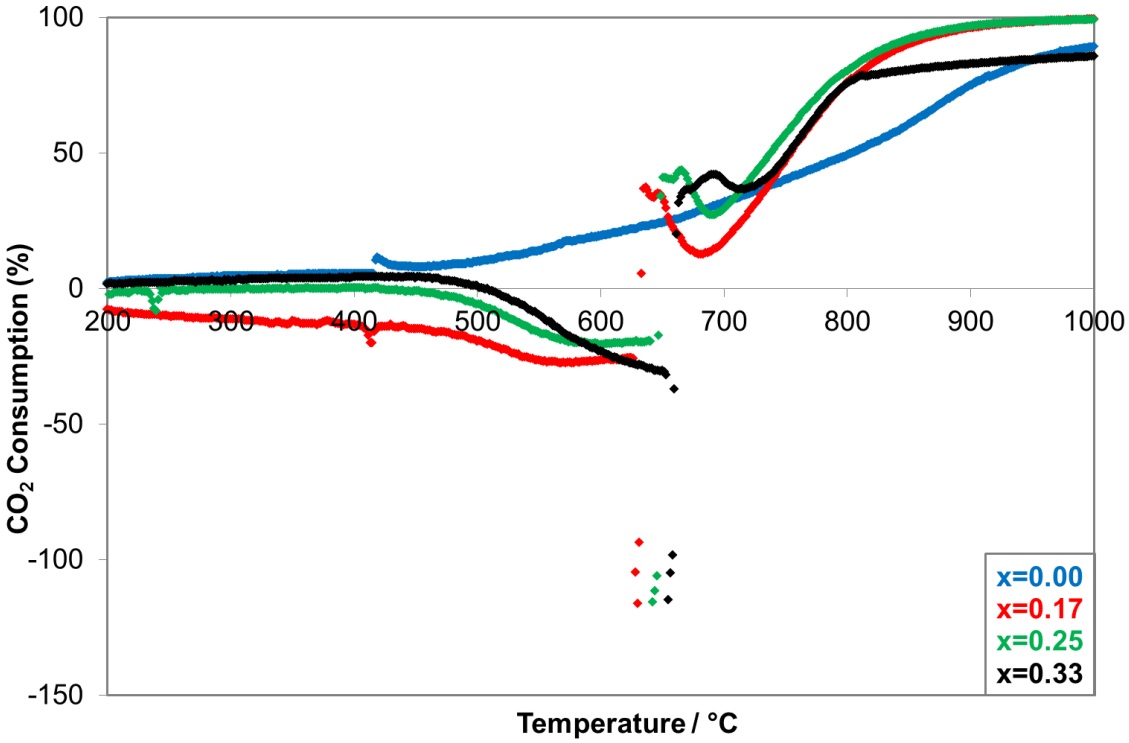

Figure 5.4: CO_2 consumption for reaction of CH_4 + 0.5CO_2 + xO_2 over Ni/YSZ during a temperature programme

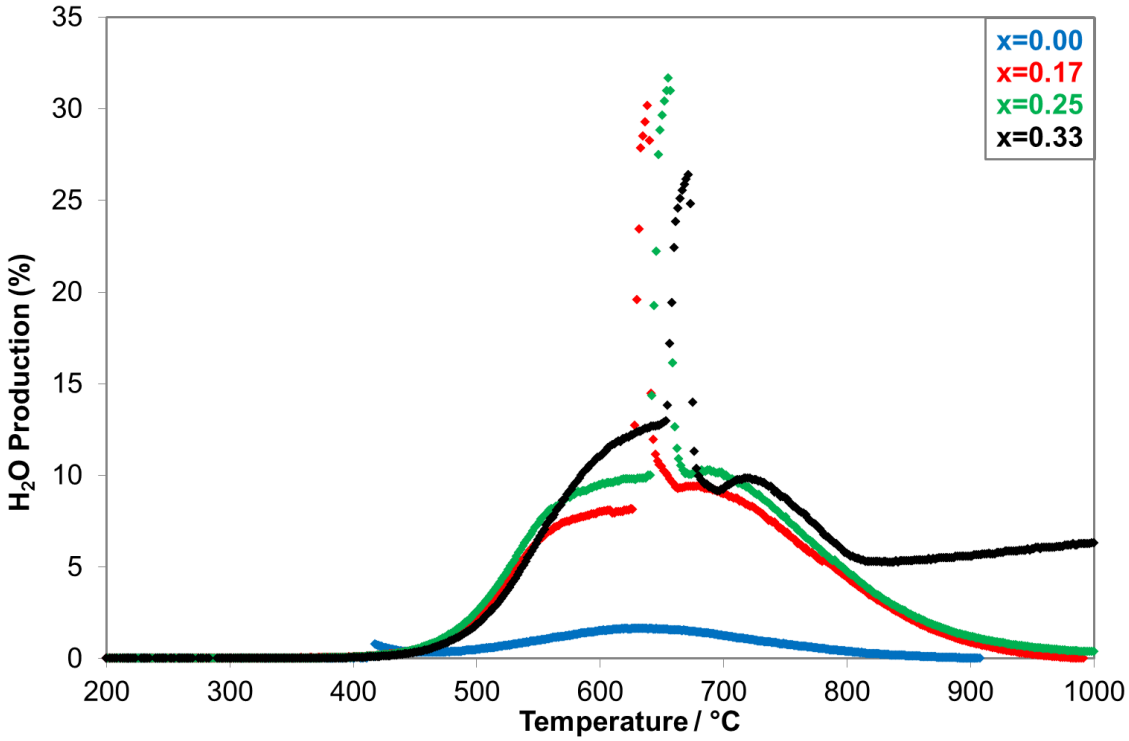

Figure 5.5: H_2O production for reaction of CH_4 + 0.5CO_2 + xO_2 over Ni/YSZ along a temperature programme

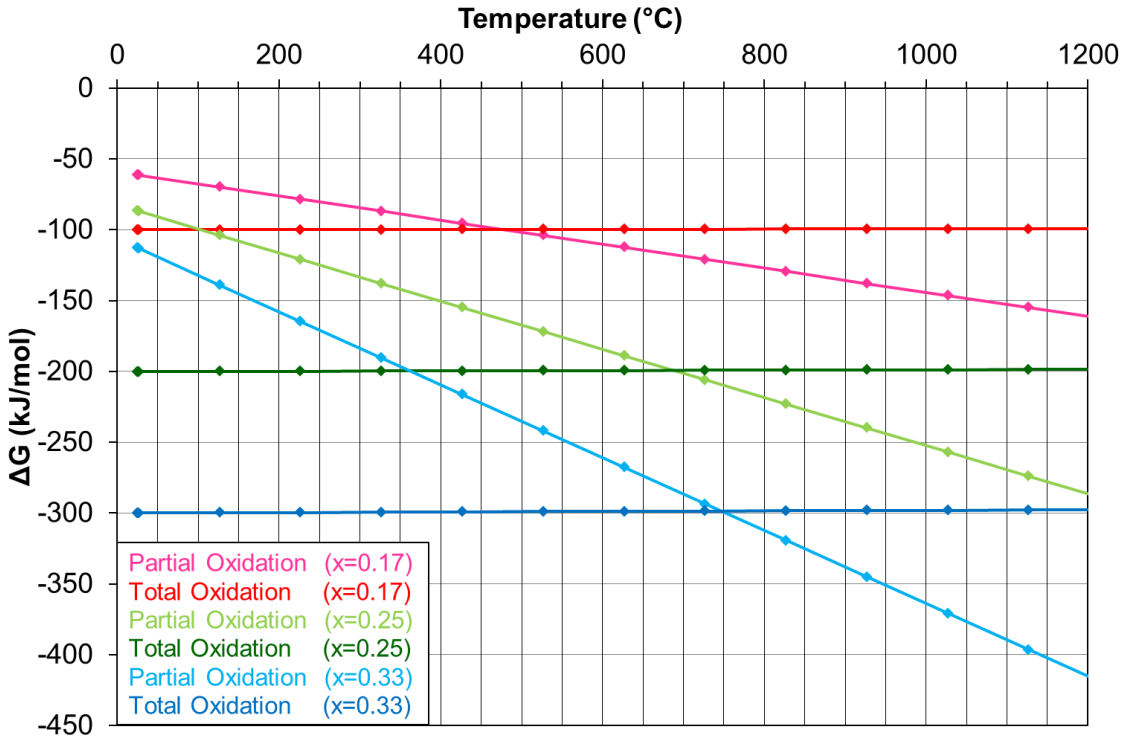

Figure 5.6: Ellingham diagram illustrating the thermodynamic potential for partial oxidation and total oxidation of methane with xO_2:$CH_4$where x=0.17, 0.25 and 0.33. Data taken from Lide [6].

5.3 CO_2 reforming of CH_4 over Ni/YSZ with and without addition of O_2

Following the temperature programmed studies, conventional catalytic studies were carried out over the 600–1000 °C temperature range at 100 °C intervals over a 20 hour period to examine the reaction characteristics over time and the influence of O_2 on the reaction characteristics. The reaction temperatures range was selected on the basis of the activity shown in the temperature programmed experiments. The influence of O_2 addition and variation with time has been assessed for each isothermal temperature and then the variations across the temperature range are analysed. All variations with time discussed are from after 5 hours reaction duration to exclude any initial activity that is uncharacteristic of the reaction. The extent to which carbon deposition occurred during the isothermal studies was measured using post-reaction temperature programmed

oxidation, as described in Section 3.6. Details of CH_4 conversion and H_2:CO ratio that are not included in this section are available in Appendix B.

5.3.1 Reaction of $CH_4 + 0.5CO_2 + xO_2$ over Ni/YSZ at 600 °C

The reforming characteristics of the reaction of $CH_4 + 0.5CO_2$ with and without oxygen addition over Ni/YSZ at 600 °C over a 20 hour period are shown in Figures 5.7–5.12. All reforming characteristics are shown for this reaction temperature to provide an illustration of the variations that can occur over the 20 hour reaction duration. For other reaction temperatures, only the reforming characteristics exhibiting substantial variation over time are shown, while those without are shown in tabular format or discussed within the text.

From the methane conversion shown in Figure 5.7, it is evident that the addition of O_2 to the CH_4/CO_2 mixture results in a significant increase in reforming activity due to the increased availability of reformant. All O_2 levels exhibit stable methane conversion over the 20 hour reaction duration.

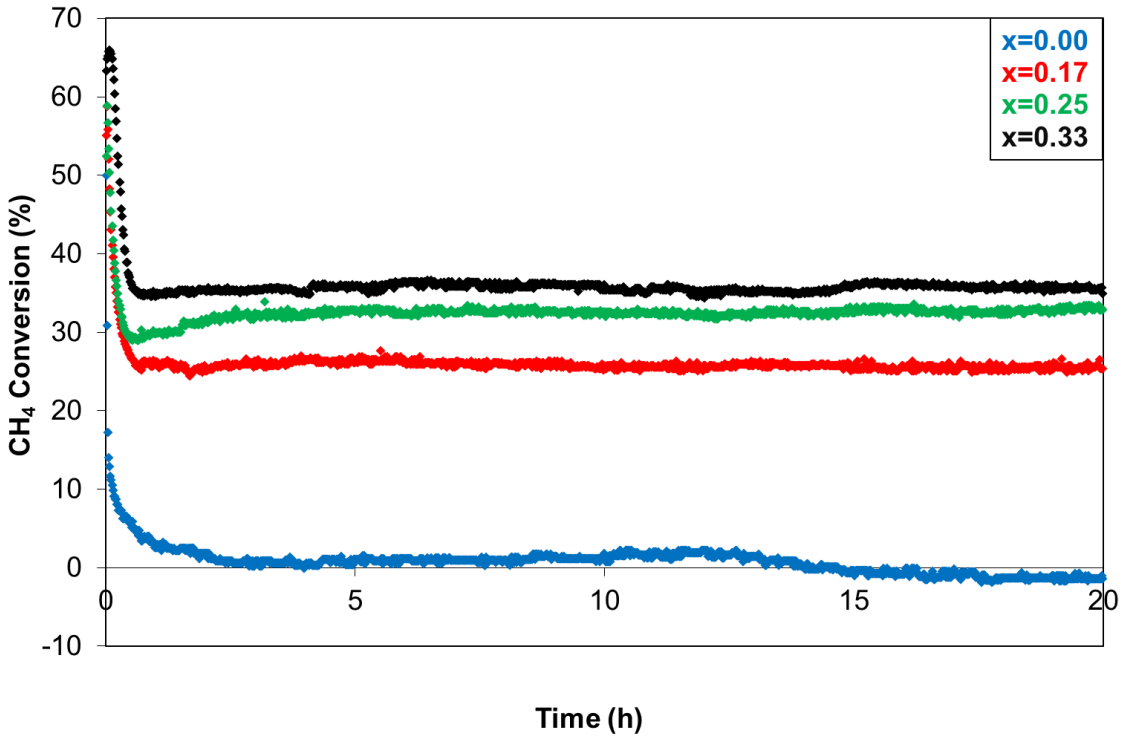

Figure 5.7: CH_4 conversion for reaction of CH_4 + 0.5CO_2 + xO_2 over Ni/YSZ at 600 °C for 20 hours (x=0.00, 0.17, 0.25, 0.33)

The hazardous nature of using methane conversion as the sole parameter to indicate activity is illustrated by the variation between methane conversion and H_2 yield. This is because of the extent to which total oxidation and other side reactions can occur. As hydrogen and carbon monoxide are the primary desired products, it is more accurate to use H_2 yield and CO yield as a measure of activity with methane conversion to provide additional insight.

The H_2 yield shown in Figure 5.8 shows a similar trend to methane conversion in that the addition of O_2 increases catalyst activity. One substantial difference is that methane conversion increases with O_2 concentration whereas the H_2 yield, and also the CO shown in Figure 5.9 is higher when x=0.17 than 0.25. One explanation for this is that total oxidation is occurring to a greater extent at higher O_2 levels, therefore reducing the H_2 and CO yields when x=0.25. However, from analysis of the CO_2 consumption and H_2O production, shown in Figure 5.11 and Figure 5.12 respectively, the extent of total oxidation occurring for x=0.25 appears to be slightly less than for x=0.17. The small differences in H_2 yield (<4 %) and CO yield (<2 %) between x=0.17 and 0.25, suggest that this

anomaly may be due to experimental error. Errors involved with H_2 and CO yield are greater than those with H_2O production or CO_2 consumption as yields incorporate all sources of H_2 and CO, whereas H_2O production and CO_2 consumption rely purely upon the changes in H_2O or CO_2 concentration.

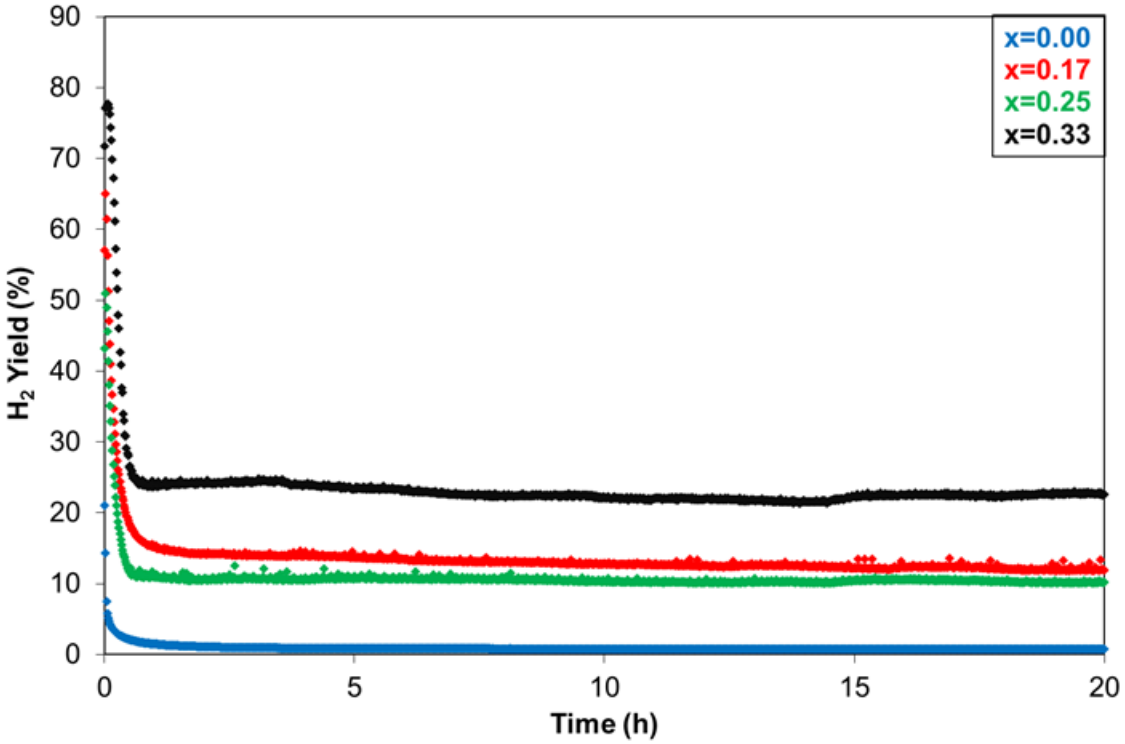

Figure 5.8: H_2 yield for reaction of CH_4 + 0.5CO_2 + xO_2 over Ni/YSZ at 600 °C for 20 hours (x=0.00, 0.17, 0.25, 0.33)

High stability is seen when x=0.25 in H_2 and CO yield over the 20 period, whereas when x=0.17 and x=0.33 there is a small reduction in yield with time. This is attributed to total oxidation occurring to a greater extent over time which can be seen in Figure 5.11 and Figure 5.12. For x=0.17, the increase in total oxidation over time may be due to carbon deposition, which can be seen in Figure 5.24, reducing the active catalyst surface area, therefore increasing the relative concentration of oxygen per available nickel site and potential for total oxidation. However, the lack of carbon deposition which occurs when x=0.33 dismisses this explanation. A possible cause for the increased total oxidation over time for x=0.33 may be a result of sintering. The high nickel content of the catalyst means there is a high potential for sintering at high temperatures. Sintering

of the catalyst would reduce the available surface area and increase the relative concentration of oxygen per nickel site. As variations are small, it may also be attributed to the reaction approaching a steady state.

In the absence of O_2, a small CO yield is exhibited (<5 %) despite almost no methane conversion and negligible H_2 yield (<1 %). This suggests that the reverse Boudouard reaction (Equation 5.3) to produce CO from deposited carbon is occurring. The very small H_2O production for x=0.00 suggests the reverse water gas shift reaction (Equation 5.4) may also be occurring. However, as the H_2O production is extremely low it may be insignificant.

$$C_{(s)} + CO_2 \rightleftharpoons 2CO \quad \textbf{(5.3)}$$

$$H_2 + CO_2 \rightleftharpoons CO + H_2O \quad \textbf{(5.4)}$$

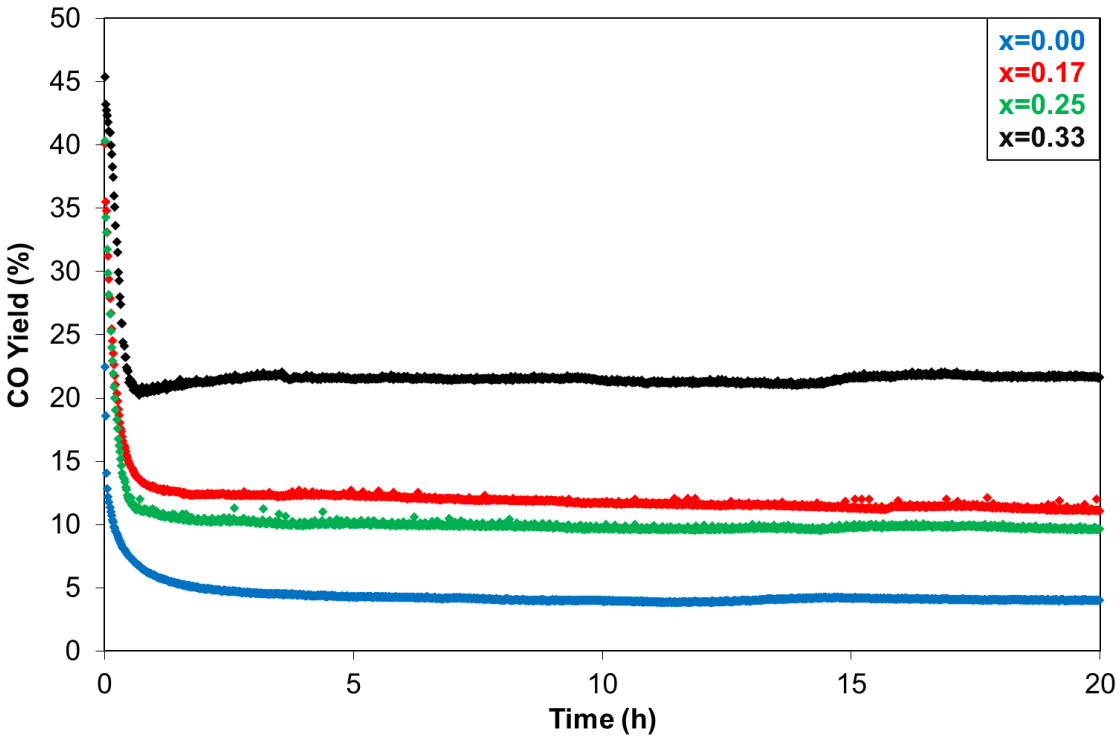

Figure 5.9: CO yield for reaction of CH_4 + 0.5CO_2 + xO_2 over Ni/YSZ at 600 °C for 20 hours (x=0.00, 0.17, 0.25, 0.33)

The H_2:CO product ratio increases upon the addition of oxygen to the CH_4:CO_2 mixture, as shown in Figure 5.10. This increase is primarily attributed to the complete lack of methane conversion in the absence of O_2 at 600 °C and the greater H_2:CO stoichiometry of the partial oxidation of methane (Equation 5.5) compared to the dry reforming of methane (Equation 5.6).

$$CH_4 + 1/2\,O_2 \rightarrow 2H_2 + CO \qquad \Delta H^{\theta}_{298} = -38\text{kJ mol}^{-1} \tag{5.5}$$

$$CH_4 + CO_2 \rightarrow 2H_2 + 2CO \qquad \Delta H^{\theta}_{298} = +247\text{kJ mol}^{-1} \tag{5.6}$$

The decreasing H_2:CO ratio over time when x=0.17 and x=0.25 can be attributed to a reduction in reforming activity coupled with the reverse Boudouard reaction (Equation 5.3) and reverse water gas shift reaction (Equation 5.4). When x=0.33, the decreasing H_2:CO is due to increased selectivity towards total oxidation over partial oxidation and the subsequent greater decrease in H_2 than CO due to the stoichiometry of the partial oxidation.

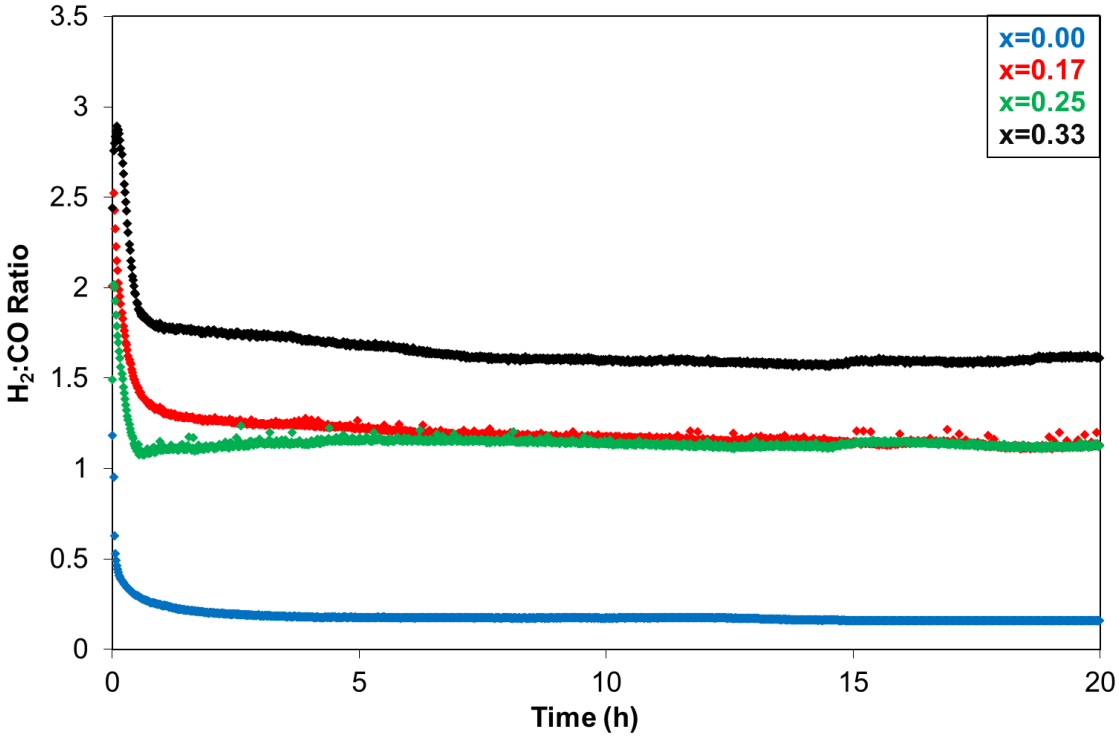

Figure 5.10: H_2:CO product ratio for reaction of CH_4 + 0.5CO_2 + xO_2 over Ni/YSZ at 600 °C for 20 hours (x=0.00, 0.17, 0.25, 0.33)

Through analysis of the CO_2 consumption and H_2O production, the extent to which total oxidation occurs can be assessed. This is an important parameter in assessing the activity of the catalyst, as has been seen earlier regarding H_2 and CO yield. The increasing extent of total oxidation when x=0.17 and 0.33 in particular has been attributed to carbon deposition and sintering respectively. A noticeable feature shown within the CO_2 consumption when x=0.00 is the increasing CO_2 consumption up to *ca.* 12 hours, followed by a sudden shift to decreasing CO_2 consumption up to the termination of the reaction. As this is not reflected through any other analysis, it is feasible to attribute this feature to a slight variation in flow of CO_2 through the reactor system.

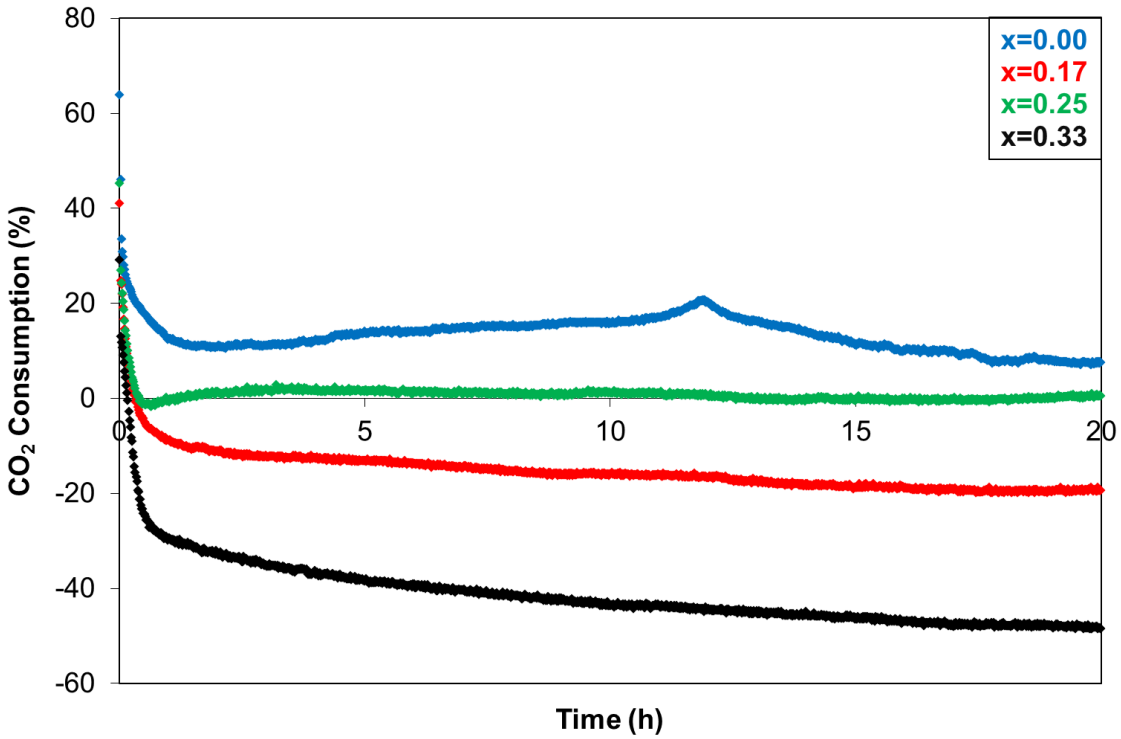

Figure 5.11: CO_2 consumption for reaction of CH_4 + 0.5CO_2 + xO_2 over Ni/YSZ at 600 °C for 20 hours.

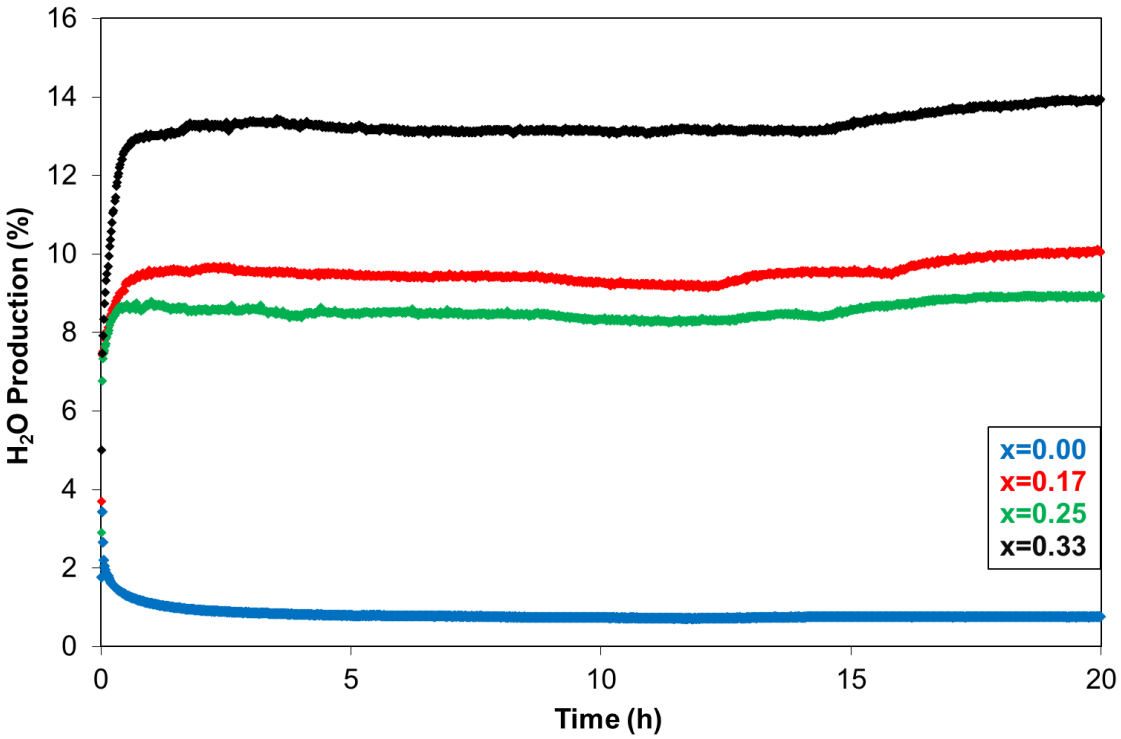

Figure 5.12: H_2O production for reaction of CH_4 + 0.5CO_2 + xO_2 over Ni/YSZ at 600 °C for 20 hours (x=0.00, 0.17, 0.25, 0.33)

5.3.2 Reaction of CH_4 + 0.5CO_2 + xO_2 over Ni/YSZ at 700 °C

At 700 °C, significant variation in reforming characteristics is seen compared to that at 600 °C. The addition of O_2 to the CH_4/CO_2 mixture results in a significant increase in methane conversion. Unlike at 600 °C however, significantly greater deactivation is observed over the 20 hour period for all O_2 levels, particularly x=0.33. This deactivation can also be seen in the corresponding H_2 and CO yield shown in Figure 5.13 and Figure 5.14 respectively.

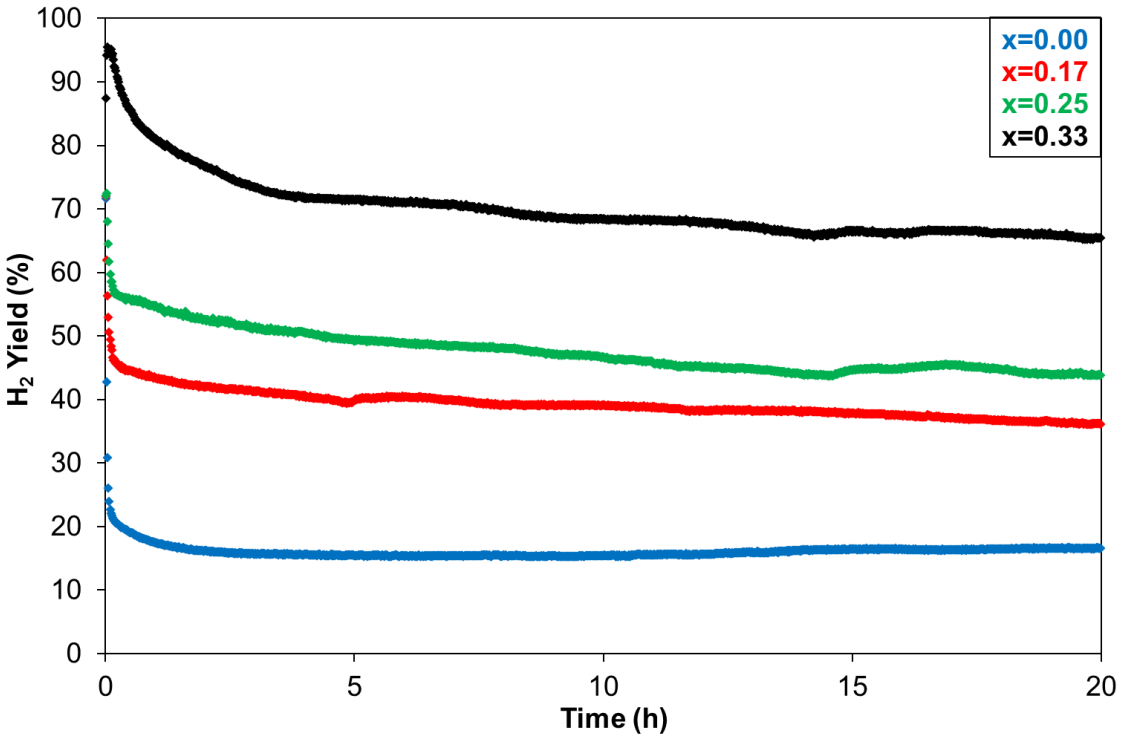

Figure 5.13: H_2 yield for reaction of $CH_4 + 0.5CO_2 + xO_2$ over Ni/YSZ at 700 °C for 20 hours (x=0.00, 0.17, 0.25, 0.33)

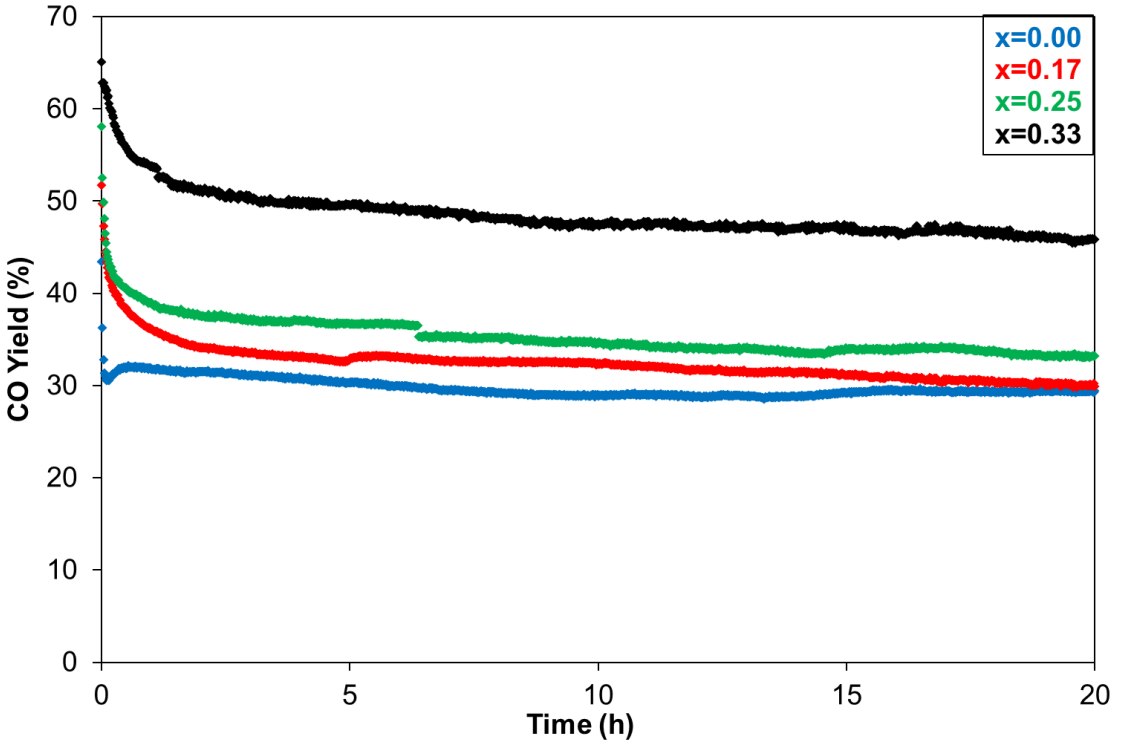

Figure 5.14: CO yield for reaction of $CH_4 + 0.5CO_2 + xO_2$ over Ni/YSZ at 700 °C for 20 hours (x=0.00, 0.17, 0.25, 0.33)

In the absence of O_2, a stable methane conversion and H_2 yield are seen together with a slight decrease (2 %) in CO yield. This may be attributed to a loss in reforming activity which is not manifested in the CH_4 conversion and H_2 yield due to an increased extent of methane decomposition (Equation 5.7). This explanation is supported by the reduction in CO_2 consumption shown in Figure 5.15, and the significant quantity of carbon deposition at this reaction temperature (Figure 5.24). Methane decomposition becomes thermodynamically favourable at temperatures above 700 °C, as shown in Figure 2.4.

$$CH_4 \rightarrow 2H_2 + C_{(s)} \quad \textbf{(5.7)}$$

The deactivation seen in the methane conversion and H_2 and CO yields for the reactions in the presence of oxygen can be attributed to an increase in the extent to which the total oxidation reaction (Equation 5.1) occurs. This can be seen in the decreasing CO_2 consumption and increasing H_2O yield in Figures 5.15 and 5.16 respectively. As may be expected, the increased concentration of oxygen favours increased potential towards total oxidation over partial oxidation.

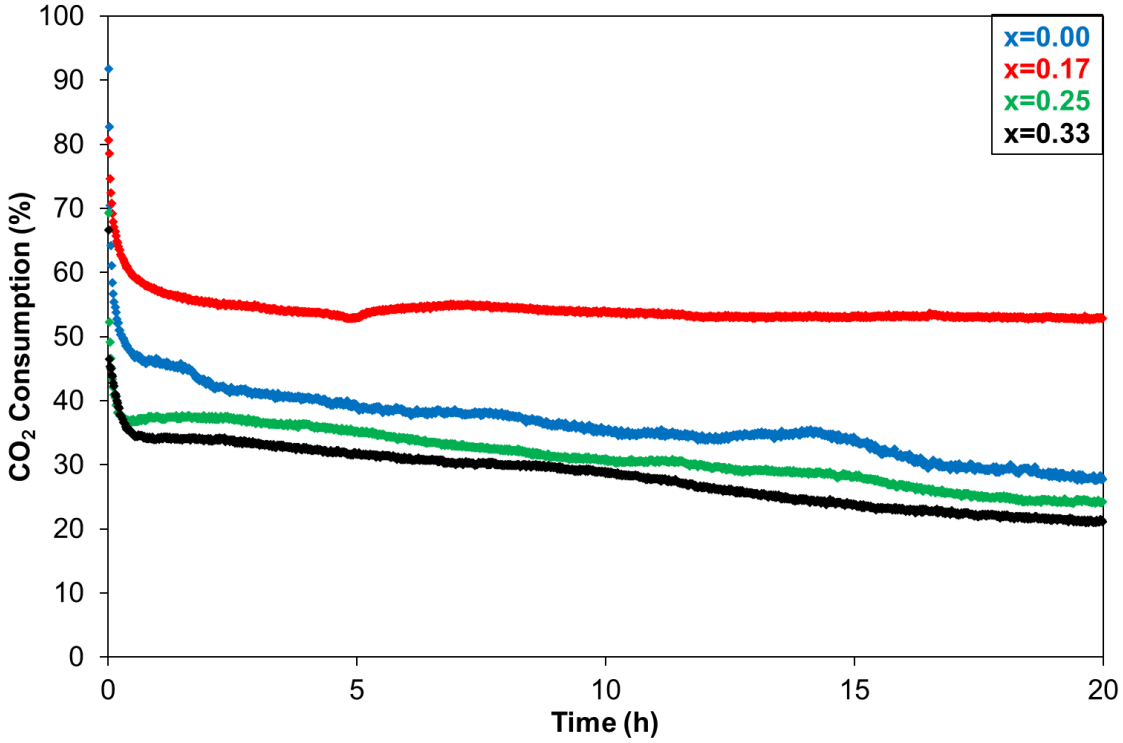

Figure 5.15: CO_2 consumption for reaction of CH_4 + 0.5CO_2 + xO_2 over Ni/YSZ at 700 °C for 20 hours (x=0.00, 0.17, 0.25, 0.33)

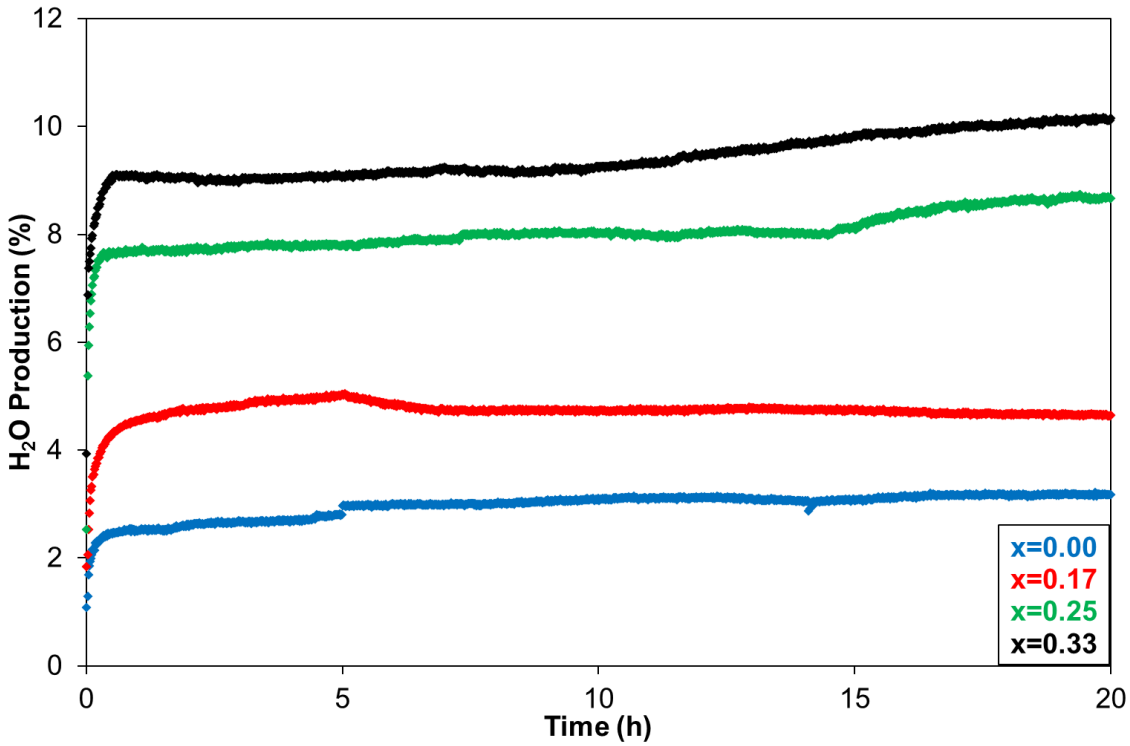

Figure 5.16: H_2O production for reaction of CH_4 + 0.5CO_2 + xO_2 over Ni/YSZ at 700 °C for 20 hours (x=0.00, 0.17, 0.25, 0.33)

As at 600 °C, the level of increase in activity upon addition of increasing quantities of oxygen is substantially greater for the H_2 yield than the CO yield, which can be attributed to the greater H_2:CO stoichiometry of the partial oxidation reaction compared to the dry reforming reaction.

The variations in H_2:CO product ratio are minor, with the H_2:CO ratio increasing with increased O_2 concentrations in a similar manner to that observed at 600 °C. This is again attributed to the occurrence of the reverse Boudouard reaction (Equation 5.3) and reverse water gas shift reaction (Equation 5.4).

5.3.3 Reaction of $CH_4 + 0.5CO_2 + xO_2$ over Ni/YSZ at 800 °C

The reaction data for the studies performed at 800 °C is shown in Table 5.1. Methane conversion follows the deactivation shown for the H_2 and CO yield and the H_2:CO ratio is highly stable (maximum variation of 0.101) for all added oxygen concentrations over the 20 hour reaction duration and are therefore excluded from the table. Values are taken after 5 hours on-line to ensure the initial saturation effect is not considered and after 20 hours to most accurately reflect the stability of the reaction.

Table 5.1: Reforming analysis for reaction of $CH_4 + CO_2 + xO_2$ (x=0.00, 0.17, 0.25, 0.33) over Ni/YSZ at 800 °C after 5 hours and 20 hours duration

	H_2 Yield (%)		CO Yield (%)		H_2O Production (%)		CO_2 Consumption (%)	
	Time (h)							
CH_4:xO_2	5	20	5	20	5	20	5	20
x=0.00	37.2	34.1	46.0	42.8	1.0	1.8	79.7	60.9
x=0.17	70.5	68.7	51.8	47.8	3.3	4.3	77.0	70.0
x=0.25	84.0	80.4	58.4	55.5	2.7	3.3	84.9	81.1
x=0.33	90.8	88.3	61.8	62.1	5.4	5.4	75.0	73.7

A small reduction in methane conversion, H_2 yield and CO yield over time is observed across all CH_4:xO_2 ratios. For the reactions in the presence of O_2, this slight reduction can be attributed to an increased extent of total oxidation, which is shown by an increasing H_2O production and decreasing CO_2 consumption. The deactivation observed in the absence of O_2 can be attributed to carbon deposition, which is confirmed by the substantial quantity of carbon detected during the post-reaction temperature programmed oxidation (Figure 5.24). The carbon deposition seen is also expected from the H_2:CO ratio as a H_2:CO ratio of greater than 1 suggests that methane decomposition is occurring. Methane decomposition is likely to be the main contributing reaction towards the deposition of carbon at this temperature and high CO_2 concentration.

The substantially greater decrease in CO_2 consumption compared with the CO yield for the reaction in the absence of O_2 suggests that the reverse Boudouard reaction (Equation 5.3) is occurring to an extent. This is consistent with the thermodynamic potential for this reaction to occur at temperatures above 700 °C shown in Figure 2.4, and also the high quantity of carbon present on the catalyst surface.

5.3.4 Reaction of $CH_4 + 0.5CO_2 + xO_2$ over Ni/YSZ at 900 °C

As for 800 °C, CH_4 conversion and H_2:CO product ratio are excluded from the table below for the reasons discussed previously. From Table 5.2, it can be seen that the reaction in the absence of oxygen shows greater stability compared to reactions carried out with the addition of oxygen. In addition to the greater stability, increases in H_2 and CO yields are also seen, whereas the reactions in the presence of oxygen exhibit deactivation with time. The increased H_2 yield (*ca*.5 %) and CO (*ca*.2 %) yield with a stable methane conversion coupled with a decrease in CO_2 (*ca*.10 %) conversion suggests that methane decomposition and the reverse Boudouard reaction are occurring to a greater extent as reaction duration increases. This is supported by the high level of carbon deposition observed for this reaction as shown in Figure 5.24. Also, the H_2:CO ratio of 1.5 for this

reaction suggests that methane decomposition is occurring as the product stoichiometry of the dry reforming reaction is 1.

Table 5.2: Reforming analysis for reaction of $CH_4 + CO_2 + xO_2$ (x=0.00, 0.17, 0.25, 0.33) over Ni/YSZ at 900 °C after 5 hours and 20 hours duration.

	H_2 Yield (%)		CO Yield (%)		H_2O Production (%)		CO_2 Consumption (%)	
	Time (h)							
CH_4:xO_2	5	20	5	20	5	20	5	20
x=0.00	38.4	43.6	40.5	42.1	0.0	0.0	100.0	90.1
x=0.17	86.6	67.9	56.9	47.4	6.8	12.9	94.3	77.9
x=0.25	112.0	98.8	73.0	67.0	0.7	2.6	97.8	88.0
x=0.33	77.6	71.3	54.3	48.6	6.4	7.3	78.8	73.9

At x=0.17 and 0.25, a substantial decrease in methane conversion, H_2 yield and CO yield is seen over the reaction duration. This can again be attributed to increased selectivity towards total oxidation of methane over partial oxidation, which can also be seen by the decreasing CO_2 consumption and increasing H_2O yield. Similar behaviour is observed for x=0.33, however less deactivation occurs due to the greater quantity of total oxidation occurring at the start of the reaction. The H_2 yield of >100 % for x=0.25 may be caused by a variation in sensitivity that is a particularly issue for H_2 due to the low H_2 sensitivity of the equipment.

5.3.5 Reaction of $CH_4 + 0.5CO_2 + xO_2$ over Ni/YSZ at 1000 °C

The reactions carried out at 1000 °C in the presence of O_2 show similar high stability to those carried out at 800 °C and 900 °C, as shown in Figure 5.17 and Table 5.3. In the absence of O_2, the reaction profile shows a significant feature at *ca.* 9 hours. This feature is due to the physical blocking of the reactor tube which is caused by a build-up of deposited carbon. This blockage

restricts gas flow through the reactor and therefore any data derived from experiments where this occurs is not accurate and, as such, are not included. The extent of carbon deposition is shown in Figure 5.24.

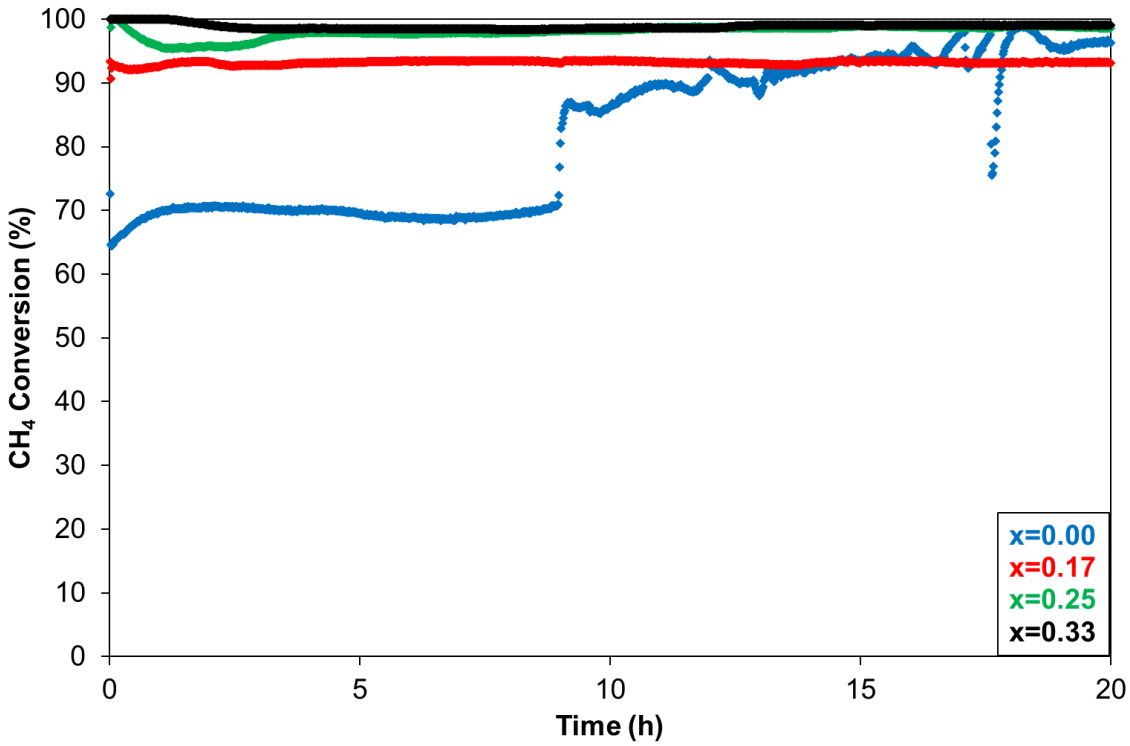

Figure 5.17: CH_4 conversion for reaction of CH_4 + 0.5CO_2 + xO_2 over Ni/YSZ at 1000 °C for 20 hours (x=0.00, 0.17, 0.25, 0.33)

For reactions with greater O_2 levels (x=0.25 and 0.33), insignificant variations (<2 %) in reforming characteristics with time are seen, whereas when x=0.17, greater variations are present. High stability is seen for the reactions when x=0.25 and x=0.33 as no carbon deposition is seen to occur (Figure 5.24) , due to a lack of unreformed methane available to decompose. Also, unlike at lower temperatures, the increased rate at which the catalytic reactions occur at this temperature would mean that any sintering and resulting loss in surface area would have substantially less effect upon performance.

The slightly greater variation shown when x=0.17 can be attributed to a greater tendency to undergo methane decomposition and carbon formation. The stability in CH_4 conversion, slight

increase in H_2 yield (*ca.*3 %) and decrease in CO yield (*ca.*3 %) coupled with a stable H_2O production, CO_2 consumption and high quantity of deposited carbon present for this reaction all suggest an increasing extent of methane decomposition occurring with time. This is attributed to the deposition of carbon reducing the active catalyst surface area, resulting in an increase in unreformed methane available to decompose. Carbon deposition is expected at this temperature and carbon:oxygen ratio due to the lack of sufficient reformant for the quantity of methane.

Table 5.3: Reforming analysis for $CH_4 + CO_2 + xO_2$ (x=0.17, 0.25, 0.33) reaction at 5 hours and 20 hours duration at 1000 °C.

	H_2 Yield (%)		**CO Yield (%)**		**H_2O Production (%)**		**CO_2 Consumption (%)**	
	Time (h)							
CH_4:xO_2	**5**	**20**	**5**	**20**	**5**	**20**	**5**	**20**
x=0.17	113.3	116.1	62.5	59.6	0.0	0.0	100.0	99.6
x=0.25	110.5	111.8	72.2	71.0	1.0	1.4	97.2	96.2
x=0.33	85.4	86.6	60.0	59.6	7.3	7.5	80.1	80.0

5.3.6 Influence of isothermal reaction temperature for reaction of $CH_4 + 0.5CO_2 + xO_2$ over Ni/YSZ using average comparisons

Averages are taken as a mean value from 2 hours to 20 hours on-line to ensure that any initial saturation effects that are uncharacteristic of the overall reaction are not considered. Despite the variations with time discussed previously, mean averages are considered as the most effective and accessible approach for analysing the influence of O_2 addition at different reaction temperatures. These average comparisons are shown in Figures 5.18 – 5.23.

As expected for all reactions with or without oxygen addition, increasing reaction temperature results in substantially greater methane conversion (Figure 5.18), due to the increase in reaction kinetics and increased thermodynamic favourability for the dry reforming and methane

decomposition reactions. This is particularly evident for the reaction in the absence of O_2 where an almost linear increase in methane conversion is seen with increasing reaction temperature.

The addition of O_2 to the CH_4:CO_2 mixture results in a substantial increase in methane conversion (Figure 5.18) as is also reported by Ruckenstein and Hu [4] and Gao *et al.*[7]. This behaviour has been attributed to the increased availability of reformant. With the addition of O_2, a different trend is observed compared to that in the absence of O_2, in that the extent of increase in conversion decreases with increasing reaction temperature. This is due to the methane-limited nature of the reaction at high temperatures. As discussed in Section 5.2.5, the average taken for the dry reforming reaction at 1000 °C is representative only from 2 hours to 8.5 hours due to the physical blockage that occurred at *ca.* 9 hours as a result of carbon deposition and consequently should be treated with caution.

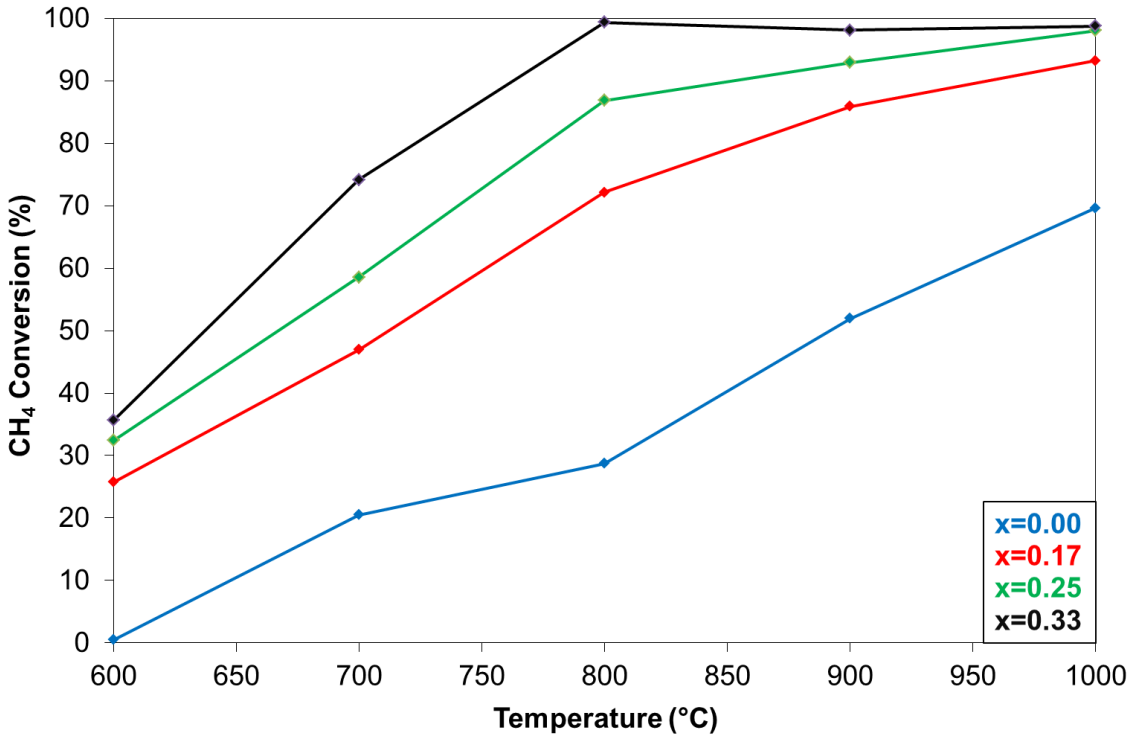

Figure 5.18: Average CH_4 conversion for reaction of CH_4 + 0.5CO_2 + xO_2 over Ni/YSZ for 20 hours across the temperature range of 600-1000 °C (x=0.00, 0.17, 0.25, 0.33)

Despite the overall similarity between the methane conversion (Figure 5.18) and H_2 yield (Figure 5.19), substantial variations are also present, in that above 800 °C the reaction with x=0.33 shows a

lower H_2 yield than the reactions with x=0.17 and 0.25, whereas methane conversion is greater with x=0.33. This is also reflected within the variation in CO yield with reaction temperature (Figure 5.20). This behaviour may be attributed to an increase in the total oxidation of methane above 800 °C or an increase in the oxidation of H_2 and CO to H_2O and CO_2 respectively. An increase in the reverse water gas shift reaction (Equation 5.4) is unlikely as this would result in decreased H_2 yield and not CO yield. The increases in H_2 yield and CO yield with x=0.33 between 900 °C and 1000 °C may be due to increased CH_4 decomposition to increase H_2 yield and the carbon deposited inducing the reverse Boudouard reaction to increase CO yield .

The substantial increase (+32.1%) in H_2 yield for x=0.17 upon increasing the temperature between 900 °C and 1000 °C suggests increased methane decomposition (Equation 5.7), which is consistent with the much smaller increase in CO yield (+5.57), and also the extent of carbon deposition, as seen in Figure 5.24. The H_2:CO ratio of greater than 2 also suggests the occurrence of methane decomposition. The less significant increase in total oxidation products also (Figure 5.21 and 5.22) suggests increased methane decomposition. The high H_2O production for x=0.17 at 900 °C (Figure 5.21) is against the trend seen for other temperatures and oxygen levels. Therefore, the possibility of it being an erroneous value should be considered.

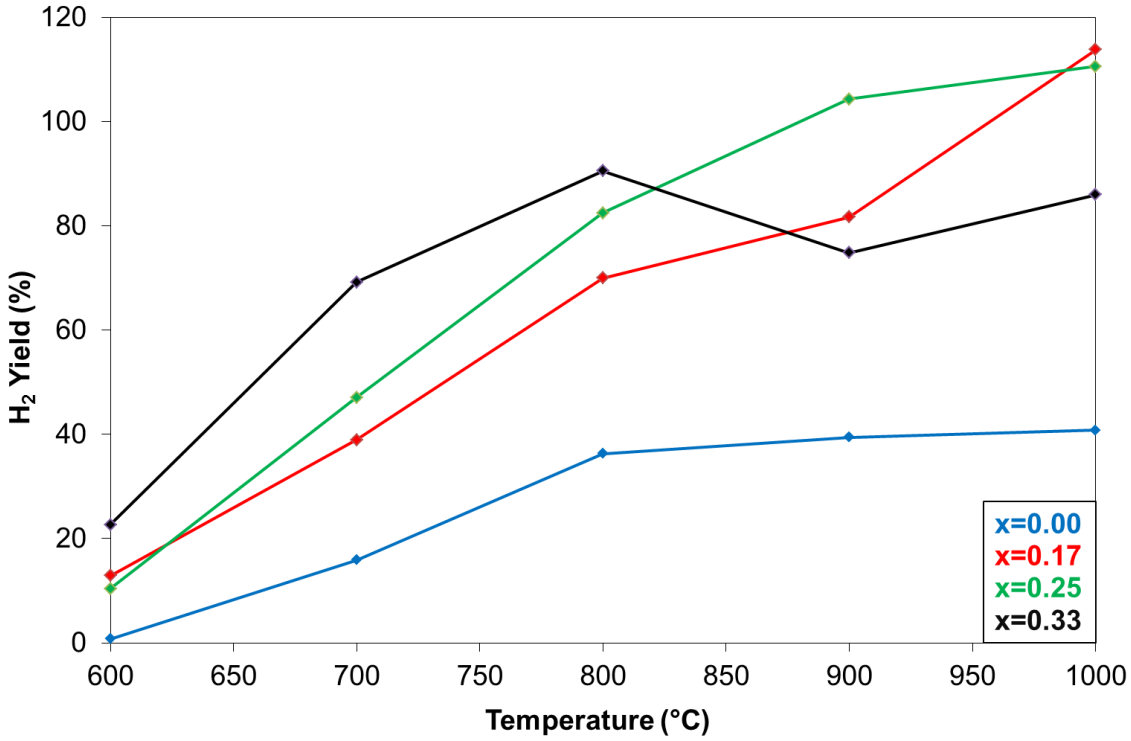

Figure 5.19: Average H_2 yield for reaction of CH_4 + 0.5CO_2 + xO_2 over Ni/YSZ for 20 hours across temperature range of 600-1000 °C (x=0.00, 0.17, 0.25, 0.33)

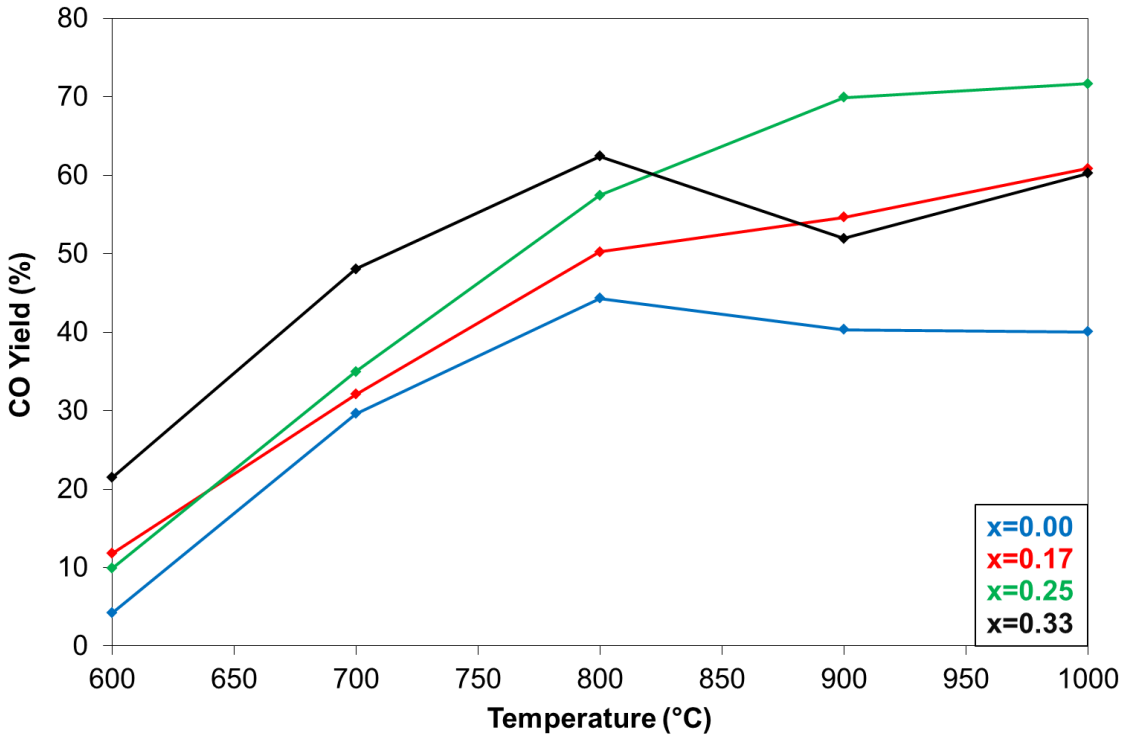

Figure 5.20: Average CO yield for reaction of CH_4 + 0.5CO_2 + xO_2 over Ni/YSZ for 20 hours across the temperature range of 600-1000 °C (x=0.00, 0.17, 0.25, 0.33)

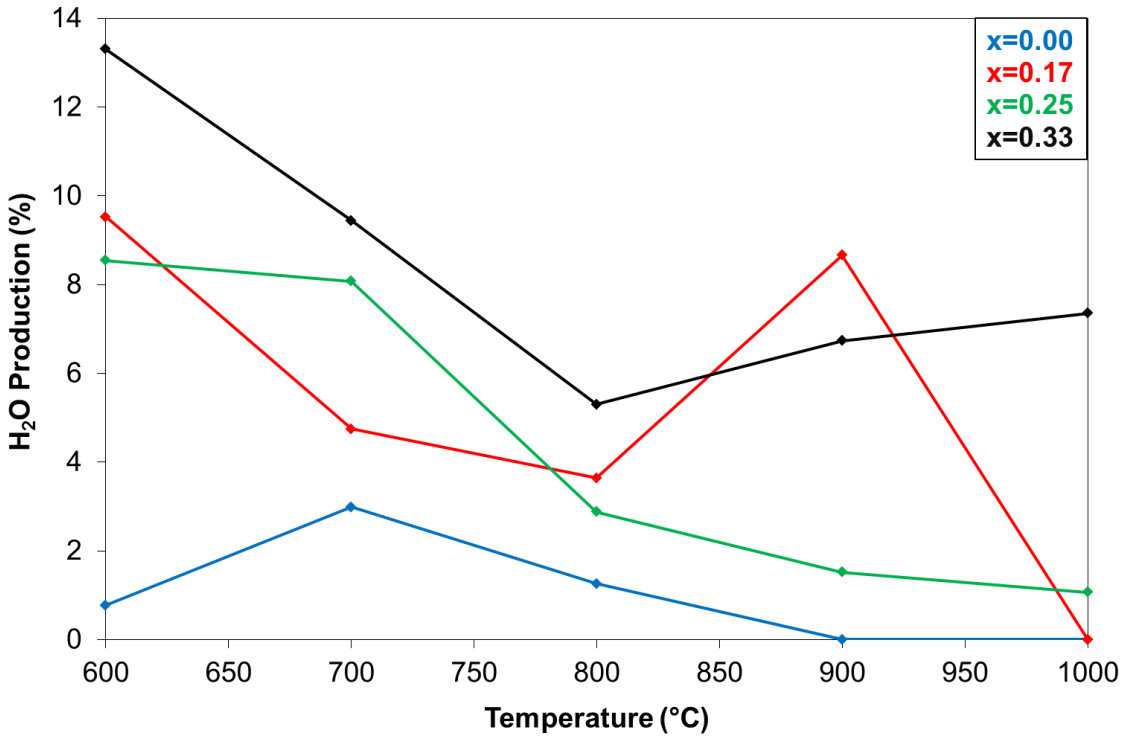

Figure 5.21: Average H_2O production for reaction of CH_4 + 0.5CO_2 + xO_2 over Ni/YSZ for 20 hours across temperatures range of 600-1000 °C (x=0.00, 0.17, 0.25, 0.33)

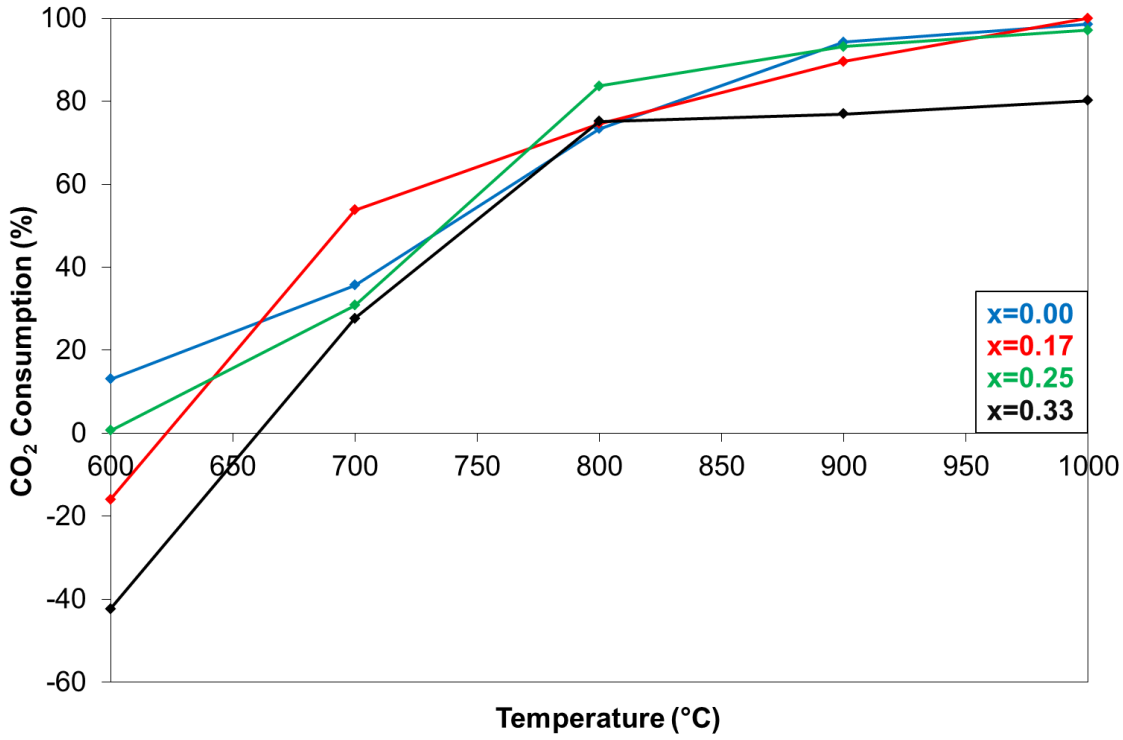

Figure 5.22: Average CO_2 consumption for reaction of CH_4 + 0.5CO_2 + xO_2 over Ni/YSZ for 20 hours across the temperatures range of 600-1000 °C (x=0.00, 0.17, 0.25, 0.33)

The addition of O_2 to the CH_4:CO_2 mixture results in a substantial increase in the H_2:CO product ratio, and the increase observed upon O_2 addition reduces with temperature (Figure 5.23). The increases in H_2:CO ratio can be attributed to the greater H_2:CO product stoichiometry of the partial oxidation reaction (Equation 5.5) compared to the dry reforming reaction (Equation 5.6). The smaller increase with temperature upon oxygen addition is due to the increased reforming activity of the dry reforming reaction with temperature coupled with the reduced thermodynamic potential for the partial oxidation reaction and also the increased thermodynamic potential for methane decomposition, as shown in Figure 2.4.

The influence of oxygen concentration on the H_2:CO product ratio seen in Figure 5.23 shows opposing effects below and above 800 °C in that below 800 °C, increasing O_2 concentration leads to an increased H_2:CO ratio, whereas the opposite is seen above 800 °C. The effect below

800 °C is attributed to the greater extent of partial oxidation occurring and the significantly greater H_2:CO stoichiometry of the partial oxidation reaction. This effect decreases with increasing reaction temperature as the extent to which the dry reforming reaction occurs increases. The greater H_2:CO ratio above 800 °C with lesser concentrations of oxygen is attributed to an increased extent of methane decomposition. The decreasing H_2:CO ratio for x=0.33 above 800 °C (illustrated in Figure 5.23) is similar to the work published by Choudhary *et al.* [8], using oxidative CO_2 reforming with excess O_2.

A discussed in Section 2.3.7, the ability to tailor the H_2:CO product ratio of a methane reforming reaction is highly desirable due to the different H_2:CO ratios required by different applications. Figure 5.23 illustrates the potential to tailor the H_2:CO ratio through variations in O_2 concentration and reaction temperature. The ability to tailor H_2:CO ratio through reaction temperature and O_2 concentration has also been studied by Guo *et al.* [9] in a fluidized bed system.

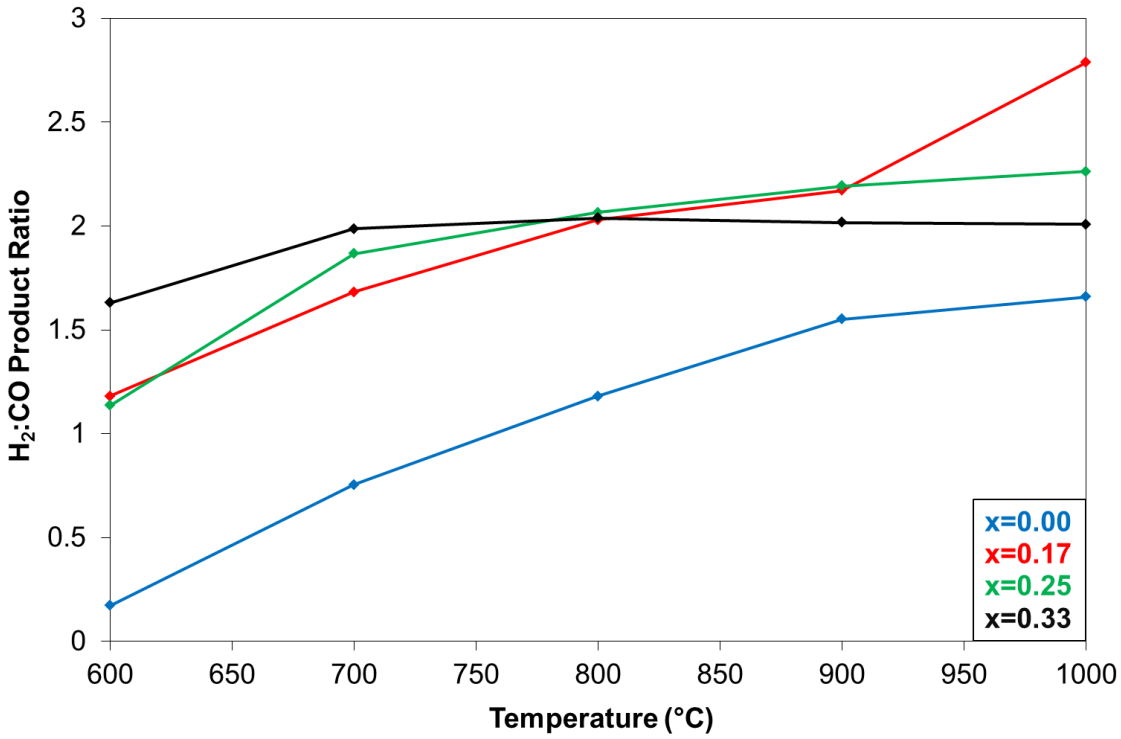

Figure 5.23: Average H_2:CO product ratio for reaction of CH_4 + 0.5CO_2 + xO_2 over Ni/YSZ for 20 hours across the temperatures range of 600-1000 °C (x=0.00, 0.17, 0.25, 0.33)

5.3.7 Carbon deposition during reaction of CH_4 + 0.5O_2 +xO_2 over Ni/YSZ as a factor of reaction temperature and O_2 concentration

The deposition of carbon onto the catalyst surface during the reforming reaction is one of the primary methods of catalyst deactivation which are discussed in Section 2.6.2. Post-reaction temperature programmed oxidation described in detail in Section 3.6 enables for the extent to which carbon was deposited in the reactor and over the catalyst material during the 20 hour reactions to be estimated. For those reactions in which an excess of 30 mg carbon was deposited, incomplete combustion of carbon occurred in which all oxygen was consumed, and is illustrated with an arrowhead in Figure 5.24. This behaviour is discussed in greater detail in Section 3.6.

From Figure 5.24 it is apparent that the addition of O_2 to the CH_4:CO_2 mixture significantly reduces the extent of carbon deposition, and that increasing the O_2 concentration results in a further reduction in carbon deposition. This is due to a reduction in the extent of methane available to decompose, an increased availability of CO_2 to induce the reverse Boudouard reaction to remove surface carbon and an increased potential for oxidation of any carbon deposited during the reaction. This is consistent with the findings of O'Connor and Ross [1].

For the reaction in the absence of O_2, the mass of carbon deposited increases substantially with temperature. This is attributed to an increase in methane decomposition and also a decrease in the availability of CO_2 to induce the reverse Boudouard reaction and remove carbon. Carbon formed at lower temperatures (≤700 °C) is likely to be produced though the Boudouard reaction, whereas at higher temperatures (≥700 °C), carbon can primarily be attributed to methane decomposition. This is illustrated by the thermodynamic potentials shown in Figure 2.4. When x=0.17 and 0.25, small quantities of carbon (<2 mg) are produced at 600 and 700 °C through the Boudouard reaction. Substantial carbon (>30 mg) is deposited for x=0.17 at 1000 °C via methane decomposition which occurs at this oxygen concentration due to the availability of unreformed methane. The lack of carbon deposition observed for x=0.17 at 800 and 900 °C is unexpected when compared to the significant carbon deposition seen at 1000 °C. One potential cause for this may be a slight error in the experiments and therefore the carbon deposition should be viewed with caution.

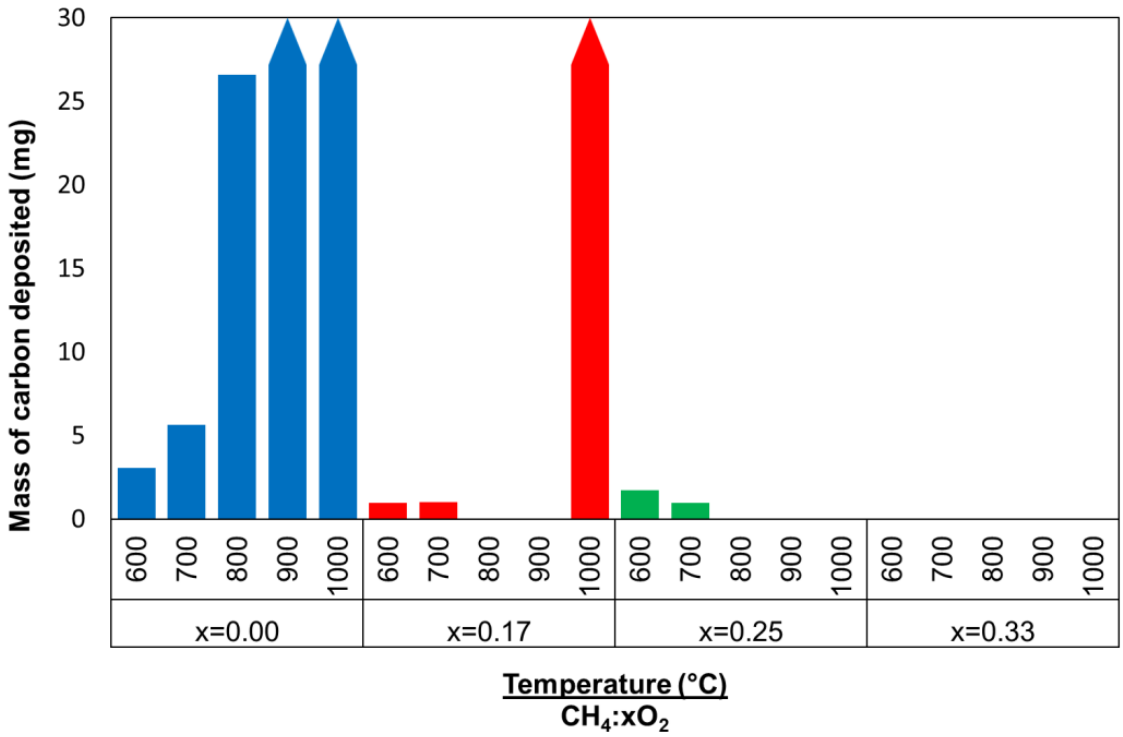

Figure 5.24: Mass of carbon deposited during 20 hour isothermal reaction of CH_4 + 0.5CO_2 + xO_2 at temperatures between 600 – 1000 °C. Carbon masses measured through post-reaction temperature programmed oxidation and limited to 30 mg of carbon deposited. An arrowhead is used in the figure to illustrate where mass of carbon exceeds 30 mg.

The determination of the nature of the carbon deposits by temperature programmed oxidation is limited. The varying mass of carbon can mask information that may be present regarding separate carbon oxidation peaks. This is illustrated in the post-reaction temperature programmed oxidation profiles from the reactions in the absence of O_2, which are shown in Figure 5.25. Despite this masking effect, evident particularly for the reactions at 900 °C and 1000 °C, a slight trend is visible in that the major peak temperature increases as the reaction temperature increases. This may be explained by the source of the carbon affecting its stability [10] or purely by the temperature at which the carbon deposit was formed affecting its stability. Similar behaviour has been published by numerous research groups including He and Hill [11], Baker and Metcalfe [12] and this research group [13-15] which was attributed to the thermal aging of carbon deposits.

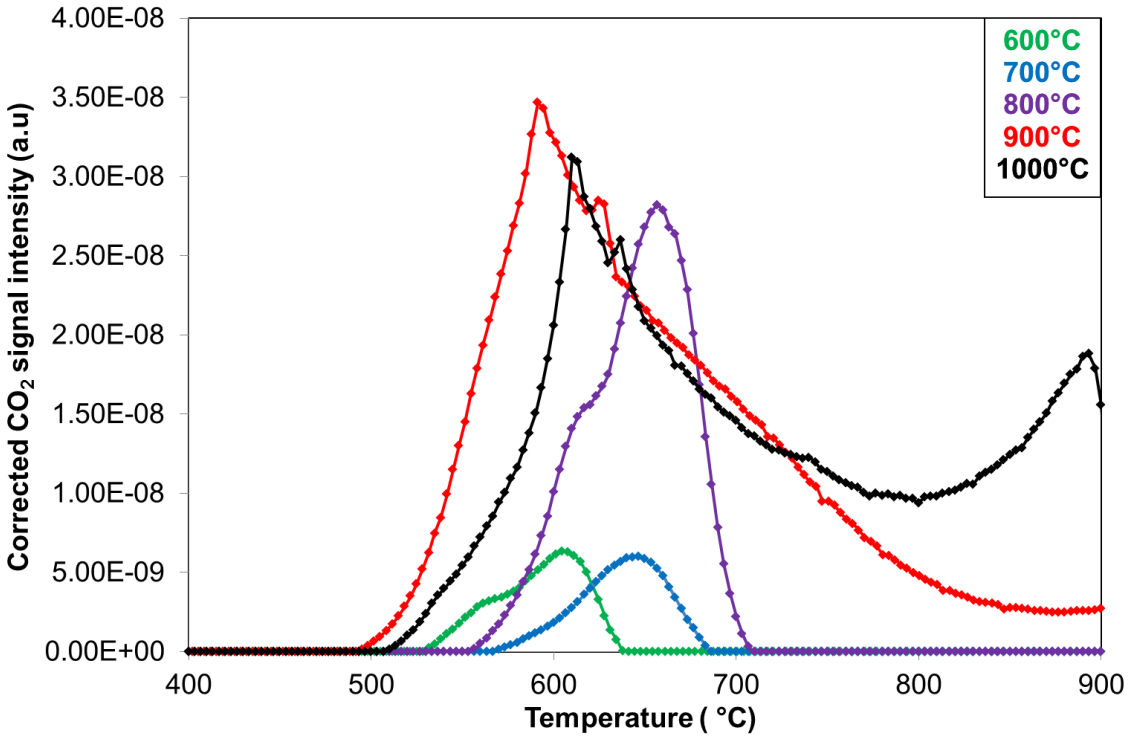

Figure 5.25: Temperature programmed oxidation profiles showing CO_2 generation from oxidation of carbon deposited during reaction of CH_4 + 0.5CO_2 over Ni/YSZ for 20 hours at temperatures between 600 – 1000 °C.

One useful feature of temperature programmed oxidation analysis is the ability to distinguish different carbon species by the temperature at which they are oxidized from the catalyst surface. This is illustrated in Figure 5.26, where potentially two carbon species are visible in the temperature programmed oxidation profile. The multiple peaks within temperature programmed oxidation studies may be caused by a difference in carbon morphology or location of carbon. The location of carbon is more plausible than differences in carbon morphology due to the relatively small difference in stability between carbon species. Also, carbon morphologies formed at higher temperatures have been suggested to exhibit less thermal stability [12, 16]. More accessible carbon is likely to be oxidized at a lower temperature than less accessible carbon, whilst carbon deposited on the support material is likely to be oxidized at a lower temperature than that deposited on the nickel surface due to a weaker interaction between the support and deposited carbon [17]. The

greater reduction temperature suggests that the respective nickel form has a greater activation energy.

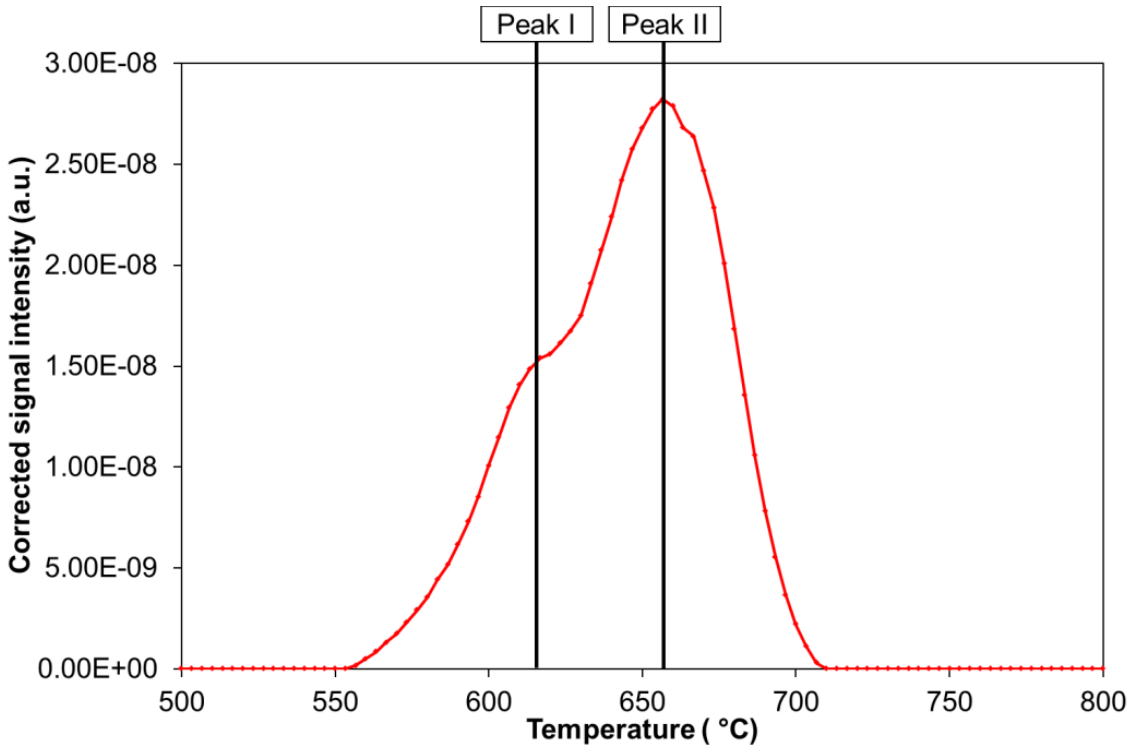

Figure 5.26: Temperature programmed oxidation profile showing CO_2 generation from oxidation of carbon deposited during reaction of CH_4 + 0.5CO_2 over Ni/YSZ at 800 °C for 20 hours

From the analysis of the reactions with time shown in Sections 5.2.1 – 5.2.5, particularly those in which substantial carbon deposition occurs, it is apparent that the extent of deactivation through carbon deposition is relatively small unless physical blocking occurs. This relatively small deactivation suggests that the morphology of carbon deposited is primarily amorphous or filamentous carbon and not encapsulating [18]. The different carbon morphologies and the extent to which they induce deactivation are discussed in detail in Section 2.6.2.1.

5.4 Summary of catalytic behaviour for $CH_4 + 0.5CO_2 + xO_2$ reactions over Ni/YSZ with both temperature programmed and isothermal studies

Within this chapter, the influence of oxygen addition in varied quantities to CH_4:CO_2 biogas simulated mixture on the reforming characteristics has been studied and discussed using information provided through temperature programmed and conventional catalytic methods.

A temperature programmed reaction profile has been obtained across a range of oxygen concentrations. It has been seen that the presence of O_2 within the CH_4:CO_2 mixture results in a light-off feature, whilst increasing O_2 concentration delays the point at which this light off occurs. This is due to the increased selectivity towards total oxidation with increased O_2 addition. The addition of O_2 results in a substantial increase in reforming activity, however when x=0.33, the occurrence of total oxidation is more prevalent and results in a reduced H_2 and CO yield.

Conventional isothermal studies carried out across a range of reaction temperatures have provided an insight into the stability of the catalyst with time and the reforming characteristics at specific temperatures. Relative stability is seen across all reaction temperatures and oxygen concentrations, with the exceptions of when x=0.17 and 0.25 at 900 °C, which became more selective towards total oxidation of methane, which has been attributed to sintering. Dry reforming at 1000 °C showed high instability, as carbon deposition caused mechanical deactivation through reactor blockage.

Similar behaviour is observed to the temperature programmed studies in that the addition of O_2 significantly increases the reforming activity. However, the extent of enhanced reforming activity lessens with increasing temperature due to the increased potential for the dry reforming and methane decomposition reactions. Increasing O_2 concentration further enhances reforming activity, however this increase lessens with reaction temperature as the reaction becomes methane limited at high temperatures.

The addition of O_2 also increases the H_2:CO product ratio substantially due to the greater H_2:CO product stoichiometry of the partial oxidation reaction compared to the dry reforming reaction. The

influence of O_2 on reaction selectivity across the temperature range varies; at lower reaction temperatures greater H_2:CO ratio is seen with increased O_2 levels, whereas the opposite is seen at higher reaction temperatures. This is attributed to the increased potential for total oxidation with greater O_2 concentrations and greater methane decomposition potential at lower O_2 concentrations.

The ability to tailor the H_2:CO ratio is a very significant finding in that it offers the capacity for the process to be applied to industry requirements, therefore becoming more economically viable as an approach synthesis gas production.

5.5 References

1. A.M. O'Connor and J.R.H. Ross, *The effect of O_2 addition on the carbon dioxide reforming of methane over Pt/ZrO_2 catalysts.* Catalysis Today, 1998. **46**(2-3): p. 203-210.
2. C.S. Lau, A. Tsolakis, and M.L. Wyszynski, *Biogas upgrade to syn-gas (H_2-CO) via dry and oxidative reforming.* International Journal of Hydrogen Energy, 2011. **36**(1): p. 397-404.
3. A.T. Ashcroft, A.K. Cheetham, M.L.H. Green, and P.D.F. Vernon, *Partial oxidation of methane to synthesis gas using carbon dioxide.* Nature, 1991. **352**: p. 225-226.
4. E. Ruckenstein and Y.H. Hu, *Combination of CO_2 reforming and partial oxidation of methane over NiO/MgO solid solution catalysts.* Industrial & Engineering Chemistry Research, 1998. **37**(5): p. 1744-1747.
5. S. Eriksson, S. Rojas, M. Boutonnet, and J.L.G. Fierro, *Effect of Ce-doping on Rh/ZrO_2 catalysts for partial oxidation of methane.* Applied Catalysis A: General, 2007. **326**(1): p. 8-16.
6. D.R. Lide, ed. *CRC Handbook of Chemistry and Physics*. 76th ed. 1995: Chapter 5.
7. J. Gao, J. Guo, D. Liang, Z. Hou, J. Fei, and X. Zheng, *Production of syngas via authothermal reforming of methane in a fluidized-bed reactor over a combined CeO_2-ZrO_2/SiO_2 supported Ni catalysts.* Int. J. Hydrogen Energy, 2008. **33**: p. 5493-5500.
8. V.R. Choudhary, K.C. Mondal, and T.V. Choudhary, *Oxy-CO_2 reforming of methane to syngas over CoO_x/MgO/SA-5205 catalyst.* Fuel, 2006. **85**: p. 2484-2488.
9. J. Guo, Z. Hou, J. Gao, and X. Zheng, *Syngas production via combined oxy-CO_2 reforming of methane over Gd_2O_3-modified Ni/SiO_2 catalysts in a fluidized-bed reactor.* Fuel, 2008. **87**(7): p. 1348-1354.
10. N.C. Triantafyllopoulos and S.G. Neophytides, *The nature and binding strength of carbon adspecies formed during the equilibrium dissociative adsorption of CH_4 on Ni-YSZ cermet catalysts.* Journal of Catalysis, 2003. **217**(2): p. 324-333.

11. H. He and J.M. Hill, *Carbon deposition on Ni/YSZ composites exposed to humidified methane.* Applied Catalysis A: General, 2007. **317**(2): p. 284-292.

12. R.T. Baker and I.S. Metcalfe, *Study of the Activity and deactivation of Ni-YSZ cermet in dry CH_4 using temperature programmed techniques.* Ind. Eng. Chem. Res., 1995. **34**: p. 1558-1565.

13. C.M. Finnerty, N.J. Coe, R.H. Cunningham, and R.M. Ormerod, *Carbon formation on and deactivation of nickel-based/zirconia anodes in solid oxide fuel cells running on methane*. Catalysis Today, 1998. **46**(2-3): p. 137-145.

14. C.M. Finnerty, R.H. Cunningham, and R.M. Ormerod, *In situ catalytic and electrocatalytic studies of internal reforming in solid oxide fuel cells running on natural gas.* Studies in Surface Science and Catalysis, 2000. **130**: p. 425-430.

15. C.M. Finnerty and R.M. Ormerod, *Internal reforming over nickel/zirconia anodes in SOFC operating on methane: influence of anode formulation, pre-treatment and operating conditions.* Journal of Power Sources, 2000. **86**: p. 390-394.

16. C.H. Bartholomew, *Mechanisms of catalyst deactivation.* Applied Catalysis A: General, 2001. **212**(1-2): p. 17-60.

17. J.-H. Koh, Y.-S. Yoo, J.-W. Park, and H.C. Lim, *Carbon deposition and cell performance of Ni-YSZ anode support SOFC with methane fuel.* Solid State Ionics, 2002. **149**(3-4): p. 157-166.

18. G. Italiano, C. Espro, F. Arena, F. Frusteri, and A. Parmaliana, *Catalytic decomposition of natural gas for CO_x-free hydrogen production in a structured multilayer reactor.* Applied Catalysis A: General, 2009. **357**(1): p. 58-65.

6 Influence of 5 mol% CeO_2 addition to Ni/YSZ on CO_2 reforming of CH_4 with and without O_2 addition

Within this chapter, the temperature programmed and conventional catalytic studies of CO_2 reforming of CH_4 with and without the addition of O_2 in varied concentrations have been conducted over 5 mol% Ceria-doped Ni/YSZ. The behaviour of the 5 mol% Ceria-doped Ni/YSZ is compared to that of undoped Ni/YSZ under equivalent conditions.

6.1 Cerium (IV) Oxide (Ceria, CeO_2)

One approach for enhancing the activity, selectivity and stability of catalyst materials is through the addition of dopants. Ceria is used extensively as a dopant within catalytic applications. Cerium is the most abundant lanthanide and is found in numerous minerals such as bastnasite, monazite and loparite [1, 2]. Cerium has an electronic configuration of [Xe] $4f^2 6s^2$ and can easily achieve 3+ and 4+ oxidation states, whilst the 2+ oxidation state is rare. The multiple oxidation states of Ce allows for the oxide of cerium to shift between Ce_2O_3 with Ce in the 3+ oxidation state and CeO_2 with Ce in the 4+ oxidation state.

CeO_2 has a cubic fluorite structure with a face centred cubic unit cell and upon reduction, develops both ionic and electronic conductivity through the formation of defects. The structure of CeO_2 is such that the oxygen atoms between unit cells are positioned within a plane. As CeO_2 is reduced, an oxygen vacancy is formed which allows for oxygen ions to move between unit cells and provide ionic conductivity. Reduction of CeO_2 results in Ce changing oxidation state from 4+ to 3+ and the resulting electron emission provides the basis for electronic conductivity. This therefore classifies reduced CeO_2 as an n-type semiconductor.

The mixed electronic and ionic conductivity of CeO_2 is highly desirable within catalysis and particularly as an anode material within solid oxide fuel cells (SOFC's). The ionic conductivity is

also advantageous as it can actively distribute oxygen throughout the catalyst. The ability of Ce to move between oxidation states allows it to act as an oxygen sink to maintain a more continuous supply of oxygen whilst also increasing the oxygen concentration on the catalyst surface. This property, known as the oxygen storage capacity, allows for oxygen to be available in low oxygen conditions (fuel rich) and to recover/store oxygen in high oxygen (fuel lean) conditions.

The beneficial use of ceria in catalysts is illustrated through the extensive use within three-way car exhaust catalysts or catalytic converters. Three-way catalysts (TWC's) were first introduced in the 1980's and have become widespread due to the compliance with the European Emissions Standard [1-4]. All vehicles that do not comply with this standard must be fitted with a TWC to lower the emissions, resulting in over 750 million passenger vehicles being sold equipped with TWC's up to 2011 [5]. The oxidising/reducing ability of ceria is used within TWC's to convert harmful and environmentally detrimental exhaust gases, particularly carbon monoxide, nitrogen oxides and unburnt hydrocarbons into less harmful carbon dioxide, nitrogen, and H_2O and CO_2 respectively. These reactions are shown in Equations 6.1 – 6.3 [3].

$$CeO_2 + xCO \rightleftharpoons CeO_{2-x} + xCO_2 \quad \textbf{(6.1)}$$

$$CeO_{2-x} + xNO \rightleftharpoons CeO_2 + 0.5xN_2 \quad \textbf{(6.2)}$$

$$CeO_2 + C_xH_y \rightleftharpoons CeO_{2-(2x+0.5y)} + xCO_2 + 0.5yH_2O \quad \textbf{(6.3)}$$

Ceria has been shown to be active for methane reforming (Equation 6.4) [6-10], and also aids CO and H_2 formation through CO_2 and H_2O dissociation, shown in Equation 6.5 and 6.6 respectively [7, 11, 12]. Ceria has also been shown to increase the activity of other metal catalysts through increasing metal dispersion, and therefore increasing surface area and reducing particle size [13-18]. This is achieved through a reduction in sintering as CeO_2 acts as a barrier between metal particles (Section 2.6.3). The particle sizes for both catalyst materials are illustrated in Table 4.1.

$$CeO_2 + xCH_4 \rightleftharpoons CeO_{2-x} + xCO + 2xH_2 \quad \textbf{(6.4)}$$

$$CeO_{2-x} + xCO_2 \rightleftharpoons CeO_2 + xCO \quad \textbf{(6.5)}$$

$$CeO_{2-x} + xH_2O \rightleftharpoons CeO_2 + xH_2 \quad \textbf{(6.6)}$$

6.2 Temperature programmed CO_2 reforming of CH_4 over 5 mol% CeO_2-Ni/YSZ with and without addition of O_2

Temperature programmed experiments were carried out over 5 mol% CeO_2-Ni/YSZ using the same operating conditions as over Ni/YSZ (Section 5-2). From Figures 6.1 – 6.6, it can be seen that 5 mol% CeO_2-Ni/YSZ shows very similar behaviour to that for Ni/YSZ for these particular operating conditions.

In the absence of O_2, reforming activity increases steadily with temperature due to an increased kinetic rate as well as the endothermic nature of the dry reforming reaction. As over Ni/YSZ, low methane conversion (<50 %) is seen at lower temperatures (<800 °C) due to the reaction stoichiometry and limited CO_2 availability. Likewise, methane conversion exceeds 50 % at high temperatures (>800 °C), indicating methane decomposition.

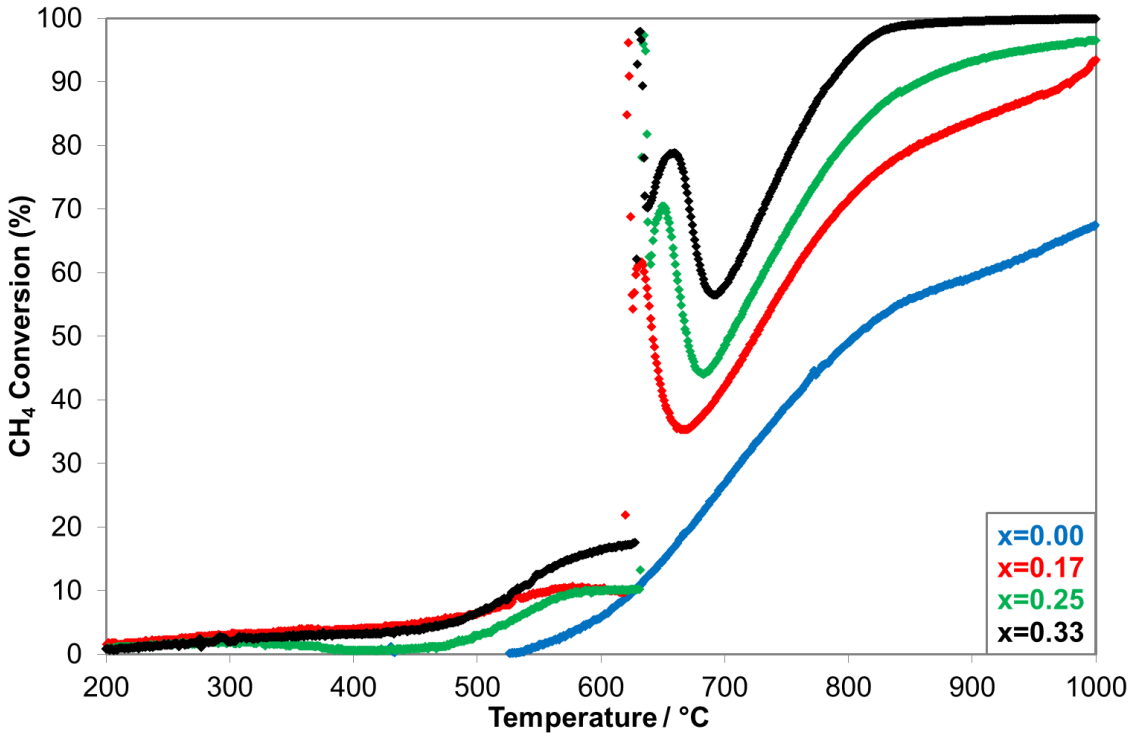

Figure 6.1: CH_4 conversion for reaction of CH_4 + CO_2 +xO_2 over 5 mol% CeO_2-Ni/YSZ during a temperature programme

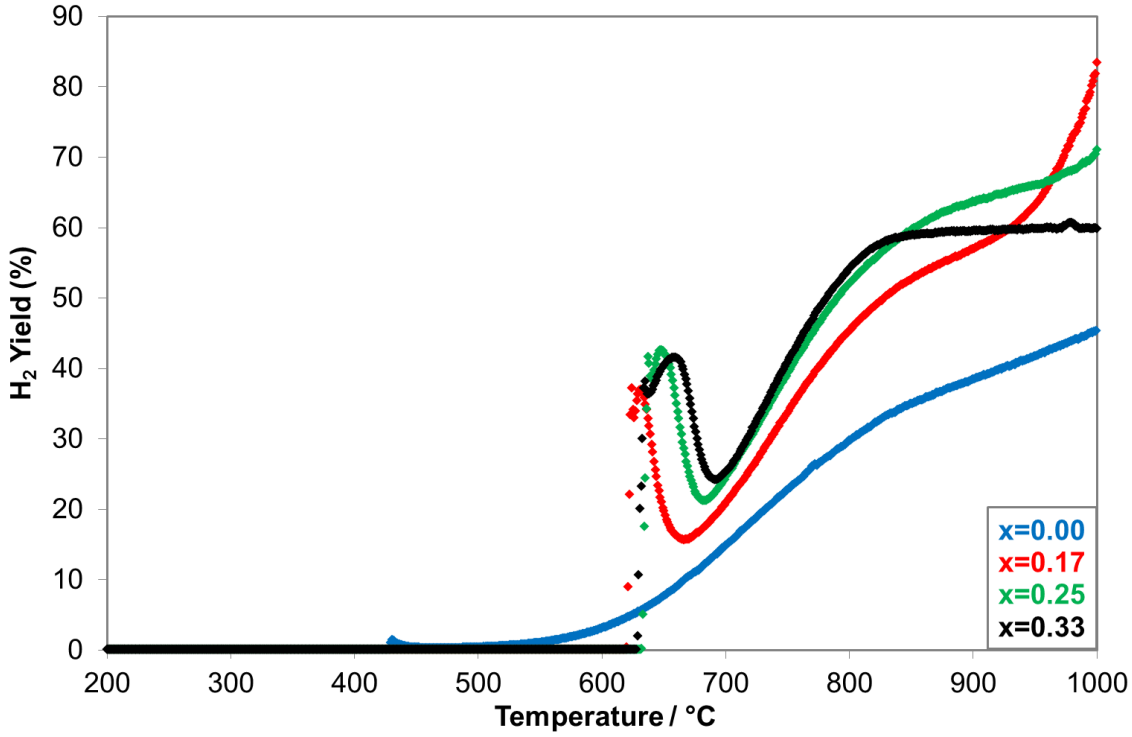

Figure 6.2: H_2 yield for reaction of CH_4 + CO_2 + xO_2 over 5 mol% CeO_2-Ni/YSZ during a temperature programme

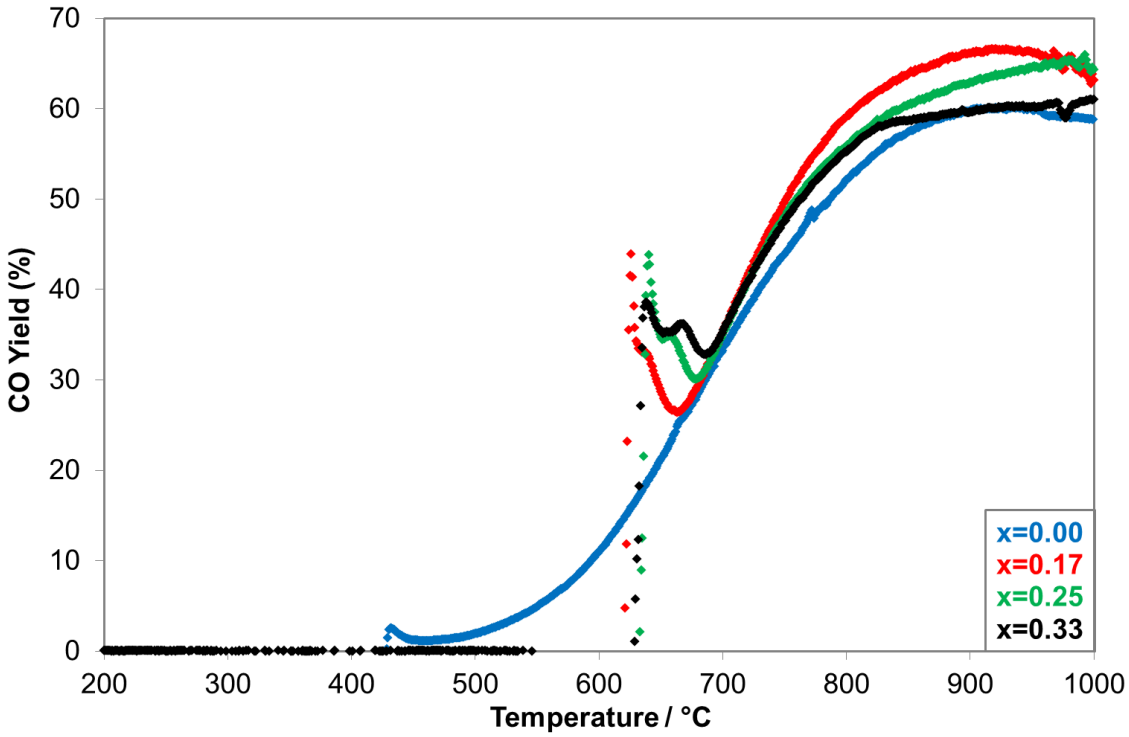

Figure 6.3: CO yield for reaction of CH_4 + CO_2 + xO_2 over 5 mol% CeO_2-Ni/YSZ during a temperature programme

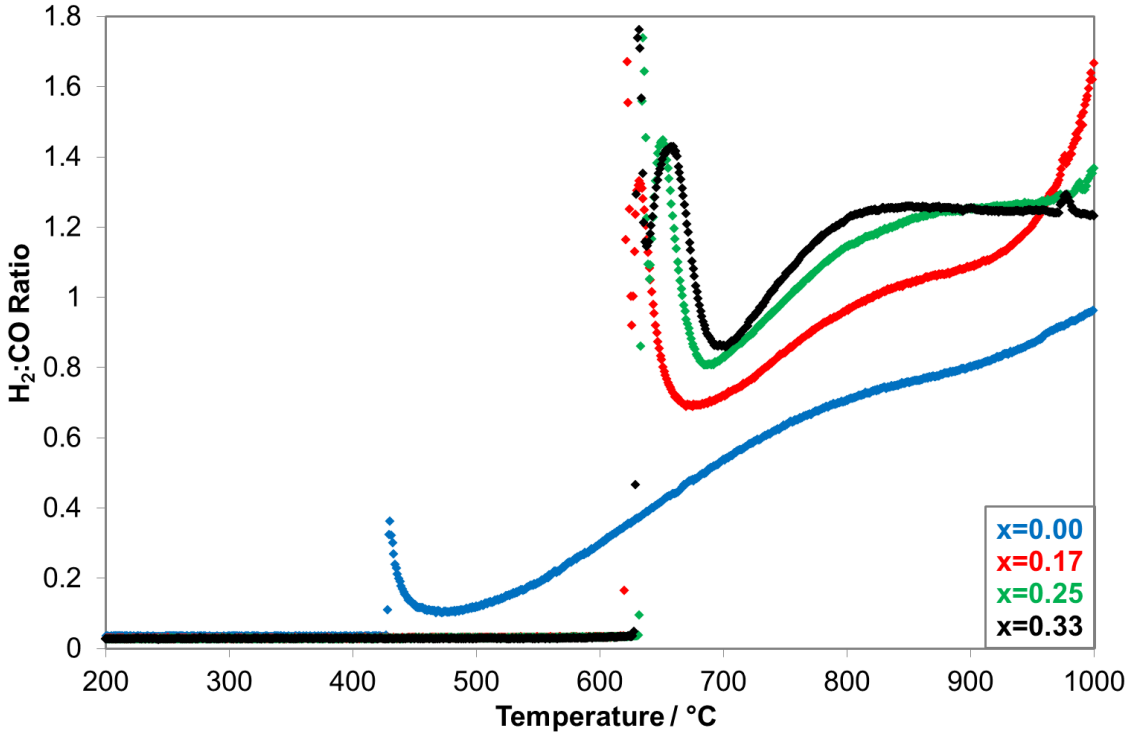

Figure 6.4: H_2:CO product ratio for reaction of CH_4 + CO_2 + xO_2 over 5 mol% CeO_2-Ni/YSZ during a temperature programme

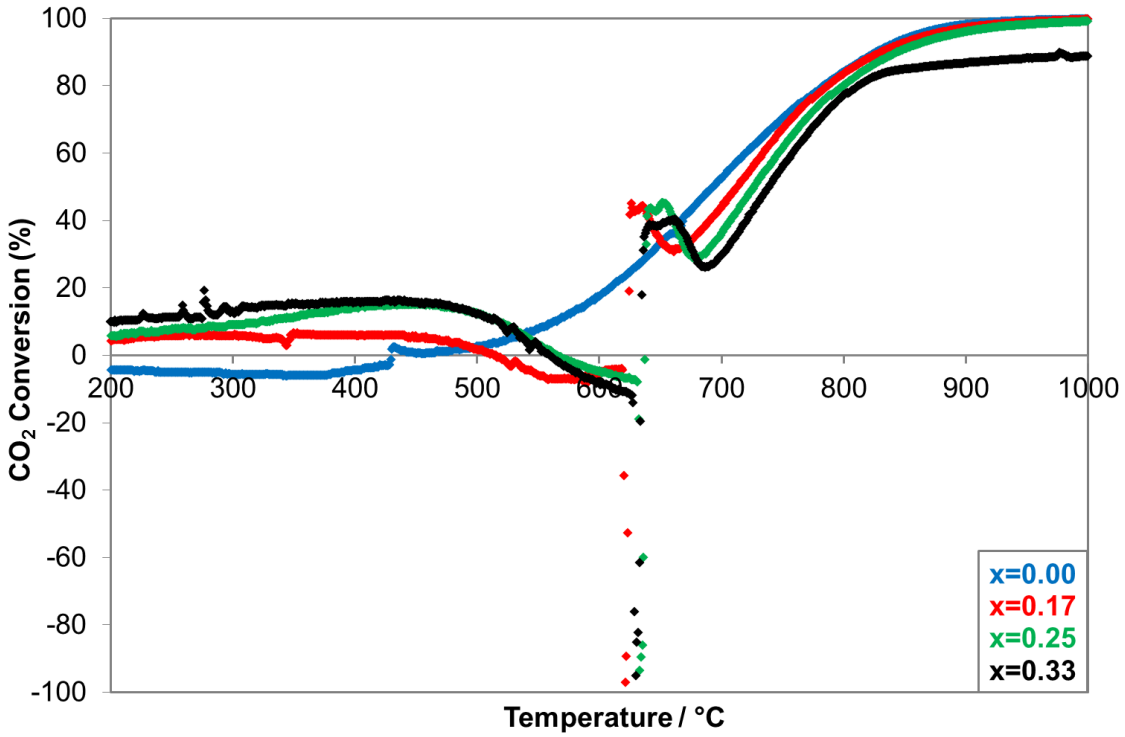

Figure 6.5: CO_2 conversion for reaction of CH_4 + CO_2 + xO_2 over 5 mol% CeO_2-Ni/YSZ during a temperature programme

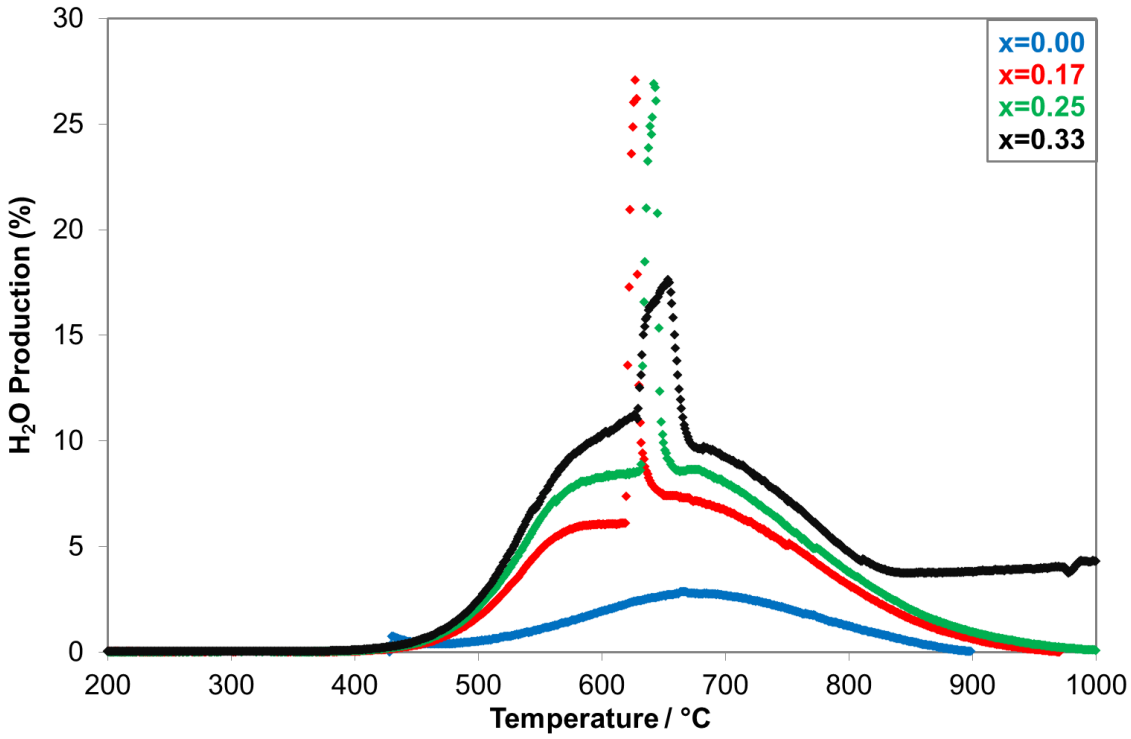

Figure 6.6: H_2O production for reaction of CH_4 + CO_2 + xO_2 over 5 mol% CeO_2-Ni/YSZ during a temperature programme

One visible difference between the two catalysts is in the methane conversion for the reaction in the absence of O_2 is the profile of the slope above 700 °C shown in Figure 5.1. Over Ni/YSZ (shown in Figure 5.1), the increase in CH_4 conversion with temperature is greater whereas over 5 mol% CeO_2-Ni/YSZ (shown in Figure 6.1), the opposite behaviour is observed. The profile for Ni/YSZ can be explained by the increasing capacity for dry reforming at high temperatures and also a greater capacity for methane decomposition. The different profile for 5 mol% CeO_2-Ni/YSZ may be attributed to the variation in carbon deposition that is observed within this chapter (See Section 6.3.7), resulting in increased deactivation at higher temperatures. Doping with ceria can encourage the dry reforming of methane through the dissociation of CO_2 to oxidise any Ce_2O_3 present to produce CO (Equation 6.5) and the CeO_2 can then donate oxygen to encourage the partial oxidation of methane (Equation 6.4).

The addition of O_2 to the CH_4:CO_2 mixture over 5 mol% CeO_2-Ni/YSZ results in similar behaviour to Ni/YSZ, in that a substantial increase in activity is observed, and that this increase is enhanced with higher O_2 concentration. This is due to the increased availability of reformant. From comparison of the temperature profiles for the reforming in the presence of oxygen over Ni/YSZ and 5 mol% CeO_2-Ni/YSZ, it can be seen that the light-off temperatures are slightly lower for the reaction over 5 mol% CeO_2-Ni/YSZ than Ni/YSZ, as shown in Table 6 .1. This may be attributed to CeO_2 acting to encourage partial oxidation through distribution of oxygen across the catalyst surface.

Table 6.1: Light-off temperatures (°C) for temperature programmed reactions of CH_4+0.5CO_2+xO_2 over Ni/YSZ and 5 mol% CeO_2-Ni/YSZ. Light-off temperatures recorded where H_2 yield = 10%.

	Light off temperature/ °C	
CH_4:xO_2	**Ni/YSZ**	**5 mol% CeO_2-Ni/YSZ**
x=0.17	629	621
x=0.25	643	634
x=0.33	655	630

A substantial variation between the two catalysts is seen in the reactions at high temperatures (>800 °C), in that the catalyst activity for 5 mol% CeO_2-Ni/YSZ (Figures 6.2 and 6.3) is significantly lower than for Ni/YSZ (Figures 5.2 and 5.3). This may be explained by the greater H_2:CO_2 and CO:CO_2 atmosphere at higher temperatures resulting in the reduction of the CeO_2 to Ce_2O_3. This reducing atmosphere and low CO_2 concentration minimises the potential for Ce_2O_3 oxidation to CeO_2 and unlike CeO_2, Ce_2O_3 does not encourage methane reforming. Thermal reduction of CeO_2 to Ce_2O_3, reduction in H_2 or CO-rich conditions and the lack of activity of Ce_2O_3 towards methane reforming have been reported in the literature [7, 19].

6.3 CO_2 reforming of CH_4 over 5 mol% CeO_2-Ni/YSZ with and without addition of O_2

To assess the influence of ceria doping to Ni/YSZ on long-term activity and selectivity, a number of 20 hour studies were carried out over the temperature range 600-1000 °C at 100 °C intervals. Changes in catalyst behaviour with time are discussed for each reaction temperature and variations across the temperature range are also discussed. The extent to which carbon deposition occurred during the reaction was measured using post-reaction temperature programmed oxidation techniques (Section 3.6). Details of CH_4 conversion and H_2:CO ratio that are not included in this section are available in Appendix B.

6.3.1 Reaction of CH_4 + 0.5CO_2+ xO_2 over 5 mol% CeO_2-Ni/YSZ at 600 °C

At 600 °C, analysis at 5 and 20 hours is shown in Table 6.2. The methane conversion and H_2:CO product ratio are not shown in

Table 6.2 as they show high stability over the 20 hour reaction period and it is considered that H_2 and CO yield represent catalyst activity and selectivity more accurately than methane conversion. Values were taken after 5 hours on-line to ensure that the initial reaction characteristics are not

considered as these can be unstable and uncharacteristic, and after 20 hours to most accurately reflect reaction characteristics after a significant time period.

Table 6.2: Reforming analysis for reaction of $CH_4 + CO_2 + xO_2$ (x=0.00, 0.17, 0.25, 0.33) over 5 mol% CeO_2-Ni/YSZ at 600 °C after 5 hours and 20 hours

	Time (h)							
	H_2 Yield (%)		CO Yield (%)		H_2O Production (%)		CO_2 Consumption (%)	
CH_4:xO_2	5	20	5	20	5	20	5	20
x=0.00	6.24	5.78	16.11	14.57	2.83	2.40	47.67	51.63
x=0.17	13.10	13.10	19.80	20.43	8.34	8.01	18.67	17.41
x=0.25	15.29	15.68	19.13	18.85	10.69	10.25	11.12	15.60
x=0.33	21.81	22.04	23.64	23.11	13.79	14.00	-9.39	-10.19

From Table 6.2, it can be seen that the reactions in both the absence and presence of oxygen exhibit very high stability (<4 % variation) over the reaction duration of 20 hours. The table shows that the addition of oxygen to the CH_4:CO_2 mixture results in a substantial increase in reforming activity, particularly in H_2 yield. The greater increase in H_2 yield compared to CO yield may be due to the greater H_2:CO product ratio of the partial oxidation reaction compared to the dry reforming reaction and the increased potential for CO_2 to reoxidise Ce_2O_3 (Equation 6.5) and produce CO. This difference is also exhibited in the greater H_2:CO product ratios for the reactions in the presence of O_2, as shown in Table 6.3 below.

Table 6.3: Average H_2:CO product ratios for reaction of $CH_4 + CO_2 + xO_2$ (x=0.00, 0.17, 0.25. 0.33) over 5 mol% CeO_2-Ni/YSZ at 600 °C Average taken from 2-20 hours.

CH_4:xO_2	Average H_2:CO product ratio
x=0.00	0.52
x=0.17	0.73
x=0.25	0.88
x=0.33	1.06

The high stability at this temperature may be due to decreased deactivation from carbon deposition and sintering. Similar stable behaviour is observed for Ni/YSZ (Figures 5.7 – 5.10) at this temperature, however a slightly greater variation over time is seen in that total oxidation becomes more favoured with time. This may be attributed to sintering occurring to a lesser extent with 5 mol% CeO_2-Ni/YSZ than for Ni/YSZ, due to the ability of CeO_2 to minimize metal sintering as discussed in Section 2.6.3 [11, 17, 18].

It is evident that both Ni/YSZ and 5 mol% CeO_2-Ni/YSZ catalysts show high stability over the 20 hour reaction duration at 600 °C.

6.3.2 Reaction of $CH_4 + 0.5CO_2 + xO_2$ over 5 mol% CeO_2-Ni/YSZ at 700 °C

At 700 °C (shown in Figures 5.9 – 5.12), the reaction profile shows significant variation from that at 600 °C, in that unusual behaviour is seen for the reactions performed in the presence of oxygen. This unusual behaviour will be termed as 'cycling' throughout this study due to its alternating yet regular nature. Cycling in this situation is likely caused by the continuous transition between cerium oxidation states of 4+ (CeO_2) and 3+ (Ce_2O_3), as shown schematically in Figure 6.7. Such behaviour is not present in the equivalent studies performed over Ni/YSZ. The nature of the cycling would also indicate that cerium is the underlying cause due to the stable baseline provided by nickel within each reaction and the small enhancement seen from this baseline, as is shown in Figure 6.8.

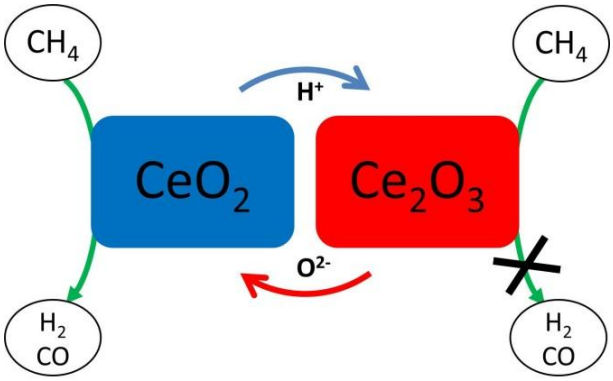

Figure 6.7: Schematic diagram of transition between Ce^{3+} and Ce^{4+} and influence on reforming products

The cycling occurs in that CeO_2 is reduced through activating methane reforming, resulting in increased catalytic activity. Subsequent reduced Ce_2O_3 is inactive for methane reforming resulting in catalyst activity falling to the baseline maintained by methane reforming through nickel. The Ce_2O_3 is reoxidized by O_2 and CO_2 to CeO_2 which is then active for methane reforming and catalyst activity increases. This process occurs continuously throughout the course of the reaction. From the reaction profiles shown in subsequent figures, it is evident that increased oxygen concentration in the gas feed increases the magnitude to which product cycling occurs. This may be attributed to the increased potential for Ce_2O_3 reoxidation with increased oxygen.

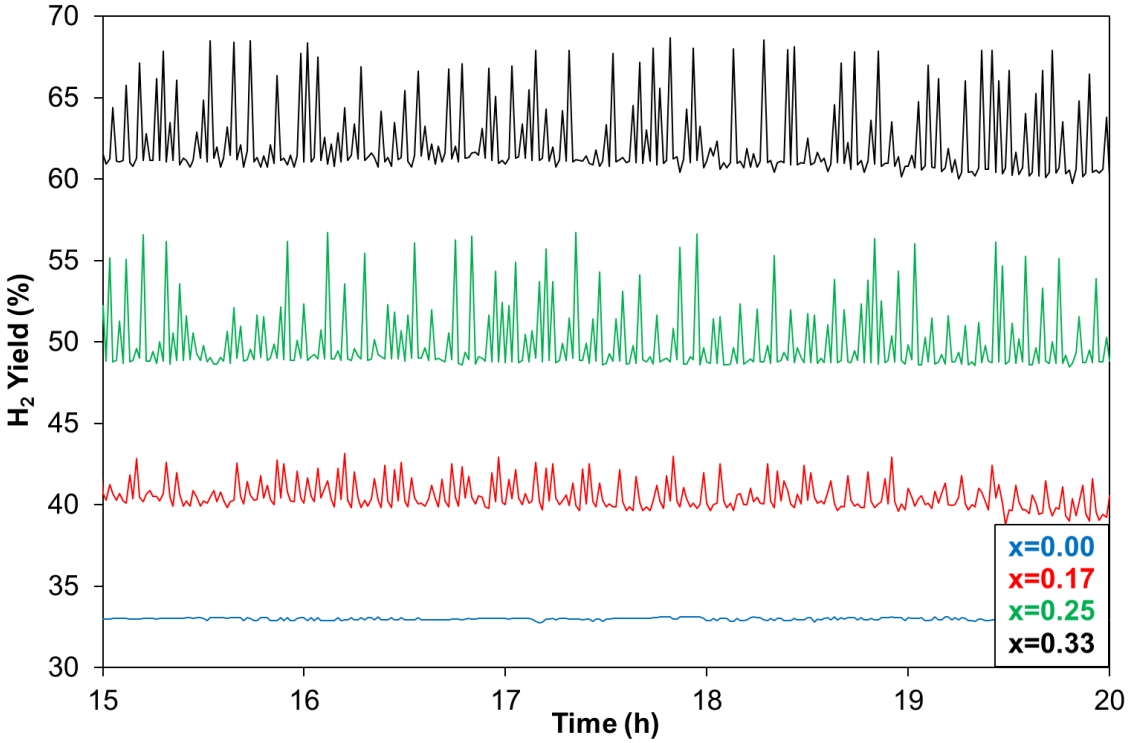

Figure 6.8: Extract from Figure 6.9 to illustrate the nature of cycling for the reaction of CH_4 + 0.5CO_2 + xO_2 over 5 mol% CeO_2-Ni/YSZ at 700 °C (x=0.00, 0.17, 0.25, 0.33). Data points are connected to visually enhance cycling nature

Cycling may be caused by the transient direct oxidation and reduction of nickel where oxygen is present in the gas feed. However, cycling behaviour is not seen for the reactions performed over Ni/YSZ (Figures 5.13 – 5.16). The greater extent of the cycling for the total oxidation products with increased oxygen addition (see Figures 6.11 and 6.12), suggests that either the presence of CeO_2 directly encourages the total oxidation of methane reaction (Equation 6.7) or increases oxygen donation to oxidise nickel and indirectly encourages total oxidation.

$$CH_4 + 2O_2 \rightleftharpoons 2H_2O + CO_2 \qquad \textbf{(6.7)}$$

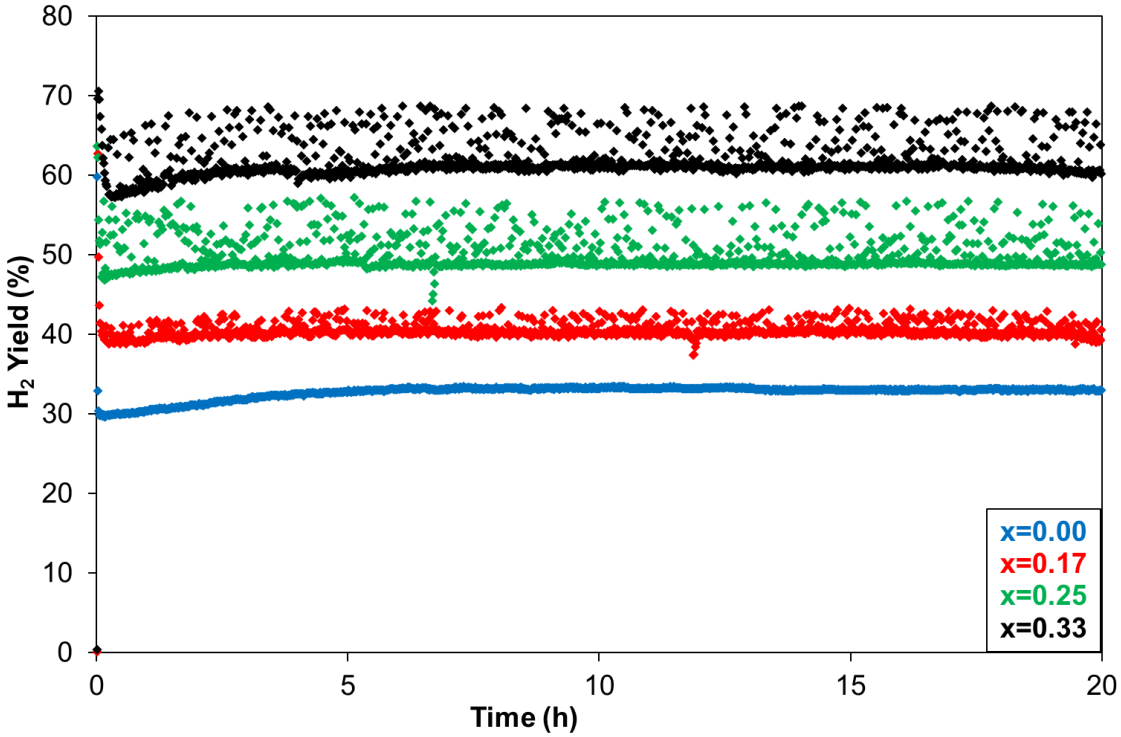

Figure 6.9: H_2 yield for the reaction of CH_4 + 0.5CO_2 + xO_2 over 5%CeO_2-Ni/YSZ at 700 °C for 20 hours (x=0.00, 0.17, 0.25, 0.33)

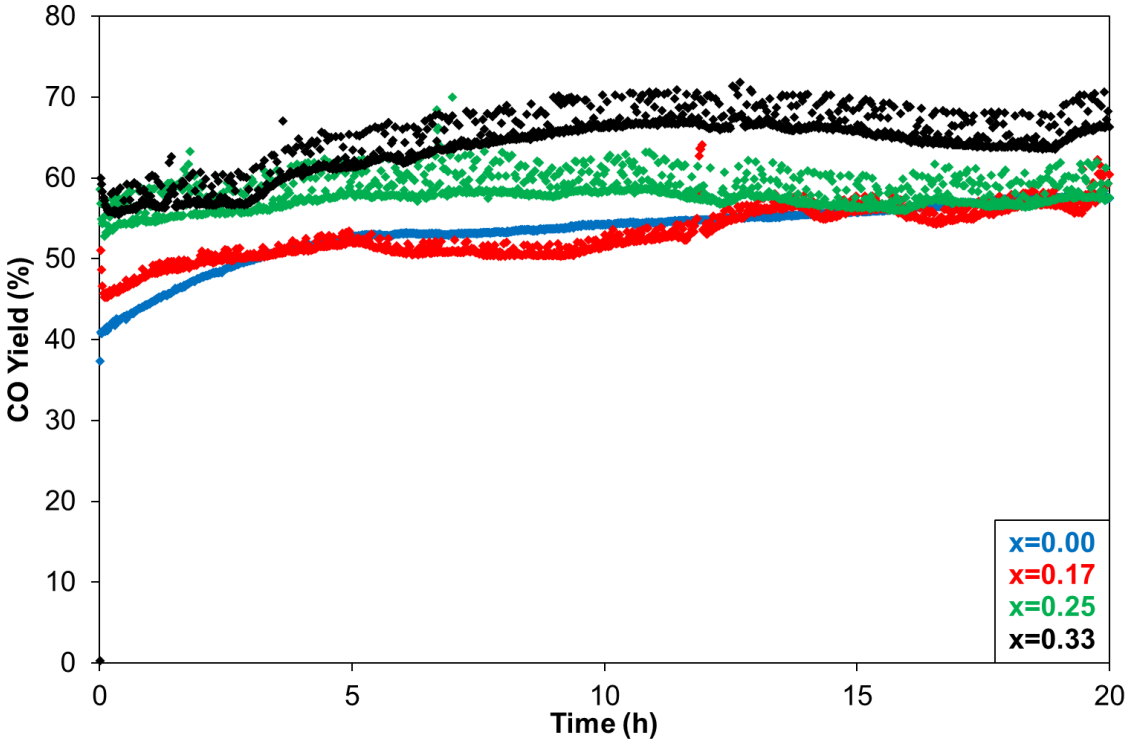

Figure 6.10: CO yield for reaction of CH_4 + 0.5CO_2 + xO_2 over 5%CeO_2-Ni/YSZ at 700 °C for 20 hours (x=0.00, 0.17, 0.25, 0.33)

The percentage H_2 yields for different levels of added O_2 presented in Figure 6.9 shows good stability over the duration of the reaction. This stable performance is also reflected in the H_2O production shown in Figure 6.12. However, this is not reflected in the CO yield and CO_2 consumption shown in Figures 6.10 and 6.11 respectively. The lower stability observed for the CO yield compared to the H_2 yield may partially be caused by the potential for oxidation of deposited carbon and the reverse Boudouard reaction. The lower signal intensity and therefore greater noise levels for CO compared to H_2 may also contribute to the reduced stability with time.

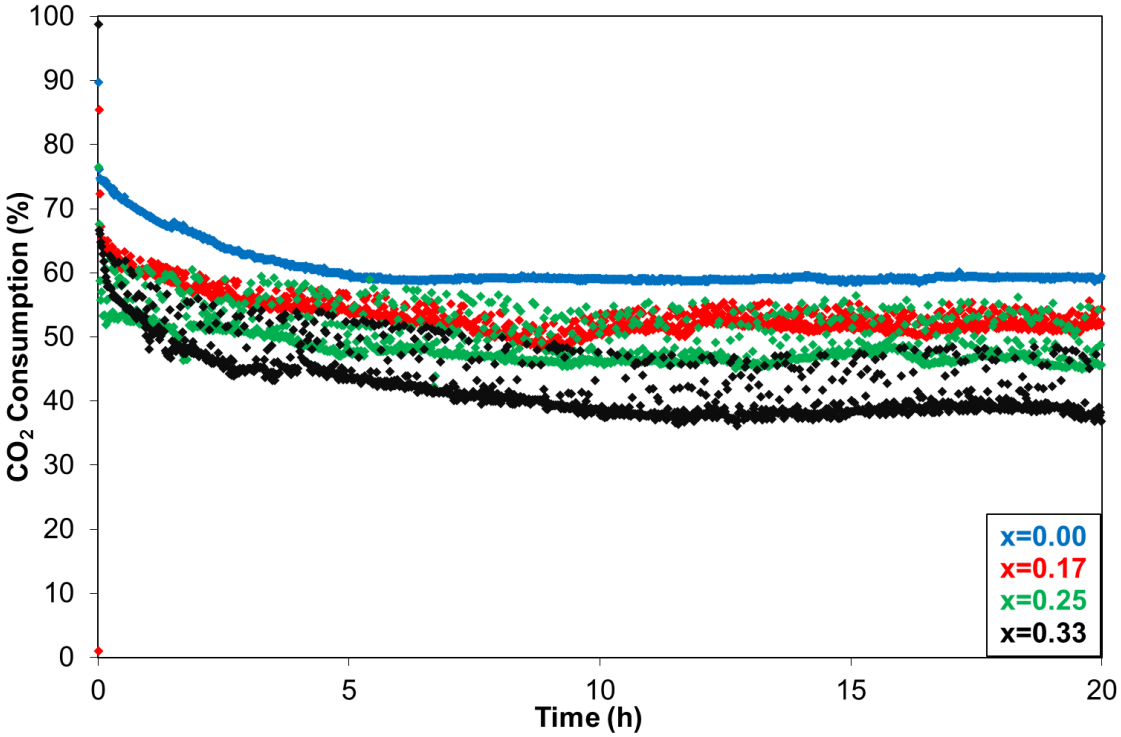

Figure 6.11: CO_2 consumption for the reaction of CH_4 + 0.5CO_2 + xO_2 over 5%CeO_2-Ni/YSZ at 700 °C for 20 hours (x=0.00, 0.17, 0.25, 0.33)

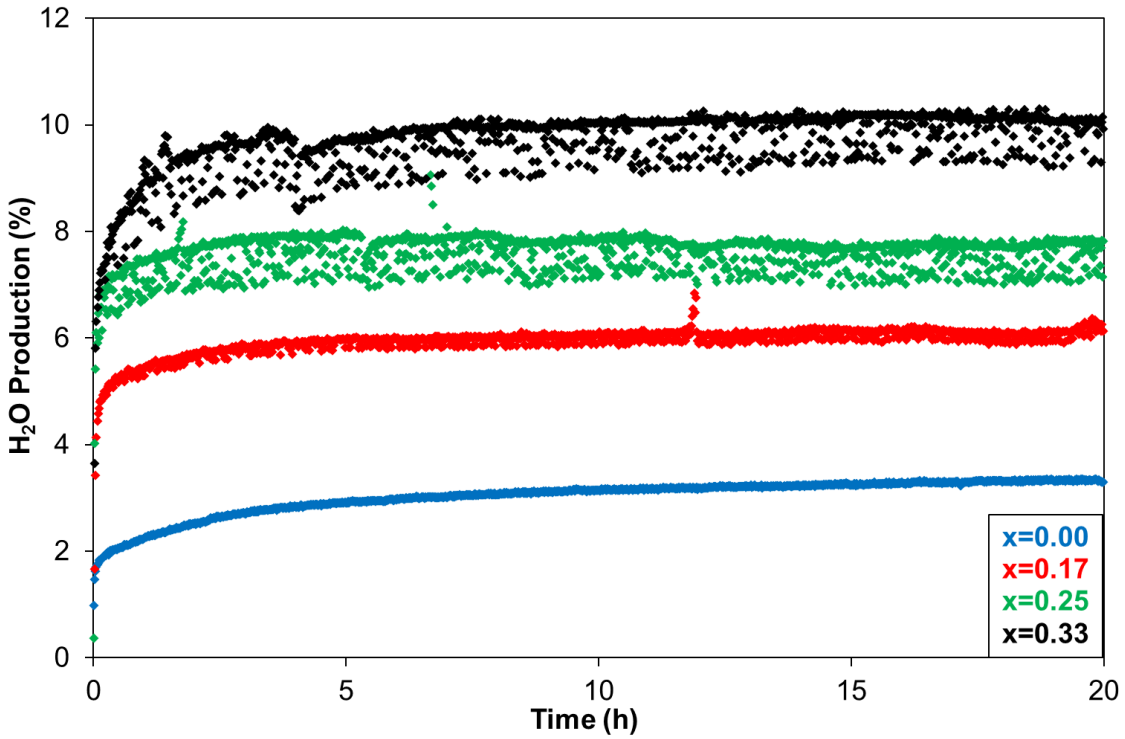

Figure 6.12: H_2O production for the reaction of CH_4 + 0.5CO_2 + xO_2 over 5%CeO_2-Ni/YSZ at 700 °C for 20 hours (x=0.00, 0.17, 0.25, 0.33)

The variation in CO yield and CO_2 consumption over time, shown in Figures 6.10 and 6.11 respectively, may be due to carbon deposition and carbon removal through an increase in the reverse Boudouard reaction (Equation 6.8) or oxidation through lattice oxygen (Equations 6.9 and 6.10)

$$C_{(s)} + CO_2 \rightleftharpoons 2CO \quad \textbf{(6.8)}$$

$$CeO_2 + C \leftrightarrows Ce_2O_3 + CO \quad \textbf{(6.9)}$$

$$2CeO_2 + C \leftrightarrows 2Ce_2O_3 + CO_2 \quad \textbf{(6.10)}$$

The influence of carbon deposition on the reforming characteristics is supported by the quantity of carbon detected in the post-reaction temperature programmed oxidation (Figure 6.31). The H_2:CO ratios of approximately one are also consistent with the occurrence of the reverse Boudouard

reaction, as both partial oxidation of methane (Equation 6.11) and methane decomposition (Equation 6.12) would result in a greater H_2:CO ratio.

$$CH_4 + 0.5O_2 \rightleftharpoons 2H_2 + CO \quad \textbf{(6.11)}$$

$$CH_4 \rightleftharpoons 2H_2 + C_{(s)} \quad \textbf{(6.12)}$$

From comparison with the measurements carried out at 700 °C over Ni/YSZ (Section 5.3.2), it can be seen that 5 mol% CeO_2-Ni/YSZ shows greater stability over time. The maximum difference in H_2 yield between 5 hours and 20 hours is 5.92 % and 0.54 % for Ni/YSZ and 5 mol% CeO_2-Ni/YSZ respectively. There is no significant shift towards total oxidation of methane (maximum difference in H_2O production between 5 and 20 hours is +0.39 %) compared to that seen over Ni/YSZ. The behaviour over Ni/YSZ may be attributed to sintering of the catalyst which may be reduced with the 5 mol% CeO_2-Ni/YSZ as discussed in Section 2.6.3.

6.3.3 Reaction of $CH_4 + 0.5CO_2 + xO_2$ over 5 mol% CeO_2-Ni/YSZ at 800 °C

At 800 °C, similar behaviour is observed to at 700 °C, particularly with the occurrence of substantial cycling behaviour. However, differences are visible between the reaction temperatures, particularly regarding the nature and extent of the cycling behaviour.

In the absence of O_2, both H_2 (Figure 6.13) and CO yield (Figure 6.14) show an increase with reaction time, particularly the CO yield which shows a significant increase of approximately 20 %. An increase in H_2 yield, to where the total yield increases above 50 %, indicates that methane decomposition may be occurring. This increase over time may be caused by the deposited carbon acting as an active surface for methane decomposition [20, 21]. This is supported by the substantial quantity of carbon detected during post-reaction temperature programmed oxidation (Figure 6.31).

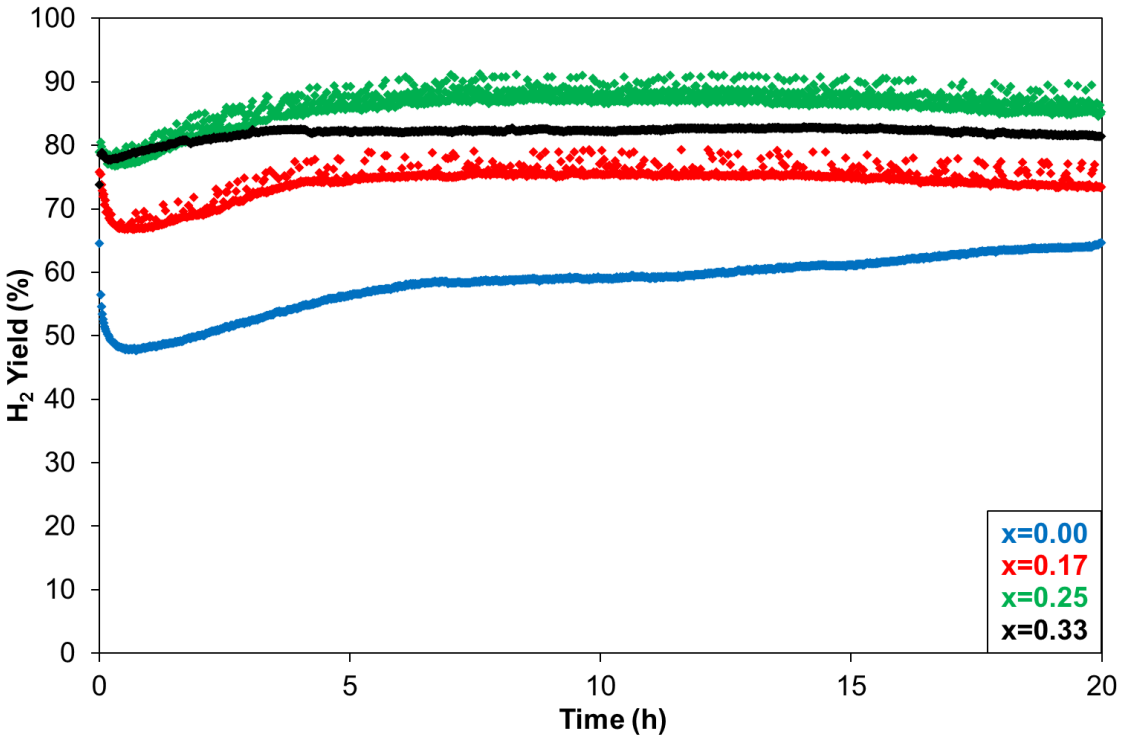

Figure 6.13: H_2 yield for the reaction of CH_4 + 0.5CO_2 + xO_2 over 5 mol% CeO_2-Ni/YSZ at 800 °C for 20 hours (x=0.00, 0.17, 0.25, 0.33)

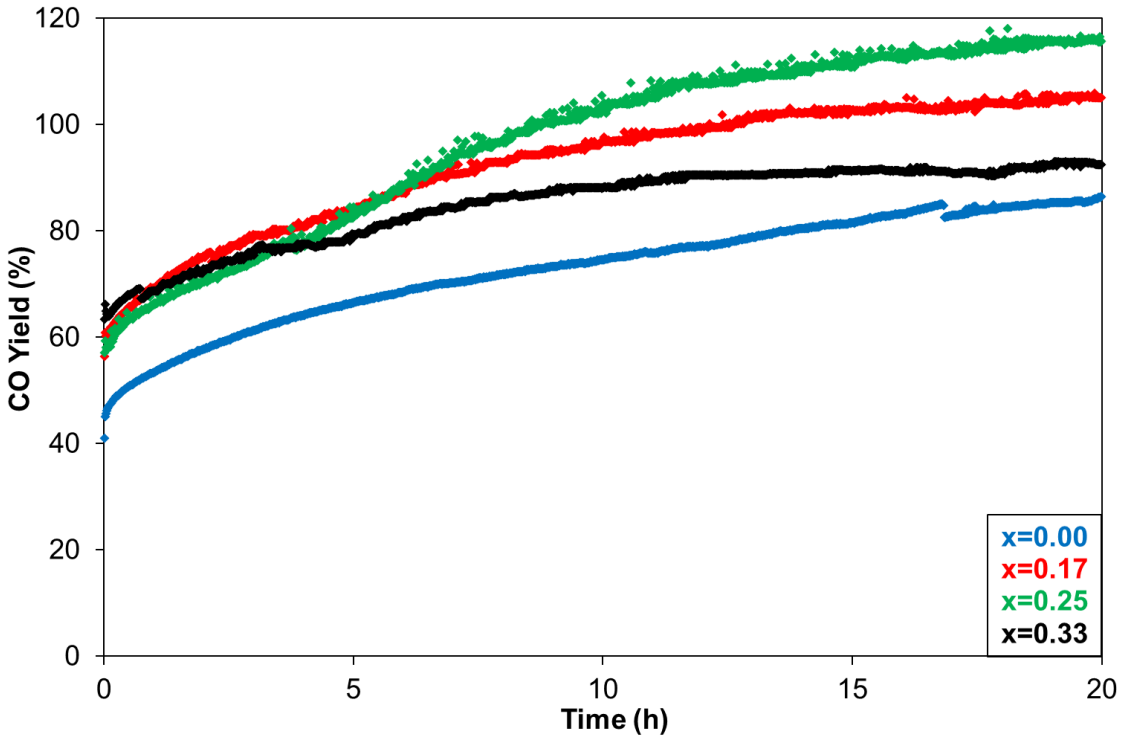

Figure 6.14: CO yield for the reaction of CH_4 + 0.5CO_2 + xO_2 over 5 mol% CeO_2-Ni/YSZ at 800 °C for 20 hours (x=0.00, 0.17, 0.25, 0.33)

The substantial quantity of carbon deposition occurring during the reaction in the absence of O_2 is likely to be the dominant cause of the increasing CO yield over time. As carbon is deposited on the catalyst surface, CO_2 will be consumed to a lesser extent through methane reforming due to a reduced active metal surface area. However, the CO_2 will react with deposited carbon to produce carbon monoxide through the reverse Boudouard reaction (Equation 6.8). This is supported by the stable CO_2 consumption over time (Figure 6.15), with the increasing consumption from increased reverse Boudouard reaction compensating for the decreasing consumption from a reduced extent of methane reforming. Ceria doping enhances the production of CO from surface carbon as CO_2 reacts with Ce_2O_3 to produce CeO_2 and CO (Equation 6.5). The CeO_2 can then encourage removal of deposited carbon through oxidation with lattice oxygen to produce further CO (Equation 6.9) [6, 14, 22].

When oxygen is present in the reaction gas mixture, relatively stable H_2 production is observed with a small quantity of cycling present when x=0.17 and 0.25, whereas no cycling is observed when x=0.33. The reduction in the extent of cycling at 800 °C compared to that shown at 700 °C is attributed to the increased reforming activity at 800 °C. As methane reforming increases, the reaction atmosphere becomes increasing H_2 rich, encouraging the reduction of CeO_2 to Ce_2O_3. Also, the increased consumption of CO_2 through the reforming reaction results in reduced availability of CO_2 to reoxidise Ce_2O_3 to CeO_2.

Both the increased H_2 and decreased CO_2 concentrations reduce the extent to which ceria is present in the CeO_2 form, therefore reducing the extent to which the catalytic activity can increase above the baseline provided through nickel activity [7]. The absence of cycling behaviour at 800 °C when x=0.33 may be due to a greater catalyst bed temperature resulting from increased exothermic total and partial oxidation reactions. The CeO_2 structure is less favourable at high temperatures as CeO_2 can lose oxygen into the reaction atmosphere [19]. Another explanation may be that when x=0.33, sufficient CO_2 is available to ensure that CeO_2 predominates over Ce_2O_3 and that the reduction-oxidation reaction occurs so rapidly it is not visible in the activity data, which is stored at 1 minute intervals.

Lower H_2 and CO yields are also seen where x=0.33 than 0.25. This is due to an increased extent of total oxidation of methane, which can be seen through the lesser CO_2 consumption and greater H_2O production, shown in Figures 6.15 and 6.16.

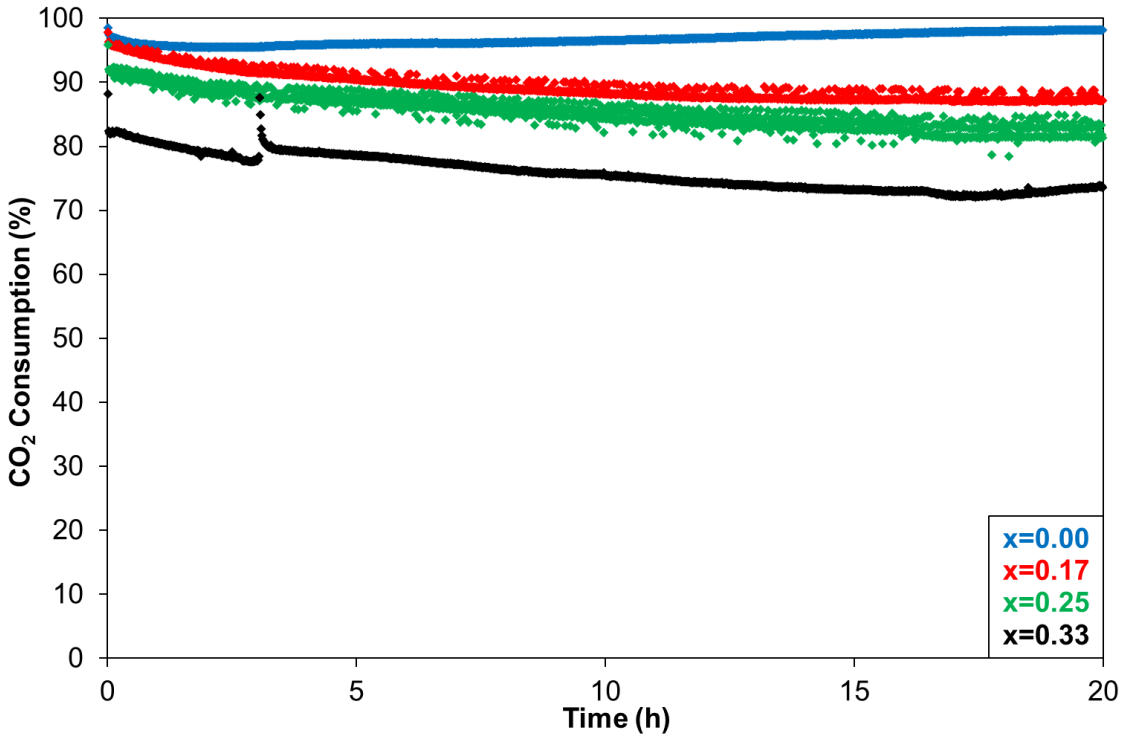

Figure 6.15: CO_2 consumption for the reaction of CH_4 + 0.5CO_2 + xO_2 over 5 mol% CeO_2-Ni/YSZ at 800 °C for 20 hours (x=0.00, 0.17, 0.25, 0.33)

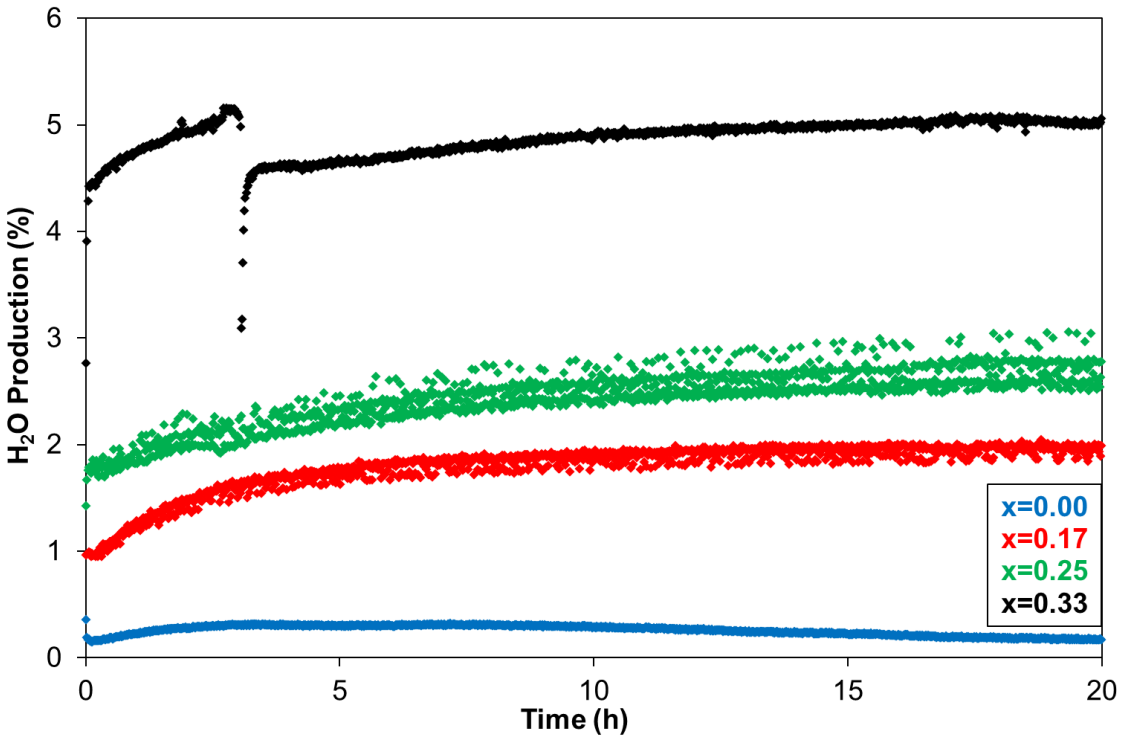

Figure 6.16: H_2O production for the reaction of CH_4 + 0.5CO_2 + xO_2 over 5 mol% CeO_2-Ni/YSZ at 800 °C for 20 hours (x=0.00, 0.17, 0.25, 0.33)

As with the reaction at 700 °C, a substantial increase in CO yield is seen over time at 800 °C. This may again be attributed to significant carbon deposition and subsequent increased extent of the reverse Boudouard reaction to produce CO over time, which is supported through the quantity of carbon deposited (See Figure 6.31). The increasing CO yield where x=0.33 may be a factor of the reaction approaching a steady state as the CO yield is already becoming significantly more stable by 20 hours on-line.

In comparison with Ni/YSZ (Section 5.3.3), it can be seen that 5 mol% CeO_2-Ni/YSZ shows enhanced stability over time at 800 °C (apart from cycling) in terms of the H_2 yield. However, 5 mol% CeO_2-Ni/YSZ shows significantly greater variation in CO yield with time, which may be attributed to the greater extent of carbon deposition occurring and that CeO_2 encourages CO_2 disproportionation to CO. Increased CO production can not only be used as a fuel within a solid oxide fuel cell but lower H_2:CO ratios are desirable for certain industrial process such as oxo-synthesis (discussed in Section 4.2)

6.3.4 Reaction of CH_4 + 0.5CO_2+ xO_2 over 5 mol% CeO_2-Ni/YSZ at 900 °C

At 900 °C (shown in Figures 6.17 – 6.20), significantly different catalytic behaviour is observed compared to lower temperatures in that no cycling behaviour is observed across all reaction conditions. In the absence of O_2, substantial decreases are seen in both H_2 and CO yield over time. This deactivation is caused primarily through carbon deposition to an extent at which partial physical blocking of the reactor tube occurs restricting gas flow through the reactor. Complete blockage and potential reactor tube damage are likely to occur if these reaction conditions were operated for a longer duration. A similar blockage due to carbon deposition has also been observed previously for Ni/YSZ at 1000 °C (shown in Fig. 5.17).

When O_2 is added to the reaction gas mixture, high stability with time is observed in the H_2 yield for all O_2 concentrations (Figure 6.17). The lack of cycling seen at this temperature is due to the high reforming activity and subsequent H_2-rich atmosphere and almost complete CO_2 consumption, meaning that the ceria will be present primarily in the reduced form. The lack of redox behaviour is expected as CeO_2 will undergo reduction at such high temperatures and H_2-rich conditions as discussed previously [19].

The CO yield (Figure 6.18) shows significant variation with time when O_2 is present in the reaction gas mixture. As at 800 °C, this increase with time may be attributed to carbon deposition and an increasing extent of the reverse Boudouard reaction. This is supported by the substantial quantities of carbon deposited, as detected in the post-reaction TPO (Figure 6.31). The increasing CO yield when x=0.33 may be due to the reaction approaching a steady state, or through increased oxidation of any carbon deposits by lattice oxygen. When x=0.33, substantial total oxidation is also occurring, as can be seen from the CO_2 consumption and H_2O production in Figure 6.19 and 6.20 respectively.

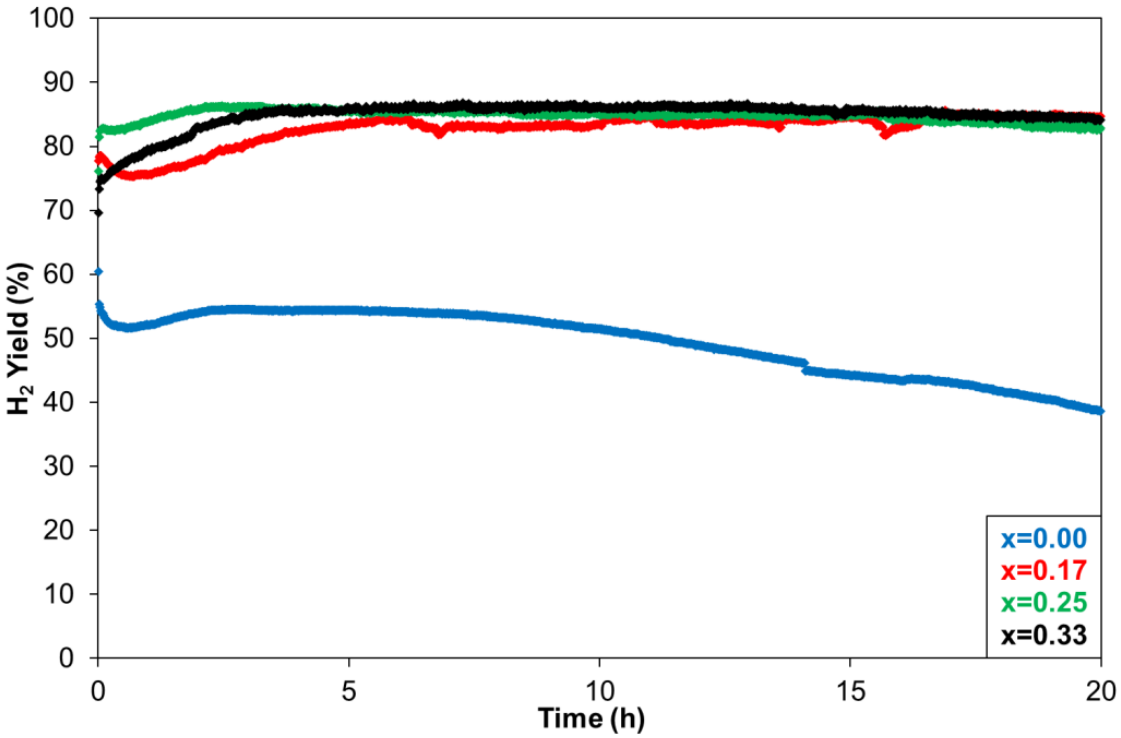

Figure 6.17: H_2 yield for reaction of CH_4 + 0.5CO_2 + xO_2 over 5 mol% CeO_2-Ni/YSZ at 900 °C for 20 hours (x=0.00, 0.17, 0.25, 0.33)

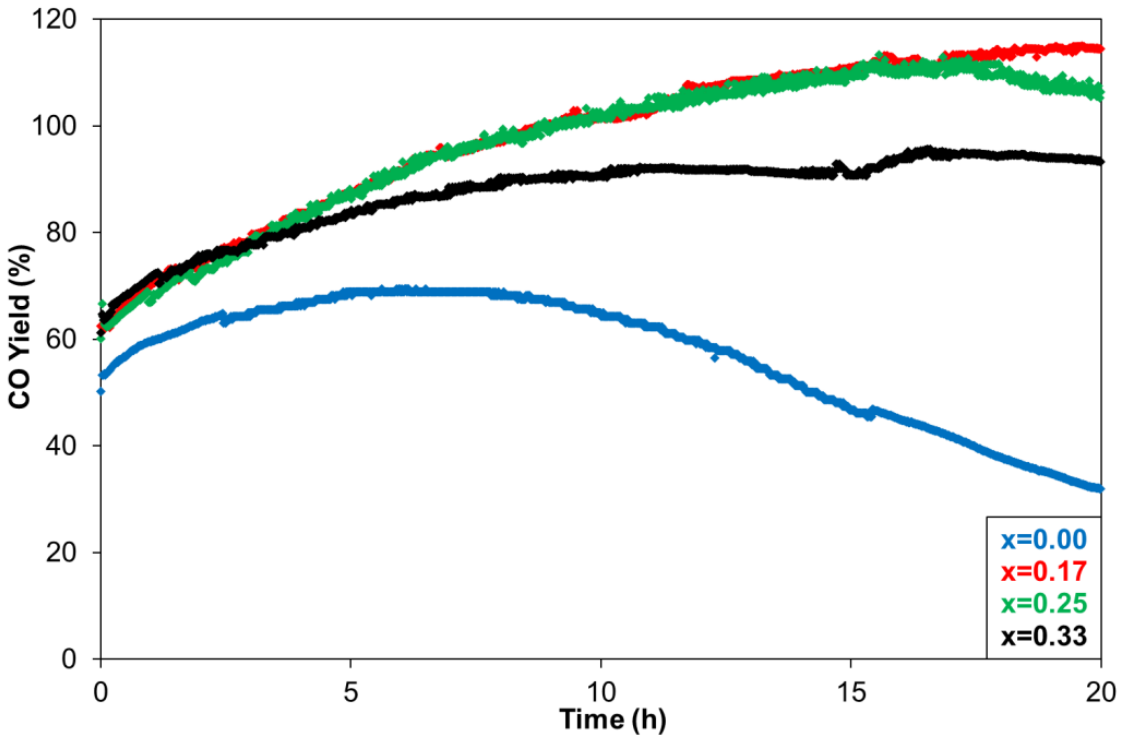

Figure 6.18: CO yield for reaction of CH_4 + 0.5CO_2 + xO_2 over 5 mol% CeO_2-Ni/YSZ at 900 °C for 20 hours (x=0.00, 0.17, 0.25, 0.33)

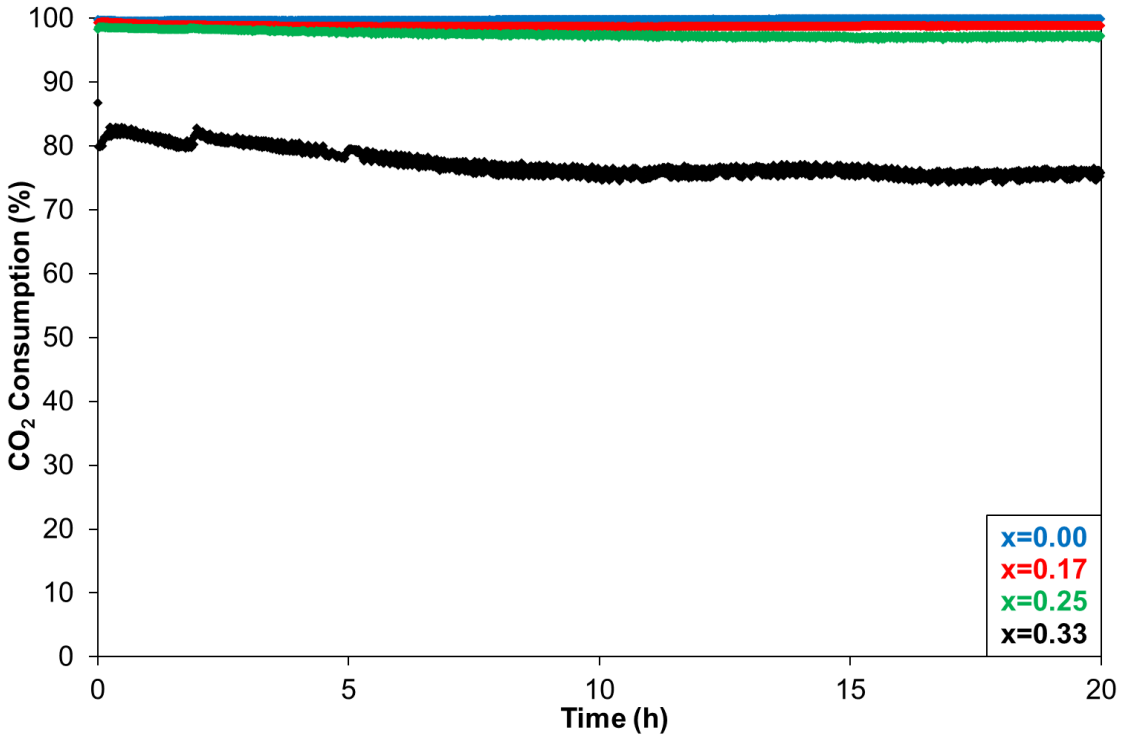

Figure 6.19: CO_2 consumption for reaction of CH_4 + 0.5CO_2 + xO_2 over 5 mol% CeO_2-Ni/YSZ at 900 °C for 20 hours (x=0.00, 0.17, 0.25, 0.33)

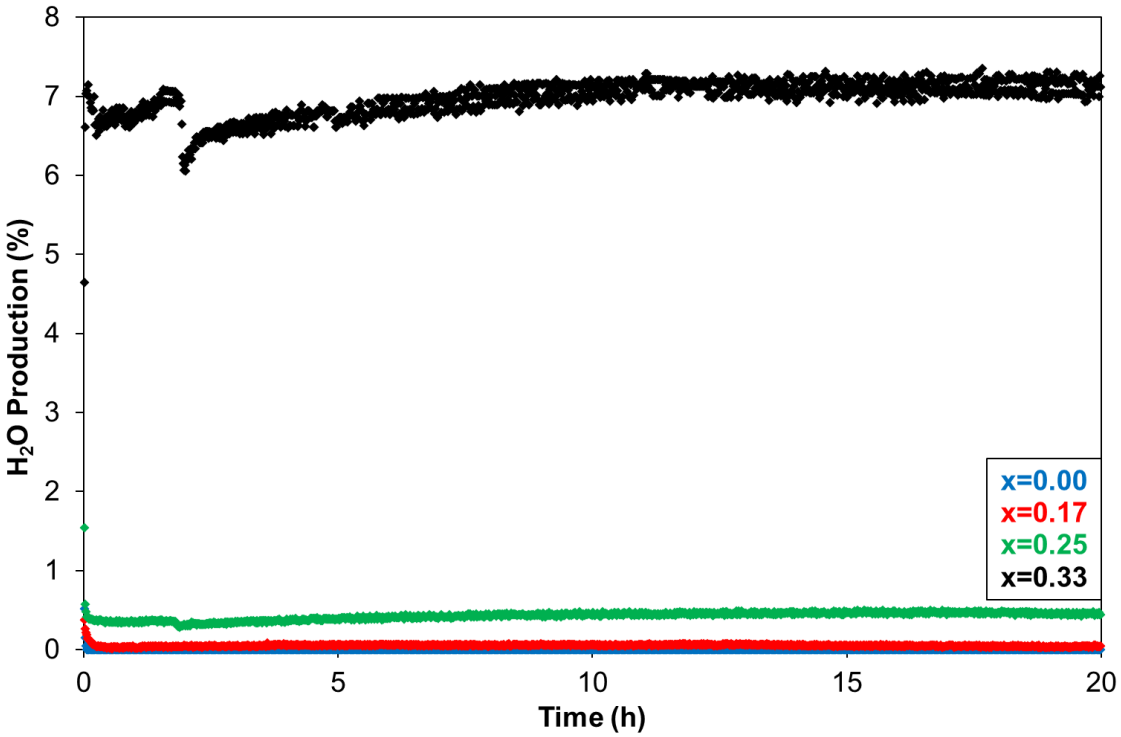

Figure 6.20: H_2O production for reaction of CH_4 + 0.5CO_2 + xO_2 over 5 mol% CeO_2-Ni/YSZ at 900 °C for 20 hours (x=0.00, 0.17, 0.25, 0.33)

From comparison with the equivalent reactions over Ni/YSZ (Section 5.3.4), it can be seen that 5 mol% CeO_2-Ni/YSZ exhibits slightly greater stability in H_2 yield than Ni/YSZ, with the exception of the reaction in the absence of O_2 which undergoes deactivation through carbon deposition, which is not seen over Ni/YSZ. This greater stability may be due to an increased resistance towards sintering of the 5 mol% CeO_2-Ni/YSZ catalyst, as discussed in Section 2.6.3. Significantly less stability in the CO yield is observed for 5 mol% CeO_2-Ni/YSZ compared to Ni/YSZ in that the CO yield decreases with time over Ni/YSZ but increases with time over 5 mol% CeO_2-Ni/YSZ. This has been attributed to the increased carbon deposition and potential for the reverse Boudouard reaction over 5 mol% CeO_2-Ni/YSZ than Ni/YSZ.

6.3.5 Reaction of CH_4 + 0.5CO_2+ xO_2 over 5 mol% CeO_2-Ni/YSZ at 1000 °C

At 1000 °C (Figures 6.21 – 6.24), similar behaviour is observed to that at 900 °C (Figures 6.17 – 6.20), with the exception of the physical blocking of the reactor tube due to carbon deposition when x=0.17 at 1000 °C. The sudden feature in the reaction profile present at *ca.* 18 hours in the absence of oxygen (Figures 6.21 – 6.23) is attributed to total physical blocking of the reactor tube through carbon deposition. As at 900 °C, where x=0.25 and 0.33, the H_2 yield (Figure 6.21) shows high stability with no cycling behaviour and CO yield (Figure 6.22) increases over time. The lack of cycling may be due to the high reforming activity, whilst the variation in CO yield may be due to carbon deposition and increasing reverse Boudouard reaction. Substantial carbon is detected for all O_2 conditions except when x=0.33 (Figure 6.31).

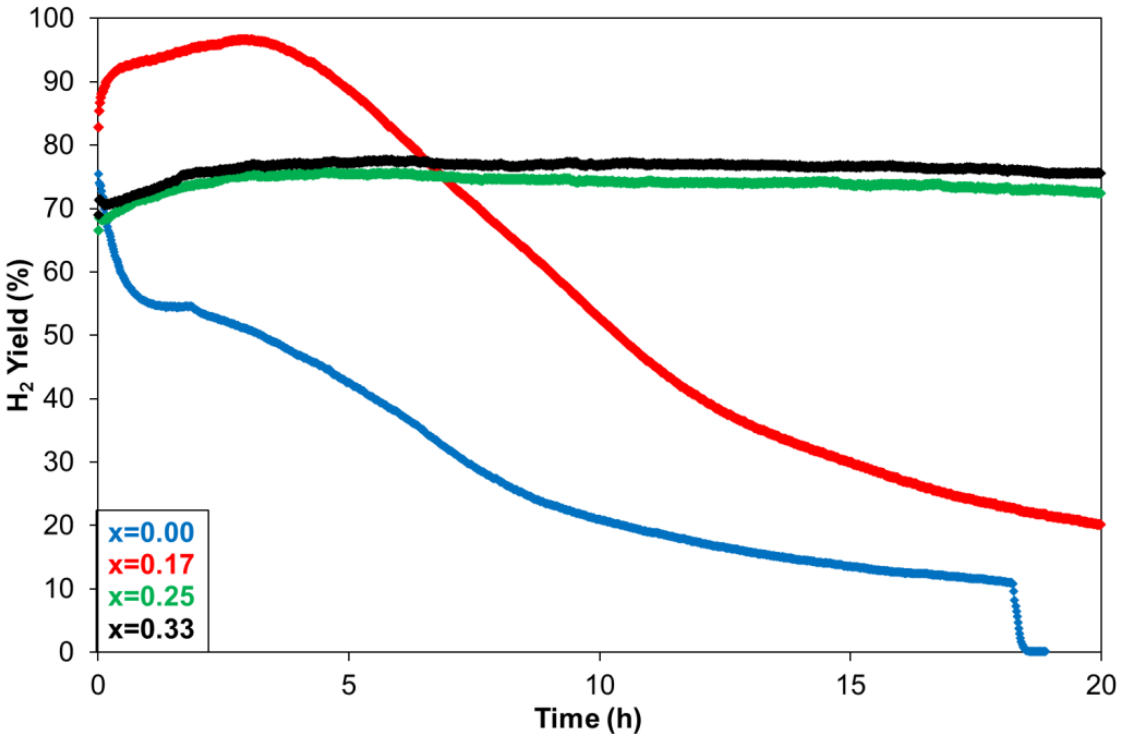

Figure 6.21: H_2 yield for reaction of CH_4 + 0.5CO_2 + xO_2 over 5 mol% CeO_2-Ni/YSZ at 1000 °C for 20 hours (x=0.00, 0.17, 0.25, 0.33)

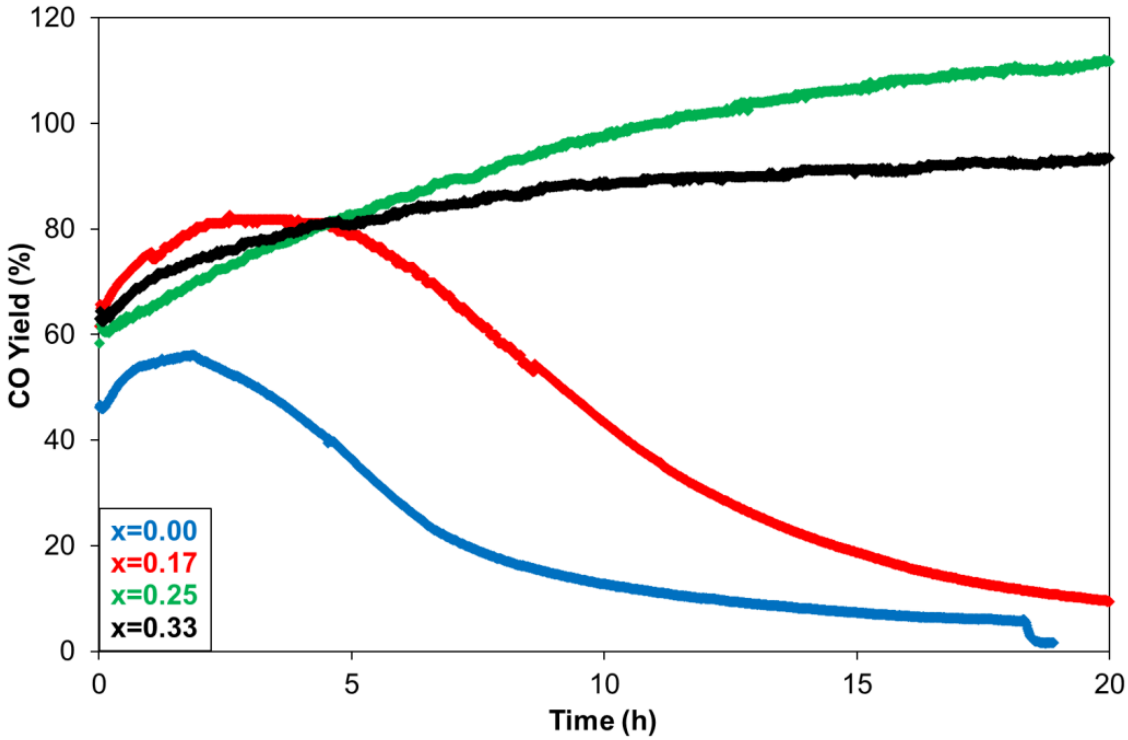

Figure 6.22: CO yield for reaction of CH_4 + 0.5CO_2 + xO_2 over 5 mol% CeO_2-Ni/YSZ at 1000 °C for 20 hours (x=0.00, 0.17, 0.25, 0.33)

The most notable difference in behaviour between Ni/YSZ (Figure 5.17 and Table 5.3) and 5 mol% CeO_2-Ni/YSZ (Figures 6.21 – 6.24) at 1000 °C is the physical deactivation through carbon deposition when x=0.17 over 5 mol% CeO_2-Ni/YSZ, which is not observed over Ni/YSZ. Additionally, the rate of deactivation through physical blocking differs between catalysts; over Ni/YSZ in the absence of O_2 at 1000 °C, physical blocking through carbon deposition is not apparent until approximately eight hours on-line when a sudden change is seen. However, for the same reaction conditions over 5 mol% CeO_2-Ni/YSZ, deactivation is more progressive with time and occurs from approximately two hours on-line. This variation may suggest the formation of different carbon morphologies. The more severe deactivation observed over 5 mol% CeO_2-Ni/YSZ may suggest a more structured carbon morphology such as filamentous carbon, which would more actively cause physical blocking as discussed in Section 2.6.2 [23]. Electron microscopy is an analytical technique that could be used to provide a greater insight into different carbon morphologies [24].

The extent of carbon deposition, shown in Figure 6.31, may also explain the nature of deactivation through physical blocking and that simply a greater quantity of carbon deposition over 5 mol% CeO_2-Ni/YSZ causes more severe deactivation. Although the TPO method of measuring the mass of carbon deposited during the reaction is limited in accuracy to <30 mg due to a shift from complete to incomplete combustion above this quantity, it is possible to gain a qualitative indication of amount of carbon deposited. This can be achieved through comparing the length of time in which carbon oxides are detected for each catalyst (Table 6.4). Over Ni/YSZ, carbon oxides were detected from approximately 500 – 900 °C and for 6 minutes when the temperature was held at 900 °C, whereas for 5 mol% CeO_2-Ni/YSZ, carbon oxides were detected from approximately 300 – 900 °C and for over 1 hour when the temperature was held at 900 °C. This indicates that a greater quantity of carbon was deposited over 5 mol% CeO_2-Ni/YSZ than Ni/YSZ at 1000 °C.

When x=0.25 and 0.33, the CO yield is stable with Ni/YSZ but increases over time with 5 mol% CeO_2-Ni/YSZ. This, as at lower temperatures, is attributed to the increased extent of carbon deposition and potential for the reverse Boudouard reaction.

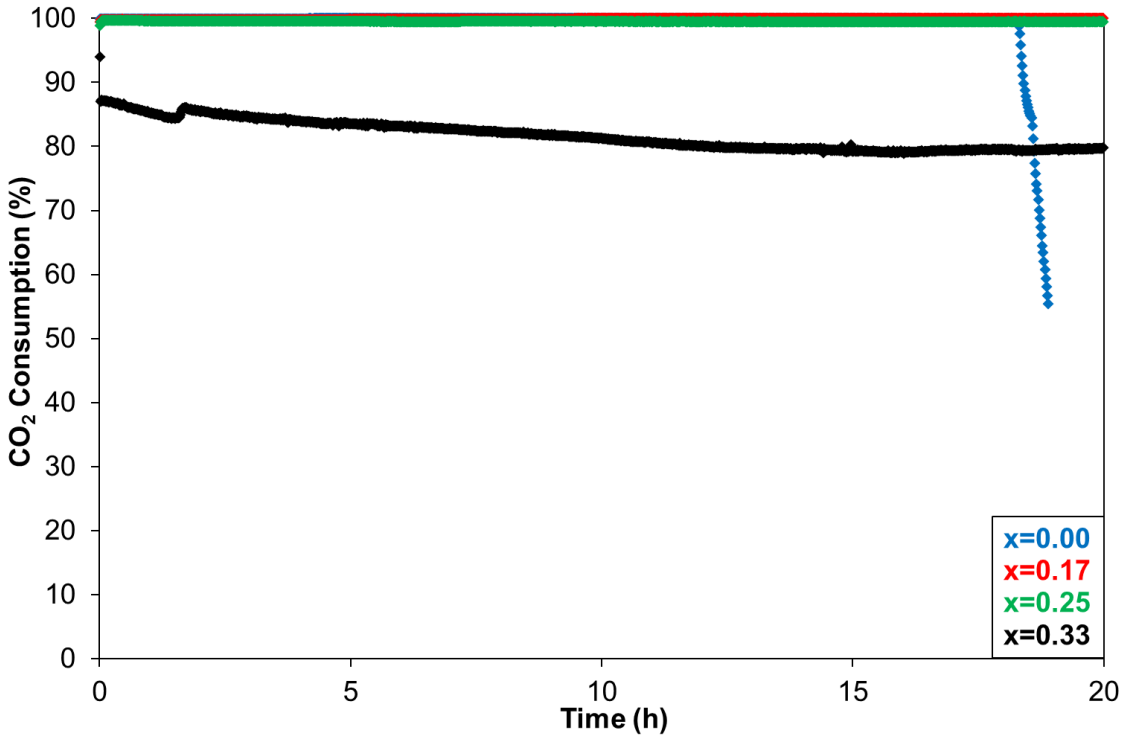

Figure 6.23: CO_2 consumption for reaction of CH_4 + 0.5CO_2 + xO_2 over 5 mol% CeO_2-Ni/YSZ at 1000 °C for 20 hours (x=0.00, 0.17, 0.25, 0.33)

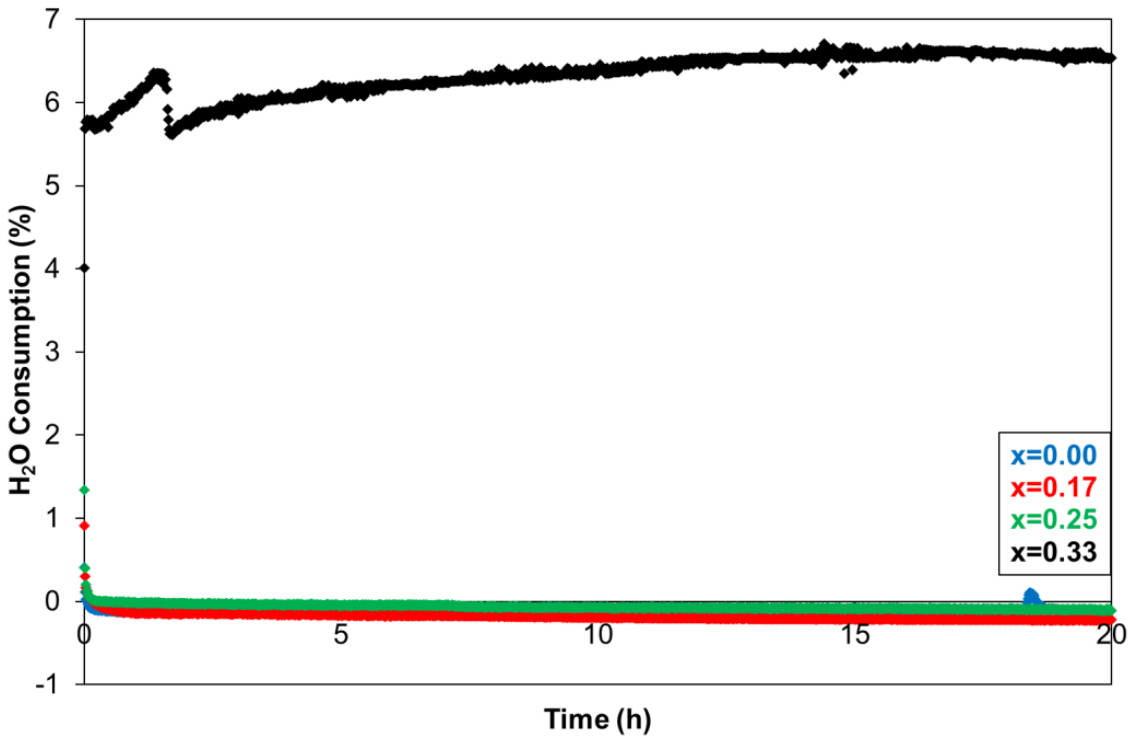

Figure 6.24: H_2O production for reaction of CH_4 + 0.5CO_2 + xO_2 over 5 mol% CeO_2-Ni/YSZ at 1000 °C for 20 hours (x=0.00, 0.17, 0.25, 0.33)

6.3.6 Influence of reaction temperature for reaction of CH_4 + 0.5O_2 +xO_2 over Ni/YSZ and 5 mol% CeO_2-Ni/YSZ

To compare the influence of temperature across the temperature range for both catalyst materials and different gas ratios in a user friendly way, average values are taken as the mean value between 2 hours and 20 hours on-line to limit the influence of initial saturation effects that are uncharacteristic of the overall reaction. Although substantial variations are exhibited over time, particularly in CO yield, the use of mean averages is considered as the most accessible and effective approach to compare certain parameters across such a range of different variables.

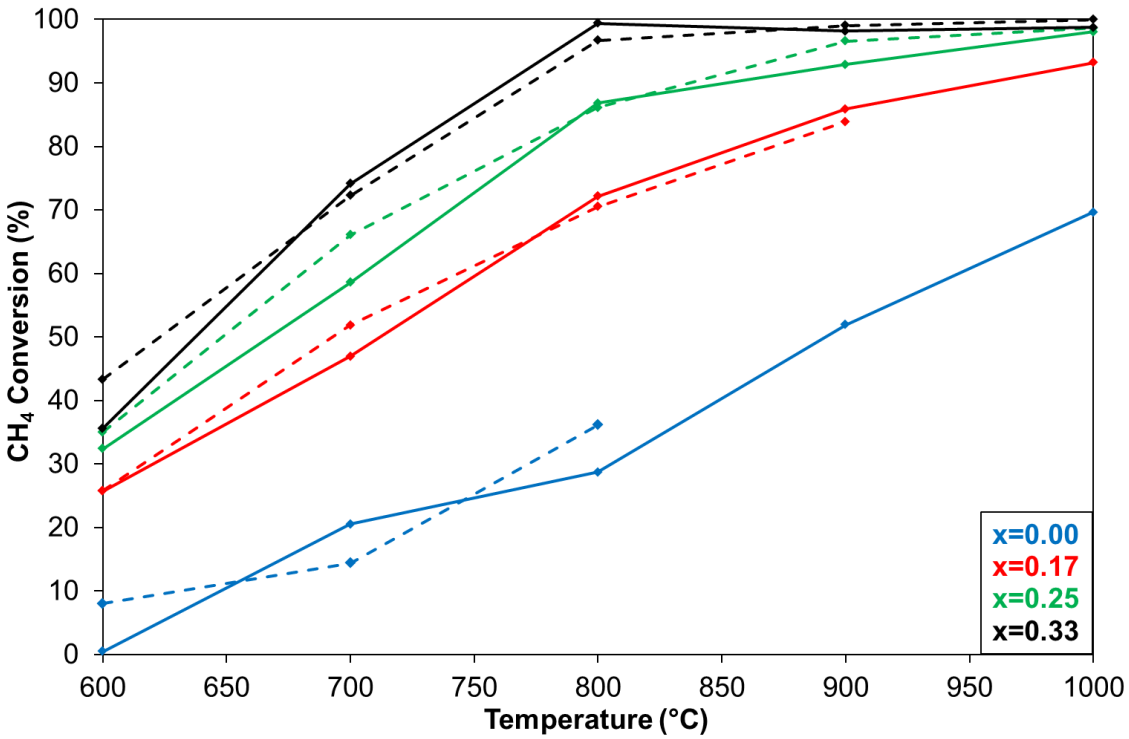

Figure 6.25: Average CH_4 conversion for reaction of CH_4 + 0.5CO_2 + xO_2 over 5 mol% CeO_2-Ni/YSZ (dashed) and Ni/YSZ (solid) for 20 hours across the temperature range of 600-1000 °C (x=0.00, 0.17, 0.25, 0.33)

Over 5 mol% CeO_2-Ni/YSZ, a very similar influence of O_2 addition on the CH_4 + CO_2 reaction with increasing temperature is observed with respect to methane conversion (Figure 6.25). The data points when x=0.00 at 900 °C and 1000 °C and x=0.17 at 1000 °C are not included as the averages are not representative due to the significant deactivation from carbon deposition.

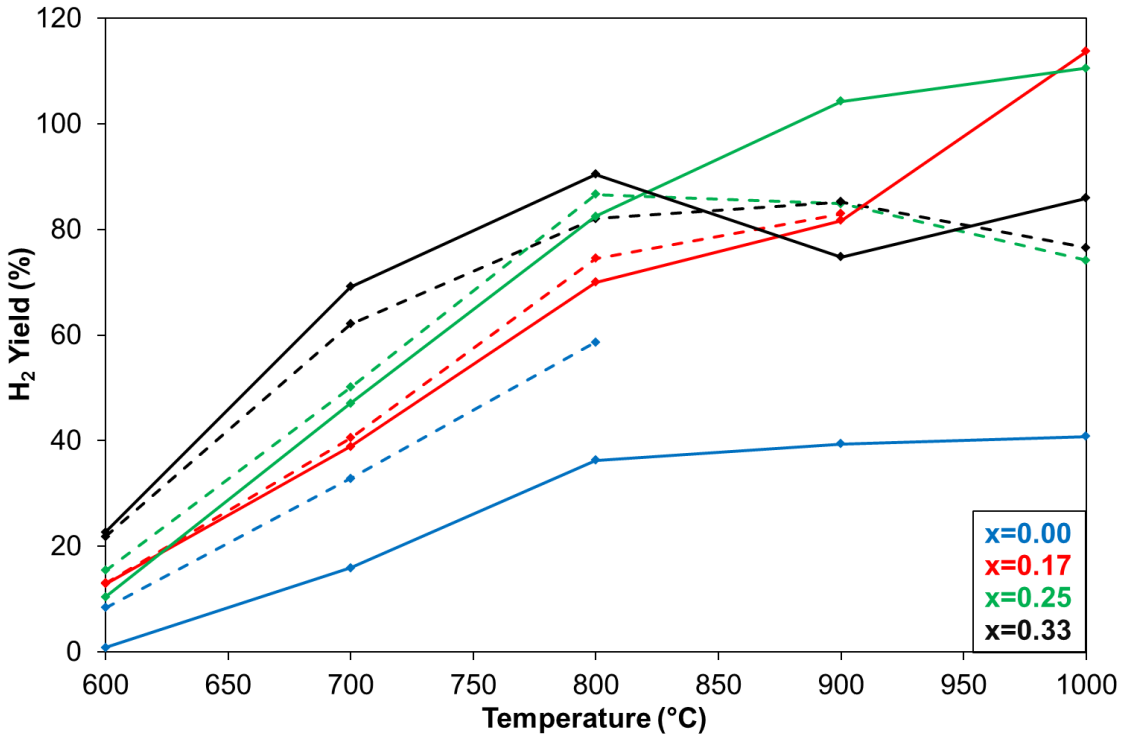

Figure 6.26: Average H_2 conversion for reaction of CH_4 + 0.5CO_2 + xO_2 over 5 mol% CeO_2-Ni/YSZ (dashed) and Ni/YSZ (solid) for 20 hours across the temperature range of 600-1000 °C (x=0.00, 0.17, 0.25, 0.33)

Greater variation between 5 mol% CeO_2-Ni/YSZ and Ni/YSZ is seen in the H_2 yield (Figure 6.26) than methane conversion (Figure 6.25). In the absence of O_2, the H_2 yield for 5 mol% CeO_2-Ni/YSZ is significantly greater than for Ni/YSZ for reaction temperatures up to 800 °C. This may be attributed to the ability of ceria to promote methane reforming through the ability of CO_2 to oxidise Ce_2O_3, which can then donate oxygen to assist methane reforming.

When O_2 is added to the CH_4/CO_2 reaction gas mixture, 5 mol% CeO_2-Ni/YSZ show similar H_2 yields (from 600-800 °C) as Ni/YSZ. The slightly lower H_2 yield when x=0.33 between 600 °C to 800 °C may be due to a small amount of methane coupling resulting in the production of higher hydrocarbons. Methane coupling products such as ethane and ethene were not detected, however the high mass 28 signal contributed from carbon monoxide makes the detection of small quantities of products such as ethane and ethene very difficult.

For the reactions carried out over Ni/YSZ, H_2 yield increases with temperature except when x=0.33, where the H_2 yield decreases slightly above 800 °C. This increase in H_2 yield is due to an increase in both the reforming and methane decomposition reactions. The slight decrease is attributed to increasing total oxidation of methane. With 5 mol% CeO_2-Ni/YSZ however, the H_2 yield for the reactions in the presence of O_2 from 600 °C - 800 °C is similar to that for Ni/YSZ, but is lower at 900 °C when x=0.25 and at 1000 °C with all CH_4:xO_2 ratios. This behaviour may suggest that methane coupling is occurring over 5 mol% CeO_2-Ni/YSZ at higher temperatures as no respective reduction in methane conversion or increase in total oxidation products are observed.

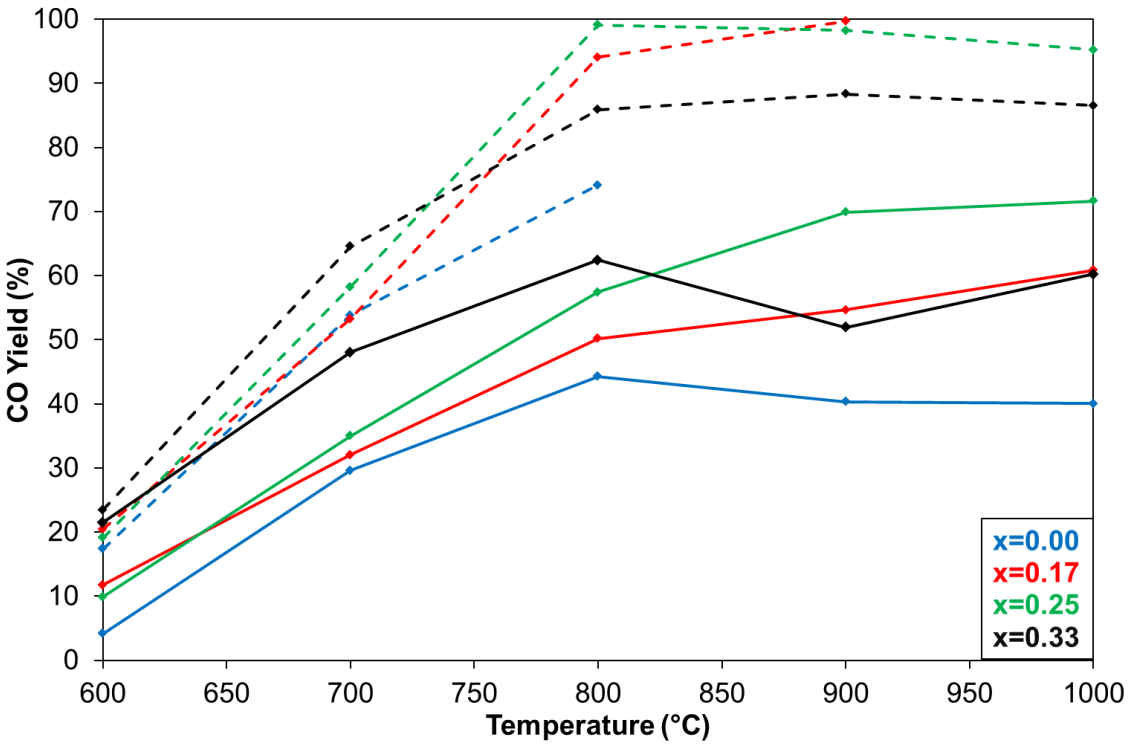

Figure 6.27: Average CO yield for reaction of CH_4 + 0.5CO_2 + xO_2 over 5 mol% CeO_2-Ni/YSZ (dashed) and Ni/YSZ (solid) for 20 hours across the temperatures range of 600-1000 °C (x=0.00, 0.17, 0.25, 0.33)

The influence of O_2 addition to the CH_4 + CO_2 reaction on the CO yield ((Figure 6.27) at different temperatures varies significantly with the nature of the catalyst. With the Ni/YSZ catalyst, the CO yield increases with temperature due to an increase in the rate of methane reforming with the exception when x=0.33, where CO yield decreases above 800 °C. This may be due to an increase in

total oxidation of methane, which is supported by the increase in total oxidation products. Despite similar behaviour in CO yield with reaction temperature over 5 mol% CeO_2-Ni/YSZ, the CO yield is substantially greater than that seen over Ni/YSZ at all temperatures and CH_4:O_2 ratios. This can be attributed to the increased potential for dry reforming of methane with ceria [7, 9, 11], increased CO formation through the reaction of CO_2 to oxidise Ce^{3+} to CeO_2 [7, 25] and also through oxidation of surface carbon deposits on the catalyst surface by lattice oxygen provided by CeO_2 [13, 15].

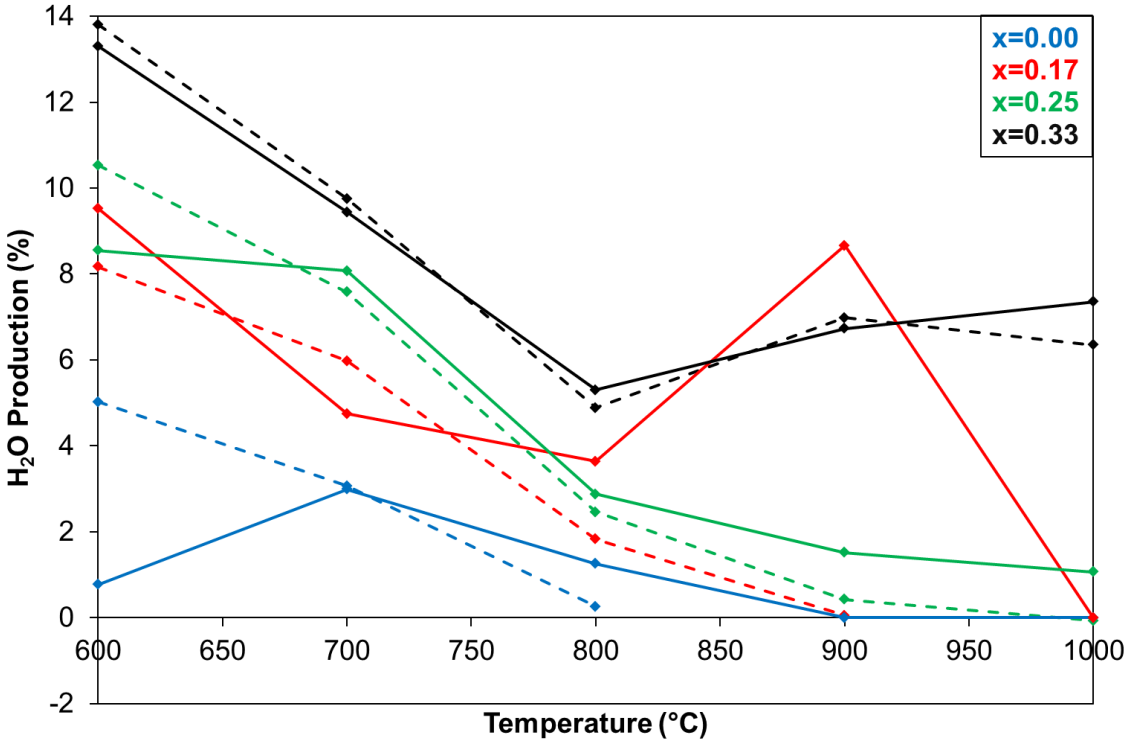

Figure 6.28: Average H_2O production for reaction of CH_4 + 0.5CO_2 + xO_2 over 5 mol% CeO_2-Ni/YSZ (dashed) and Ni/YSZ (solid) for 20 hours across the temperature range of 600-1000 °C (x=0.00, 0.17, 0.25, 0.33)

The H_2O production and CO_2 consumption used to assess the extent of total oxidation show similar profiles with reaction temperature for the two catalysts (Figures 6.28 and 6.29 respectively). The greater H_2O production over 5 mol% CeO_2-Ni/YSZ at 600 °C in the absence of O_2 can be attributed to the oxidation of H_2 by CeO_2 (Equation 6.13). The greater CO_2 consumption across all CH_4:O_2

ratios and temperatures over 5 mol% CeO_2-Ni/YSZ supports the suggestion of increased reforming activity and reverse Boudouard reaction occurring over 5 mol% CeO_2-Ni/YSZ.

$$CeO_2 + H_2 \rightleftharpoons Ce_2O_3 + H_2O \quad \textbf{(6-13)}$$

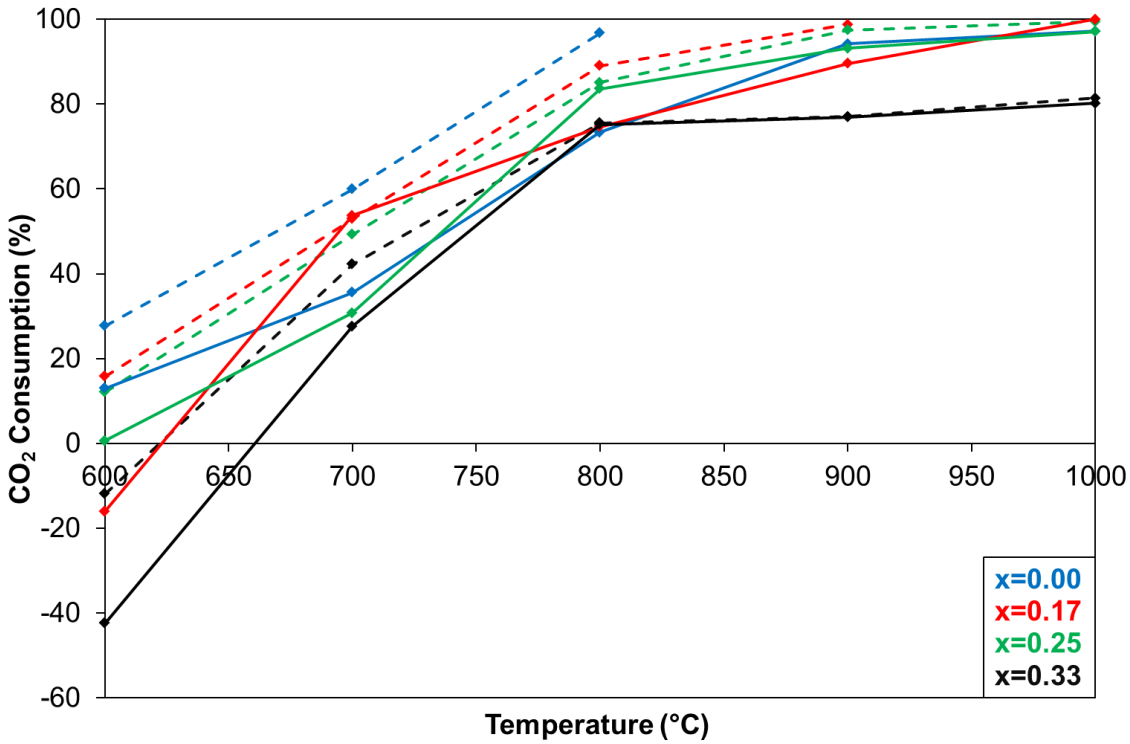

Figure 6.29: Average CO_2 consumption for reaction of CH_4 + 0.5CO_2 + xO_2 over 5 mol% CeO_2-Ni/YSZ (dashed) and Ni/YSZ (solid) for 20 hours across the temperature range of 600-1000 °C (x=0.00, 0.17, 0.25, 0.33)

Doping of Ni/YSZ with 5 mol% CeO_2 has a very significant influence on reducing the H_2:CO ratio (Figure 6.30) and making it less susceptible to changes in temperature and CH_4:O_2 ratios. The lower H_2:CO ratio for 5 mol% CeO_2-Ni/YSZ supports the suggestion that ceria favours dry reforming of methane. Increased reaction of CO_2 with Ce_2O_3 will also reduce the H_2:CO ratio. At higher reaction temperatures, the lower H_2:CO ratio suggests that ceria reduces the potential for methane decomposition, whilst methane coupling may also contribute to a lower H_2:CO ratio.

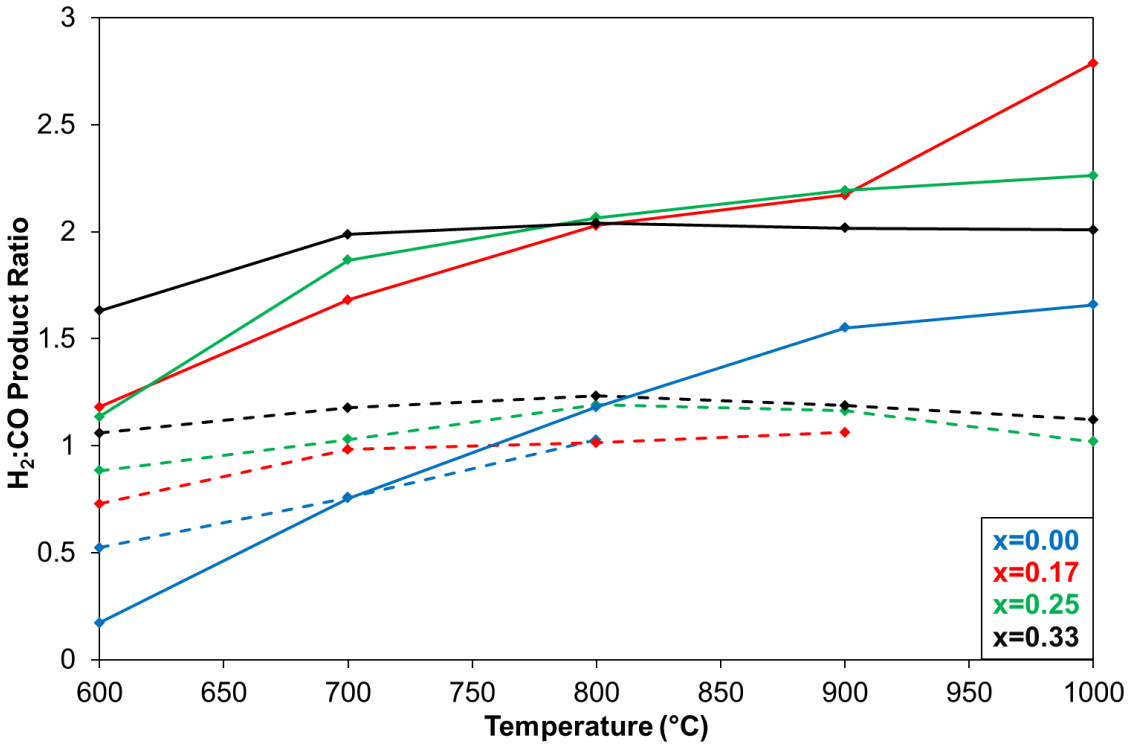

Figure 6.30: Average H_2:CO product ratio for reaction of CH_4 + 0.5CO_2 + xO_2 over 5 mol% CeO_2-Ni/YSZ (dashed) and Ni/YSZ (solid) for 20 hours across the temperature range of 600-1000 °C (x=0.00, 0.17, 0.25, 0.33)

6.3.7 Carbon deposition during reactions of CH_4 + 0.5CO_2 + xO_2 over 5 mol% CeO_2-Ni/YSZ across the temperatures range of 600-1000 °C and different O_2 concentrations

From analysis of the reaction studies discussed previously, it is evident that carbon deposition has a substantial influence on the activity, selectivity and stability of the 5 mol% CeO_2-Ni/YSZ catalyst, particularly at higher reaction temperatures. Post-reaction temperature programmed oxidation measurements (discussed in Section 3.6) were performed for all catalytic reactions carried out over 5 mol% CeO_2-Ni/YSZ and are shown in Figure 6.31.

Where carbon deposition exceeds 30 mg, all oxygen is consumed and incomplete combustion of carbon occurs. Such situations are illustrated with an arrowhead in Figure 6.31.

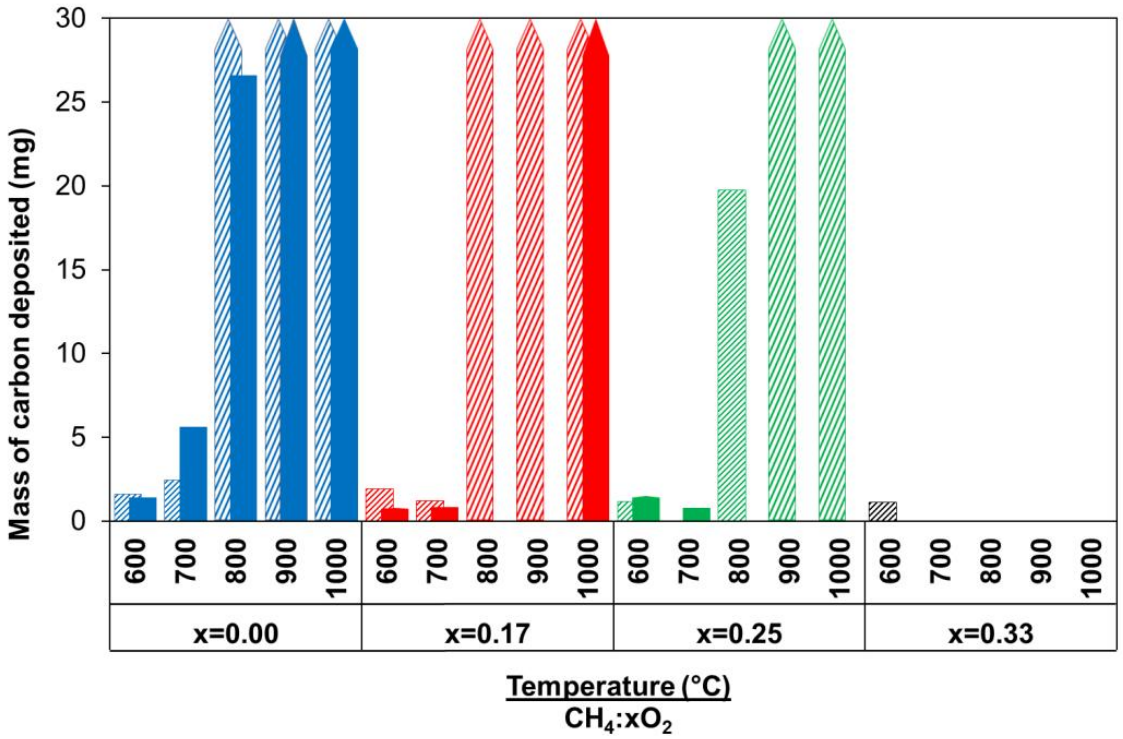

Figure 6.31: Mass of carbon deposited during 20 hour reactions of CH_4+ 0.5CO_2 + xO_2 over Ni/YSZ (Solid) and 5 mol% CeO_2-Ni/YSZ (Patterned) at temperatures between 600-1000 °C. Carbon masses measured through post-reaction temperature programmed oxidation and limited to 30 mg of carbon deposited. Greater masses are illustrated with an arrowhead.

Where carbon is produced to a greater extent than 30 mg, accurate mass analysis is difficult due to a variation in oxidation regime, as illustrated in Figure 3.8. However, by comparison of the length of time which carbon oxides were produced, it is possible to obtain a qualitative indication of the extent of carbon deposition and this is summarised in Table 6.4. From Table 6.4, it is apparent that

the addition of O_2 results in a substantial decrease in the extent of carbon deposited on 5 mol% CeO_2-Ni/YSZ and greater quantities of O_2 further reduce carbon deposition.

Table 6.4: Duration of carbon oxide generation during post-reaction temperature programmed oxidation following reactions of CH_4 + CO_2 + xO_2 over 5 mol% CeO_2-Ni/YSZ at temperatures between 800-1000 °C (x=0.00, 0.17, 0.25)

	Isothermal temperature (°C)		
	800	**900**	**1000**
CH_4:xO_2	**Duration of carbon oxide generation (minutes)**		
x=0.00	45	90	110
x=0.17	20	40	70
x=0.25	N/A	20	30

From Figure 6.31, it can be seen that the extent of carbon deposition is substantially greater over 5 mol% CeO_2-Ni/YSZ than over Ni/YSZ apart from at 600 °C and 700 °C. The greater carbon deposition over 5 mol% CeO_2-Ni/YSZ over Ni/YSZ at lower oxygen levels (x=0.00, 0.17 and 0.25), and high temperatures of 800 °C and above suggests that doping Ni/YSZ with 5 mol% CeO_2 encourages the decomposition of methane. The occurrence of other carbon depositing reactions such as CO hydrogenation and the Boudouard reaction are thermodynamically unfavourable above 700 °C (Figure 2.4). The possibility of erroneous measurements for x=0.17 at 800 and 900 °C is discussed in Section 5.3.7.

This greater extent of carbon deposition with CeO_2 doping is in disagreement with the majority of literature on the subject [10, 15, 17, 25, 26]. The literature generally reports that doping of nickel with CeO_2 reduces carbon deposition through oxidation of surface carbon with lattice oxygen and also through reduced sintering and subsequent smaller nickel particle size, which in turn is proposed to reduce carbon deposition [24, 27, 28]. The influence of particle size on carbon formation is discussed in greater detail in Section 2.6.2.2.

The larger particle size measured for 5 mol% CeO_2-Ni/YSZ than Ni/YSZ (shown in Section 4.4), may explain the greater carbon deposition over 5 mol% CeO_2-Ni/YSZ. Another explanation may also be that at reaction temperatures of 800 °C and above and at lower oxygen levels (x=0.00, 0.17 and 0.25), the ceria exists primarily in the reduced Ce_2O_3 form due to the H_2 rich atmosphere. Ce_2O_3 can attract electron density from adjacent nickel atoms to reduce the electron density of the nickel. This reduced electron density may then encourage C-H bond cleavage to donate an electron to the unfilled d-orbital of nickel, therefore encouraging methane decomposition.

The doping of ceria onto Ni/YSZ and proposed effect on particle size may suggest the formation of different carbon types. However, little variation is observed between the catalysts in the temperature programmed oxidation profiles shown in Figure 6.32. Where carbon is present over Ni/YSZ, two potential types/locations of carbon are observed, as shown in detail in Figure 5.26. The TPO profile for removal of carbon deposited on 5 mol% CeO_2-Ni/YSZ at 800 °C (Figure 6.32) shows a much broader CO_2 desorption peak than for Ni/YSZ, suggesting a less defined carbon type. In addition, a shoulder is seen at *ca*. 570 °C, whereas for Ni/YSZ this peak is observed at *ca*. 610 °C. The lower carbon desorption temperature for 5 mol% CeO_2-Ni/YSZ than Ni/YSZ was also observed by Stagg-Williams *et al*. [25], who suggests that doping of Ni/YSZ with CeO_2 increases the ability to oxidise carbon at lower temperatures. The variation in oxidation temperature of the carbon deposits between the two catalysts may suggest a difference in type or location of carbon deposits or simply that the presence of ceria increases the potential for carbon oxidation through an increased oxygen availability.

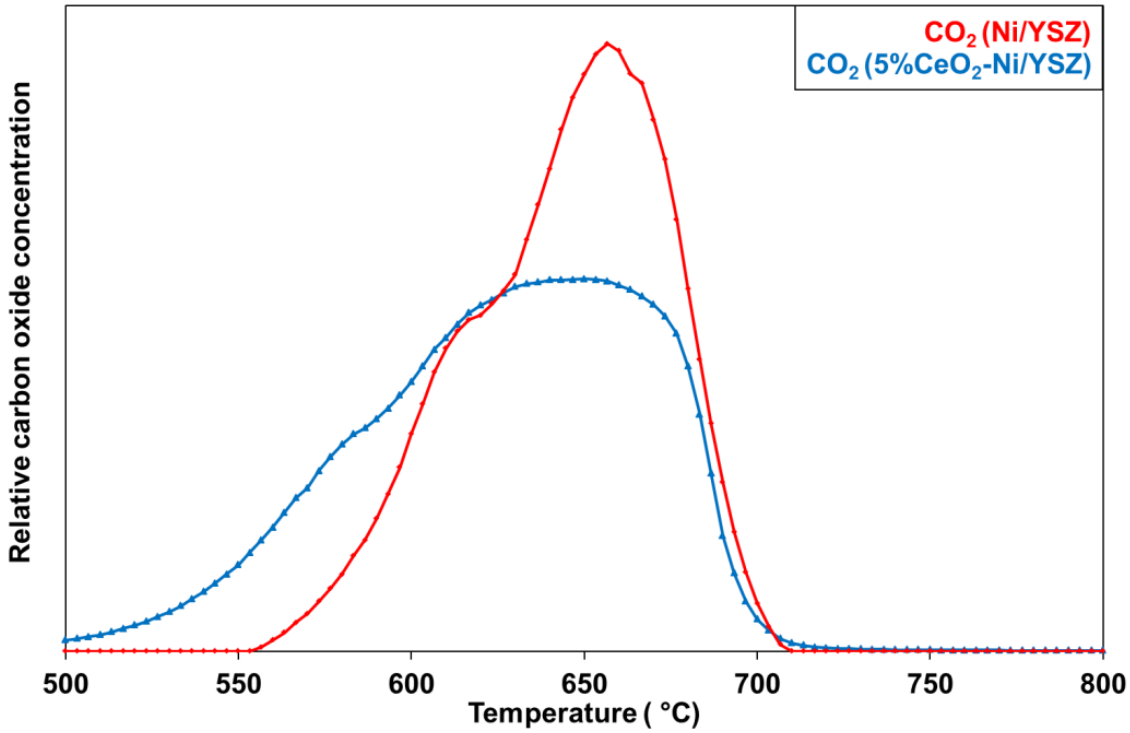

Figure 6.32: Post-reaction TPO profile showing CO_2 generation from oxidation of carbon deposited during isothermal reaction of CH_4 + 0.5CO_2 + 0.17O_2 over Ni/YSZ and 5 mol% CeO_2-Ni/YSZ at 800 °C

As with Ni/YSZ, reactions carried out over 5 mol% CeO_2-Ni/YSZ show very little deactivation over time through carbon deposition unless physical blocking occurs. This lack of extensive deactivation, despite the substantial amount of carbon deposition detected suggests the presence of carbon morphologies such as amorphous or filamentous carbon which are suggested to induce minimal deactivation and not highly deactivating morphologies such as encapsulating carbon (discussed in Section 2.6.2.1).

6.4 Summary of the influence of CeO_2 doping upon Ni/YSZ for the catalytic behaviour for reaction of $CH_4 + 0.5CO_2 + xO_2$

Temperature-programmed reaction and conventional catalytic reaction studies have been used to assess how doping Ni/YSZ with 5 mol% CeO_2 affects the reforming of simulated biogas and the influence of O_2 addition in varied quantities in relation to activity, selectivity and stability.

Temperature-programmed reaction studies show similar behaviour for both catalysts with both temperature variation and O_2 addition, with a slight variation at higher temperatures in that 5 mol% CeO_2-Ni/YSZ shows a lower activity than Ni/YSZ. This has been attributed to either a reduced potential for methane decomposition or a reduced active nickel surface area. A slightly lower light-off temperature was observed for the 5 mol% CeO_2-Ni/YSZ which suggests that ceria doping encourages selective oxidation over total oxidation.

The conventional reaction studies performed over each catalyst show significant variation, particularly in the occurrence of reaction cycling observed over 5 mol% CeO_2-Ni/YSZ. This cycling is due to the transient reduction-oxidation cycle of ceria. Cycling behaviour is seen at 700 °C and to a lesser extent at 800 °C. The reduced extent of cycling at increased temperatures is attributed to increased methane reforming and a subsequent H_2-rich atmosphere and reduced availability of CO_2.

Similar H_2 yields are observed at reaction temperatures between 600 °C - 800 °C for all O_2:CH_4 ratios. In the absence of oxygen, a greater yield is observed over 5 mol% CeO_2-Ni/YSZ due to the ability of Ce_2O_3 to react with CO_2 and promote methane reforming through lattice oxygen. The lower H_2 yield at higher temperatures over 5 mol% CeO_2-Ni/YSZ may be due either to reduced methane decomposition or a reduced active nickel surface area.

With regards to CO yield, doping of Ni/YSZ with 5 mol% CeO_2 has been shown to significantly influence stability, particularly at high temperatures (≥800 °C), in that the CO yield increases over time with 5 mol% CeO_2-Ni/YSZ, whereas it is stable over Ni/YSZ. This has been attributed to

greater carbon deposition, resulting in a greater extent of the reverse Boudouard reaction or oxidation of surface carbon through lattice oxygen to produce CO. The influence of ceria doping on Ni/YSZ is also illustrated in the significantly more stable H_2:CO ratio. This more stable H_2:CO is undesirable as the greater capacity to tailor the product ratio makes the process more economically viable, as discussed in Section 2.3.7 and 5.4.

Substantially greater carbon deposition was observed on 5 mol% CeO_2-Ni/YSZ catalyst compared to on Ni/YSZ, especially above 800 °C. The increased carbon deposition may be explained by either the greater particle size or the potential for Ce_2O_3 to encourage C-H bond cleavage.

6.5 References

1. A. Trovarelli, ed. *Catalysis by Ceria and Related Materials*. Catalytic Science Series, ed. G.J. Hutchings. 2002, Imperial College Press.
2. J. Beckers and G. Rothenberg, *Sustainable selective oxidations using ceria-based materials.* Green Chemistry, 2010. **12**(6): p. 939-948.
3. A. Trovarelli, C. de Leitenburg, M. Boaro, and G. Dolcetti, *The utilization of ceria in industrial catalysis.* Catalysis Today, 1999. **50**(2): p. 353-367.
4. H.S. Gandhi, G.W. Graham, and R.W. McCabe, *Automotive exhaust catalysis.* Journal of Catalysis, 2003. **216**(1-2): p. 433-442.
5. Manufacturers-of-Emission-Controls-Association (2011) *The Catalytic Converter: Technology for Clean Air*. Clean Air Facts.
6. W.S. Dong, K.W. Jun, H.S. Roh, Z.W. Liu, and S.E. Park, *Comparative study on partial oxidation of methane over Ni/ZrO_2, Ni/CeO_2 and Ni/Ce-ZrO_2 catalysts.* Catalysis Letters, 2002. **78**(1-4): p. 215-222.
7. N. Laosiripojana and S. Assabumrungrat, *Catalytic dry reforming of methane over high surface area ceria.* Applied Catalysis B: Environmental, 2005. **60**(1-2): p. 107-116.
8. S. Eriksson, S. Rojas, M. Boutonnet, and J.L.G. Fierro, *Effect of Ce-doping on Rh/ZrO_2 catalysts for partial oxidation of methane.* Applied Catalysis A: General, 2007. **326**(1): p. 8-16.
9. H. He and J.M. Hill, *Carbon deposition on Ni/YSZ composites exposed to humidified methane.* Applied Catalysis A: General, 2007. **317**(2): p. 284-292.
10. N. Laosiripojana, W. Sutthisripok, and S. Assabumrungrat, *Synthesis gas production from dry refoming of methane over CeO_2 doped Ni/Al_2O_3: Influence of the doping ceria on the resistance toward carbon formation.* Chem. Eng. J., 2005. **112**: p. 13-22.
11. K.Y. Koo, H.S. Roh, U.H. Jung, and W.L. Yoon, *CeO_2 Promoted Ni/Al_2O_3 Catalyst in Combined Steam and Carbon Dioxide Reforming of Methane for Gas to Liquid (GTL) Process.* Catalysis Letters, 2009. **130**(1-2): p. 217-221.

12. C. Xu, J.W. Zondlo, M. Gong, F. Elizalde-Blancas, X. Liu, and I.B. Celik, *Tolerance tests of H_2S-laden biogas fuel on solid oxide fuel cells.* Journal of Power Sources, 2010. **195**(15): p. 4583-4592.

13. M. Rezaei, S.M. Alavi, S. Sahebdelfar, and Z.-F. Yan, *A highly stable catalyst in methane reforming with carbon dioxide.* Scripta Materialia, 2009. **61**(2): p. 173-176.

14. F.B. Passos, E.R. de Oliveira, L.V. Mattos, and F.B. Noronha, *Partial oxidation of methane to synthesis gas on Pt/Ce_xZr_1-xO_2 catalysts: the effect of the support reducibility and of the metal dispersion on the stability of the catalysts.* Catalysis Today, 2005. **101**(1): p. 23-30.

15. S. Wang and G.Q. Lu, *Role of CeO_2 in Ni/CeO_2-Al_2O_3 catalysts for carbon dioxide reforming of methane.* Applied Catalysis B: Environmental, 1998. **19**(3-4): p. 267-277.

16. S. Xu and X. Wang, *Highly active and coking resistant Ni/CeO_2-ZrO_2 catalyst for partial oxidation of methane.* Fuel, 2005. **84**(5): p. 563-567.

17. H.-S. Roh, H.S. Potdar, and K.-W. Jun, *Carbon dioxide reforming of methane over co-precipitated Ni-CeO_2, Ni-ZrO_2 and Ni-Ce-ZrO_2 catalysts.* Catalysis Today, 2004. **93-95**: p. 39-44.

18. F. Pompeo, D. Gazzoli, and N.N. Nichio, *Stability improvements of Ni/[alpha]-Al_2O_3 catalysts to obtain hydrogen from methane reforming.* International Journal of Hydrogen Energy, 2009. **34**(5): p. 2260-2268.

19. E. Mamontov, T. Egami, R. Brezny, M. Koranne, and S. Tyagi, *Lattice Defects and Oxygen Storage Capacity of Nanocrystalline Ceria and Ceria-Zirconia.* The Journal of Physical Chemistry B, 2000. **104**(47): p. 11110-11116.

20. S. Naito, *Methane conversion by various metal, metal oxide and metal carbide catalysts.* Catalysis Surveys from Japan, 2000. **4**(1): p. 3-15.

21. N. Muradov, *Catalysis of methane decomposition over elemental carbon.* Catalysis Communications, 2001. **2**(3-4): p. 89-94.

22. S. Xu, X. Yan, and X. Wang, *Catalytic performances of NiO-CeO_2 for the reforming of methane with CO_2 and O_2.* Fuel, 2006. **85**(14-15): p. 2243-2247.

23. S. Tang, L. Ji, J. Lin, H.C. Zeng, K.L. Tan, and K. Li, *CO_2 Reforming of Methane to Synthesis Gas over Sol-Gel-made Ni/[gamma]-Al_2O_3 Catalysts from Organometallic Precursors.* Journal of Catalysis, 2000. **194**(2): p. 424-430.

24. Y.H. Hu and E. Ruckenstein, *High-resolution transmission electron microscopy study of carbon deposited on the NiO MgO solid solution catalysts.* Journal of Catalysis, 1999. **184**(1): p. 298-302.

25. S.M. Stagg-Williams, F.B. Noronha, G. Fendley, and D.E. Resasco, *CO_2 Reforming of CH_4 over Pt/ZrO_2 Catalysts Promoted with La and Ce Oxides.* Journal of Catalysis, 2000. **194**(2): p. 240-249.

26. H.S. Roh, K.W. Jun, S.C. Baek, and S.E. Park, *A highly active and stable catalyst for carbon dioxide reforming of methane: Ni/Ce-ZrO_2/theta-Al_2O_3.* Catalysis Letters, 2002. **81**(3-4): p. 147-151.

27. S. Corthals, J. Van Nederkassel, J. Geboers, H. De Winne, J. Van Noyen, B. Moens, B. Sels, and P. Jacobs, *Influence of composition of $MgAl_2O_4$ supported $NiCeO_2ZrO_2$ catalysts on coke formation and catalyst stability for dry reforming of methane.* Catalysis Today, 2008. **138**(1-2): p. 28-32.

28. K.O. Christensen, D. Chen, R. Lødeng, and A. Holmen, *Effect of supports and Ni crystal size on carbon formation and sintering during steam methane reforming.* Applied Catalysis A: General, 2006. **314**(1): p. 9-22.

7 Influence of O_2 addition in varied concentrations on the tolerance of Ni/YSZ and 5 mol% CeO_2-Ni/YSZ to H_2S deactivation during CO_2 reforming of CH_4

7.1 Detrimental nature of hydrogen sulfide for biogas reforming over supported nickel based catalysts

Various sulfur containing compounds are present within biogas, of which hydrogen sulfide (H_2S) is the most prevalent [1]. The variable composition of biogas means that the H_2S concentration can vary widely, with concentrations of thousands of parts per million reported [2]. Industrial natural gas utilisation systems often implement desulfurization techniques to reduce H_2S concentrations to <100 ppm levels due to the harmful and corrosive nature of H_2S.

The presence of H_2S within biogas presents a significant issue for reforming over nickel based catalysts in that sulfur is known to induce substantial deactivation of nickel catalysts [3]. This deactivation occurs through the binding of sulfur onto the nickel surface, preventing the adsorption of methane and reformant (CO_2, O_2, H_2O) [4, 5]. The nature of deactivation by sulfur poisoning is discussed in detail in Section 2.6.1. Due to the cost and increased size associated with implementing desulfurization techniques, the development of increasingly sulfur tolerant systems for biogas reforming over nickel based catalysts is highly desirable.

To establish the influence of H_2S towards the dry reforming of methane with and without O_2 addition over nickel based catalysts, a series of reactions have been carried out over the temperature range of 600-1000 °C used to date in this study and the standard reactant gas compositions used previously, but with the addition of 5ppm H_2S relative to the methane concentration.

7.2 CO_2 reforming of CH_4 over Ni/YSZ in the presence of 5ppm H_2S with and without addition of O_2

For the conventional studies carried out with the addition of H_2S, H_2 yield has been used as the sole parameter to assess the tolerance of the system towards deactivation by sulfur. The methane conversion has not been used due to the increased potential for total oxidation of methane as sulfur is adsorbed onto the nickel surface. This is shown in Figure 7.1 where significant water production is observed at *ca.* 8 hours. Similar behaviour has been reported by Choudhary *et al.* [6]. This increase in total oxidation influences methane conversion and therefore provides an inaccurate illustration of the activity of the system for synthesis gas production.

Carbon monoxide yield could also be used to illustrate the reaction characteristics, however the CO yield shows almost identical behaviour to that of H_2 yield in terms of deactivation rate. CO yield is therefore not shown, however it does reinforce the appropriateness of using H_2 yield to study deactivation rate and catalyst behaviour. An example of the variation between H_2 and CO yield over time within the same experiment is shown in Figure 7.2. Details of CH_4 conversion, CO yield and H_2:CO ratio that are not included in this section are available in Appendix B.

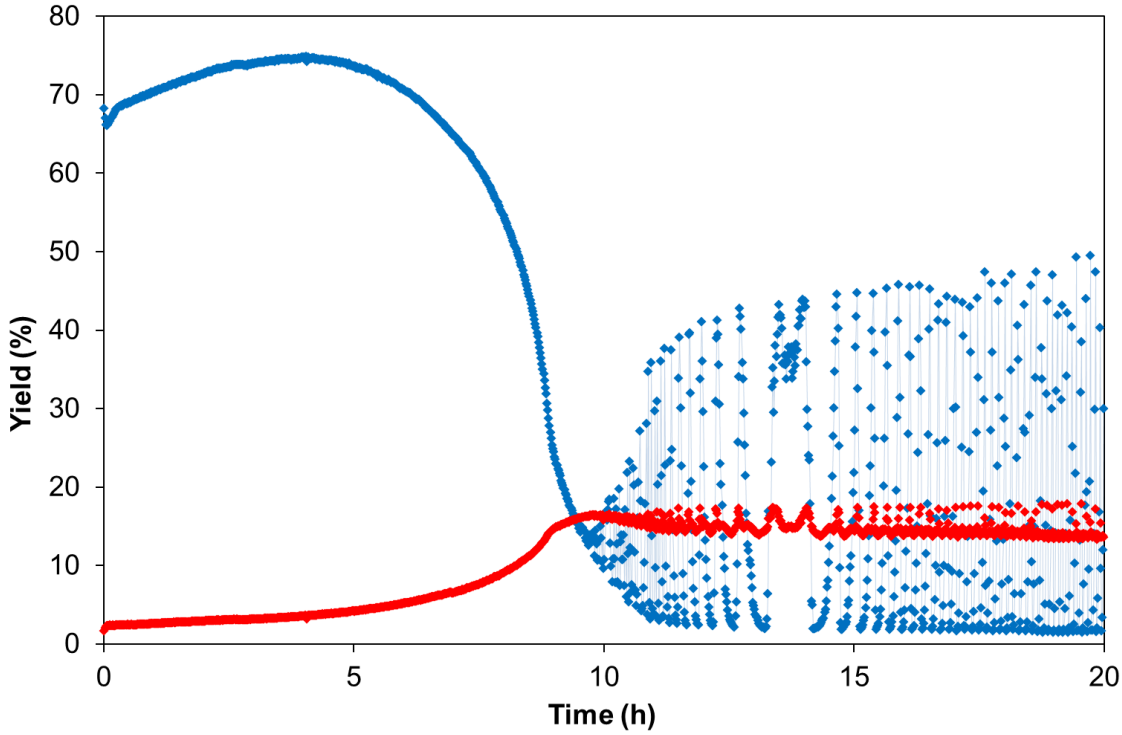

Figure 7.1: H_2 yield (Blue) and H_2O production (Red) for reaction of CH_4 + 0.5CO_2 + 0.25O_2 + 5 ppm H_2S over Ni/YSZ at 800 °C for 20 hours. Data points for H_2 yield are connected to illustrate cycling nature.

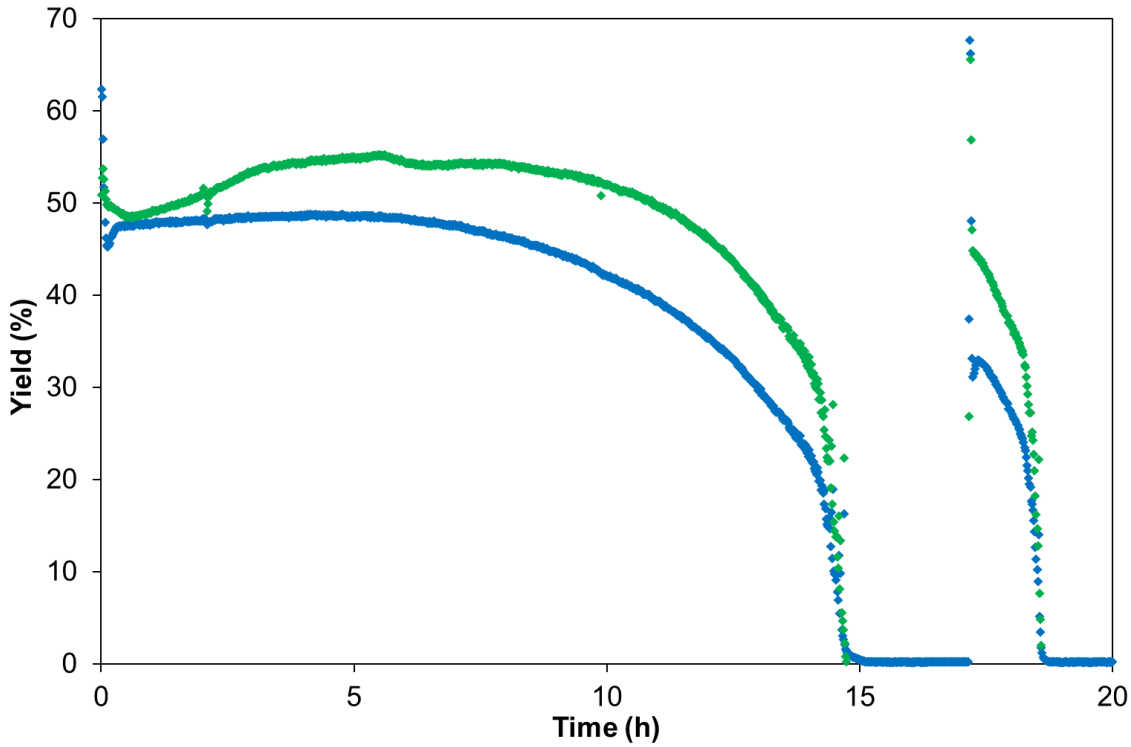

Figure 7.2: H_2 (Blue) and CO (Green) yield for reaction of CH_4 + 0.5CO_2 + 0.25O_2 + 5ppm H_2S over Ni/YSZ at 700 °C for 20 hours

7.2.1 Reaction of CH_4 + 0.5CO_2 + xO_2 over Ni/YSZ at 600 °C in the presence of 5ppm H_2S

The measurements carried out at 600 °C (Figure 7.3) show the extent of deactivation by sulfur over nickel catalysts, in that with every O_2:CH_4 ratio used, complete deactivation occurred within the 20 hour reaction duration. In the absence of O_2, the influence of H_2S on catalyst activity is difficult to assess due to the minimal activity for the reaction at this temperature, as shown in Figure 5.8. Upon addition of 0.17 O_2 to the CH_4:CO_2 mixture, there is a significant increase in the initial activity which steadily decreases due to deactivation until complete deactivation occurs after *ca.* 18 hours.

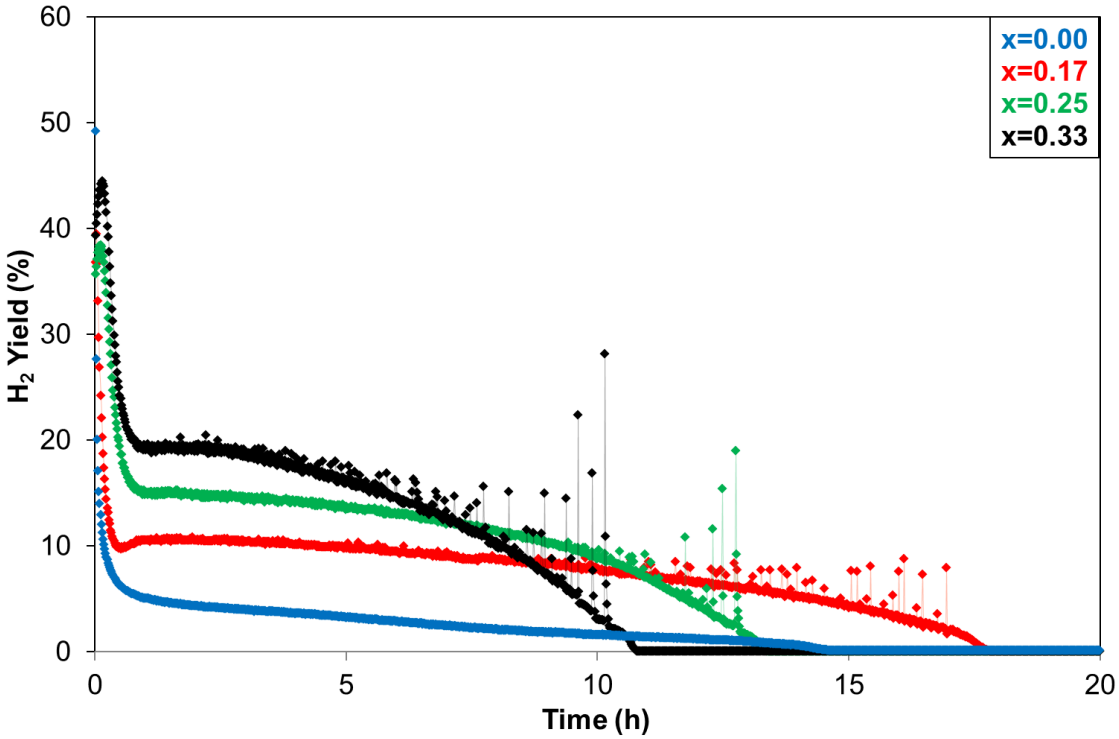

Figure 7.3: H_2 yield for reaction of CH_4 + 0.5CO_2 + xO_2 + 5ppm H_2S over Ni/YSZ at 600 °C for 20 hours (x=0.00, 0.17, 0.25, 0.33). Data points for H_2 yield are connected to illustrate cycling nature.

The reduction in activity with time can be attributed to sulfur poisoning as no deactivation is observed for the reaction under these conditions in the absence of H_2S (Section 5.3.1). A significant feature visible for the reactions with the addition of O_2 is the cycling nature, similar to that observed over 5 mol% CeO_2-Ni/YSZ (Section 6.3.1). In the absence of H_2S, the cycling behaviour over 5 mol% CeO_2-Ni/YSZ was attributed to the transient oxidation and reduction of

CeO_2, whereas the cycling observed here is considered to be due to the adsorption and desorption of sulfur on to the nickel surface. This cycling nature is shown schematically in Figure 7.4.

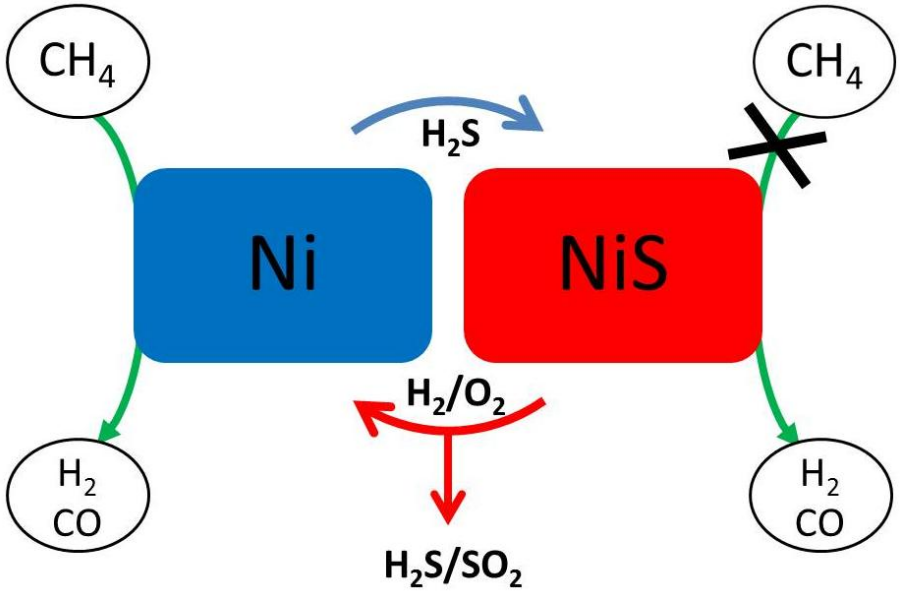

Figure 7.4: Schematic representation of sulfur adsorption and desorption on nickel and the influence on catalyst activity

As the quantity of O_2 in the gas feed increases, the initial activity also increases due to the greater availability of reformant. However, the rate of deactivation through sulfur poisoning also increases. As the O_2 content increases, so does the propensity for catalyst saturation with O_2. Therefore, a greater area of free nickel will be required to favour partial oxidation over total oxidation as O_2 content increases. The occurrence of the partial oxidation reaction can also assist in reducing the rate of deactivation by sulfur poisoning, as an increased H_2-rich atmosphere can encourage sulfur removal from the nickel surface by the formation of H_2S (Equation 7.2). However, this does not appear to be the situation under these reaction conditions.

$$NiS + H_2 \rightleftharpoons Ni + H_2S \qquad \textbf{(7.2)}$$

7.2.2 Reaction of CH_4 + 0.5CO_2 + xO_2 over Ni/YSZ at 700 °C in the presence of 5ppm H_2S

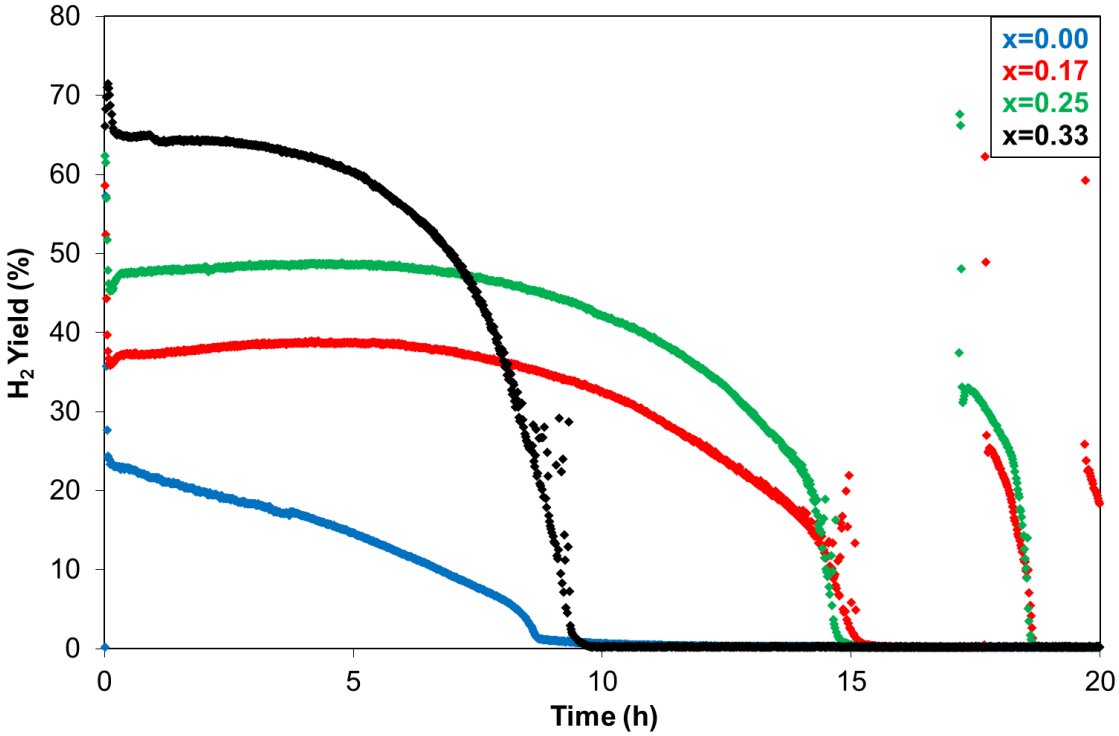

Figure 7.5: H_2 yield for reaction of CH_4 + 0.5CO_2 + xO_2 + 5ppm H_2S over Ni/YSZ at 700 °C for 20 hours (x=0.00, 0.17, 0.25, 0.33)

The influence of H_2S on the catalytic activity and stability of Ni/YSZ for the CH_4 + CO_2 reaction at 700 °C can be seen in Figure 7.5. It is apparent from Figure 7.5 that the addition of O_2 to the CH_4:CO_2 mixture not only increases the initial activity but also significantly delays the rate at which deactivation through sulfur poisoning occurs, except where the greatest O_2 concentration is added. This increased tolerance to sulfur poisoning with the addition of O_2 may be due to the potential oxidation of sulfur from the nickel surface to produce SO_2 (Equation 7.3). The higher rate of deactivation with the greatest O_2 concentration added may be due to the increased potential for total oxidation, as discussed for the reaction at 600 °C.

$$NiS + O_2 \rightleftharpoons Ni + SO_2 \qquad \textbf{(7.3)}$$

For the reactions with x=0.17 and 0.25, different cycling behaviour is seen where complete deactivation occurs after *ca.*15 hours, followed by a sudden recovery at *ca.*18 hours, which then quickly deactivates to completion. A similar cycle commences just as the reaction is terminated. This type of cycling is possibly due to complete coverage of the catalyst surface by sulfur resulting in complete deactivation. At this point, the oxygen concentration at the catalyst surface increases to a point where extensive oxidation of the NiS occurs. This induces a sudden onset of methane reforming which results in the rapid increase in H_2 yield. The sudden availability of free nickel sites then enables rapid adsorption of sulfur onto the nickel surface and subsequent deactivation through sulfur poisoning.

7.2.3 Reaction of CH_4 + 0.5CO_2 + xO_2 over Ni/YSZ at 800 °C in the presence of 5ppm H_2S

The influence of O_2 addition to the CH_4:CO_2 mixture towards increasing tolerance to sulfur deactivation is significantly reduced at 800 °C compared to 700 °C shown in Figures 7.6 and 7.5 respectively. This may be attributed to the increased rate of sulfur adsorption onto the nickel surface at this temperature. The specific influence of temperature on sulfur deactivation is shown separately in Figures 7.16 – 7.18. As at lower reaction temperatures, the addition of O_2 to the CH_4:CO_2 mixture results in both an increase in initial activity and tolerance to sulfur poisoning. As at lower temperatures, increasing the concentration of added O_2 above a certain level (x=0.25) causes a reduced increase in sulfur tolerance.

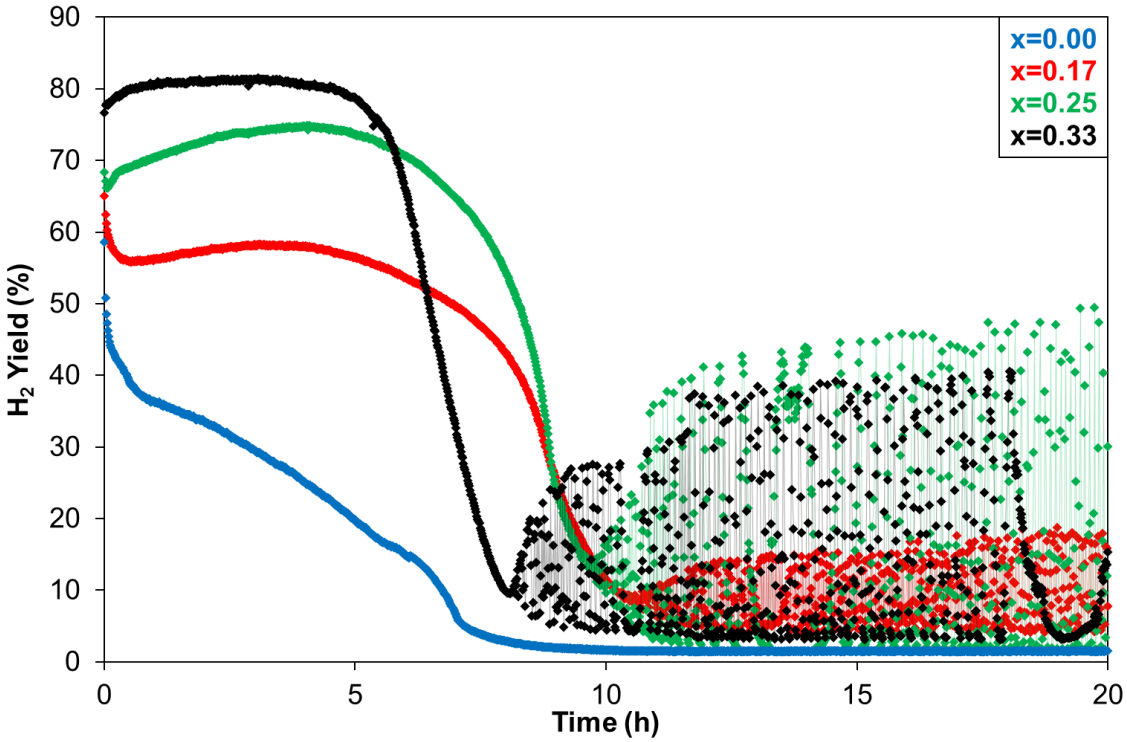

Figure 7.6: H_2 yield for reaction of CH_4 + 0.5CO_2 + xO_2 + 5ppm H_2S over Ni/YSZ at 800 °C for 20 hours (x=0.00, 0.17, 0.25, 0.33). Data points for H_2 yield are connected to illustrate cycling nature.

At 800 °C (Figure 7.6), cycling occurs at a significantly greater rate than at lower temperatures. This increased rate of cycling can be attributed to the increased rate of sulfur oxidation from the nickel surface and the increased rate of subsequent sulfur re-adsorption onto the available nickel. At higher temperatures, the capacity for sulfur removal from the nickel surface by desorption as S_2 is greater. However, no cycling or partial activity is observed in the absence of oxygen, which suggests that the primary mode of sulfur removal is through oxidation to SO_2. This is further supported by the increased extent of cycling as the O_2 concentration is increased from x=0.17.

7.2.4 Reaction of CH_4 + 0.5CO_2 + xO_2 over Ni/YSZ at 900 °C in the presence of 5ppm H_2S

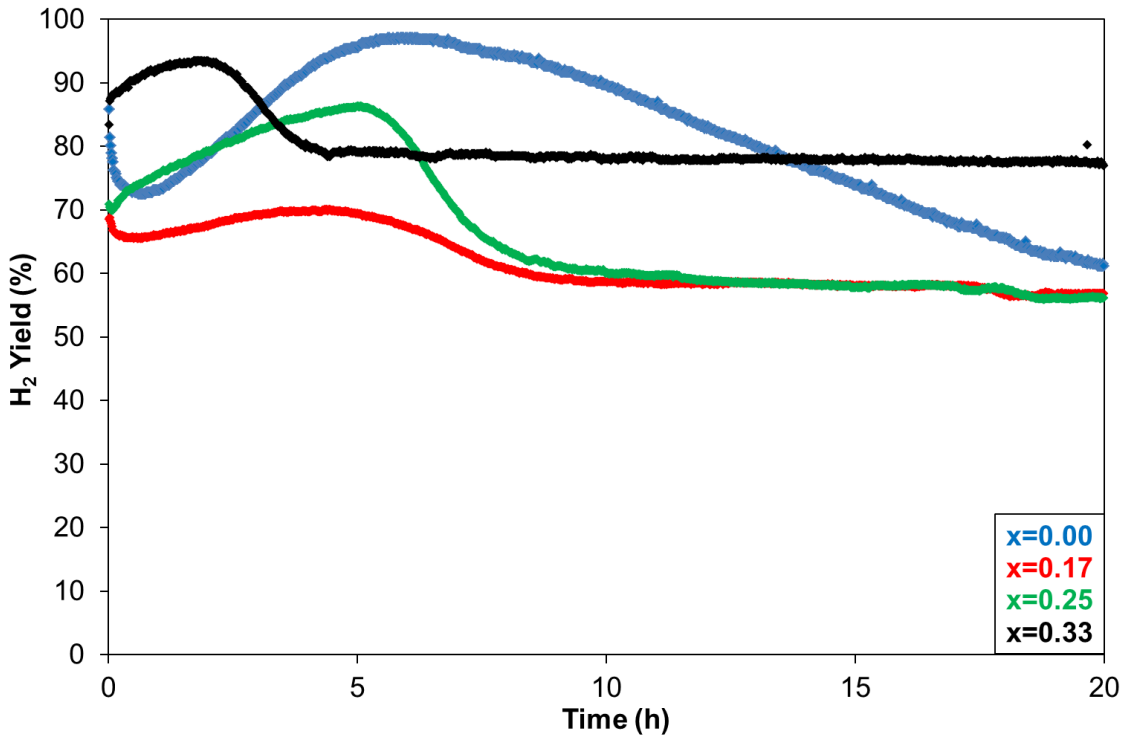

Figure 7.7: H_2 yield for reaction of CH_4 + 0.5CO_2 + xO_2 + 5ppm H_2S over Ni/YSZ at 900 °C for 20 hours (x=0.00, 0.17, 0.25, 0.33)

At 900 °C (Figure 7.7), completely different behaviour is observed to at lower temperatures, in that complete deactivation via sulfur poisoning does not occur. In the absence of O_2, the deactivation observed is primarily caused by partial physical blocking of the reactor tube due to extensive carbon deposition, rather than sulfur poisoning. This behaviour arises when carbon is deposited to a point where it builds up and physically blocks the tube and restricts the flow of gases through the system. This extent of carbon deposition under these reaction conditions is unexpected as physical blocking did not occur with the same reaction conditions in the absence of H_2S. This may suggest that the presence of H_2S on the catalyst surface leads to the formation of different carbon morphologies [7]. A future study focused on characterisation studies on the carbon formed with and without the presence of H_2S in the reaction mixture could be particularly interesting.

It is apparent that for reactions carried out in the presence of added O_2, greater initial activity and also an increased tolerance towards sulfur deactivation is present with increased O_2 concentrations. Unlike at lower temperatures, the greatest O_2 concentration shows the highest activity and tolerance to sulfur deactivation. Sulfur desorption from the nickel surface is greater at higher temperatures and as such, there is a greater area of nickel without adsorbed sulfur. Therefore, although the potential for total oxidation is greater with increased O_2 concentrations, it is significantly less likely to dominate over partial oxidation, especially at higher temperature where partial oxidation is thermodynamically favoured over total oxidation. The primary objective with O_2 addition is the increased tolerance of the system towards deactivation rather than the initial activity as the increased tolerance is the main factor influencing the viability of the systems for long-term operation.

For the reactions where x=0.17 and 0.25, two phases of deactivation are visible in the reaction profile. These phases have been shown specifically for x=0.25 in Figure 7.8.

The first deactivation phase (Phase I) shows much more rapid and extensive deactivation than Phase II and has been attributed to the chemisorption of sulfur onto the nickel surface [8]. This phase ends when either the catalyst surface becomes saturated with sulfur, or the equilibrium between sulfur chemisorption on and removal from the catalyst surface is reached.

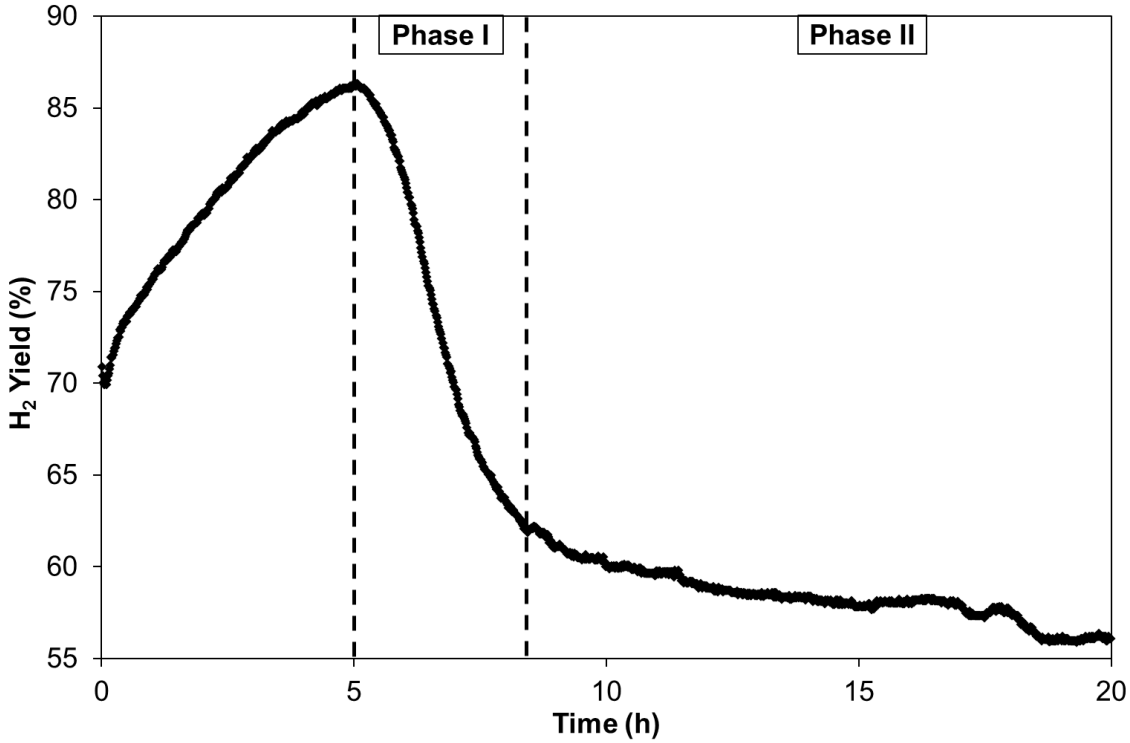

Figure 7.8: H_2 yield for reaction of CH_4 + 0.5CO_2 + 0.25O_2 + 5ppm H_2S over Ni/YSZ at 900 °C for 20 hours.

A change in the deactivation behaviour may explain the presence of Phase II in that either sintering of the catalyst is occurring or that sulfur is inducing further deactivation in a manner other than chemisorption onto the nickel surface. Alternatively, Phase II may be a consequence of the reaction slowly approaching steady state behaviour.

Sintering of the catalyst can occur at higher temperatures, and the enhanced sintering of nickel with adsorbed sulfur has been reported [9]. Separate phases of deactivation attributed to different sulfur deactivation processes have been reported by numerous researchers [10-14]. Deactivation mechanisms and processes suggested include the adsorption of sulfur onto less accessible nickel, restructuring of the nickel surface caused by sulfur and also the formation of bulk nickel sulfides.

In contrast to the reactions carried out at lower temperatures, no cycling is observed for any CH_4:CO_2:xO_2 ratio at 900 °C. This lack of cycling can be attributed to the high O_2 consumption in

the reforming reactions at this temperature and with cycling occurring so rapidly to not cause periodic changes in activity.

7.2.5 Reaction of CH_4 + 0.5CO_2 + xO_2 over Ni/YSZ at 1000 °C with the addition of 5ppm H_2S

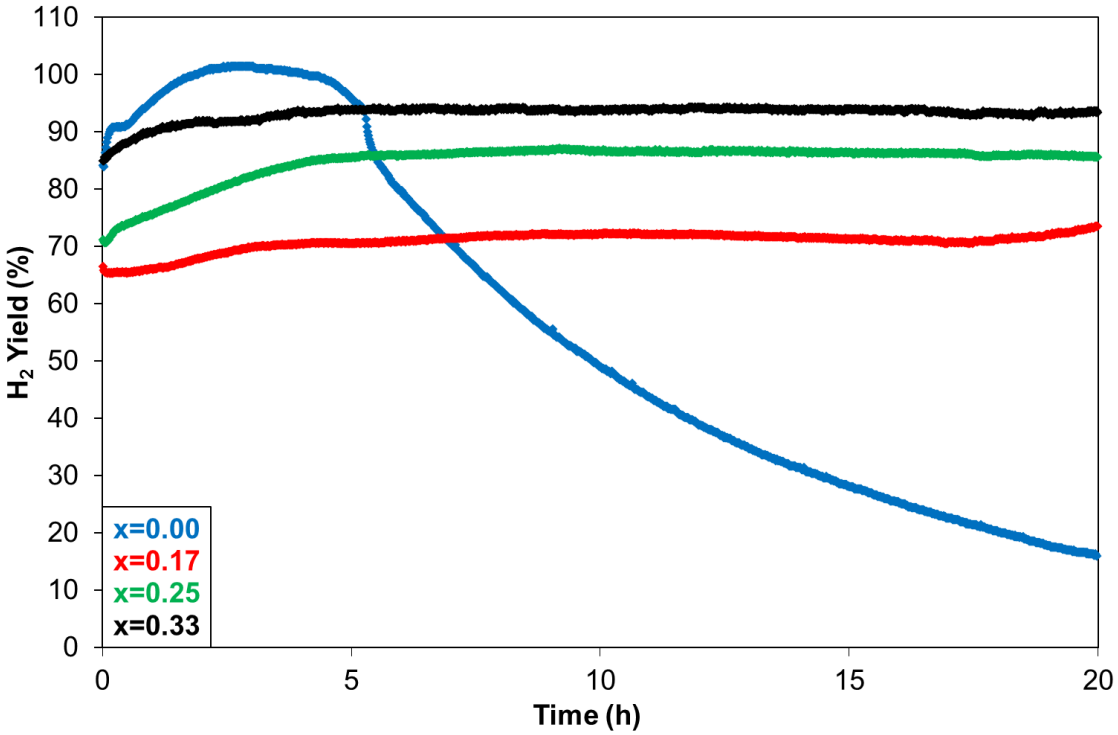

Figure 7.9: H_2 yield for reaction of CH_4 + 0.5CO_2 + xO_2 + 5ppm H_2S over Ni/YSZ at 1000 °C for 20 hours (x=0.00, 0.17, 0.25, 0.33)

As at 900 °C (Figure 7.7), partial physical blocking is seen for the reaction at 1000 °C (Figure 7.9) in the absence of O_2. Partial physical blocking was also observed under equivalent reaction conditions in the absence of H_2S.

When O_2 is added to the CH_4:CO_2 mixture, high activity and stability are observed, and increased O_2 levels further increase activity. At this temperature, the potential for sustained chemisorption of sulfur onto the nickel surface is low due its exothermic nature [15].

Although no deactivation is observed within the individual reactions, comparison with the reactions carried out at this temperature without the addition of H_2S (Table 7.1) shows that the presence of H_2S decreases activity, with the exception of x=0.33. This may be caused by the reaction of O_2 with H_2S reducing the quantity of O_2 available to induce methane reforming. The greater activity with x=0.33 in the presence of H_2S may illustrate the utilisation of O_2 in sulfur oxidation and therefore reduced oxygen availability for total oxidation. The lack of cycling observed at this temperature may be due to the rapid removal of sulfur from the nickel.

Table 7.1: H_2 yield for reaction of $CH_4 + CO_2 + xO_2$ (x=0.00, 0.17, 0.25, 0.33) over Ni/YSZ at 1000 °C after 5 hours and 20 hours with and without the presence of 5ppm H_2S

	Absence of H_2S		**Presence of H_2S**	
	Time (h)			
CH_4:xO_2	**5**	**20**	**5**	**20**
x=0.00	38.4	43.6	95.8	15.9
x=0.17	86.6	67.9	70.5	73.4
x=0.25	112.0	98.8	85.4	85.6
x=0.33	77.6	71.3	93.9	93.3

7.3 CO_2 reforming of CH_4 over 5 mol% CeO_2-Ni/YSZ in the presence of 5ppm H_2S with and without addition of O_2

The sulfur tolerance of 5 mol% CeO_2-Ni/YSZ is again assessed solely using H_2 yield as with the equivalent reactions shown for Ni/YSZ for the reasons discussed previously.

7.3.1 Reaction of $CH_4 + 0.5CO_2 + xO_2$ over 5 mol% CeO_2-Ni/YSZ at 600 °C in the presence of 5ppm H_2S

In the absence of O_2 at 600 °C (Figure 7.10), slightly increased initial activity is observed over 5 mol% CeO_2-Ni/YSZ, compared to Ni/YSZ. This increased activity due to CeO_2 doping has also

been observed in Section 6 and has been attributed to the dissociation of CO_2 on Ce_2O_3 (Equation 7.4) [16, 17].

$$Ce_2O_3 + CO_2 \rightleftharpoons CeO_2 + CO \quad \textbf{(7.4)}$$

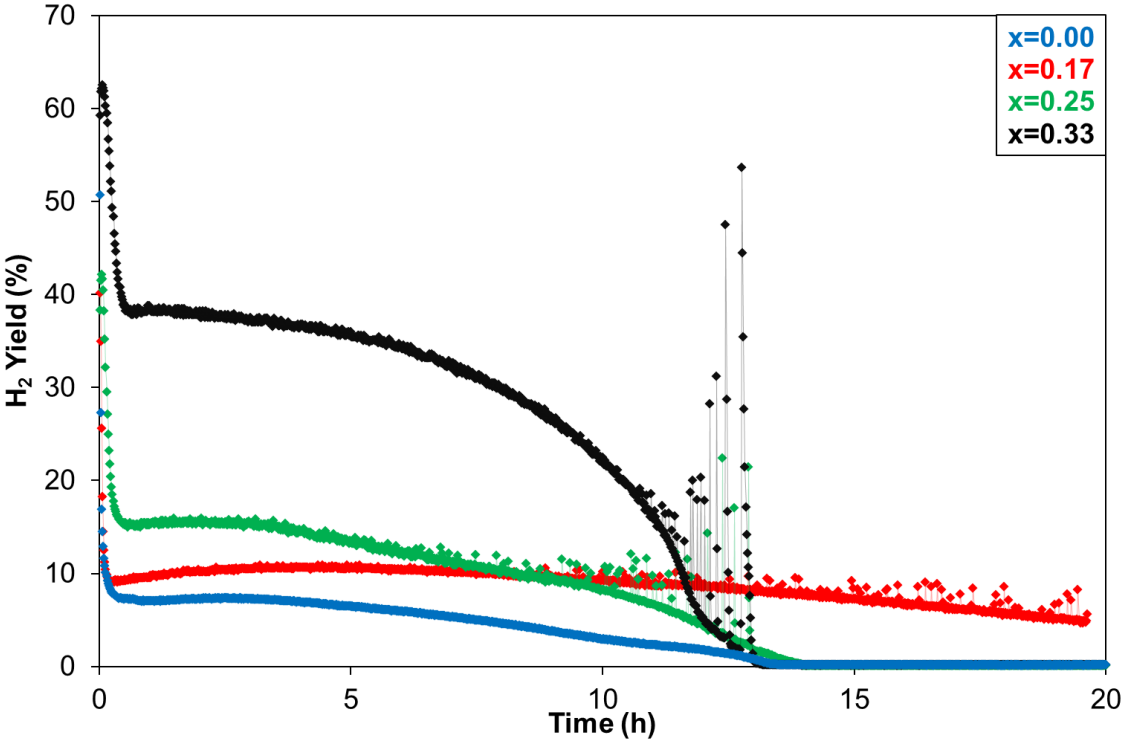

Figure 7.10: H_2 yield for reaction of CH_4 + 0.5CO_2 + xO_2 + 5ppm H_2S over 5 mol% CeO_2-Ni/YSZ at 600 °C for 20 hours (x=0.00, 0.17, 0.25, 0.33). Data points for H_2 yield are connected to illustrate cycling nature.

A similar influence of O_2 addition on sulfur tolerance is seen over 5 mol% CeO_2-Ni/YSZ as over undoped Ni/YSZ (Figure 7.3) in that the addition of O_2 to the CH_4:CO_2 mixture increases the initial activity. Additionally, increasing O_2 concentration further increases the initial activity but reduces the tolerance to deactivation through an increased potential towards total oxidation.

It is apparent that at this temperature, the sulfur tolerance of 5 mol% CeO_2-Ni/YSZ is slightly greater than Ni/YSZ with the addition of O_2 to the simulated biogas mixture which may be due to the adsorption of S onto Ce_2O_3 (Equation 7.5) to reduce the extent of sulfur adsorption onto the nickel surface.

$$Ce_2O_3 + H_2S \rightleftharpoons Ce_2O_2S + H_2O \quad \textbf{(7.5)}$$

7.3.2 Reaction of CH_4 + 0.5CO_2 + xO_2 over 5 mol% CeO_2-Ni/YSZ at 700 °C in the presence of 5ppm H_2S

The effect of O_2 addition on increasing the tolerance of the catalysts material to deactivation through sulfur poisoning is much more apparent at 700 °C (Figure 7.11) than at 600 °C (Figure 7.10). Upon addition of O_2 to the CH_4:CO_2 mixture, initial activity increases by *ca.* 50% and complete deactivation does not occur within the 20 hour reaction duration. However, it is apparent that complete deactivation is likely to occur soon after this time if the reaction had been continued for a longer duration. Unlike for Ni/YSZ (Figure 7.5), increasing O_2:CH_4 ratio from 0.17 to 0.25 results in a decreased tolerance to sulfur poisoning for 5 mol% CeO_2-Ni/YSZ, although the tolerance is still significantly greater than in the absence of added oxygen. This may be caused by the greater activity observed for x=0.17 compared to x=0.25, which may be due to the increased potential for CO_2 dissociation in the presence of Ce_2O_3.

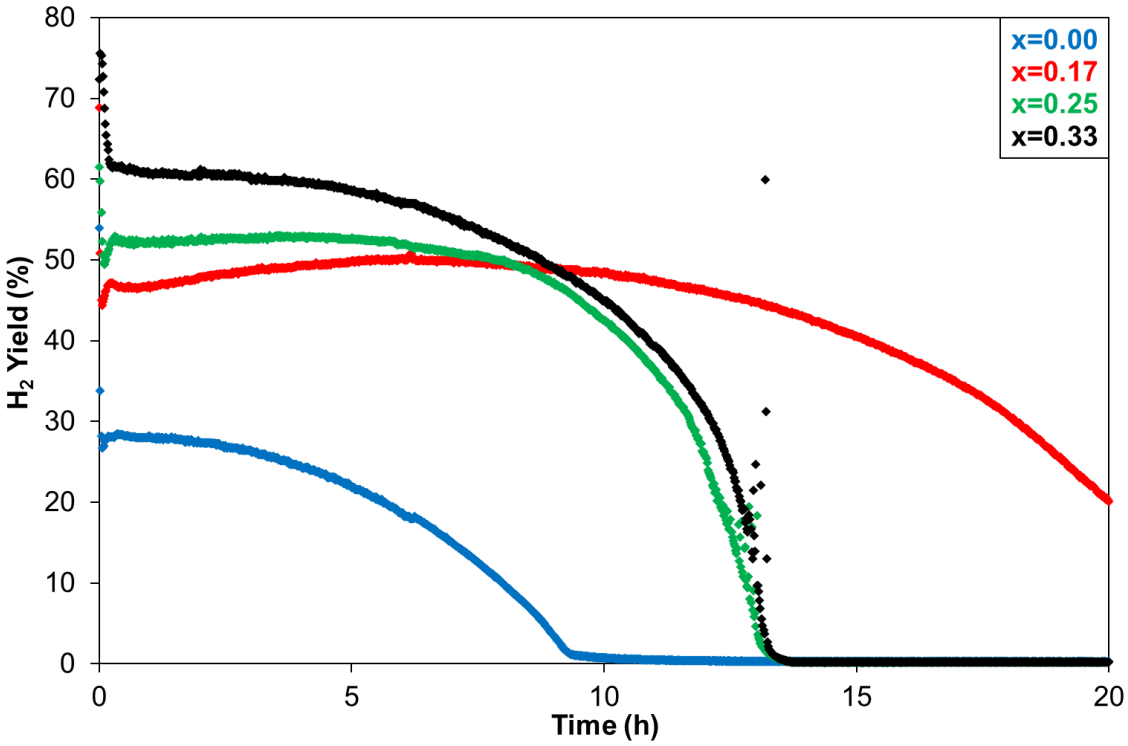

Figure 7.11: H_2 yield for reaction of CH_4 + 0.5CO_2 + xO_2 + 5ppm H_2S over 5 mol% CeO_2-Ni/YSZ at 700 °C for 20 hours (x=0.00, 0.17, 0.25, 0.33)

As at 600 °C, the deactivation rate does not increase with increasing O_2:CH_4 ratio from 0.25 to 0.33. This suggests that the extent of sulfur oxidation is limited at 700 °C due to the rate at which oxidation of sulfur from the nickel surface can occur.

In contrast to the reaction behaviour over Ni/YSZ (Figure 7.5) at this temperature, very little cycling is observed over 5 mol% CeO_2-Ni/YSZ. This may be attributed to an increased potential for total oxidation with CeO_2, even if the sulfur is removed from the catalyst surface. There is no significant difference observed in the H_2O production between the two catalysts for the studies with H_2S present however, the increased capacity for total oxidation with 5 mol% CeO_2-Ni/YSZ is seen in Section 6.

7.3.3 Reaction of CH_4 + 0.5CO_2 + xO_2 over 5 mol% CeO_2-Ni/YSZ at 800 °C in the presence of 5ppm H_2S

At 800 °C (Figure 7.12) in the absence of O_2, a significant increase in sulfur tolerance is observed compared to lower temperatures in that complete deactivation does not occur over the 20 hour reaction time. In contrast, under equivalent reaction conditions, Ni/YSZ (Figure 7.6) deactivates completely after *ca.* 7 hours. This significantly increased tolerance with ceria doping may be attributed to the potential of ceria to promote CO_2 dissociation, from which the oxygen liberated can be used to reform CH_4. The subsequent increase in H_2 concentration from methane reforming can then increase sulfur removal as H_2S. The oxygen from CO_2 dissociation may also be used to directly oxidise nickel bound sulfur to SO_2. Alternatively, desorption of sulfur from ceria (Equation 7.3) may be more favourable at this temperature than desorption from the nickel surface.

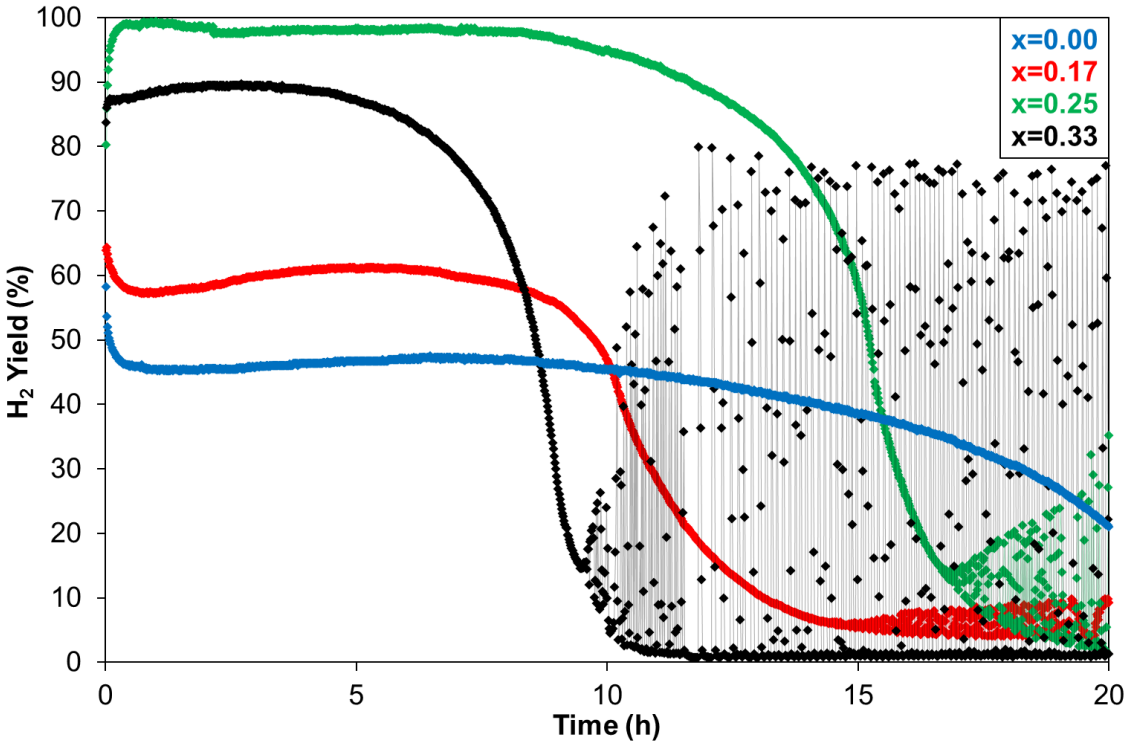

Figure 7.12: H_2 yield for reaction of CH_4 + 0.5CO_2 + xO_2 + 5ppm H_2S over 5 mol% CeO_2-Ni/YSZ at 800 °C for 20 hours (x=0.00, 0.17, 0.25, 0.33). Data points for H_2 yield are connected to illustrate cycling nature.

Interestingly, unlike for any of the other reaction conditions studied, the addition of O_2 to the CH_4:CO_2 mixture at 800 °C actually reduces the tolerance towards deactivation through sulfur poisoning. This may simple be a consequence of the increased sulfur tolerance of 5 mol% CeO_2-Ni/YSZ for the reaction in the absence of O_2 and the increased total oxidation potential upon the addition of O_2. As the O_2:CH_4 ratio is increased from 0.17 to 0.25, a substantial increase in initial activity and also sulfur tolerance is observed. This behaviour is the opposite to that seen at lower temperatures and may be attributed to the increased rate of sulfur oxidation from the nickel surface and the subsequent increased area of nickel available for reforming. This means that a greater O_2 concentration is required for total oxidation of methane to be favoured over partial oxidation of methane. This is seen when x=0.33, where the initial activity and sulfur tolerance are lower than when x=0.25, due to the increased total oxidation when x=0.33.

As was observed for these reactions over Ni/YSZ, substantial product cycling is observed over 5 mol% CeO_2-Ni/YSZ for the reactions with O_2 addition. However, the extent of cycling when x=0.17 and 0.25 is significantly less over 5 mol% CeO_2-Ni/YSZ compared to undoped Ni/YSZ. This may be attributed to the increased extent of total oxidation, even as the nickel surface becomes sulfur free. In addition, ceria doping may encourage the formation of different sulfur species that are more difficult to remove or that the oxidation of sulfur from CeO_2 occurs to produce SO_3, therefore reducing the quantity of O_2 available for oxidation of nickel-bound sulfur. The extent of recovery from sulfur poisoning over each catalyst is analysed in detail in Section 8.

7.3.4 Reaction of $CH_4 + 0.5CO_2 + xO_2$ over 5 mol% CeO_2-Ni/YSZ at 900 °C in the presence of 5ppm H_2S

At 900 °C (Figure 7.13), significantly greater stability and tolerance to sulfur poisoning is observed than at lower temperatures. This is due to the increased potential for sulfur removal by surface oxygen or hydrogen or potentially by desorption as S_2. The deactivation observed in the absence of O_2 is attributed to extensive carbon deposition. A small level of product cycling is seen when

x=0.17. This may be due to cycles of sulfur adsorption and removal, though it could also be due to the cycling of ceria which is observed for the reaction carried out in the absence of H_2S at this temperature (Section 6.3.4).

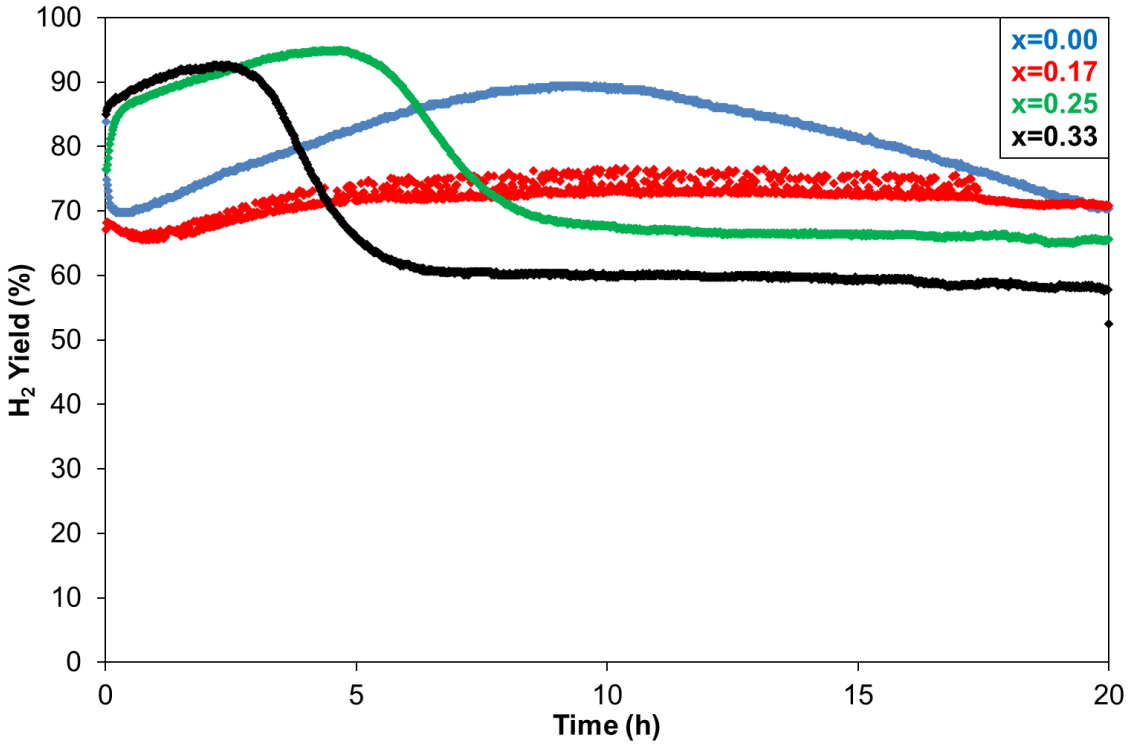

Figure 7.13: H_2 yield for reaction of CH_4 + 0.5CO_2 + xO_2 + 5ppm H_2S over 5 mol% CeO_2-Ni/YSZ at 900 °C for 20 hours (x=0.00, 0.17, 0.25, 0.33)

As the concentration of O_2 added is increased, an increase in initial activity is observed. However, this higher initial activity is then followed by substantial deactivation resulting in a lower final activity with increased O_2 levels. This can be attributed to the increased extent of total oxidation with increasing O_2 concentration. In addition, the deposition of carbon during the reaction when x=0.17, in contrast to the lack of carbon deposited when x=0.25 and 0.33, may improve activity as deposited carbon can inhibit chemisorption of sulfur and subsequent deactivation. As carbon deposition has been shown to induce little deactivation except through physical blocking (See Section 5.3.7 and 6.3.7), an overall increased tolerance to deactivation may be observed.

7.3.5 Reaction of CH_4 + 0.5CO_2 + xO_2 over 5 mol% CeO_2-Ni/YSZ at 1000 °C in the presence of 5ppm H_2S

At 1000 °C (Figure 7.14), as with Ni/YSZ (Figure 7.9), complete deactivation is not observed over 5 mol% CeO_2-Ni/YSZ over the 20 hour reaction period. The deactivation seen for the reaction in the absence of O_2 and when x=0.17 is due to carbon deposition. Carbon deposition, to an extent where physical blocking occurs, is also seen in the absence of oxygen over Ni/YSZ with H_2S present and over 5 mol% CeO_2-Ni/YSZ in the absence of H_2S. However, carbon deposition is not observed to this extent when x=0.17 over Ni/YSZ in the presence of H_2S. This supports the suggestion proposed earlier (Sections 6.3.5 and 7.2.4) that CeO_2 doping of Ni/YSZ can either increase the extent of carbon deposition or change the morphology of carbon deposits.

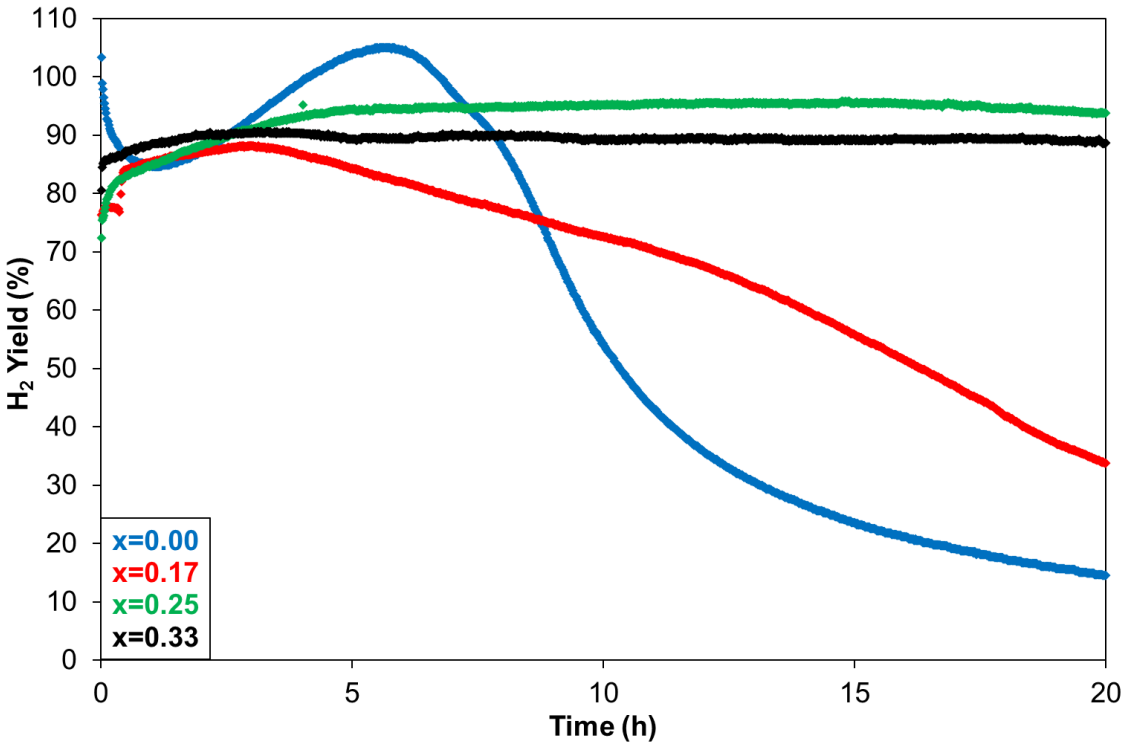

Figure 7.14: H_2 yield for reaction of CH_4 + 0.5CO_2 + xO_2 + 5ppm H_2S over 5 mol% CeO_2-Ni/YSZ at 1000 °C for 20 hours (x=0.00, 0.17, 0.25, 0.33)

High reaction stability is observed when x=0.25 and 0.33 due to the lack of carbon deposited and the high potential for sulfur desorption from the catalyst surface under such conditions. As seen at

900 °C (Figure 7.13), an increase in O_2:CH_4 ratio from 0.25 to 0.33 results in a decreased H_2 yield due to the increased extent of total oxidation. This behaviour is not observed under equivalent reaction conditions over Ni/YSZ due to the lower activity when x=0.25, which highlights the potential of ceria doping to increase oxidation potential at high temperatures.

7.4 Influence of temperature on the sulfur tolerance of Ni/YSZ and 5%CeO_2-Ni/YSZ during reactions of CH_4 + 0.5CO_2 + xO_2

The influence of temperature on the reaction of CH_4 and CO_2 in the absence and presence of 0.25 O_2 over Ni/YSZ is shown in Figure 7.15. It is apparent that for both reaction gas compositions, increasing the reaction temperature from 600 °C to 800 °C increases the rate of deactivation through sulfur poisoning. This is particularly evident between 700 °C and 800 °C. As discussed previously, this is attributed to the increased rate of sulfur adsorption onto the nickel surface, resulting in more rapid saturation of the nickel surface [8]. As the reaction temperature exceeds 800 °C, sulfur chemisorption becomes thermodynamically less favoured and sulfur removal is increasingly favoured, resulting in a significant increase in the tolerance to deactivation [15, 18-20].

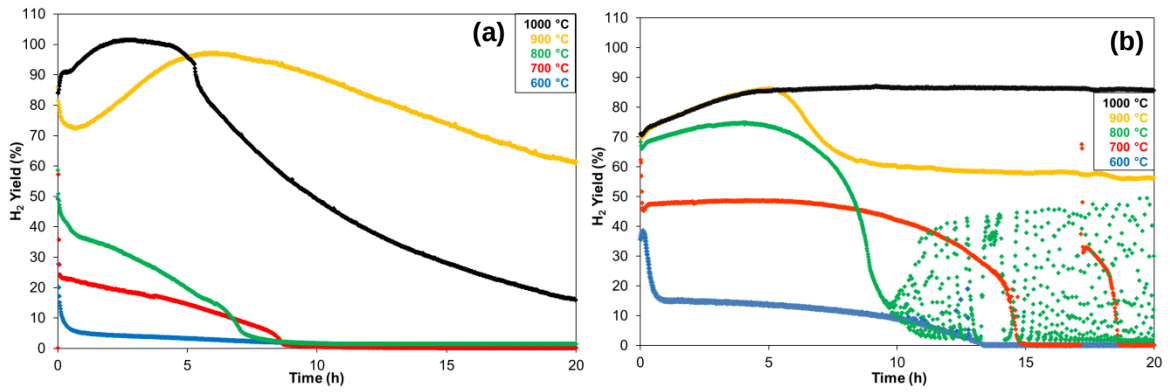

Figure 7.15: H_2 yield for reaction of (a) CH_4 + 0.5CO_2 and (b) CH_4 + 0.5CO_2+ 0.25O_2 over Ni/YSZ at temperatures between 600-1000 °C for 20 hours with 5ppm H_2S

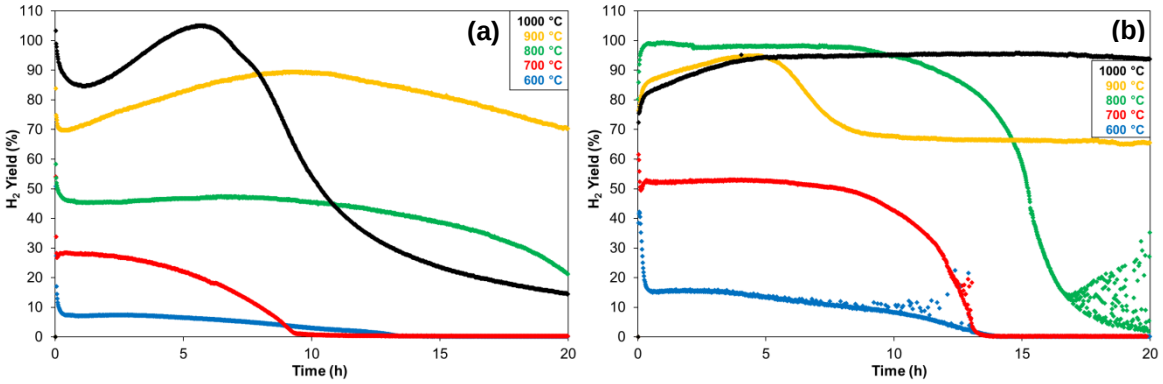

Figure 7.16: H_2 yield for reaction of (a) CH_4 + 0.5CO_2 and (b) CH_4 + 0.5CO_2+ 0.25O_2 over 5 mol% CeO_2-Ni/YSZ at temperatures between 600-1000 °C for 20 hours with 5ppm H_2S

In contrast to Ni/YSZ (Figure 7.15), the increased rate of deactivation with increasing temperature from 600°C - 800 °C is not observed for 5 mol% CeO_2-Ni/YSZ (Figure 7.16). This may be attributed to the potential of ceria to assist in sulfur oxidation by increasing the O_2 concentration on the catalyst surface or that ceria-bound sulfur is more easily removed than nickel-bound sulfur. The increased tolerance towards deactivation in the absence of O_2 with ceria doping is also apparent. This has previously been attributed to the ability of Ce_2O_3 to dissociate CO_2. A change in the surface structure of the catalyst that may occur when CeO_2 is present in the catalyst could also contribute to the greater tolerance of the 5 mol%CeO_2-Ni/YSZ.

7.5 Influence of H_2S addition towards carbon deposition during reactions of CH_4 + 0.5CO_2 + xO_2 over Ni/YSZ and 5 mol% CeO_2-Ni/YSZ

The competitive relationship between sulfur poisoning and carbon deposition over nickel based catalysts is well documented. It has been reported that the presence of H_2S within the gas feed will reduce the extent of carbon deposition [3, 7, 21-24]. The nature in which this occurs is discussed in Section 2.6.1.3. Throughout this study, the quantity of carbon deposited has been determined using post-reaction temperature programmed oxidation. As complete deactivation is observed for the

reactions performed from 600°C to 800°C, no direct comparison can be made between the mass of carbon deposited due to the varying duration of activity. For reactions at 900 °C and 1000 °C which did not exhibit complete deactivation, the extent of carbon deposition has been analysed. The incomplete oxidation (discussed in Section 3.7.2.4), observed during post-reaction TPO for the reaction in the absence of O_2 and with the addition of 0.17 O_2 makes comparisons difficult. The lack of carbon deposited during the reaction with the addition of 0.33 O_2 in the absence of H_2S is also observed in the presence of H_2S. A significant reduction in carbon has been observed for the reaction over 5 mol% CeO_2-Ni/YSZ at 900 °C and 1000 °C with the addition of 0.25 O_2 in the presence of H_2S. The reaction at this temperature in the absence of H_2S resulted in substantial carbon deposition in excess of 30 mg. However, for the reaction in the presence of 5 ppm H_2S, minimal carbon deposition (<1 mg) was observed. This finding supports the literature that the presence of H_2S can reduce the extent of carbon deposition, although further work into the extent of carbon deposition would be beneficial.

7.6 Summary of sulfur tolerance studies for reaction of $CH_4 + 0.5CO_2 + xO_2$ over Ni/YSZ and 5 mol% CeO_2-Ni/YSZ

In this chapter, the influence of O_2 addition towards the tolerance of Ni/YSZ and 5 mol% CeO_2-Ni/YSZ to sulfur poisoning for the $CH_4 + CO_2$ reaction has been investigated. The addition of O_2 to the CH_4:CO_2 mixture largely results in increasing both the initial activity and the sulfur tolerance of both catalysts. Despite a further increase in initial activity on increasing O_2 concentration, a reduction in sulfur tolerance was observed at 600 °C to 800 °C for Ni/YSZ and 600 °C to 700 °C for 5 mol% CeO_2-Ni/YSZ. This could be attributed to an increase in the extent of total oxidation with increased O_2.

At higher reaction temperatures of 900 °C and 1000 °C, substantial carbon deposition is observed when x=0.00, resulting in physical blocking over both catalysts. This behaviour also occurred over 5 mol% CeO_2-Ni/YSZ at 1000 °C when x=0.17, suggesting that ceria doping can influence the

extent or morphology of carbon deposition. For greater O_2 concentrations at these temperatures, a further increase in initial activity and sulfur tolerance was observed over Ni/YSZ. In contrast, increasing O_2 concentration reduced the activity over 5 mol% CeO_2-Ni/YSZ but significant stability was achieved. This variation has been attributed to the ability of ceria to encourage total oxidation through increasing O_2 concentration on the catalyst surface.

The respective values for CO yield are shown in Appendix B, although the point and rate at which deactivation was observed for CO production is very similar to H_2 production, as shown in Figure 7.3.

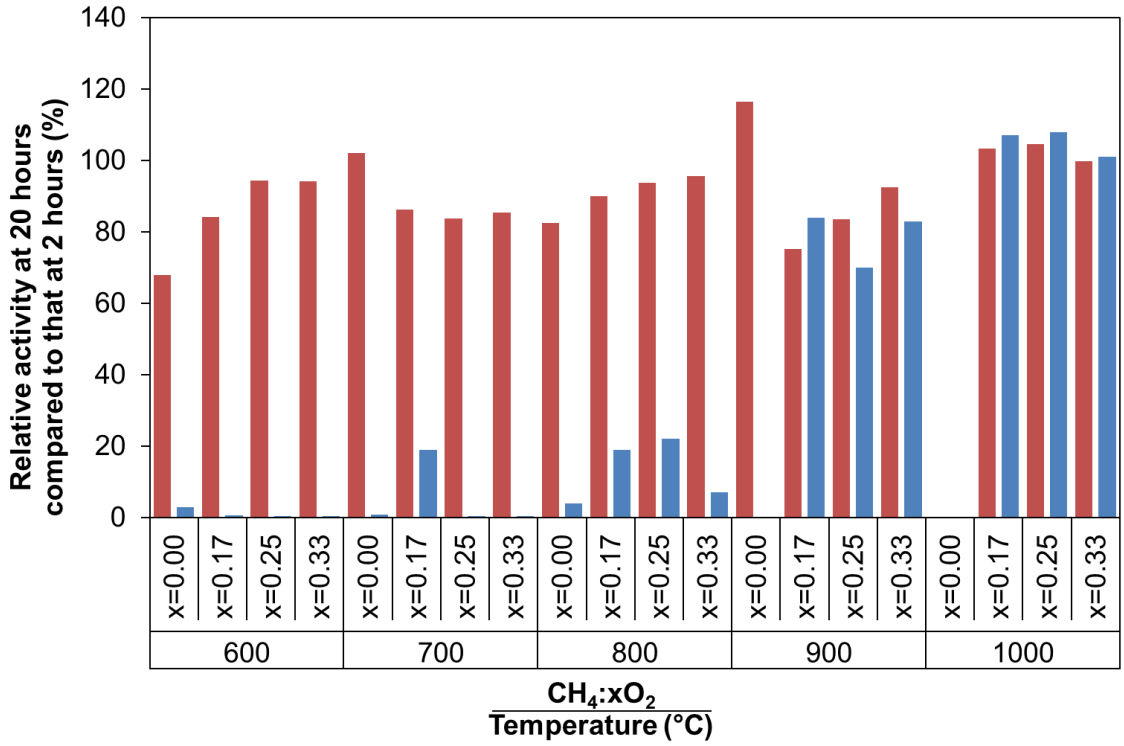

Figure 7.17: H_2 yield at 20 hours relative to that at 2 hours for CH_4 + 0.5CO_2 + xO_2 over Ni/YSZ without 5ppm H_2S (Red) and with 5ppm H_2S (Blue).

The relative resistance towards deactivation with and without the addition of 5 ppm H_2S across the range of reaction conditions for Ni/YSZ and 5 mol% CeO_2-Ni/YSZ is shown in Figures 7.17 and 7.18 respectively. These values were calculated using the average yield from 19-20 hours reaction duration as a percentage of the yield at 2 hours reaction duration. An average was taken due to the occurrence of product cycling in numerous reactions.

From these figures, it is apparent that the presence of 5 ppm H_2S results in substantial losses in activity, particularly at lower reaction temperatures. Although significant increases in initial activity can be gained with the addition of O_2, and that added O_2 can also enhance sulfur tolerance, it is evident that temperature is the primary controlling variable regarding extent of deactivation through sulfur. Doping of Ni/YSZ with CeO_2 has also been seen to enhance sulfur tolerance, particularly at lower reaction temperatures and O_2 concentrations.

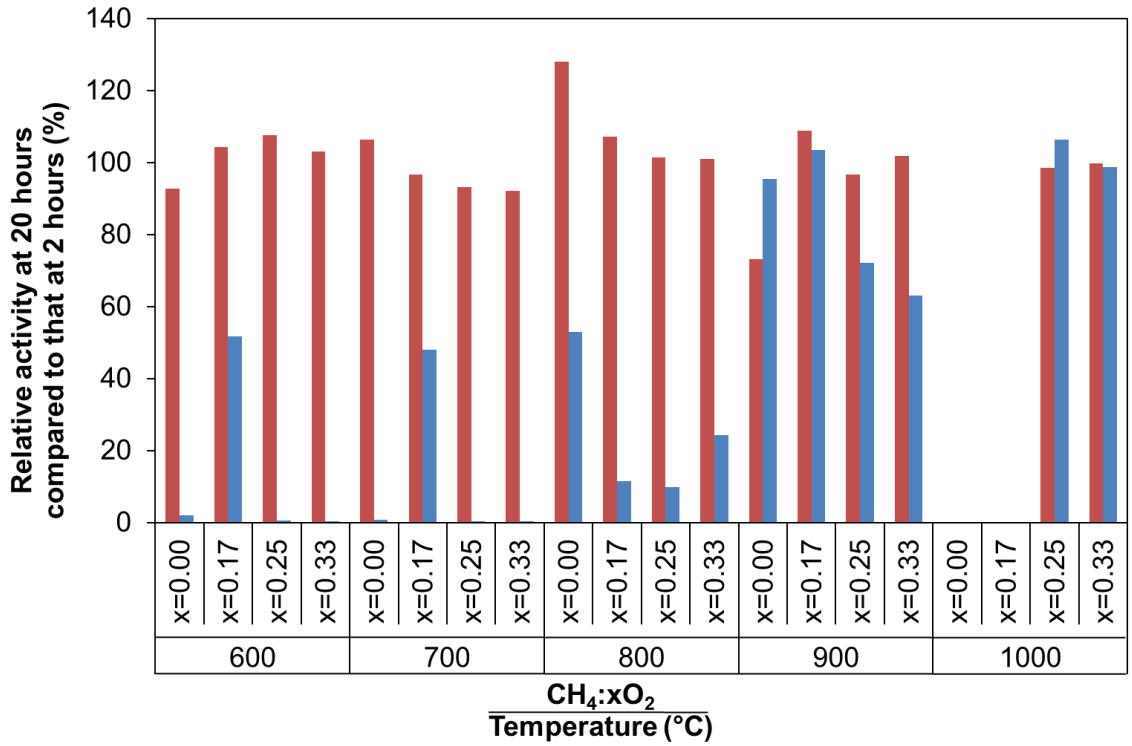

Figure 7.18: H_2 yield at 20 hours relative to that at 2 hours for CH_4 + 0.5CO_2 + xO_2 over 5 mol% CeO_2-Ni/YSZ without 5ppm H_2S (Red) and with 5ppm H_2S (Blue).

The presence of H_2S in the reactant gas feed has been shown briefly to assist the reduction of carbon deposition. However, more research is required to support this suggestion and to assess the influence of H_2S towards the morphology of carbon deposited. The stable operation of the system through the use of temperature and oxygen addition provides a very promising basis for the long term operation of catalytic systems fuelled with biogas containing sulfur species.

7.7 References

1. S. Rasi, A. Veijanen, and J. Rintala, *Trace compounds of biogas from different biogas production plants.* Energy, 2007. **32**(8): p. 1375-1380.
2. F. Osorio and J.C. Torres, *Biogas purification from anaerobic digestion in a wastewater treatment plant for biofuel production.* Renewable Energy, 2009. **34**(10): p. 2164-2171.
3. J.N. Kuhn, N. Lakshminarayanan, and U.S. Ozkan, *Effect of hydrogen sulfide on the catalytic activity of Ni-YSZ cermets.* Journal of Molecular Catalysis A: Chemical, 2008. **282**(1-2): p. 9-21.
4. C.H. Bartholomew and R.B. Pannell, *Sulfur poisoning of hydrogen and carbon monoxide adsorption on supported nickel.* Applied Catalysis, 1982. **2**(1-2): p. 39-49.
5. J.R. Rostrup-Nielsen, *Promotion by Poisoning*, in *Studies in Surface Science and Catalysis*, C.H. Bartholomew and J.B. Butt, Editors. 1991, Elsevier. p. 85-101.
6. V.R. Choudhary, K.C. Mondal, and T.V. Choudhary, *Oxy-methane reforming over high temperature stable $NiCoMgCeO_x$ and $NiCoMgO_x$ supported on zirconia-hafnia catalysts: Accelerated sulfur deactivation and regeneration.* Catal. Commun., 2007. **8**: p. 561-564.
7. J.R. Rostrup-Nielsen, *Sulfur-passivated nickel catalysts for carbon-free steam reforming of methane.* Journal of Catalysis, 1984. **85**(1): p. 31-43.
8. C.J. Laycock, J.Z. Staniforth, and R.M. Ormerod, *Biogas as a fuel for solid oxide fuel cells and synthesis gas production: effects of ceria-doping and hydrogen sulfide on the performance of nickel-based anode materials.* Dalton Transactions, 2011. **40**(20): p. 5494-5504.
9. E.J. Erekson and C.H. Bartholomew, *Sulfur poisoning of nickel methanation catalysts: II. Effects of H_2S concentration, CO and H_2O partial pressures and temperature on reactivation rates.* Applied Catalysis, 1983. **5**(3): p. 323-336.
10. Z. Cheng and M. Liu, *Characterization of sulfur poisoning of Ni-YSZ anodes for solid oxide fuel cells using in situ Raman microspectroscopy.* Solid State Ionics, 2007. **178**(13-14): p. 925-935.

11. J.-H. Wang and M. Liu, *Computational study of sulfur-nickel interactions: A new S-Ni phase diagram.* Electrochemistry Communications, 2007. **9**(9): p. 2212-2217.

12. C.H. Bartholomew, G.D. Weatherbee, and G.A. Jarvi, *Sulfur poisoning of nickel methanation catalysts : I. in situ deactivation by H_2S of nickel and nickel bimetallics.* Journal of Catalysis, 1979. **60**(2): p. 257-269.

13. J.L. Oliphant, R.W. Fowler, R.B. Pannell, and C.H. Bartholomew, *Chemisorption of hydrogen sulfide on nickel and ruthenium catalysts : I. Desorption isotherms.* Journal of Catalysis, 1978. **51**(2): p. 229-242.

14. F. Zaza, C. Paoletti, R. LoPresti, E. Simonetti, and M. Pasquali, *Studies on sulfur poisoning and development of advanced anodic materials for waste-to-energy fuel cells applications.* Journal of Power Sources, 2010. **195**(13): p. 4043-4050.

15. L. Li, C. Howard, D.L. King, M. Gerber, R. Dagle, and D. Stevens, *Regeneration of Sulfur Deactivated Ni-Based Biomass Syngas Cleaning Catalysts.* Industrial & Engineering Chemistry Research, 2010. **49**(20): p. 10144-10148.

16. H. Devianto, S.P. Yoon, S.W. Nam, J. Han, and T.-H. Lim, *The effect of a ceria coating on the H_2S tolerance of a molten carbonate fuel cell.* Journal of Power Sources, 2006. **159**(2): p. 1147-1152.

17. Y. Zeng, S. Kaytakoglu, and D.P. Harrison, *Reduced cerium oxide as an efficient and durable high temperature desulfurization sorbent.* Chemical Engineering Science, 2000. **55**(21): p. 4893-4900.

18. J. Hepola and P. Simell, *Sulphur poisoning of nickel-based hot gas cleaning catalysts in synthetic gasification gas: II. Chemisorption of hydrogen sulphide.* Applied Catalysis B: Environmental, 1997. **14**(3-4): p. 305-321.

19. J. Hepola and P. Simell, *Sulphur poisoning of nickel-based hot gas cleaning catalysts in synthetic gasification gas: I. Effect of different process parameters.* Applied Catalysis B: Environmental, 1997. **14**(3-4): p. 287-303.

20. N.M. Galea, J.M.H. Lo, and T. Ziegler, *A DFT study on the removal of adsorbed sulfur from a nickel(111) surface: Reducing anode poisoning.* Journal of Catalysis, 2009. **263**(2): p. 380-389.

21. J.R. Rostrup-Nielsen and K. Pedersen, *Sulfur poisoning of Boudouard and methanation reactions on nickel catalysts.* Journal of Catalysis, 1979. **59**(3): p. 395-404.

22. F. Abild-Pedersen, O. Lytken, J. Engbæk, G. Nielsen, I. Chorkendorff, and J.K. Nørskov, *Methane activation on Ni(1 1 1): Effects of poisons and step defects.* Surface Science, 2005. **590**(2-3): p. 127-137.

23. H.C. Dibbern, P. Olesen, J.R. Rostrupnielsen, P.B. Tottrup, and N.R. Udengaard, *Make low H_2/CO syngas using sulfur passivated reforming.* Hydrocarbon Processing, 1986. **65**(1): p. 71-74.

24. J.F.B. Rasmussen and A. Hagen, *The effect of H_2S on the performance of Ni-YSZ anodes in solid oxide fuel cells.* J. Power Sources, 2009. **191**: p. 534-541.

8 Regeneration of Ni/YSZ and 5 mol% CeO_2-Ni/YSZ deactivated via sulfur poisoning during CO_2 reforming of CH_4: Influence of O_2 addition and concentration on rate of regeneration

8.1 Requirement for, and approaches towards the regeneration of systems deactivated by sulfur poisoning

Despite displaying an increased tolerance to H_2S upon addition of oxygen to the biogas mixture, complete deactivation via sulfur poisoning was observed for all CH_4:0.5CO_2:xO_2 reactant gas mixtures at reaction temperatures of 800 °C and below, over both Ni/YSZ (Figure 7.6) and 5 mol% CeO_2-Ni/YSZ (Figure 7.12). The greater cost, both environmentally and economically, of operating systems at increased temperatures makes the viable operation at lower temperatures highly desirable. In particular, the use of SOFC's above 900 °C can lead to problems regarding thermal failure, as discussed in Section 3.

One approach to improving the viability of nickel-based catalysts for the reforming of biogas, with or without the addition of O_2, would be to periodically regenerate the catalyst. This approach has been discussed in Section 2.6.1.2 and could be performed using inert gas, hydrogen, oxygen or H_2S-free fuel gas.

The use of inert gas was tested for its ability to regenerate a catalyst at 800 °C that had been completely deactivated by sulfur. However, no regeneration was observed over 50 hours on stream. Operating above 800 °C to increase the rate of regeneration with inert gas reduces the environmental and economic viability of this approach. The use of oxygen or hydrogen were excluded as possible methods for regeneration, as oxygen can result in extensive oxidation of the nickel catalyst, whilst hydrogen is the primary desired product with the greatest value.

The use of H_2S-free fuel gas was considered the most practical and potentially viable method of regeneration as the only requirement is the use of a sulfur-free source of methane such as natural gas to be used as a replacement fuel source.

All regeneration studies have been carried out following reactions at 700 °C as all CH_4:CO_2:O_2 reactant gas mixtures used underwent complete deactivation via H_2S poisoning within the 20 hour reaction duration. Also, the reduced extent of cycling allowed for a more accurate determination that complete deactivation had been reached. The regeneration temperature was kept at 700 °C to reduce the amount of change in operating conditions required for inducing recovery and to allow for the relative extent of recovery to be calculated.

Each regeneration experiment commenced after the original reaction in the presence of H_2S was fully deactivated for 1 hour. At this point, the H_2S feed was stopped and the reaction continued for 25 hours to gain an insight into the regeneration behaviour. Figures 8.1 and 8.2 show the extent of regeneration in H_2 yield as a percentage of the H_2 yield after 2 hours of the original reaction in the presence of H_2S. The horizontal axis used for the figures shows the time from the point at which the H_2S feed was stopped. This gives an insight into the influence of O_2 concentration on the regeneration rate. The H_2 yield is again used as the primary mode of analysis for the reasons discussed in Section 7.

8.2 Reaction of $CH_4 + 0.5CO_2 + xO_2$ over Ni/YSZ deactivated by sulfur poisoning at 700 °C

The ability of O_2 in the reactant gas mixture to facilitate sulfur removal and Ni/YSZ regeneration is shown in Figure 8.1. In the absence of O_2, no regeneration of catalyst activity was observed. This may be due to the high stability of CO_2 and that sulfur desorption as S_2 is thermodynamically unfavourable at this temperature [1]. However, upon addition of O_2 to the CH_4:CO_2 mixture, a sudden, extensive increase in H_2 yield is observed. This sudden regeneration of catalyst activity is attributed to the adsorption of oxygen on the catalyst surface to induce extensive sulfur removal

from the catalyst surface as SO_2, enabling methane reforming. This behaviour was seen under similar conditions in Section 7.2.2.

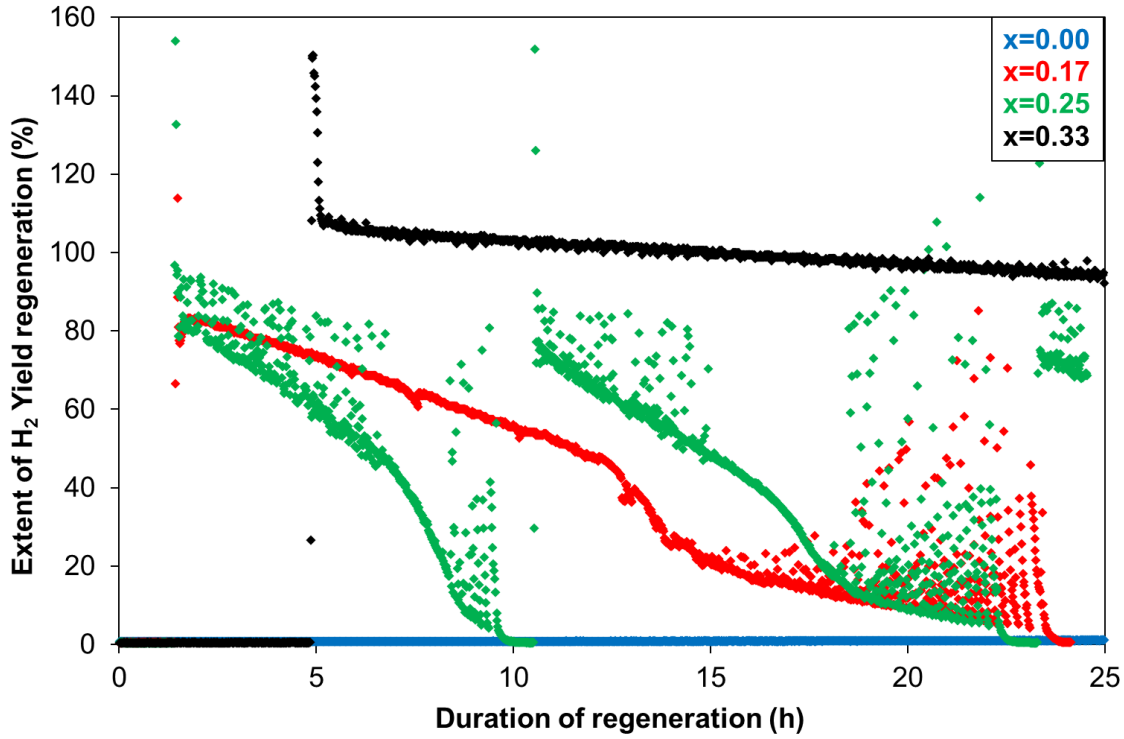

Figure 8.1: Regeneration behaviour with H_2S-free fuel gas following reaction of CH_4 + $0.5CO_2$ + xO_2 + 5ppm H_2S over Ni/YSZ at 700 °C where complete deactivation occurred through sulfur poisoning (x=0.00, 0.17, 0.25, 0.33)

It is apparent from Figure 8.1 that for all concentrations of O_2 added, secondary deactivation follows the initial regeneration. This secondary phase may be attributed to the high mobility of sulfur within nickel in that as sulfur is removed from the nickel surface, sulfur present within the bulk of the catalyst can migrate to the surface and induce deactivation.

For the reaction with x=0.17, a relatively linear rate of deactivation is observed until *ca.* 12 hours, where the rate of deactivation increases slightly and then an increasing extent of cycling occurs until complete deactivation is reached. The increase in deactivation rate at *ca.* 12 hours may be due to the greater potential for total oxidation as the majority of the catalyst surface becomes deactivated. The reducing area of nickel free of sulfur with time may also cause the increased cycling observed as more O_2 becomes available to remove sulfur and briefly increase activity. The

complete deactivation seen suggests that the rate at which sulfur can migrate to the nickel surface is greater than the rate of sulfur oxidation from the nickel surface or that different forms of sulfur are present which are more difficult to remove.

As the concentration of O_2 added is increased from 0.17 to 0.25, no significant variation is seen in the period prior to initial regeneration. However, a significantly greater rate of secondary deactivation exhibiting 'microcycling' is observed with x=0.25, which is followed by two similar 'macrocycles' over the duration of the reaction. A 'macrocycle' is used to describe the period between the extensive surge in activity to the point at which complete deactivation is reached, whilst a 'microcyle' refers to the cycling to and from the baseline within a 'macrocycle'.

The similar time period prior to initial regeneration at x=0.17 and 0.25 suggests that the rate at which surface saturation with oxygen is reached is limited by the rate of oxygen adsorption and diffusion on the nickel surface at this temperature rather than the concentration of O_2 present.

The greater rate of secondary deactivation on increasing the O_2 concentration from 0.17 to 0.25 may be attributed to the greater potential for nickel oxidation to increase the extent of total oxidation and reduce H_2 yield, as seen in Figure 8.2. The relationship between sulfur oxidation from the nickel surface with different O_2 quantities has also been discussed by Bartholomew *et al.* [2 and references therein]. Alternatively, the greater oxygen concentration may facilitate the formation of $NiSO_4$ (Equation 8.2), therefore reducing the extent of surface oxygen available to remove sulfur as SO_2 [3, 4], whilst $NiSO_4$ would also reduce activity by blocking active nickel sites.

$$NiS + 2O_2 \rightleftharpoons NiSO_4 \qquad \textbf{(8.2)}$$

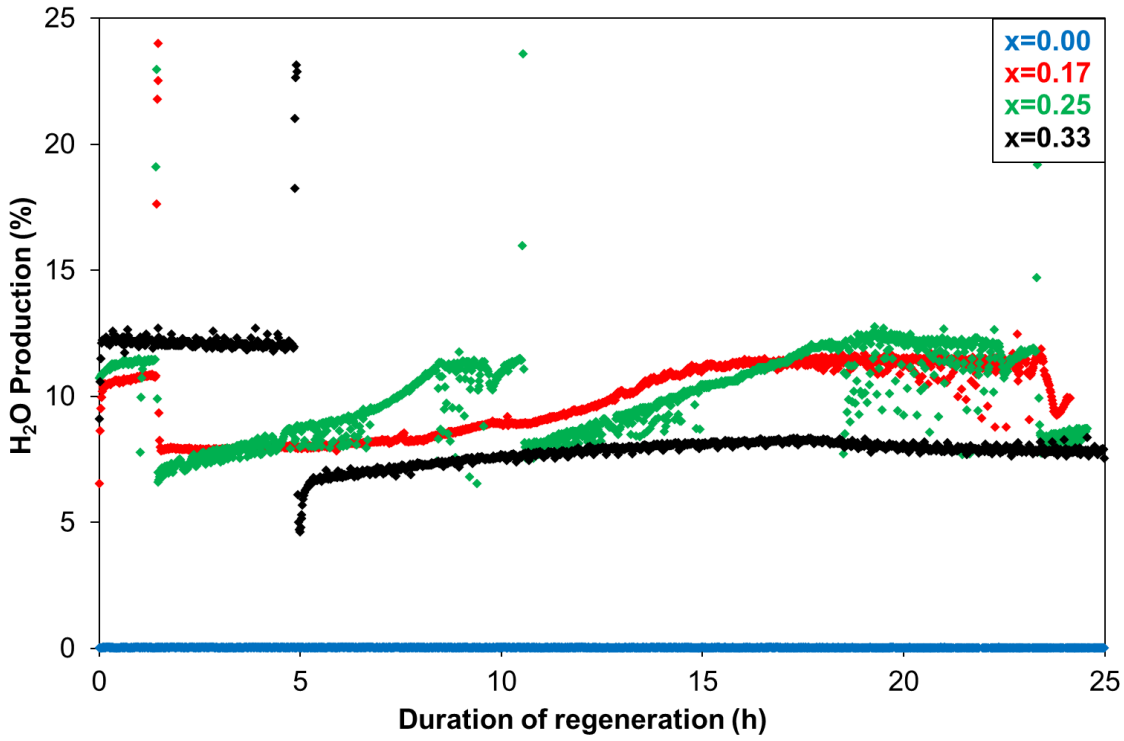

Figure 8.2: H_2O production with H_2S-free fuel gas following reaction of CH_4 + 0.5CO_2 + xO_2 + 5ppm H_2S over Ni/YSZ at 700 °C where complete deactivation occurred through sulfur poisoning (x=0.00, 0.17, 0.25, 0.33)

Where the greatest quantity of oxygen is added, a substantial variation in regeneration behaviour is observed in that the time prior to initial regeneration is increased significantly from *ca.* 90 minutes to *ca.* 5 hours. In addition, although secondary deactivation is observed, the rate at which it occurs is significantly reduced and complete deactivation is not observed during the duration of the study.

The greater period prior to initial regeneration may be due to the increased potential for the formation of $NiSO_4$ at high oxygen concentrations, and therefore a reduction in the availability of oxygen to saturate the catalyst surface and remove chemisorbed sulfur as SO_2. Also, the increased tendency towards total oxidation can effectively delay the onset of sulfur removal and partial oxidation to produce H_2, as shown by the H_2O production in Figure 8.2. The significantly reduced rate of deactivation with 0.33 O_2 suggests that the extent of sulfur removal is significantly greater with such a high quantity of O_2, despite the potential formation of $NiSO_4$.

8.3 Reaction of CH_4 + 0.5CO_2 + xO_2 over 5 mol% CeO_2-Ni/YSZ deactivated by sulfur poisoning at 700 °C

Doping of Ni/YSZ with ceria has a substantial influence on the regeneration behaviour using H_2S-free fuel gas mixtures, with and without the addition of O_2 in varied concentrations.

As observed over Ni/YSZ (Figure 8.1), 5 mol% CeO_2-Ni/YSZ, shown in Figure 8.3, exhibits no significant regeneration in the absence of O_2 during the 25 hour study. This may be due to the low reactivity of CO_2 and lack of S_2 desorption at this temperature. The ability of Ce_2O_3 to dissociate CO_2 may encourage sulfur oxidation, however the results suggest that an extensive time period is likely to be required for saturation of the catalyst surface with oxygen to be achieved via this mechanism.

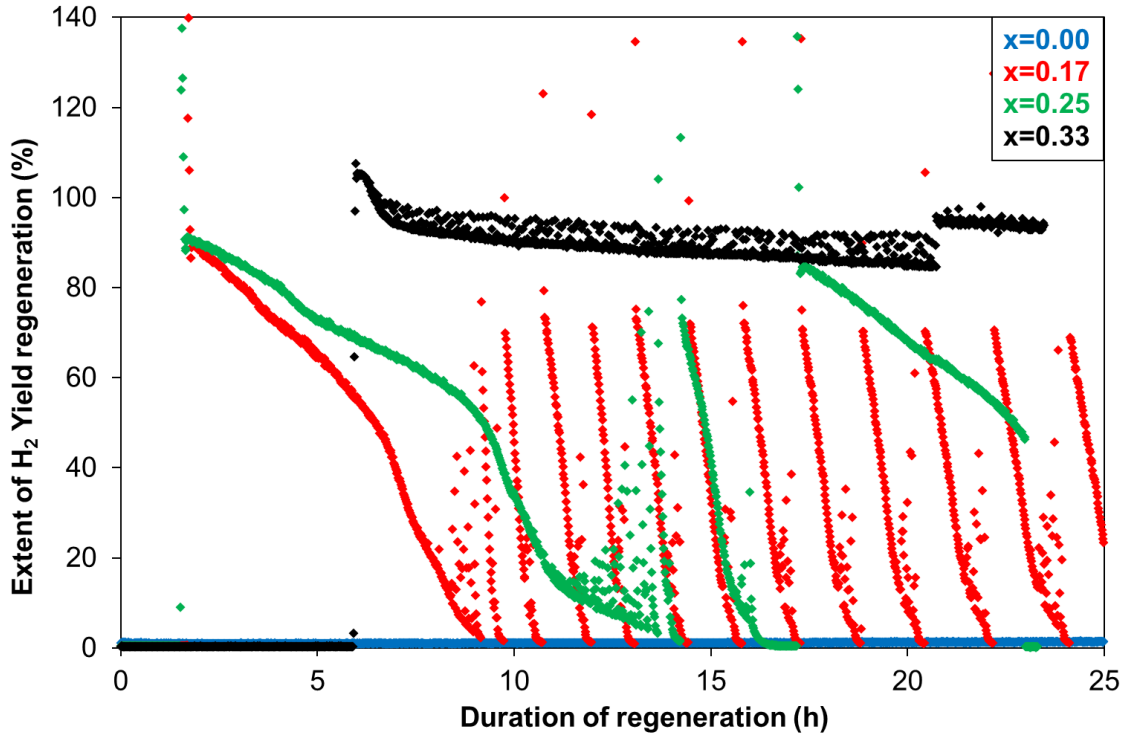

Figure 8.3: Regeneration behaviour with H_2S-free fuel gas following reaction of CH_4 + 0.5CO_2 + xO_2 + 5ppm H_2S over 5 mol% CeO_2-Ni/YSZ at 700 °C where complete deactivation occurred through sulfur poisoning (x=0.00, 0.17, 0.25, 0.33)

The addition of O_2 to the simulated biogas mixture results in a substantial initial regeneration and secondary deactivation of 5 mol% CeO_2-Ni/YSZ, as was seen for Ni/YSZ. When x=0.17, the rate of secondary deactivation is significantly greater than when x=0.25, which is the opposite behaviour to that observed for Ni/YSZ. This is due to a combination of an increased rate of deactivation when x=0.17 and a reduced rate of deactivation when x=0.25 over 5 mol% CeO_2-Ni/YSZ.

The greater deactivation rate apparent when x=0.17 over 5 mol% CeO_2-Ni/YSZ may be attributed to the greater tendency for O_2 to adsorb onto Ce_2O_3 rather than nickel. This therefore reduces the quantity of oxygen available to continuously remove sulfur from the nickel surface through oxidation. Alternatively, the presence of ceria may increase the mobility of sulfur through the nickel, increasing the rate at which bulk sulfur migrates to the surface.

Increasing the O_2 concentration from 0.17 to 0.25 may reduce the deactivation rate as there may be sufficient oxygen present to ensure that oxidation of sulfur-bound nickel occurs despite the adsorption of oxygen onto Ce_2O_3. In addition, the greater O_2 concentration may also maintain oxidation of Ce_2O_3 to CeO_2, ensuring a high oxygen concentration on the catalyst surface to facilitate sulfur oxidation.

With the exception of the initial macrocycle for x=0.25, the rate of macrocycling is significantly greater over 5 mol% CeO_2-Ni/YSZ than over Ni/YSZ. This may be attributed to the ability of CeO_2 to distribute oxygen across the catalyst surface and achieve higher oxygen surface concentrations. The increased rate of deactivation within each macrocycle may also be due to the increased potential for total oxidation of methane with ceria as shown in Figure 8.4.

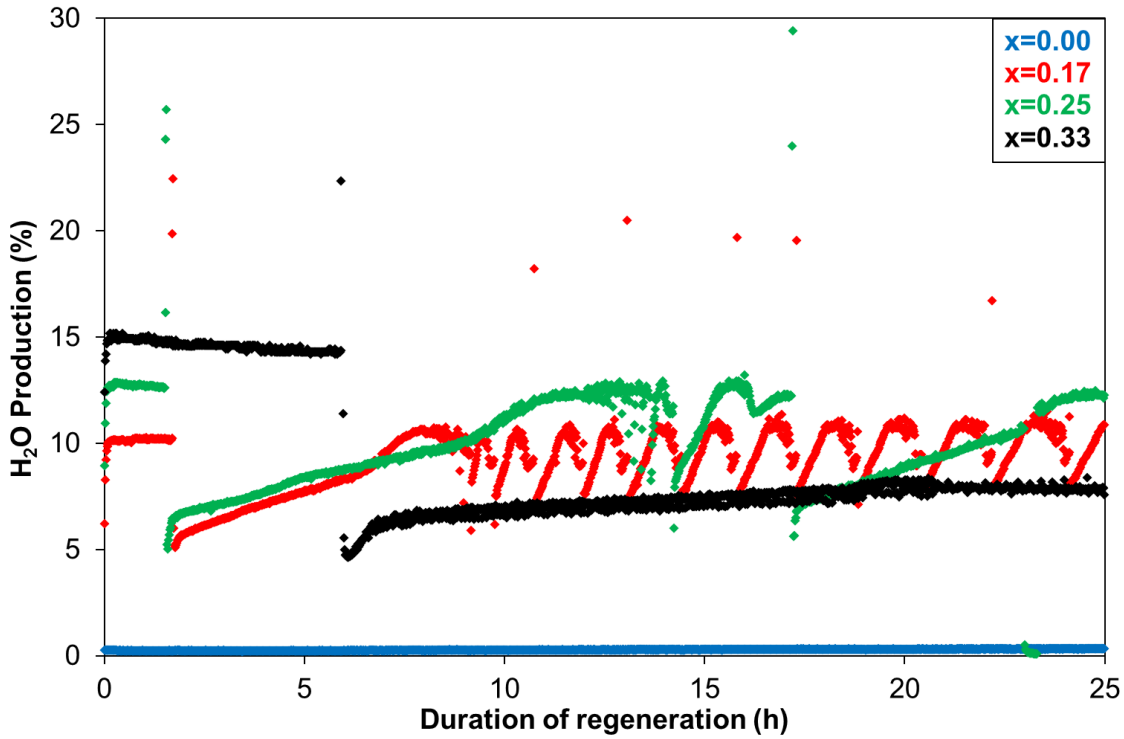

Figure 8.4: H_2O production with H_2S-free fuel gas following reaction of CH_4 + 0.5CO_2 + xO_2 + 5ppm H_2S over 5 mol% CeO_2-Ni/YSZ at 700 °C where complete deactivation occurred through sulfur poisoning (x=0.00, 0.17, 0.25, 0.33)

Lower oxygen concentrations require a smaller nickel surface area free of sulfur to favour methane reforming over total oxidation of methane. The lower surface area free of surface sulfur may also mean that complete secondary deactivation will occur faster than with a larger surface area, which may explain the increased rate of deactivation within each macrocycle when x=0.17 than 0.25.

Similar to the behaviour observed for Ni/YSZ, the addition of 0.33 O_2 to the simulated biogas mixture results in a significantly greater period before initial regeneration occurs. In addition, complete deactivation is not observed over the 25 hour period unlike with other O_2 concentrations. Also, the reaction over 5 mol% CeO_2-Ni/YSZ exhibits a greater period before initial deactivation occurs than over Ni/YSZ. This may be attributed to the greater potential for total oxidation of methane, which can be seen in Figure 8.4, and the formation of $NiSO_4$ in the presence of ceria due to the increased oxygen concentration on the catalyst surface.

A greater extent of microcycling is observed over 5 mol% CeO_2-Ni/YSZ at this temperature when x=0.33, which may be due to the cycling of ceria (Figure 6.8) as this behaviour is significantly less prevalent in the absence of CeO_2. Similar behaviour has been seen previously over 5 mol% CeO_2-Ni/YSZ with and also without the presence of 5ppm H_2S (Section 7.3.2 and 6.3.2 respectively).

8.4 Summary of the influence of O_2 addition towards the regeneration behaviour using H_2S free fuel at 700 °C over Ni/YSZ and 5 mol% CeO_2-Ni/YSZ

In this section, the ability of O_2 when added to the simulated biogas mixture to facilitate the removal of sulfur from both the Ni/YSZ and 5 mol% CeO_2-Ni/YSZ surfaces to regenerate methane reforming activity and increase H_2 yield has been studied. This is particularly apparent through the complete lack of regeneration of catalytic activity observed in the absence of O_2.

The regeneration process involves a sudden initial increase in activity, followed by a secondary deactivation process which occurs in a cyclic manner when xO_2:CH_4 = 0.17 and 0.25. This initial increase is attributed to the saturation of oxygen on the nickel surface leading to extensive sulfur removal through oxidation. This initial regeneration is significantly delayed when O_2 concentration is increased to 0.33, which has been attributed to an increased extent of total oxidation and the formation of $NiSO_4$.

The cycling of regeneration and subsequent deactivation observed when x=0.17 and 0.25 has been attributed to the mobility of sulfur on nickel and migration from the nickel sub-surface and bulk to the nickel catalyst surface. This behaviour was not observed when x=0.33 as at this O_2 concentration, sufficient oxygen is available to maintain continuous removal of surface nickel-bound sulfur through oxidation.

The rate of deactivation and cycling when x=0.17 and 0.25 is influenced substantially by ceria doping. For Ni/YSZ, increasing O_2 concentration results in an increased rate of deactivation, whereas the opposite occurs with 5 mol% CeO_2-Ni/YSZ. This has been attributed to the increased

potential for total oxidation and $NiSO_4$ formation with increasing O_2 concentration over Ni/YSZ. Ceria doping reduces this potential by distributing oxygen concentration across the catalyst surface.

The absence of completely reversible regeneration suggests the formation of irreversible nickel sulfide species which are not removed using these reaction conditions. Incomplete regeneration has been reported by numerous researchers [5-7].

From this section, it has been shown that the use of a xO_2:CH_4 ratio of 0.33 is the optimum condition for recovering the system and for long term operation. In the 20 hour timescale used, the 5 mol% CeO_2-Ni/YSZ catalyst appears to offer a more practical and viable catalyst option than Ni/YSZ for operation of the system. However, longer term experiments are required to accurately indicate the viability of the two catalysts for operation over significant timescales.

8.5 References

1. J.R. Rostrup-Nielsen, *Some principles relating to the regeneration of sulfur-poisoned nickel catalysts.* Journal of Catalysis, 1971. **21**(2): p. 171-178.
2. C.H. Bartholomew, P.K. Agrawal, and J.R. Katzer, *Sulfur Poisoning of Metals*, in *Advances in Catalysis*. 1982, Academic Press. p. 135-242.
3. A.R. Chughtai and J.R. Riter, *Thermodynamic model for the regeneration of sulfur-poisoned nickel catalyst. 1. Using thermodynamic properties of bulk nickel compounds only.* The Journal of Physical Chemistry, 1979. **83**(21): p. 2771-2773.
4. L. Li, C. Howard, D.L. King, M. Gerber, R. Dagle, and D. Stevens, *Regeneration of Sulfur Deactivated Ni-Based Biomass Syngas Cleaning Catalysts.* Industrial & Engineering Chemistry Research, 2010. **49**(20): p. 10144-10148.
5. T.R. Smith, A. Wood, and V.I. Birss, *Effect of hydrogen sulfide on the direct internal reforming of methane in solid oxide fuel cells.* Applied Catalysis A: General, 2009. **354**(1-2): p. 1-7.
6. R.B. Pannell, K.S. Chung, and C.H. Bartholomew, *The stoichiometry and poisoning by sulfur of hydrogen, oxygen and carbon monoxide chemisorption on unsupported nickel.* Journal of Catalysis, 1977. **46**(3): p. 340-347.
7. C.H. Bartholomew, G.D. Weatherbee, and G.A. Jarvi, *Sulfur poisoning of nickel methanation catalysts : I. in situ deactivation by H_2S of nickel and nickel bimetallics.* Journal of Catalysis, 1979. **60**(2): p. 257-269.

9 Ni/YSZ and 5 mol% CeO_2-Ni/YSZ as anode materials for solid oxide fuel cells operating directly on simulated biogas with and without O_2 addition

A final part of this study involved assessing the potential for operating solid oxide fuel cells on simulated biogas, and the influence of oxygen addition in varied concentration on the electrical performance.

9.1 Introduction

Fuel cells have the potential to significantly influence low carbon energy generation due to their high efficiency and low emissions. However, the growth of this technology has been restricted by the requirement of a hydrogen infrastructure for low temperature fuel cells, the high cost of manufacture and also that the primary source of hydrogen is from natural gas, which is a fossil fuel.

There are numerous types of fuel cells that vary primarily in nature of the electrolyte material used. These different types are discussed in detail in Section 2.5. Solid Oxide Fuel Cells (SOFCs) show significantly greater potential for use as a primary technology than some other fuel cell types due to the use of an oxygen conducting, ceramic electrolyte which provides the thermal stability to allow for high temperature operation [1].

This high operating temperature eliminates the requirement for a hydrogen fuel source, due to the capacity for hydrocarbon reforming to produce hydrogen, as has been illustrated in previous chapters. The high operating temperature also provides the potential for nickel to be used as a catalyst material, therefore significantly reducing the manufacturing cost. In addition, methane and other hydrocarbons can be used as a fuel source, for which there is a substantial potential market for methane generation through waste, as discussed in Section 2.1.

9.2 Solid Oxide Fuel Cells (SOFCs) and biogas as a fuel

The operation of solid oxide fuel cells using landfill gas as the primary fuel source has been reported previously by several research groups, including the research group at Keele University led by Prof. R. Mark Ormerod [2, 3], in which both the high activity and also significant issues of deactivation and loss of performance over time have been illustrated. The potential for landfill gas and other sources of biogas to be used as fuel sources for fuel cell operation due to the potential use of CO_2 present in the biogas as a reformant and also of CO as a fuel source is discussed in detail in Section 2.

The electrochemical oxidizing potential provided at the cathode means that the concentration of oxygen added to the simulated biogas mixture can significantly influence the potential for total oxidation of methane for variations in applied loads.

9.3 Experimental considerations and analysis

The cell manufacture details and modifications to the experimental test system that were implemented to allow for fuel cell testing are discussed in Section 3.10.

One of the common approaches used to study the performance analysis of fuel cells is through potentiodynamic testing of cells to produce current-voltage (*i-V*) curves, of which an example is shown in Figure 9.1.

i-V curves are generated through a variation in the voltage applied across the cell and measuring the cell current at specific voltages. *i-V* curves and power density curves provide a direct indication of the fuel cell performance under controlled operating conditions. Power density curves are produced by multiplying the voltage by the current density to obtain the power density in mW cm^{-2}. This power density provides a more informative illustration of fuel cell performance with respect to overall energy generation. Fuel cells are highly susceptible to changes in applied load due to the

irreversible losses that occur with increasing voltage. These losses are separated into three types; Activation, Ohmic and Concentration [4, 5].

Activation losses are caused by the activation energies required for the electrochemical reactions at both the anode and cathode. A proportion of the applied voltage is used to overcome these activation barriers. However, as the activation energies for the anode and cathode are different and vary with fuel choice, this can cause an imbalance across the cell and reduce current.

Ohmic losses are caused by the voltage gradient across the cell and the voltage that is used for charge transport within the cell, which reduces the flow of electrons from the anode through the external circuit. The resistance of the electrolyte material to oxygen ion transport and also electrical circuit resistance results in ohmic losses. The ohmic losses generated from the electrolyte material increase with increasing voltage due to the reduction in defects available caused by the increased oxidising potential.

Concentration losses are caused by the electrochemical reactions occurring at a different rate to the diffusion of ions into the electrode, causing a concentration gradient.

The extent of these losses can be influenced by variations in operating conditions such as gas flow and composition, temperature and also the electrode and electrolyte materials used. The influence of reaction conditions, fuel composition and anode material are discussed in this section.

9.4 Initial solid oxide fuel cell operation using H_2 as a fuel

Potentiodynamic tests were carried out on solid oxide fuel cells with Ni/YSZ or 5 mol% CeO_2-Ni/YSZ anodes using H_2 as a fuel at 600 °C, 700 °C, 800 °C and 900 °C. The performance of these fuel cells operating on H_2 and the influence of both temperature and catalyst material provides a standard to which the performance of the cells, when operating on biogas, can be compared.

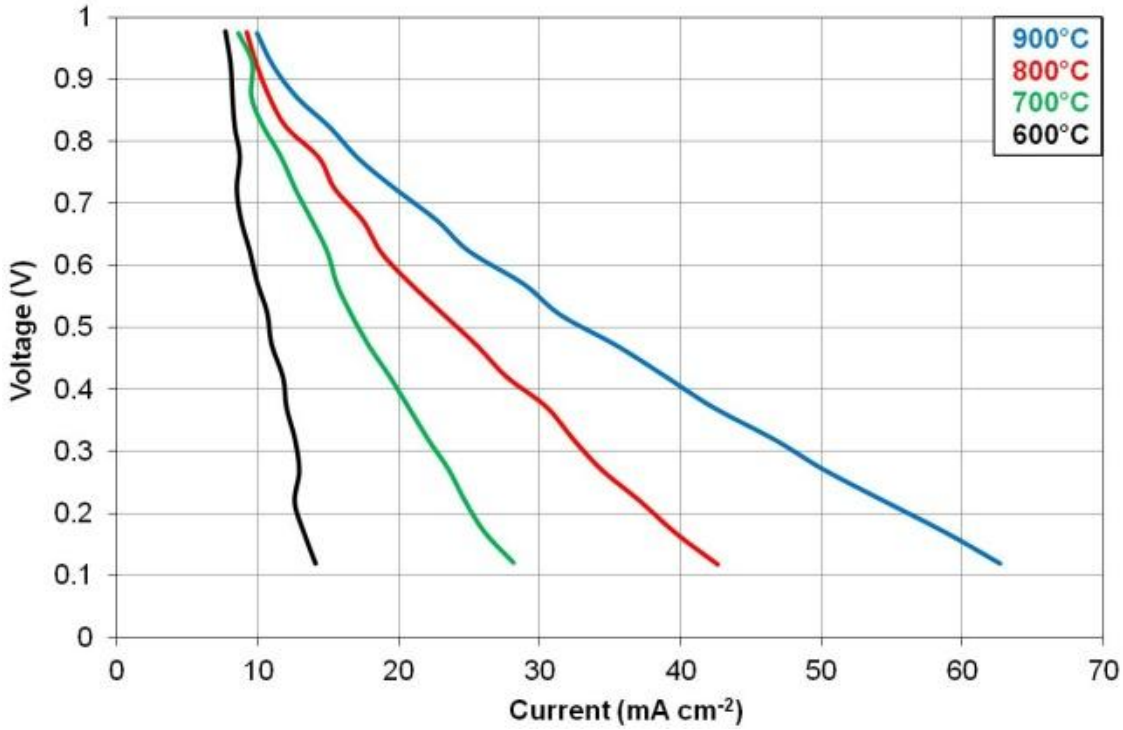

Figure 9.1: *i-V* curves for a SOFC with a Ni/YSZ anode operating on H_2 at 600, 700, 800 and 900 °C

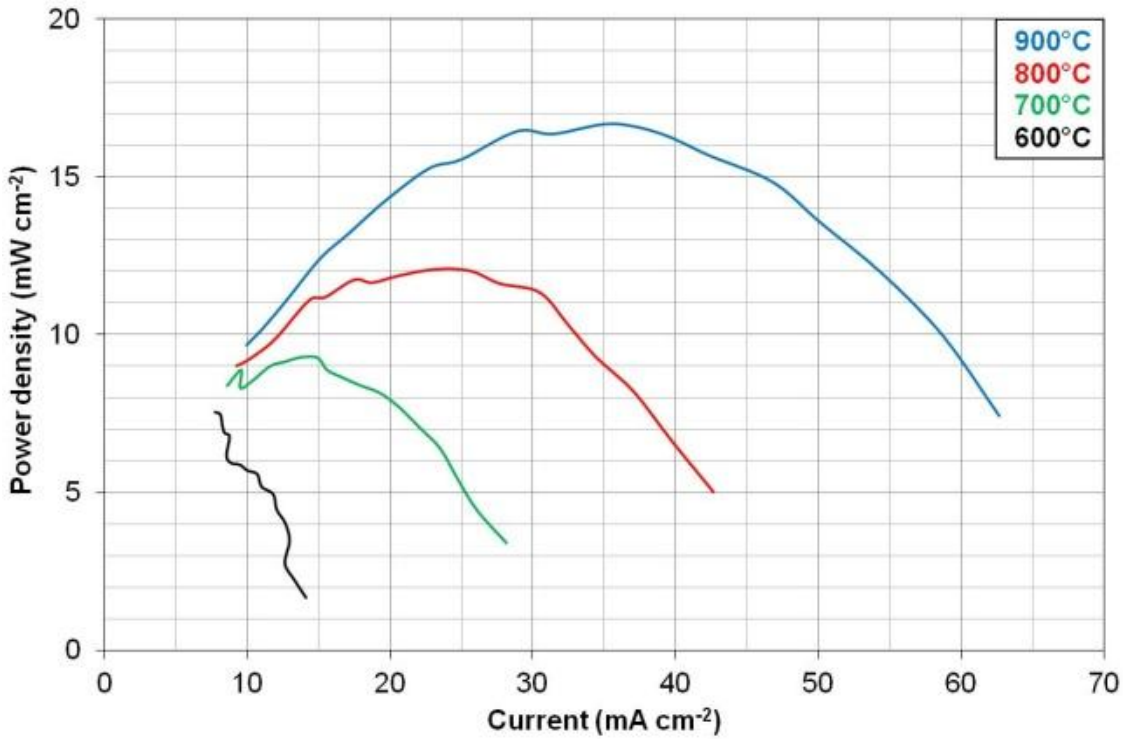

Figure 9.2: Power density curves for an SOFC with a Ni/YSZ anode operating on H_2 at 600, 700, 800 and 900 °C

It is clear from the *i-V* and power density curves shown in Figure 9.1 and 9.2 respectively, that the operating temperature of the cell has a significant influence on performance. The electrical performance of the cell at 600 °C is very poor but as the operating temperature increases, the electrical performance also increases. This increase in performance with temperature can be attributed to simple reaction kinetics and thermodynamics and also increased oxide ion mobility and transport across the electrolyte. The decreased power output above an optimum with increasing current is due to the irreversible losses that are discussed previously in Section 9.3.

The substantially greater optimum power density that can be obtained at higher operating temperatures (shown in Fig 9.2) illustrates the potential to reduce electrochemical losses with increased temperature. At higher temperatures, the increased potential for interstitials within the YSZ electrolyte can result in increased ion conductivity and reduced ohmic losses [4, 6]. Goula *et al.* [7] have reported the use of a fuel cell with the Ni/YSZ anode, YSZ electrolyte and LSM cathode material configuration similar to that used in this research and their studies of methane dry reforming at 875 °C show an optimum power density of 50mW/cm^2.

Doping the Ni/YSZ anode material with 5 mol% CeO_2 results in a significantly greater electrical performance, as shown in Figures 9.3 and 9.4. This greater electrical performance is present across the full range of operating temperatures and increases with temperature, observed as with the Ni/YSZ anode-containing cell. The performance of the 5mol% CeO_2-Ni/YSZ is comparable to the results reported by Laycock *et al.* [8] for a similar cell operating on hydrogen at 850 °C.

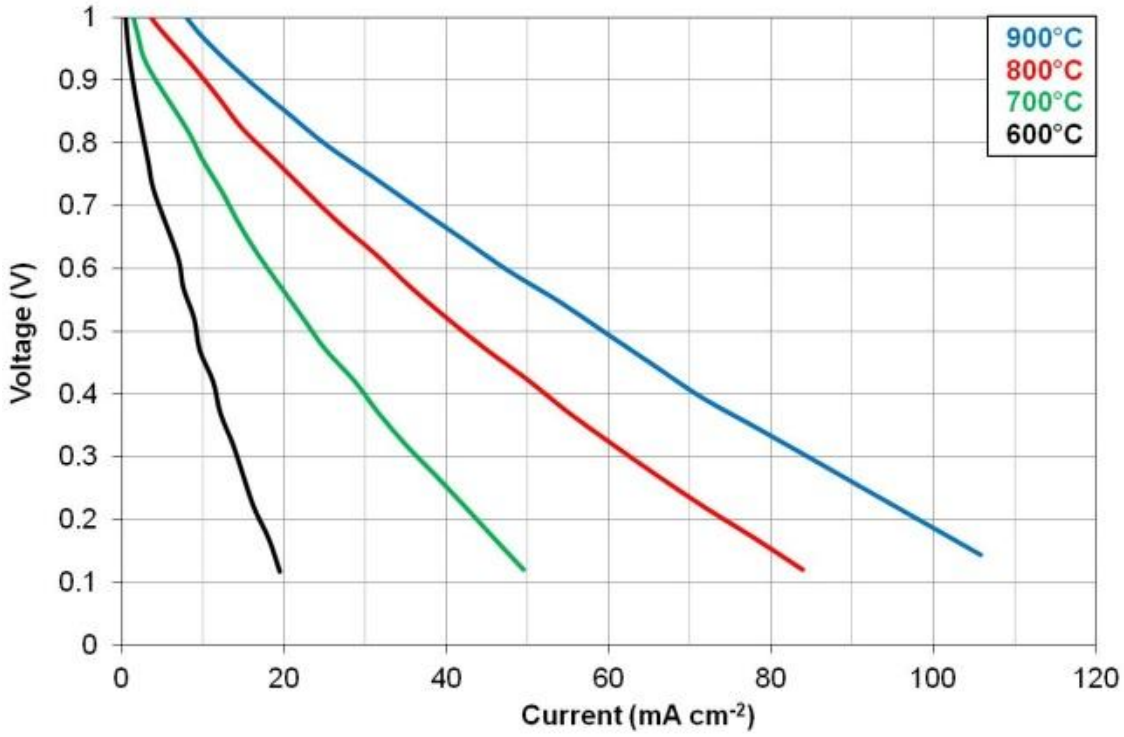

Figure 9.3: *i-V* density curves for an SOFC with a 5 mol% CeO_2-Ni/YSZ anode operating on H_2 at 600, 700, 800 and 900 °C

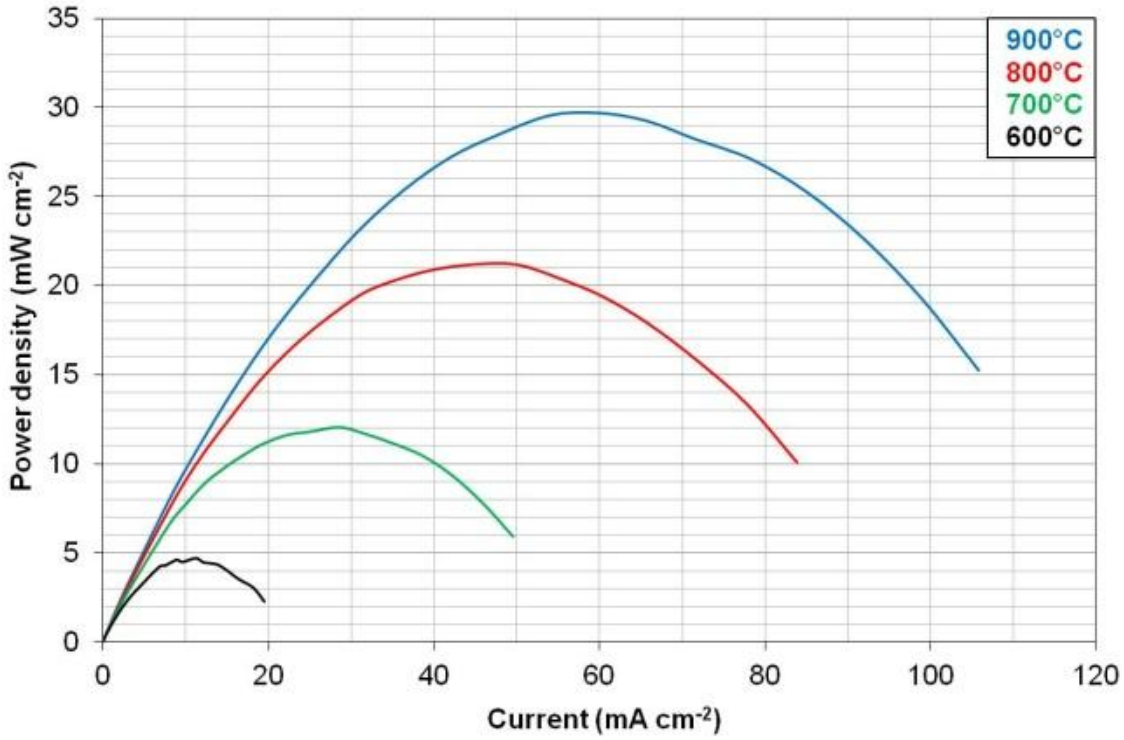

Figure 9.4: Power density curves for an SOFC with a 5 mol% CeO_2-Ni/YSZ anode operating on H_2 at 600, 700, 800 and 900 °C

The use of CeO_2 as a dopant on Ni/YSZ to improve catalytic performance and also increase tolerance to sulfur deactivation has been discussed previously in Sections 6 and 7 respectively. The enhanced fuel cell performance with the 5mol% CeO2-Ni/YSZ cell can be attribute to redox capability of ceria discussed in these sections and also the ability of CeO_2 to facilitate oxide transfer. Gorte *et al.* [5, 9] reported the use of a similar cell with a Cu/YSZ anode material that exhibited an optimum power density of *ca*.50mW/cm^2 and how the presence of ceria within a solid oxide fuel cell enhanced the electrical output to an optimum power density of *ca*. 300mW/cm^2. This was attributed this improvement to CeO_2 acting as an oxidation catalyst and also increasing charge transfer at the three phase boundary between anode and electrolyte material. The decreased performance above an optimum with increasing current can be attributed to increased irreversible losses as discussed for the Ni/YSZ anode containing cell.

9.5 Solid oxide fuel cell operation containing a Ni/YSZ anode using simulated biogas with and without the addition of oxygen

To assess the performance of an SOFC with a Ni/YSZ anode operating directly on simulated biogas (CH_4 + 0.5CO_2) with the addition of O_2, *i-V* tests were carried out. The power density curves are shown at 700 °C, 800 °C and 900 °C with different oxygen concentrations in Figures 9.5, 9.6 and 9.7 respectively. These measurements were carried out equivalent to when the cells were fuelled with hydrogen to enable direct comparisons.

From Figures 9.5 – 9.7, it is apparent that the influence of temperature on the electrical performance when operating on simulated biogas with the addition of oxygen is very similar to when operating on pure hydrogen, in that increased temperature substantially improves performance. This can again be attributed to the increased rate of electronic reaction, charge transfer and ion conductivity. Increased temperature can also influence the rate of methane

reforming that occurs on the anode surface. The influence of temperature on methane reforming has been discussed in detail in Sections 6 and 7.

Tests were carried out at 600 °C, however no activity was observed at this temperature. This lack of activity may be attributed to the very low rate and extent of methane reforming and subsequent hydrogen generation at this temperature, in addition to very low oxygen ion conductivity at this temperature.

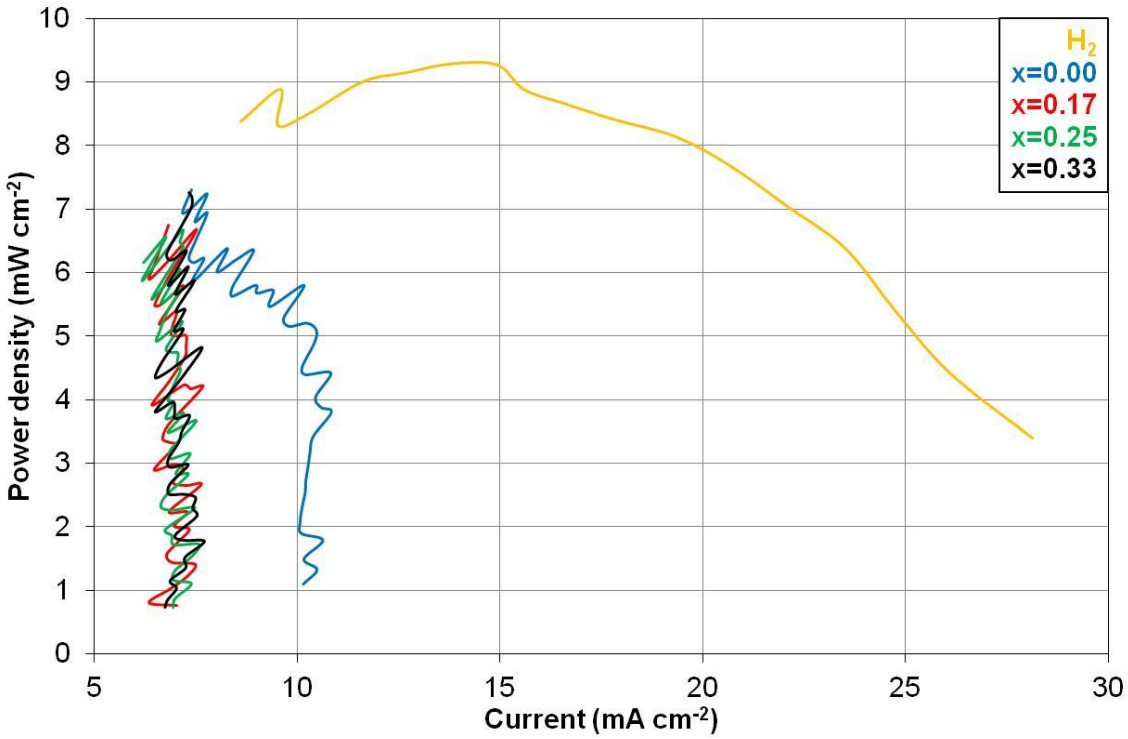

Figure 9.5: Power density curves for an SOFC with a Ni/YSZ anode operating on H_2 and simulated biogas (CH_4 + 0.5CO_2) at 700 °C with different added O_2 levels (x=0.00, x=0.17, x=0.25, x=0.33).

At 700 °C (Figure 9.5), the electrical performance of the cell operating on biogas is very poor compared with the performance using hydrogen as the fuel. This can be attributed to the small level of methane reforming that is occurring over the anode material at this temperature, and therefore the low concentration of hydrogen and carbon monoxide available to be oxidised. Interestingly, the addition of oxygen to the biogas mixture actually results in decreased performance, to an extent

where the output is almost zero. This may be due to the potential for total oxidation of methane at this temperature and also the oxidation with the oxygen added of any hydrogen and carbon monoxide that may be present on the anode surface. This therefore reduces the quantity of hydrogen available for electrochemical oxidation.

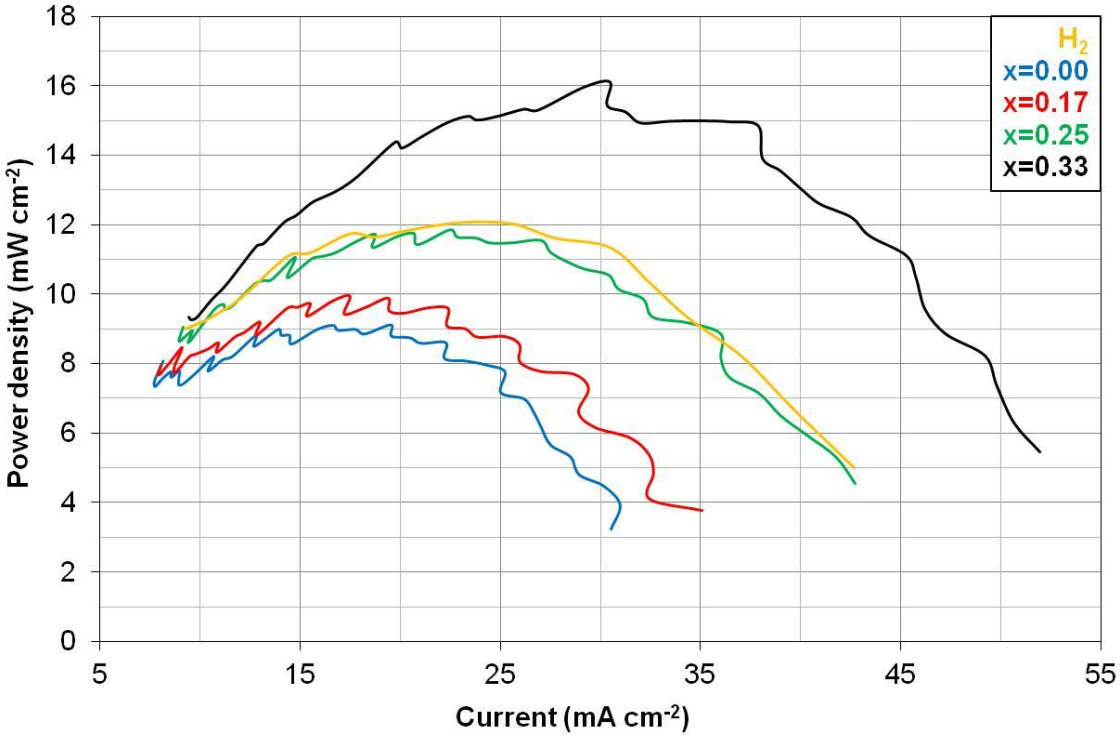

Figure 9.6: Power density curves for an SOFC with a Ni/YSZ anode operating on H_2 and simulated biogas (CH_4 + 0.5CO_2) at 800 °C with different added O_2 levels (x=0.00, x=0.17, x=0.25, x=0.33).

At 800 °C (Figure 9.6), there is a significant improvement in the electrical performance of the fuel cell for all fuel compositions used. In contrast to the behaviour seen at 700 °C (Figure 9.5), the addition of oxygen to the simulated biogas (CH_4 + 0.5CO_2) mixture improves the electrical performance, and this improvement increases progressively with greater quantities of added oxygen. This behaviour may be attributed to the increased potential for methane reforming to synthesis gas at these temperatures, and therefore increased hydrogen and CO production, and subsequent electrochemical oxidation. This increase in methane reforming to produce synthesis gas

with the addition of oxygen is shown in Section 5. At the same time, the increased temperatures also enhance the ion conductivity of the cell.

The performance of the cell operating when x=0.25 shows comparable performance to operation with hydrogen whilst when x=0.33, a significantly improved performance compared to operation with H_2 is observed. This suggests that even when high oxygen levels are added to the biogas simulated mixture with an O_2:CH_4 ratio of 0.33, methane partial oxidation is favoured over total oxidation, and that the direct oxidation of the hydrogen and carbon monoxide products from methane reforming is not occurring to any significant extent, with very efficient electrochemical oxidation of the hydrogen and CO occurring. This does not exclude the possibility of direct electrochemical oxidation or total oxidation of methane producing water and carbon dioxide, which can then activate methane reforming [8].

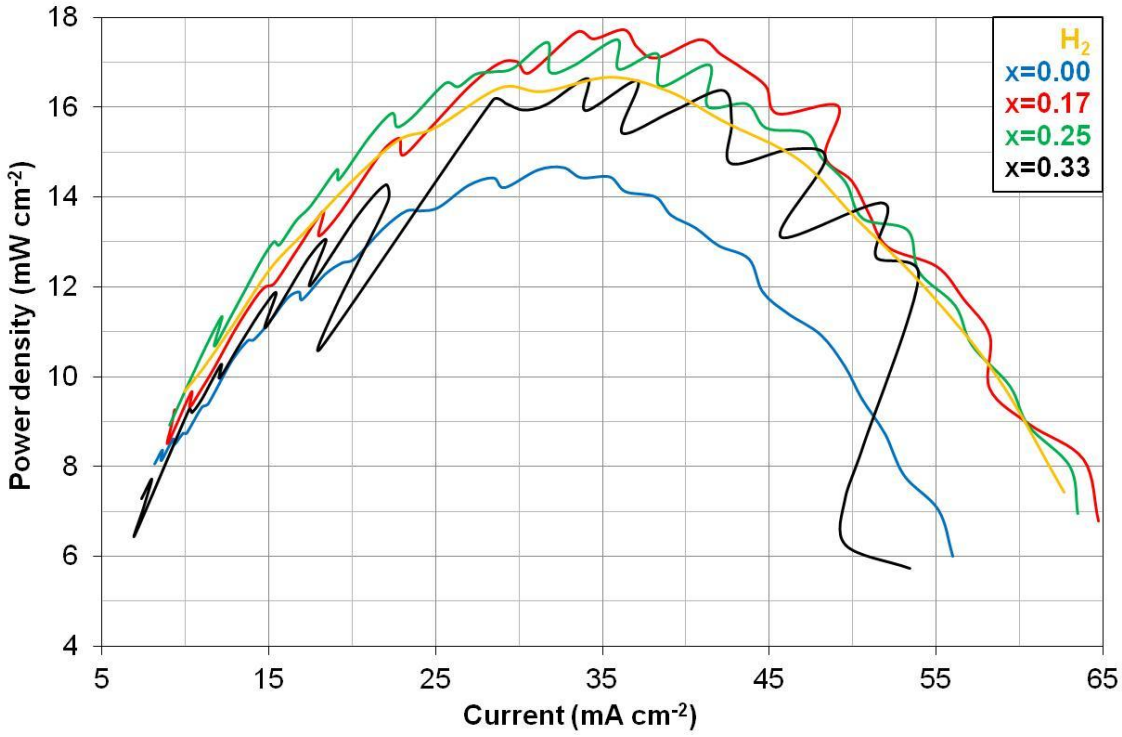

Figure 9.7: Power density curves for an SOFC with a Ni/YSZ anode operating on H_2 and simulated biogas (CH_4 + 0.5CO_2) at 900 °C with different added O_2 levels (x=0.00, x=0.17, x=0.25, x=0.33).

The electrical performance of the SOFC fuelled on simulated biogas without oxygen addition at 900 °C (Figure 9.7) is substantially greater than at 700 °C (Figure 9.5) and 800 °C (Figure 9.6). This is shown in that the maximum power output increases by over 60 % from 800 °C to 900 °C, apart from when x=0.33 where comparable performance at 800 °C to 900 °C is observed. This increase can be attributed to the significantly greater extent of methane reforming by CO_2 with increased temperature as shown in Section 5.

The addition of 0.17 O_2 to the simulated biogas mixture results in significantly increased electrical performance, as seen at lower operating temperatures. However, in contrast to lower temperatures, further increased addition of O_2 to the simulated biogas mixture results in a slight reduction in electrical performance. This suggests that at higher oxygen concentrations, either the total oxidation of methane of direct oxidation of hydrogen and CO occurs to such an extent to reduce the capacity for electrochemical oxidation of hydrogen and CO and subsequent increased power output.

9.6 Solid oxide fuel cell operation containing a 5 mol% CeO_2-Ni/YSZ anode using simulated biogas with and without the addition of oxygen

The influence of ceria doping of the Ni/YSZ anode on the performance of an SOFC when operating on simulated biogas with oxygen addition was also investigated and is shown in Figures 9.8 – 9.10. The increased performance for an SOFC operating on hydrogen with 5 mol% CeO_2 doping on the Ni/YSZ anode was shown earlier. This increased performance was attributed to the ability of ceria to assist in charge transfer at the three phase boundary, whilst also acting as an oxidation catalyst across the anode surface promoting methane reforming [5].

This behaviour is also observed when simulated biogas with oxygen addition is used as the fuel, in that a significantly improved electrical performance across the 700 - 900 °C temperature range and across the range of gas compositions is observed in Figures 9.8 – 9.10.

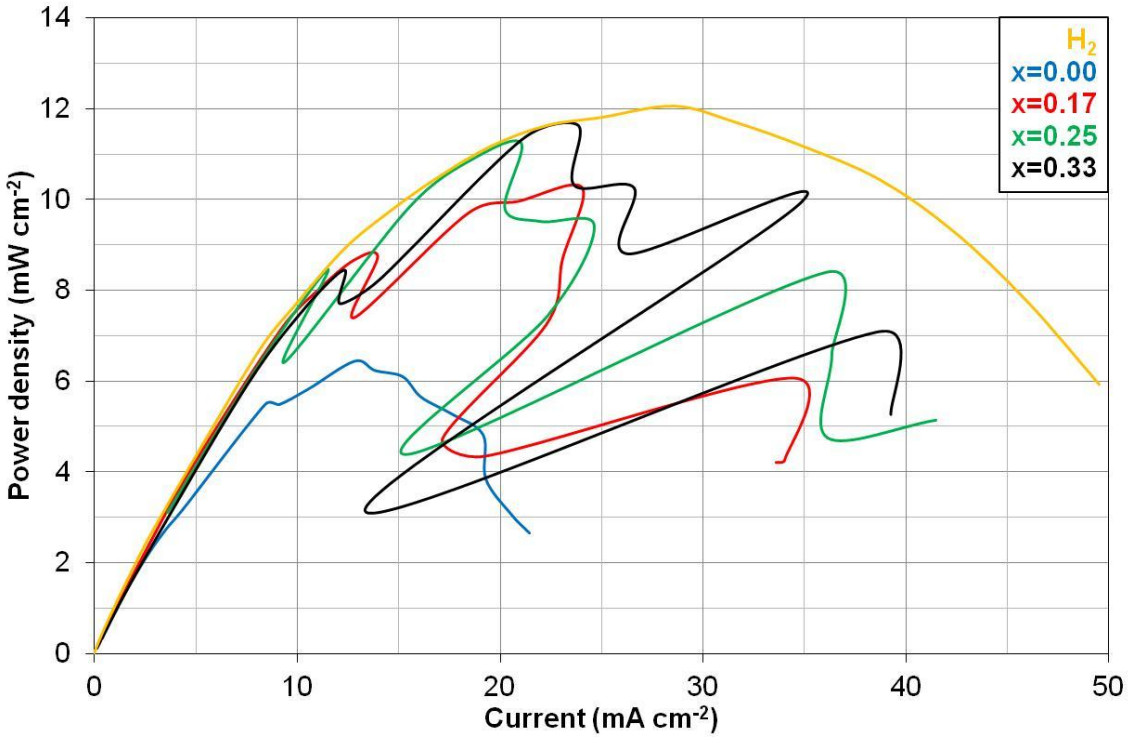

Figure 9.8: Power density curves for an SOFC with a 5 mol% CeO_2-Ni/YSZ anode operating on H_2 and simulated biogas (CH_4 + 0.5CO_2) at 700 °C with different added O_2 levels (x=0.00, x=0.17, x=0.25, x=0.33).

The tests carried out at 700 °C on a SOFC with a 5 mol% CeO_2-Ni/YSZ anode (Figure 9.8) show a significantly different behaviour to the tests carried on a SOFC with a Ni/YSZ anode (Figure 9.5) in that negligible performance was observed for the SOFC with a Ni/YSZ anode for all CH_4 + 0.5CO_2 + xO_2 compositions studied, whereas a substantial improvement in performance is observed for the cell with a ceria doped anode. Additionally, in contrast to the cell with the Ni/YSZ anode, the addition of O_2 to the simulated biogas mixture results in improved performance of the cell with a ceria doped anode. The performance of the cell when oxygen is added to the simulated biogas mixture is very sporadic at this temperature. One cause for this may be the oxygen storage capacity of ceria and the increased potential for total oxidation or direct oxidation with ceria which may cause intermittent cycles, as discussed previously in Section 6.

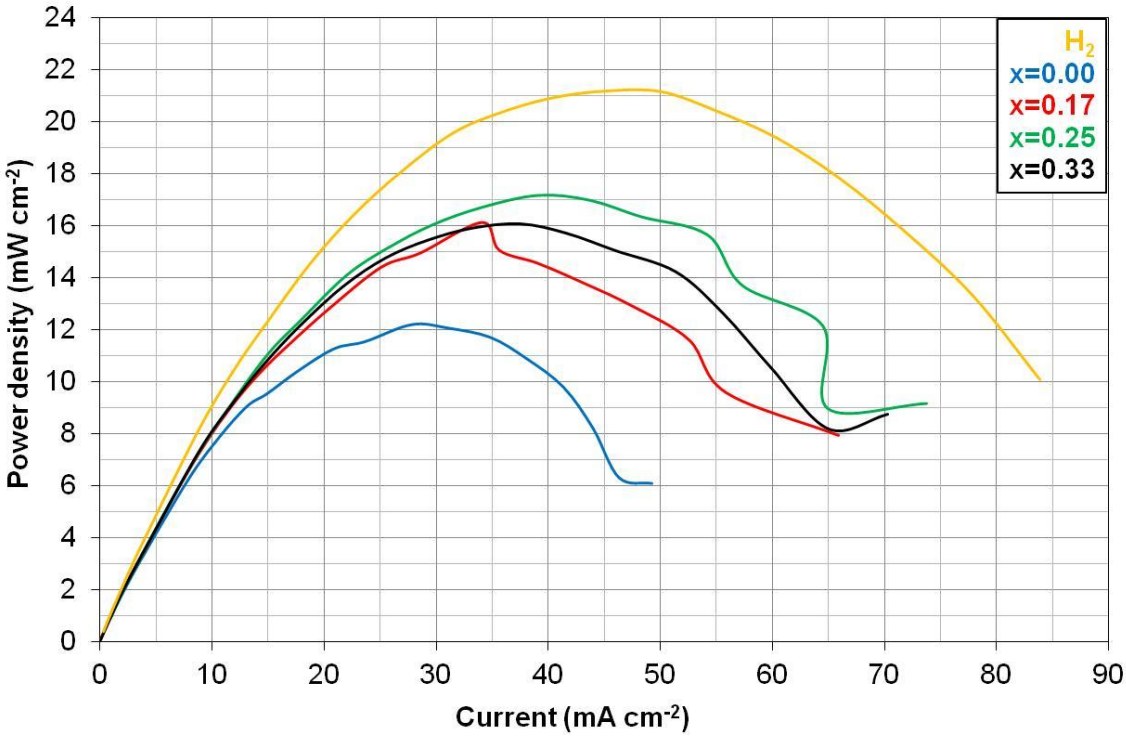

Figure 9.9: Power density curves for an SOFC with a 5 mol% CeO_2-Ni/YSZ anode operating on H_2 and simulated biogas (CH_4 + 0.5CO_2) at 800 °C with different added O_2 levels (x=0.00, x=0.17, x=0.25, x=0.33).

At 800 °C (Figure 9.9), a similar performance is observed for the cell with a ceria doped anode as with the cell with the undoped anode (Figure 9.6), in that electrical performance increases as O_2 is added to the simulated biogas mixture. The performance increases further as the O_2 concentration is increased from 0.17 to 0.25. However, in contrast to the cell with the undoped anode, increasing the O_2 concentration from 0.25 to 0.33 results in a small decrease in performance of the cell with the ceria doped anode. This may again be attributed to the increased potential for total or direct oxidation with the presence of ceria in the anode, due to its high oxygen storage capacity.

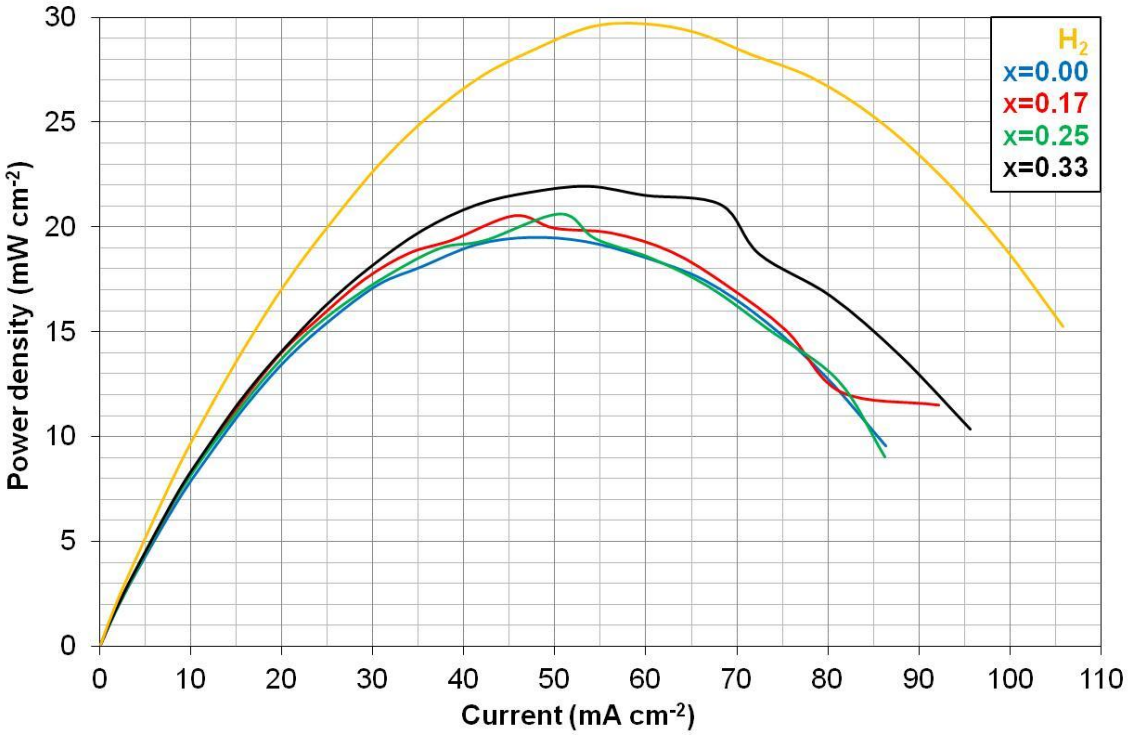

Figure 9.10: Power density curves for an SOFC with a 5 mol% CeO_2-Ni/YSZ anode operating on H_2 and simulated biogas (CH_4 + 0.5CO_2) at 900 °C with different added O_2 levels (x=0.00, x=0.17, x=0.25, x=0.33).

For the tests carried out at 900 °C (Figure 9.10), the influence of oxygen on the electrical performance is significantly reduced compared to that at lower temperatures. The addition of x=0.17 and 0.25 to the simulated biogas mixture results in only a very marginal improvement in performance. However, when x=0.33, there is a slight increase in electrical performance. This is in contrast to the behaviour seen for the Ni/YSZ anode cell (Figure 9.7), where an increase is seen upon initial addition of oxygen to the simulated biogas mixture, but with increased addition of O_2, no significant increases in performance are observed. This behaviour may suggest that as the oxygen concentration added is increased to 0.33, the potential for total oxidation of methane is favoured over direct oxidation of the hydrogen and carbon monoxide products to result in increased hydrogen and carbon monoxide yield through indirect methane reforming.

9.7 Summary of solid oxide fuel cell performance with Ni/YSZ and 5 mol% CeO_2-Ni/YSZ anodes operating on pure H_2 or simulated biogas with and without oxygen addition

In this chapter, the potential use of biogas as a fuel for solid oxide fuel cells has been demonstrated. The influence of temperature, oxygen addition to the biogas and also nature of the anode material on the fuel cell performance has been studied. Measurements have been carried out using pure hydrogen as a fuel to provide a comparison.

Temperature has shown to have a significant influence on the fuel cell performance, when operated on either simulated biogas or pure hydrogen, with increasing temperature resulting in significantly increased performance as can be seen in Table 9.1. This can be attributed to an increase in the kinetic rate of both the anodic and cathodic reactions and also a decrease in the potential losses through increased formation of interstitials and therefore increased oxide ion mobility. The influence of temperature is particularly evident when simulated biogas is used as the fuel in that as temperature increases, the performance of the cell operating on biogas becomes much more similar to when operating on pure hydrogen. This is attributed to the increased potential for dry reforming of methane to H_2 and CO on the anode at increased temperatures.

Table 9.1: Optimum power output for SOFC's with varied anode material, fuel and operating temperature

		Operating temperature		
		700 °C	**800 °C**	900 °C
Anode material	**Fuel**	**Optimum power output (mW cm^{-2})**		
Ni/YSZ	**H_2**	9.27	12.03	16.67
	x=0.00	7.33	9.12	14.60
	x=0.17	6.82	9.94	17.72
	x=0.25	6.77	12.08	17.50
	x=0.33	7.33	16.10	16.38
5mol% CeO_2 - Ni/YSZ	**H_2**	12.05	21.18	29.67
	x=0.00	6.47	12.14	19.48
	x=0.17	10.24	16.05	20.54
	x=0.25	11.23	17.12	20.65
	x=0.33	11.68	16.03	21.95

An increase in cell performance is observed with the addition of oxygen to the simulated biogas mixture, with the exception of the test at 700 °C with the Ni/YSZ anode cell and is shown in Table 9.1. This increase with oxygen addition is attributed to the increased reformant availability for methane reforming. The level of improvement is increased as the quantity of oxygen added increases, apart from at 800 °C with the 5 mol% CeO_2-Ni/YSZ anode fuel cell, which may be due to an increase in the potential for total oxidation of methane or direct oxidation of hydrogen and carbon monoxide.

Doping of the fuel cell anode with 5 mol% CeO_2 results in a significant improvement in cell performance across the operating conditions studied as seen by the optimum power outputs shown in Table 9.1. This can be attributed to the oxygen storage ability of ceria increasing methane reforming and also enhancing ion transfer at the three phase boundary to increase the rate of electrochemical oxidation. The reduced improvement for the 5 mol% CeO_2-Ni/YSZ anode cell compared to the Ni/YSZ anode cell when x=0.33 may illustrate the increase in total oxidation and direct oxidation due to the oxygen storage capacity of ceria.

9.8 References

1. N.Q. Minh, *Solid oxide fuel cell technology--features and applications.* Solid State Ionics, 2004. **174**(1-4): p. 271-277.
2. J. Staniforth and K. Kendall, *Cannock landfill gas powering a small tubular solid oxide fuel cell - a case study.* J. Power Sources, 2000. **86**: p. 401-403.
3. J. Staniforth, *The use of biogas to power a small tubular solid oxide fuel cell, PhD Thesis*. 2000, Keele University.
4. R. O'Hayre, S.-W. Cha, W. Colella, and F.B. Prinz, *Fuel Cell Fundamentals*. 2006, Wiley VCH. p. 303.
5. S. McIntosh and R.J. Gorte, *Direct Hydrocarbon Solid Oxide Fuel Cells.* Chemical Reviews, 2004. **104**(10): p. 4845-4866.
6. R.F. Martins, M.C. Brant, R.Z. Domingues, R.M. Paniago, K. Sapag, and T. Matencio, *Synthesis and characterization of NiO-YSZ for SOFCs.* Mater. Res. Bull., 2009. **44**: p. 451-456.
7. G. Goula, V. Kiousis, L. Nalbandian, and I.V. Yentekakis, *Catalytic and electrocatalytic behavior of Ni-based cermet anodes under internal dry reforming of CH4 + CO2 mixtures in SOFCs.* Solid State Ionics, 2006. **177**(19-25): p. 2119-2123.
8. C.J. Laycock, J.Z. Staniforth, and R.M. Ormerod, *Biogas as a fuel for solid oxide fuel cells and synthesis gas production: effects of ceria-doping and hydrogen sulfide on the performance of nickel-based anode materials.* Dalton Transactions, 2011. **40**(20): p. 5494-5504.
9. R.J. Gorte, H. Kim, and J.M. Vohs, *Novel SOFC anodes for the direct electrochemical oxidation of hydrocarbon.* Journal of Power Sources, 2002. **106**(1-2): p. 10-15.

10 Conclusion

The addition of oxygen to a simulated biogas mixture has been shown to have a significant influence on the activity and selectivity of nickel-based catalysts for methane reforming, and also the stability over time with regards to deactivation by carbon and sulfur poisoning. The influence of oxygen on the behaviour of ceria-doping of the nickel catalyst for reforming of simulated biogas and also fuel cell operation using nickel-based anode materials has been studied.

10.1 The influence of oxygen addition on the behaviour of Ni/YSZ for the reforming of simulated biogas

From temperature programmed studies, it was observed that the addition of oxygen to a simulated biogas mixture significantly changes the reaction profile, through the introduction of a light-off feature which occurs at greater temperatures with increased oxygen concentrations. This feature has been attributed to the greater capacity for total oxidation as the oxygen concentration increases. As oxygen concentration increases, the catalyst activity also increases due to the increased availability of reformant.

Conventional catalytic studies conducted over 20 hours show the strong influence of oxygen addition on the catalyst activity, selectivity and stability. Across the complete temperature range studied (600-1000 °C), the addition of oxygen induces an increase in catalyst activity for synthesis gas formation. This increase, which is extended with increased oxygen concentration, has been attributed to the increased availability of reformant. At increased reaction temperatures, the influence of oxygen is less substantial due to the increased thermodynamic potential for methane reforming with CO_2.

The selectivity of the catalyst for methane reforming varies significantly with oxygen concentration and reaction temperature. Across all reaction temperatures, the addition of oxygen increased the H_2:CO product ratio. This is attributed to the increased H_2:CO ratio of the partial oxidation reaction compared to the CO_2 (dry) reforming reaction. At low temperatures, this increase in H_2:CO product ratio is greater with increased oxygen concentration, whereas at high temperatures the opposite is seen.

This variation in product ratio is interesting and highly desirable as it provides the potential for the product ratio to be tailored to facilitate the requirements of the process in which the product is to be used. Also, the addition of oxygen and increased oxygen content in the simulated biogas feed gas results in a significantly improved catalyst stability and durability through a reduction in carbon deposition across the complete reaction temperature range.

10.2 The influence of ceria-doping of Ni/YSZ on the catalytic behaviour for reforming of simulated biogas with oxygen addition

The equivalent temperature programmed reaction measurements carried out over 5 mol% CeO_2-Ni/YSZ exhibited a similar behaviour and influence of temperature and oxygen content to those conducted on Ni/YSZ, with the exception that 5 mol% CeO_2-Ni/YSZ shows a slightly lower activity at higher temperatures, and that the light-off temperature occurs at a slightly lower temperature. These variations have been attributed to the reduced potential for methane decomposition on CeO_2-Ni/YSZ through increased oxygen availability on the catalyst surface.

A different behaviour is observed over 5 mol% CeO_2-Ni/YSZ to that seen on Ni/YSZ during conventional (isothermal) reaction studies in that cycling behaviour was observed, which has been attributed to transient reduction and oxidation cycling of CeO_2.

In the absence of added oxygen, greater activity for biogas reforming is observed over 5 mol% CeO_2-Ni/YSZ which may be due to the capacity of Ce_2O_3 to be oxidized by CO_2 to promote

methane reforming. With oxygen addition, similar activities were observed for both catalysts at lower temperatures (600-800 °C), whereas at higher temperatures (900-1000 °C), significantly reduced activity was observed over 5 mol% CeO_2-Ni/YSZ, in addition to a reduced stability with time. This difference may be attributed to a variation in the quantity of carbon deposition, potential for oxidation of carbon deposits and also carbon morphologies that may form when ceria is present on the nickel catalyst. This is supported by the significantly greater extent of carbon deposition that was observed, following reactions over 5 mol% CeO_2-Ni/YSZ.

10.3 The influence of sulfur on the behaviour of Ni/YSZ and ceria-doped Ni/YSZ for reforming of simulated biogas with oxygen addition

Significant deactivation is observed with the addition of H_2S to the simulated biogas mixture for both Ni/YSZ and ceria-doped Ni/YSZ across all reaction temperatures and oxygen contents, particularly at lower reaction temperatures (600-800 °C), where total deactivation is seen. Addition of oxygen to the simulated biogas mixture results in both a substantial increase in activity and also an increased tolerance towards sulfur poisoning. This increase in sulfur tolerance is attributed to the oxidative removal of sulfur from the catalyst surface. Ceria doping of Ni/YSZ promotes the increased sulfur tolerance with oxygen, which may be due to the ability of ceria to increase the oxygen concentration on the catalyst surface.

Reaction temperature was found to be the primary controlling factor towards sulfur tolerance, specifically for temperatures above 800 °C, due to the rapid removal of sulfur from the catalyst surface at high temperatures. Additionally, reduced carbon deposition on the catalysts surface is observed with the presence of H_2S in the simulated biogas mixture.

10.4 Catalyst recovery from complete deactivation due to sulfur poisoning and the influence of ceria doping, temperature and oxygen addition

In the absence of oxygen, no regeneration of the catalysts was observed over a 25 hour period at 700 °C. However, the addition of oxygen to the simulated biogas mixture resulted in substantial regeneration of both Ni/YSZ and ceria-doped Ni/YSZ.

Regeneration of the catalysts from sulfur poisoning in the presence of lower added oxygen concentrations (x=0.17, 0.25) occurs in a cyclical fashion; initial extensive regeneration is observed followed by secondary deactivation to the point of total deactivation. This behaviour is attributed to the saturation of the nickel surface with oxygen resulting in sudden, extensive sulfur oxidation, and as the nickel surface becomes free of sulfur, sulfur present in the bulk of the catalyst migrates to the surface, inducing secondary deactivation.

The rate of cycling is influenced significantly by both oxygen concentration and ceria doping of the nickel catalyst. This cycling behaviour is not observed at higher oxygen concentrations (x=0.33), which may be due to the greater availability of surface oxygen to induce sulfur oxidation at high oxygen concentrations.

10.5 Operation of solid oxide fuel cells with Ni/YSZ and ceria-doped Ni/YSZ anodes on simulated biogas with oxygen addition

Both operating temperature and oxygen addition have shown a significant influence on fuel cell performance. For both anode materials and across all oxygen concentrations, increased temperature results in a significant increase in cell performance. This is particularly evident for operation on simulated biogas, which may be attributed to the significant increase in methane reforming with increased temperature.

Oxygen addition to the simulated biogas results in increased cell performance, which has been attributed to the greater availability of reformant to increase methane reforming and subsequent hydrogen and carbon monoxide production. Increased oxygen addition generally increases cell performance, however a reduction in performance was observed at the highest quantity of oxygen added, which may be attributed to the increased extent of total oxidation.

Ceria-doping of the Ni/YSZ anode material also increased electrical performance with and without the presence of added oxygen, which has been attributed to the oxygen storage capacity of ceria to facilitate methane reforming. Ceria is also proposed to assist oxygen ion transfer at the cell three phase boundary. A reduced performance was observed at the greatest level of added oxygen, which may be an indication of the increased potential for total oxidation under fuel cell operating conditions and high oxygen levels.

10.6 Closing statements

In this study, the influence of temperature, oxygen addition, ceria-doping and sulfur poisoning on the behaviour of nickel based catalysts for simulated biogas reforming has been studied. Each of these variables has been shown to influence the activity, selectivity and stability of the catalyst towards simulated biogas reforming for synthesis gas production.

Significant advances have been achieved in increasing activity and also adding a degree of control towards the synthesis gas product ratio through the addition of oxygen in varied quantities, temperature and by ceria doping. The increase in activity increases the efficiency and therefore potential viability of this approach, whilst the ability to tailor the synthesis gas ratio increases the potential applications.

These variables have also been shown to significantly improve catalyst durability by reducing the extent of carbon deposition and also the tolerance of the catalyst towards deactivation through

sulfur poisoning. These reductions in deactivation and approaches for catalyst regeneration studied increase the practical longevity of the catalysts for biogas reforming.

The optimum conditions observed for the reforming of simulated biogas is the use of the Ni/YSZ catalyst at 1000 °C with an O_2:CH_4 ratio of 0.25, whilst the Ni/YSZ catalyst at 1000 °C with an O_2:CH_4 ratio of 0.33 are the optimum conditions for the reforming of simulated biogas with the addition of 5 ppm H_2S. Recovery of the system from sulfur deactivation is most efficiently achieved using 5 mol% CeO_2-Ni/YSZ and an O_2:CH4 ratio of x=0.33 but longer term studies are needed to confirm this. For solid oxide fuel cell operation, the use of a 5 mol% CeO_2-Ni/YSZ catalyst as the anode, a temperature of 900 °C and a O_2:CH_4 ratio of x=0.33 shows the most efficient performance. However, these conditions may not be applicable to experiments over significant time durations.

The findings from this study will contribute to supporting future research and the increased viability of this approach as an efficient and environmentally friendly method of utilising a waste product for energy generation or synthesis gas production.

11 Future work

From the findings of this research study, several specific topics that have been identified that merit further research.

More detailed characterisation could provide greater insight into catalyst deactivation and methods in which it could be minimised. In particular, the influence of temperature, oxygen concentration and CeO_2 doping of the catalyst towards thermal degradation of the nickel catalyst would be beneficial as these parameters have been shown to influence the thermal behaviour of catalyst materials [1-3]. Electron microscopy (TEM and SEM) would provide additional insight into the nature of carbon deposition on the catalyst surfaces and how the temperature, reactant gas composition and catalyst material can influence both the extent and also the morphology of the carbon deposits and provide some insight into how these influence reforming behaviour [4, 5].

The variable composition of biogas is such that further research into different CH_4:CO_2 ratios and also different H_2S concentrations is important to provide a more comprehensive study of the conversion of biogas from various sources over nickel based catalysts [6]. The influence of other contaminants found in biogas, such as organic halides and trace metals, and their influence on catalytic reforming behaviour would also be a useful area of research [7].

To assess the longer term durability and stability of nickel based catalysts for biogas reforming, longer term catalytic studies could very useful. In particular, the rates of thermal degradation, carbon deposition, H_2S poisoning and also regeneration are of specific importance. Long term operation of solid oxide fuel cells on simulated biogas has not been researched within this study, but is an obvious area of future study.

The use of catalysts dopants and variations in catalyst materials have been studied within this research project. Further work could be focused towards the use of alternative dopants and also the positive influence of ceria-doping could be extended to research into different dopant levels.

Although the use of simulated biogas mixtures provides a controlled approach towards the optimisation of catalytic techniques and fuel cells, the final stage of research to assess the viability of these systems towards operation on biogas would be to test the systems with actual biogas samples from different sources, and analyse the influence of the optimisation methods studied in this research.

References

1. C.H. Bartholomew, *Mechanisms of catalyst deactivation.* Applied Catalysis A: General, 2001. **212**(1-2): p. 17-60.
2. F.B. Rasmussen, J. Sehested, H.T. Teunissen, A.M. Molenbroek, and B.S. Clausen, *Sintering of Ni/Al_2O_3 catalysts studied by anomalous small angle X-ray scattering.* Applied Catalysis A: General, 2004. **267**(1-2): p. 165-173.
3. J. Sehested, J.A.P. Gelten, and S. Helveg, *Sintering of nickel catalysts: Effects of time, atmosphere, temperature, nickel-carrier interactions, and dopants.* Applied Catalysis A: General, 2006. **309**(2): p. 237-246.
4. Y.H. Hu and E. Ruckenstein, *High-resolution transmission electron microscopy study of carbon deposited on the NiO MgO solid solution catalysts.* Journal of Catalysis, 1999. **184**(1): p. 298-302.
5. H. He and J.M. Hill, *Carbon deposition on Ni/YSZ composites exposed to humidified methane.* Applied Catalysis A: General, 2007. **317**(2): p. 284-292.
6. Y. Shiratori and K. Sasaki, *NiO-ScSZ and $Ni_{0.9}Mg_{0.1}O$-ScSZ-based anodes under internal dry reforming of simulated biogas mixtures.* J. Power Sources, 2008. **180**: p. 738-741.
7. C. Xu, J.W. Zondlo, M. Gong, F. Elizalde-Blancas, X. Liu, and I.B. Celik, *Tolerance tests of H_2S-laden biogas fuel on solid oxide fuel cells.* Journal of Power Sources, 2010. **195**(15): p. 4583-4592.

Appendix A: Determination of appropriate catalyst mass

Prior to performing any catalyst activity tests relating to the operation of simulated biogas reforming, it was necessary for an appropriate catalyst mass to be selected. Catalyst mass used can influence reaction characteristics through increasing or decreasing the potential for reforming due to availability of active surface area, mass transport effects within catalysts and also the increased likelihood of separate zones forming throughout the catalyst. This is an issue especially with simulated biogas reforming with the presence of oxygen due to the combination of the exothermic partial oxidation reaction which will occur at the front of the catalyst bed and the endothermic CO_2 reforming reaction which will occur further through the bed. This variation can have significant issues regarding thermal stability of catalysts as has been mentioned in Section 2.3.

To ensure the most appropriate catalyst mass was chosen, a series of temperature programmed reactions were performed across a range of catalyst masses for the individual partial oxidation and CO_2 reforming reactions. From these reactions the reforming characteristics across the active temperature range could be analysed and compared to select the most active catalyst mass. The temperature programmed partial oxidation reaction characteristics are shown in Figures A.1 – A.3 and the temperature programmed CO_2 reforming reaction characteristics are shown in Figure A.4 – A.6. It can be seen from relevant figures that the catalyst mass to show the highest activity for the partial oxidation reaction is between 20-40 mg. 10 mg of catalyst shows a significantly lower activity, a delayed light off temperature at ~740 °C and also an unusual cycling behaviour that is not exhibited by any other catalyst mass. This may be due to the complete oxidation of the catalyst due to the increased potential for oxidation of the catalyst with smaller catalyst mass.

Regarding the CO_2 reforming reaction, the relevant figures show that the catalyst mass to show highest activity is between 30-40 mg. This is seen through the significantly greater CH_4 conversion, H_2 yield and CO yield. The endothermic nature of CO_2 reforming means that no substantial light-off is seen.

From analysing both individual reactions across the range of Ni/YSZ masses, 30 mg was chosen as the catalyst mass to use throughout the remainder of the study. Although 40 mg showed a comparable activity for both individual reactions, 30 mg was chosen for economic reasons as well as the reduced potential for variations across the catalyst bed.

Upon conducting initial $CH_4 + CO_2 + xO_2$ reforming reactions it was discovered that the mass flow controller responsible for O_2 flow could not be limited to 0.33 ml min^{-1} required to provide 'deficient O_2 (x=0.17)' concentration with 2 ml min^{-1} CH_4 proposed.. Therefore, to accommodate for this, the CH_4 flow used was increased to 3 ml min^{-1} at which the relative 'deficient O_2 (x=0.17)' flow was 0.5 ml min^{-1} and was possible with the current mass flow controller. This required for the catalyst mass to be increased to 45 mg to maintain the same relative ratio between catalyst mass and reactant gas flow.

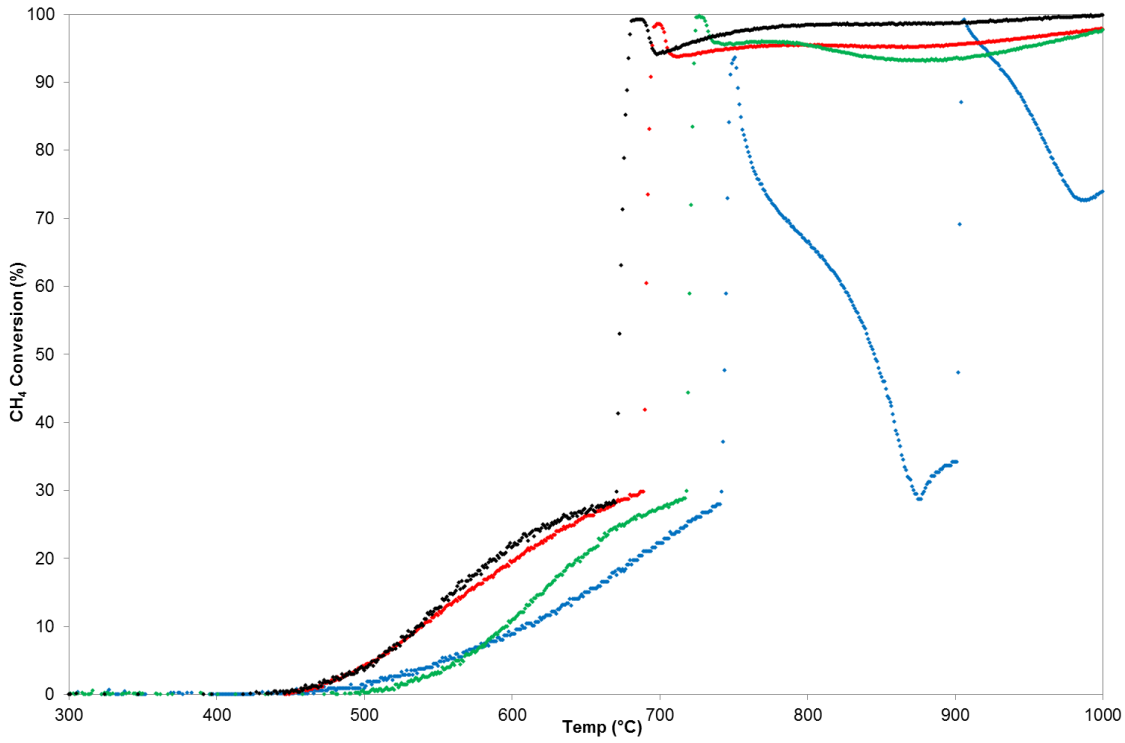

Figure A.1: CH_4 conversion during temperature programmed reaction of CH_4 + 0.5 O_2 over range of Ni/YSZ masses; 10 mg (Blue), 20 mg (Red), 30 mg (Green), 40 mg (Black).

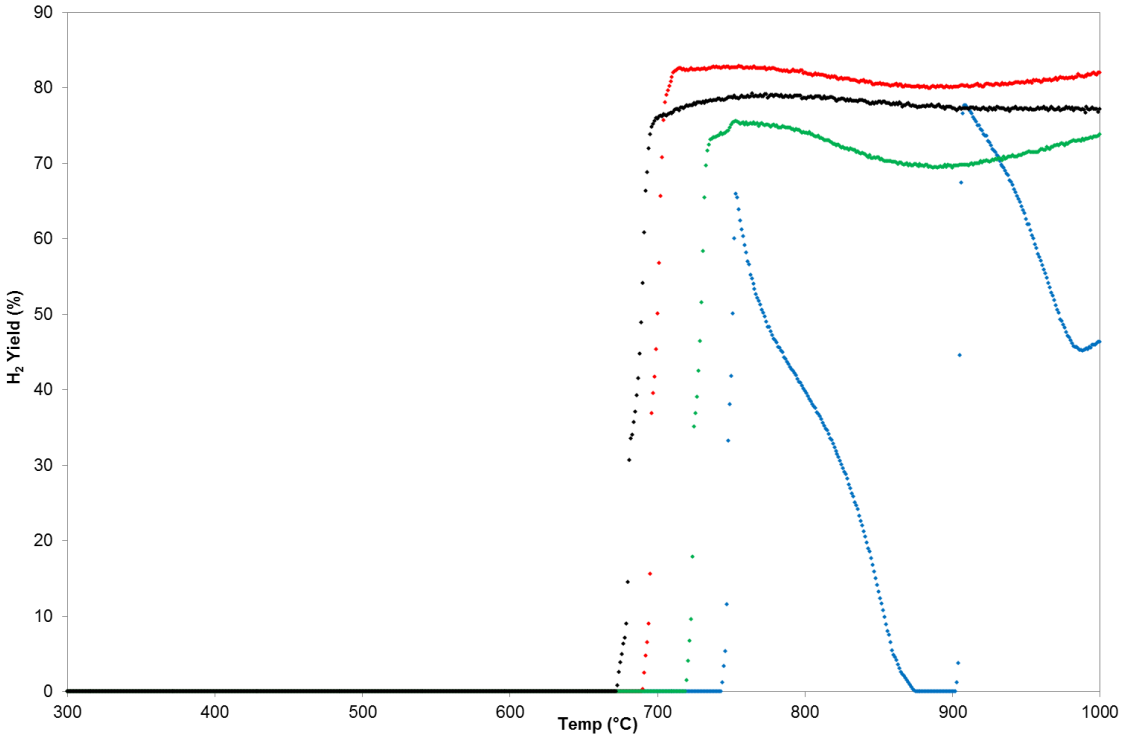

Figure A.2: H_2 yield during temperature programmed reaction of CH_4 + 0.5 O_2 over range of Ni/YSZ masses; 10 mg (Blue), 20 mg (Red), 30 mg (Green), 40 mg (Black)

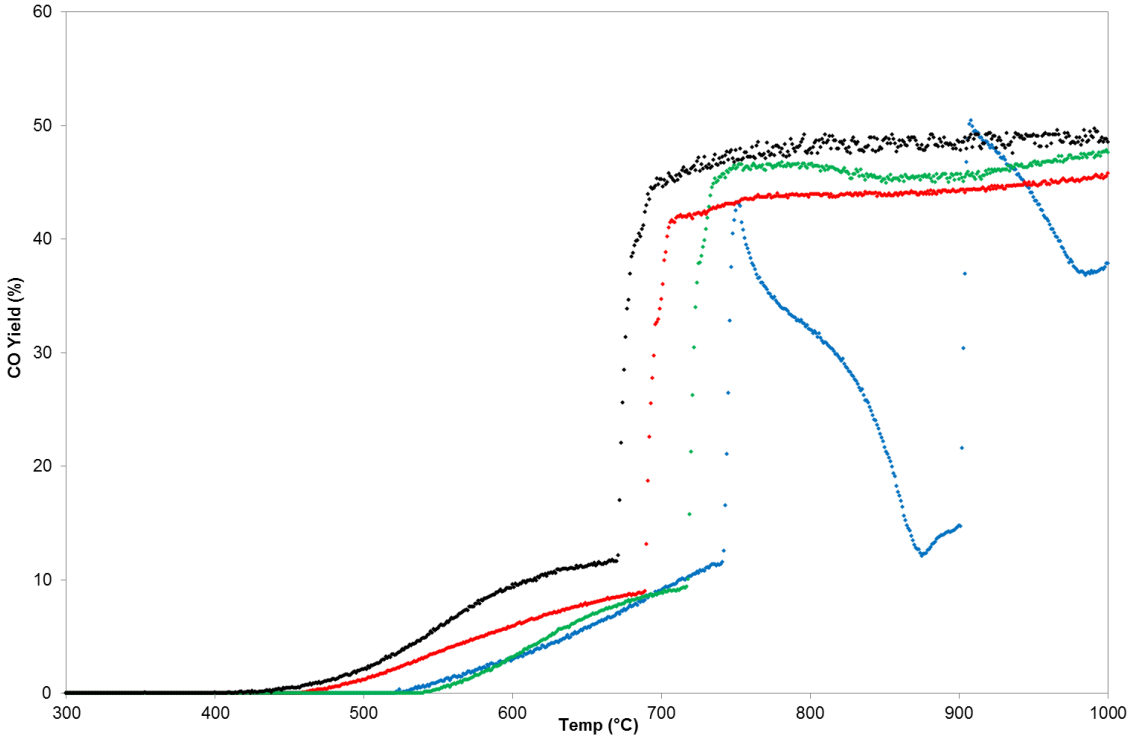

Figure A.3: CO yield during temperature programmed reaction of CH_4 + 0.5 O_2 over range of Ni/YSZ masses; 10mg (Blue), 20mg (Red), 30mg (Green), 40mg (Black).

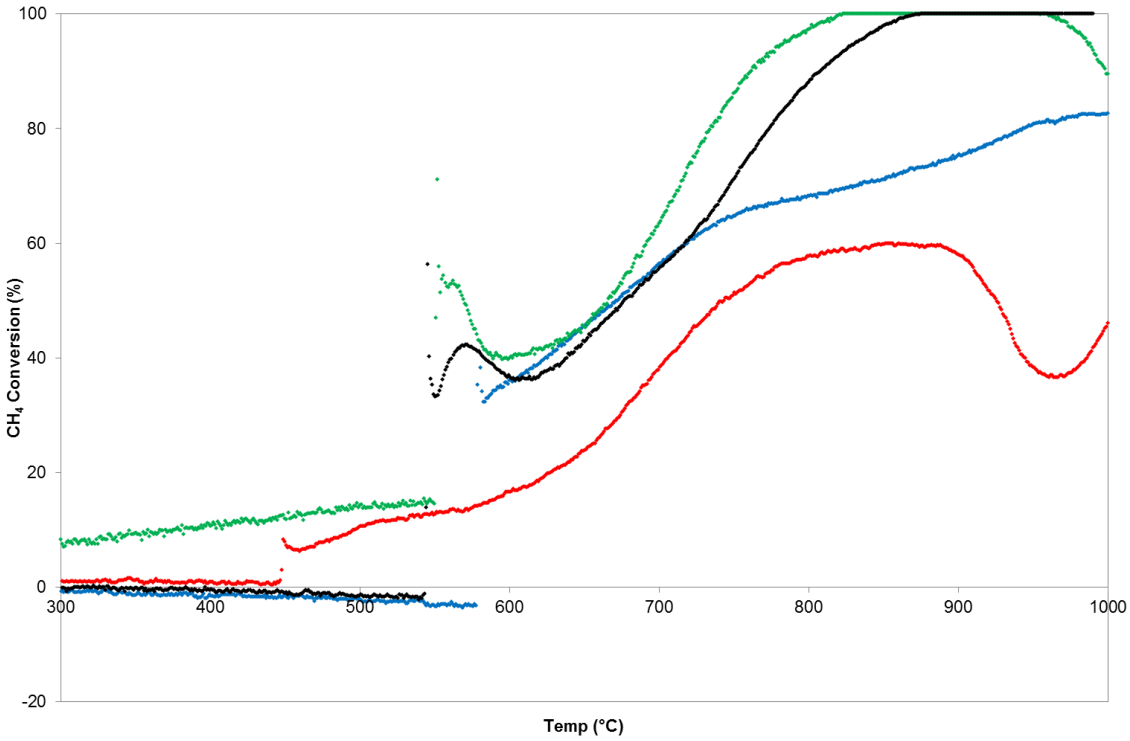

Figure A.4: CH_4 conversion during temperature programmed reaction of CH_4 + CO_2 over range of Ni/YSZ masses; 10 mg (Blue), 20 mg (Red), 30 mg (Green), 40 mg (Black).

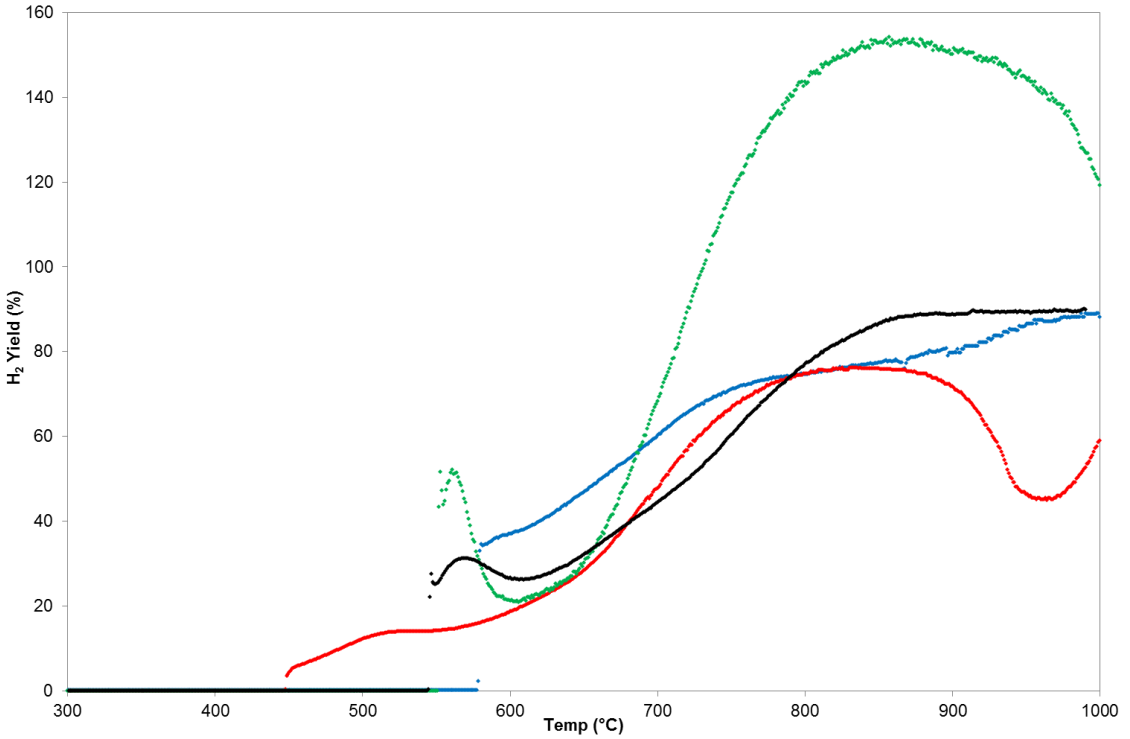

Figure A.5: H_2 yield during temperature programmed reaction of CH_4 + CO_2 over range of Ni/YSZ masses; 10 mg (Blue), 20 mg (Red), 30 mg (Green), 40 mg (Black).

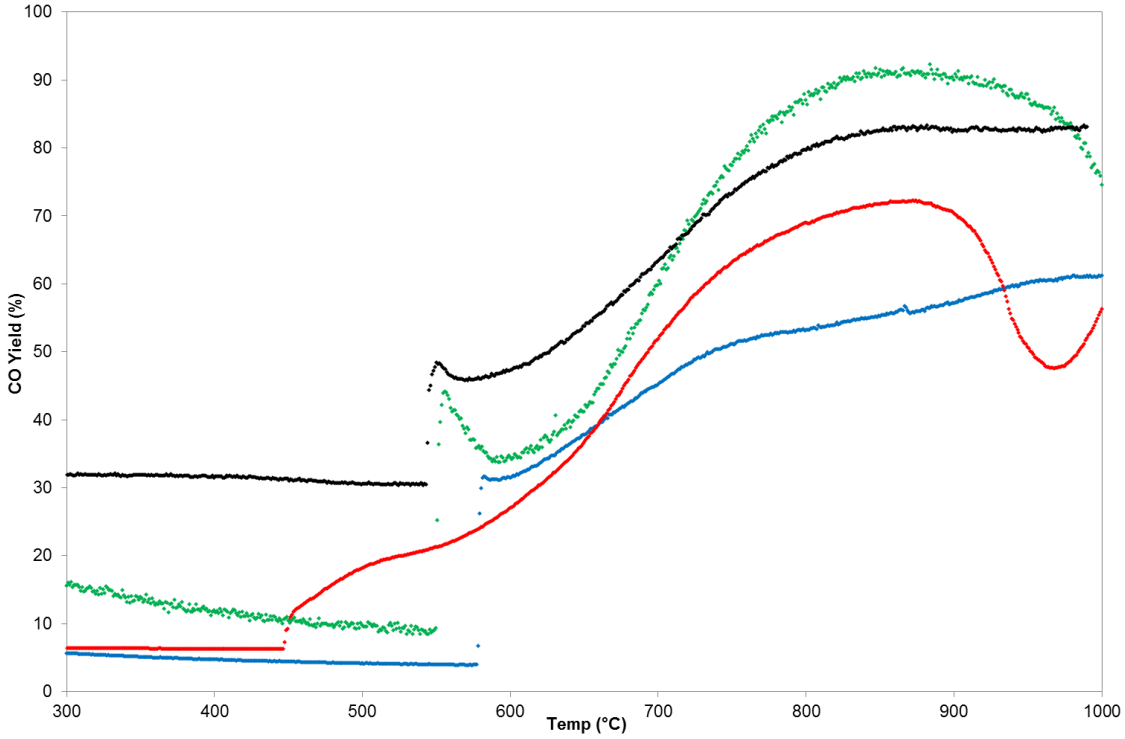

Figure A.6: Percentage CO yield during temperature programmed reaction of CH_4 + CO_2 over range of Ni/YSZ masses; 10 mg (Blue), 20 mg (Red), 30 mg (Green), 40 mg (Black).

Appendix B: Details of CH_4 conversions, CO yields and H_2:CO ratios

For the experiments conducted in the research study where CH_4 conversion and H_2:CO product ratio are not the primary function towards assessing the performance of the system, the details are not included in the main body of the text to make the document more concise. Alternatively, these details are included within this appendix.

Table A.1: Reforming analysis for reaction of CH_4 + CO_2 + xO_2 (x=0.00, 0.17, 0.25, 0.33) over Ni/YSZ at 700 °C after 5 hours and 20 hours

	Time (h)			
	CH_4 conversion (%)		**H_2:CO ratio**	
CH_4:xO_2	**5**	**20**	**5**	**20**
x=0.00	22.67	17.25	0.72	0.78
x=0.17	47.60	46.94	1.68	1.68
x=0.25	60.06	57.81	1.88	1.81
x=0.33	76.77	74.16	2.00	1.99

Table A.2: Reforming analysis for reaction of CH_4 + CO_2 + xO_2 (x=0.00, 0.17, 0.25, 0.33) over Ni/YSZ at 800 °C after 5 hours and 20 hours

	Time (h)			
	CH_4 conversion (%)		**H_2:CO ratio**	
CH_4:xO_2	**5**	**20**	**5**	**20**
x=0.00	30.84	25.08	1.17	1.27
x=0.17	73.51	70.14	1.99	2.09
x=0.25	87.58	85.85	2.07	2.08
x=0.33	99.71	99.38	2.07	2.04

Table A.3: Reforming analysis for reaction of $CH_4 + CO_2 + xO_2$ (x=0.00, 0.17, 0.25, 0.33) over Ni/YSZ at 900 °C after 5 hours and 20 hours

	Time (h)			
	CH_4 conversion (%)		H_2:CO ratio	
CH_4:xO_2	5	20	5	20
x=0.00	52.77	51.59	1.52	1.63
x=0.17	88.85	85.90	2.22	2.06
x=0.25	96.35	92.91	2.26	2.19
x=0.33	99.88	98.13	2.00	2.02

Table A.4: Reforming analysis for reaction of $CH_4 + CO_2 + xO_2$ (x=0.00, 0.17, 0.25, 0.33) over Ni/YSZ at 1000 °C after 5 hours and 20 hours

	Time (h)			
	CH_4 conversion (%)		H_2:CO ratio	
CH_4:xO_2	5	20	5	20
x=0.00	69.49	96.24	1.62	1.67
x=0.17	93.22	93.11	2.70	2.90
x=0.25	97.83	98.04	2.24	2.31
x=0.33	98.48	98.76	2.00	2.01

Table A.5: Reforming analysis for reaction of $CH_4 + CO_2 + xO_2$ (x=0.00, 0.17, 0.25, 0.33) over 5 mol% CeO_2-Ni/YSZ at 600 °C after 5 hours and 20 hours

	Time (h)			
	CH_4 conversion (%)		H_2:CO ratio	
CH_4:xO_2	5	20	5	20
x=0.00	23.24	33.73	0.44	0.46
x=0.17	23.67	27.21	0.76	0.73
x=0.25	33.87	36.26	0.88	0.92
x=0.33	43.13	43.24	1.05	1.09

Table A.6: Reforming analysis for reaction of $CH_4 + CO_2 + xO_2$ (x=0.00, 0.17, 0.25, 0.33) over 5 mol% CeO_2-Ni/YSZ at 700 °C after 5 hours and 20 hours

	Time (h)			
	CH_4 conversion (%)		H_2:CO ratio	
CH_4:xO_2	5	20	5	20
x=0.00	19.11	7.94	0.77	0.71
x=0.17	53.07	48.30	1.01	0.87
x=0.25	64.88	64.50	1.01	1.01
x=0.33	72.13	69.23	1.20	1.11

Table A.7: Reforming analysis for reaction of $CH_4 + CO_2 + xO_2$ (x=0.00, 0.17, 0.25, 0.33) over 5 mol% CeO_2-Ni/YSZ at 800 °C after 5 hours and 20 hours

	Time (h)			
	CH_4 conversion (%)		H_2:CO ratio	
CH_4:xO_2	5	20	5	20
x=0.00	39.06	32.16	1.09	0.96
x=0.17	72.36	66.73	1.12	0.88
x=0.25	85.93	83.73	1.39	0.98
x=0.33	96.76	96.46	1.34	1.13

Table A.8: Reforming analysis for reaction of $CH_4 + CO_2 + xO_2$ (x=0.00, 0.17, 0.25, 0.33) over 5 mol% CeO_2-Ni/YSZ at 900 °C after 5 hours and 20 hours

	Time (h)			
	CH_4 conversion (%)		H_2:CO ratio	
CH_4:xO_2	5	20	5	20
x=0.00	50.19	83.40	0.99	1.52
x=0.17	85.29	82.72	1.20	0.93
x=0.25	97.16	95.69	1.30	1.03
x=0.33	99.02	98.85	1.26	1.10

Table A.9: Reforming analysis for reaction of CH_4 + CO_2 + xO_2 (x=0.00, 0.17, 0.25, 0.33) over 5 mol% CeO_2-Ni/YSZ at 1000 °C after 5 hours and 20 hours

	Time (h)			
	CH_4 conversion (%)		H_2:CO ratio	
CH_4:xO_2	5	20	5	20
x=0.00	80.57	N/A	1.51	N/A
x=0.17	91.06	99.45	1.43	2.71
x=0.25	98.98	98.09	1.17	0.83
x=0.33	99.95	99.95	1.20	1.02

Table A.10: Reforming analysis for reaction of CH_4 + CO_2 + xO_2 (x=0.00, 0.17, 0.25, 0.33) with 5 ppm H_2S over Ni/YSZ at 600 °C after 5 hours and 20 hours

	Time (h)					
	CH_4 conversion (%)		H_2:CO ratio		CO yield (%)	
CH_4:xO_2	5	20	5	20	5	20
x=0.00	-6.60	-13.78	0.43	0.07	6.19	0.24
x=0.17	20.28	21.51	0.61	0.04	16.45	-1.59
x=0.25	30.62	25.00	0.84	0.03	17.87	-0.31
x=0.33	33.85	31.72	1.08	0.04	16.32	-0.21

Table A.11: Reforming analysis for reaction of $CH_4 + CO_2 + xO_2$ (x=0.00, 0.17, 0.25, 0.33) with 5 ppm H_2S over Ni/YSZ at 700 °C after 5 hours and 20 hours

	Time (h)					
	CH_4 conversion (%)		H_2:CO ratio		CO yield (%)	
CH_4:xO_2	5	20	5	20	5	20
x=0.00	-2.05	-30.17	6.19	0.24	16.52	0.12
x=0.17	50.24	27.76	16.45	-1.59	52.21	29.42
x=0.25	61.58	9.76	17.87	-0.31	54.91	-3.27
x=0.33	65.41	3.16	16.32	-0.21	59.21	0.17

Table A.12: Reforming analysis for reaction of $CH_4 + CO_2 + xO_2$ (x=0.00, 0.17, 0.25, 0.33) with 5 ppm H_2S over Ni/YSZ at 800 °C after 5 hours and 20 hours

	Time (h)					
	CH_4 conversion (%)		H_2:CO ratio		CO yield (%)	
CH_4:xO_2	5	20	5	20	5	20
x=0.00	12.51	-6.81	0.94	0.52	19.83	1.28
x=0.17	66.46	4.45	1.05	0.73	69.52	11.03
x=0.25	85.78	35.22	1.24	0.90	75.98	40.63
x=0.33	96.50	30.84	1.53	0.86	52.52	15.79

Table A.13: Reforming analysis for reaction of $CH_4 + CO_2 + xO_2$ (x=0.00, 0.17, 0.25, 0.33) with 5 ppm H_2S over Ni/YSZ at 900 °C after 5 hours and 20 hours

	Time (h)					
	CH_4 conversion (%)		H_2:CO ratio		CO yield (%)	
CH_4:xO_2	5	20	5	20	5	20
x=0.00	68.56	94.43	1.17	1.61	76.00	35.25
x=0.17	77.86	56.36	1.16	0.97	75.80	72.96
x=0.25	98.24	62.31	1.34	1.06	83.67	67.42
x=0.33	79.93	77.48	1.45	1.30	54.37	59.15

Table A.14: Reforming analysis for reaction of $CH_4 + CO_2 + xO_2$ (x=0.00, 0.17, 0.25, 0.33) with 5 ppm H_2S over Ni/YSZ at 1000 °C after 5 hours and 20 hours

	Time (h)					
	CH_4 conversion (%)		H_2:CO ratio		CO yield (%)	
CH_4:xO_2	5	20	5	20	5	20
x=0.00	91.80	100	2.35	0.34	36.40	5.21
x=0.17	85.13	79.09	1.17	1.02	76.57	91.18
x=0.25	98.62	95.96	1.23	0.94	88.75	116.42
x=0.33	98.53	99.25	1.55	1.42	62.19	67.23

Table A.15: Reforming analysis for reaction of $CH_4 + CO_2 + xO_2$ (x=0.00, 0.17, 0.25, 0.33) with 5 ppm H_2S over 5 mol% CeO_2-Ni/YSZ at 600 °C after 5 hours and 20 hours

	Time (h)					
	CH_4 conversion (%)		H_2:CO ratio		CO yield (%)	
CH_4:xO_2	5	20	5	20	5	20
x=0.00	-5.12	-18.51	0.53	0.08	10.78	0.23
x=0.17	23.60	16.98	0.69	0.59	17.31	9.91
x=0.25	23.54	23.69	0.88	0.04	16.04	-0.05
x=0.33	46.83	16.66	1.21	0.07	26.06	-3.93

Table A.16: Reforming analysis for reaction of $CH_4 + CO_2 + xO_2$ (x=0.00, 0.17, 0.25, 0.33) with 5 ppm H_2S over 5 mol% CeO_2-Ni/YSZ at 700 °C after 5 hours and 20 hours

	Time (h)					
	CH_4 conversion (%)		H_2:CO ratio		CO yield (%)	
CH_4:xO_2	5	20	5	20	5	20
x=0.00	1.61	-31.25	0.84	0.09	26.14	0.61
x=0.17	49.73	10.06	0.94	0.67	68.14	33.08
x=0.25	65.00	11.99	1.17	0.06	55.41	-1.18
x=0.33	65.58	9.34	1.37	0.08	42.94	-0.31

Table A.17: Reforming analysis for reaction of $CH_4 + CO_2 + xO_2$ (x=0.00, 0.17, 0.25, 0.33) with 5 ppm H_2S over 5 mol% CeO_2-Ni/YSZ at 800 °C after 5 hours and 20 hours

	Time (h)					
	CH_4 conversion (%)		H_2:CO ratio		CO yield (%)	
CH_4:xO_2	5	20	5	20	5	20
x=0.00	40.74	6.41	1.13	0.76	46.19	27.95
x=0.17	75.36	17.64	1.12	0.51	72.92	21.53
x=0.25	95.51	40.55	1.49	0.80	102.15	57.78
x=0.33	93.77	-3.25	1.53	0.26	60.13	0.76

Table A.18: Reforming analysis for reaction of $CH_4 + CO_2 + xO_2$ (x=0.00, 0.17, 0.25, 0.33) with 5 ppm H_2S over 5 mol% CeO_2-Ni/YSZ at 900 °C after 5 hours and 20 hours

	Time (h)					
	CH_4 conversion (%)		H_2:CO ratio		CO yield (%)	
CH_4:xO_2	5	20	5	20	5	20
x=0.00	44.35	87.46	0.84	1.39	103.17	52.53
x=0.17	82.35	75.55	1.22	0.85	78.05	110.82
x=0.25	97.17	62.95	1.35	0.95	89.84	87.87
x=0.33	69.48	52.42	1.30	1.08	52.33	49.24

Table A.19: Reforming analysis for reaction of $CH_4 + CO_2 + xO_2$ (x=0.00, 0.17, 0.25, 0.33) with 5 ppm H_2S over 5 mol% CeO_2-Ni/YSZ at 1000 °C after 5 hours and 20 hours

	Time (h)					
	CH_4 conversion (%)		**H_2:CO ratio**		**CO yield (%)**	
CH_4:xO_2	**5**	**20**	**5**	**20**	**5**	**20**
x=0.00	39.91	99.68	1.45	4.76	94.73	4.02
x=0.17	90.46	94.85	1.18	1.48	91.06	28.90
x=0.25	98.80	96.89	1.36	0.97	97.94	122.54
x=0.33	99.83	97.28	1.56	1.30	61.13	73.21